Estuaries and Coastal Zones
Dynamics and Response
to Environmental Changes

Edited by Jiayi Pan and Adam Devlin

Estuaries and Coastal Zones - Dynamics and Response to Environmental Changes

Edited by Jiayi Pan and Adam Devlin

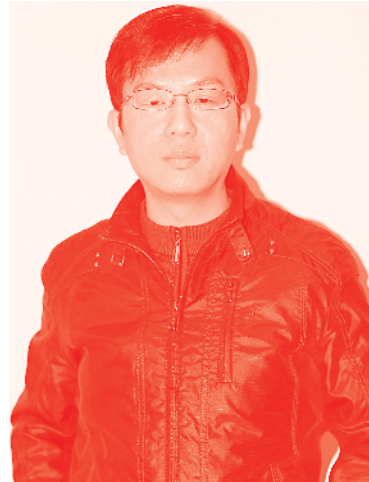IntechOpen

Supporting open minds since 2005

Notice
Statements and opinions expressed in the chapters are these of the individual contributors and not necessarily those of the editors or publisher. No responsibility is accepted for the accuracy of information contained in the published chapters. The publisher assumes no responsibility for any damage or injury to persons or property arising out of the use of any materials, instructions, methods or ideas contained in the book.

We are IntechOpen,
the world's leading publisher of
Open Access books
Built by scientists, for scientists

4,700+
Open access books available

121,000+
International authors and editors

135M+
Downloads

151
Countries delivered to

Our authors are among the
Top 1%
most cited scientists

12.2%
Contributors from top 500 universities

BOOK
CITATION
INDEX
CLARIVATE ANALYTICS
INDEXED

WEB OF SCIENCE™

Selection of our books indexed in the Book Citation Index
in Web of Science™ Core Collection (BKCI)

Interested in publishing with us?
Contact book.department@intechopen.com

Meet the editors

Professor Jiayi Pan received his Ph.D. in Physical Oceanography from the Institute of Oceanology, Chinese Academy of Sciences in 1996. He was a postdoctoral researcher at the University of Delaware from 1999 to 2003, then worked at the University of Southern Mississippi, Oregon Health and Science University, and the Portland State University in 2003-2004, 2004-2005, and 2005-2009, respectively. He became an associate professor in the Institute of Space and Earth Information Science, the Chinese University of Hong Kong in February 2009. Professor Jiayi Pan has been engaged in research on ocean remote sensing, air-sea interaction, estuarine dynamics, and internal wave dynamics for many years, and was principal investigator (PI) or Co-PI for a number of research projects. In July 2019, he joined the School of Geography and Environment, Jiangxi Normal University as a distinguished professor.

Prof. Adam T. Devlin is a physical oceanographer who analyzes the fluctuations in tides and sea level on a global and regional level, with special interest in the dynamics of the Western Pacific Ocean. He also studies the patterns of water level and meteorological changes using historical records and modern satellite data to better predict future flood scenarios and impacts to coastal populations and ecosystems. Prof. Devlin holds a PhD in Applied Physics from Portland State University, an MS in Applied Physics from Appalachian State University, and a BS in Physics from the University of Oregon. He worked at the Institute of Space and Earth Information Science, the Chinese University of Hong Kong from 2016 to 2019. Prof. Devlin joined the School of Geography and Environment, Jiangxi Normal University as a distinguished research professor in May 2019.

Contents

Preface

Estuaries and their surrounding wetland regions are among the most productive ecosystems in the world, and among the most populated, with more than half of humanity inhabiting their shores. Anthropogenic factors make estuaries highly susceptible to ecosystem degradation due to the influences of industrialization, overfishing, and pollution. Coastal waters are closely connected with human activity, and their dynamic processes may greatly affect coastal environments. It is believed that sea level rise can threaten coastal living conditions with higher probabilities of flooding and inundation, possibly amplified by local tidal changes in response to water level modifications. Estuaries are a transition zone between riverine and maritime environments, and their ecology is sensitive to physical, chemical, or biological changes. Many estuaries also discharge freshwater river plumes that may further influence coastal zone dynamics on all levels. This book provides a compendium of studies of estuarine dynamics, river plumes, and coastal water dynamics, as well as studies that have investigated the changes in estuarine and coastal zones in response to sea-level rise and other environmental factors. This book also provides a section on issues related to coastal environmental management. Topics covered in this section include consensus-based policies for the fishery industry, and efficient balancing of coastal erosion concerns with public utilization of recreation zones along the coast.

There are three sections in this book. The first section is "Coastal Tide and Sea Level Change", focusing on tide and sea level change in coastal waters. In Chapter 1 of the first section, tide, currents, and other physical properties in Elkhorn Slough waters of Monterey Bay, California, USA are analyzed to reveal the variations in a recent ~30-year period from 1970 to the early 2000s. Due to frictional effects and extensive mud flats and Salicornia marsh, tidal distortion increases, produces overtides, and compound tides; maximum tidal currents in Elkhorn Slough have increased from 0.75 to 1.50 m s^{-1} since 1970 mainly because of the increase in tidal prism between 1956 and 2003. The man-made changes and continued tidal erosion are the major reason of the tidal prism change. The second chapter reveals correlated changes in sea levels and ocean tides in the Pacific and Atlantic Oceans, and a detailed result of tide and sea level correlations in the Hong Kong coastal waters, suggesting tidal changes are likely to have the greatest effect on coastal locations, especially estuarine regions, which are often highly-developed, densely-populated, and environmentally sensitive. In Chapter 3, using numerical simulations, the influence of sea level rise (SLR) on storm responses is identified for Saco Bay, which is characterized by gentle coastal slopes, and Casco Bay, which is sheltered by barrier islands and peninsulas with steep shorelines. By comparing changes in inundation, storm currents, and salinity distribution between the two bays, the step-like bottom relief at the shoreline of Casco Bay sets up nonlinear responses to SLR. In contrast, storm responses in Saco Bay varied significantly with SLR due to alterations in river dynamics attributed to SLR-induced flooding. The conventional objections by satellite altimeters are normally inaccurate in the coastal waters due to the land effects on the return waveform; in Chapter 4, a promising technology, coastal altimetry, is described. It employs a new methodology to process the waveform from coastal waters. In a case study of the Hong Kong offshore water, it is found that the coastal

sea level trend is about twice as much as the one observed further offshore, suggesting that in the Hong Kong region, the short-term sea level trend significantly increases when approaching the coast.

The second section focuses on studies of the coastal and estuarine water with a title of "Observation and Analysis of Coastal Waters and Estuaries". The first chapter clarifies the dynamics of small river plumes, which are significantly different from that of plumes generated by large rivers. Small plumes exhibit more energetic temporal variability in response to external forcing, such as wind forcing and river discharge, the interaction between neighboring small plumes, and the generation of high-frequency internal waves in coastal ocean by small rivers. In the second chapter, a cruise survey of the Pearl River Estuary (PRE) and adjacent coastal water from May 3–11, 2014 was reported. Using the cruise data, a "sandwich" structure of the lateral salinity distribution and a two-layer structure of longitudinal circulation were identified. The Finite-Volume Community Ocean Model (FVCOM) is configured and run with high spatial resolution of 100 m in the PRE, which reveals that there is a strong neap-spring cycle for the PRE de-tided circulation. Chapter 3 analyzes the sampling data from six bimonthly surveys between November 2011 and September 2012 in the Jansen Lagoon, which is located to the northwest of São Luís Island (northern Brazil), with a significant urban influence. High levels of dissolved oxygen (DO), pH, total phosphorus, and chlorophyll-a were observed in the lagoon waters. The water quality indexes showed that the Jansen Lagoon has a poor water quality due to elevated DO and pH as well as high concentration of surfactants and phenols. Chapter 4 studies in-situ measurements of chromophoric dissolved organic matter (CDOM) absorption during a spring cruise survey in the Pearl River Estuary (PRE). The surface CDOM has higher absorption and lower spectral slope than the bottom. Horizontal transport is suggested to be the dominant hydrodynamic mechanism affecting CDOM distribution pattern in the PRE. Using an algorithm developed for the PRE environment, a time series of CDOM absorption and spectral slope in the PRE and the Hong Kong waters in spring from 2012 to 2018 is produced based on satellite images obtained by four sensors with different spatial and spectral resolutions. In Chapter 5, wind-driven coastal upwelling east of Hainan Island (UEH) in the northwestern South China Sea (SCS) is found to be sensitive to multiple scales of atmospheric forcing that are either very short-term or sudden impact, i.e., typhoon passages, or long-term variability associated with El Niño events. The study suggests that UEH has significant responses to the atmospheric forcing, and the ocean circulation also plays an important role in the modulation of the coastal upwelling.

Section 3 is "Coastal Environment Management". Chapter 1 emphasizes the importance of the coastal areas on potential of fisheries that can contribute greatly to the national economic growth. Good management requires a well-structured plan that takes into account geographical conditions and the sustainability of the plan in the future for the role of marine spatial planning. The dialogue between elite sectors of society and the public are important for the coherence and synergy of spatial planning, and consensus can be achieved based on potential spatial data integration between official spatial data and crowdsourced geographic information, which predominantly look from nontechnical perspectives. In Chapter 2, coastal environment issues such as coastal erosion, sea cliff collapses, etc. are discussed for the coasts along Northeast Brazil and northern Colombia, and how they can damage local economies. It is necessary to better plan for the occupation and uses of these coastal areas, in order to promote a sustainable development.

The chapters of this book provide detailed information on studies of coastal and estuarine environments and may help to inspire in-depth investigations in future. We are grateful to the authors and the publishing staff of IntechOpen for their excellent contributions to this book.

Professor Jiayi Pan and Professor Adam T. Devlin
Jiangxi Normal University,
Nanchang, Jiangxi, China

Section 1

Coastal Tide and Sea Level Change

Chapter 1

A 30-Year History of the Tides and Currents in Elkhorn Slough, California

William W. Broenkow and Laurence C. Breaker

Abstract

Elkhorn Slough was first exposed to the waters of Monterey Bay with the construction of Moss Landing Harbor in 1946. It follows a 10-km path inland from Moss Landing Harbor. Today, it is a habitat and sanctuary for a wide variety of marine mammals, fish, and seabirds. The currents, tides and physical properties of Elkhorn Slough have been observed since 1970. It is an ebb-dominated estuary due to the asymmetric rise and fall of the tides which produces ebb currents that dominate. Tidal distortion increases inland due to frictional effects and extensive mud flats and *Salicornia* marsh. Tidal distortion also produces overtides and compound tides. Tidal elevations and currents often reveal the characteristics of a standing wave system. The temperature and salinity of lower Elkhorn Slough reflect the influence of Monterey Bay waters, whereas the upper Slough is more sensitive to local processes. Maximum tidal currents in Elkhorn Slough have increased from ~75 to ~150 cm/s since 1970. This increase is primarily due to the change in tidal prism which has increased from ~2.5 to ~7.6 × 10^6 m^3 between 1956 and 2003. Finally, this increase is due to both man-made changes and continued tidal erosion.

Keywords: Elkhorn Slough, increasing tidal prism, ebb tide domination, erosion, standing wave system, man-made changes

1. Introduction

Since the late 1800s, human intervention has significantly altered the structure of Elkhorn Slough, and the circulation within it. Before 1946, Elkhorn Slough (ES) was a sluggish backwater with little influence from Monterey Bay. In 1946, the Army Corps of Engineers created Moss Landing Harbor located at the head of Monterey Submarine Canyon by cutting through the dune barrier that separated the Slough from Monterey Bay. ES is now a shallow, tidally-forced embayment that is directly coupled to Monterey Bay. Increased tidal action has led to a dramatic increase in tidal scouring, particularly in the lower part of the Slough [1]. The Slough was transformed from a fresh water, brackish environment to one that is primarily saltwater, and from an estuary that was primarily depositional to one that is now dominated by erosion. Since 1971, maximum tidal currents in the main channel at the mouth have increased from approximately 75 to 150 cm/s. The flood tide introduces relatively clear water from Monterey Bay while waters discharged during the ebb are laden with sediment eroded from the banks and bottom of the

Slough. This discharge creates a plume that extends 3 km or more offshore and is clearly visible in satellite imagery [2]. As erosion continues, the tidal prism and currents in ES increase, leading to further erosion. This behavior suggests a system with positive feedback, a situation that can become unstable.

Recent estimates of the erosional sediment losses from the Slough have ranged from 3.5×10^4 m³/year [3] to 8×10^4 m³/year [4]. Observations of bank erosion indicate average losses of 40 cm/year [5]. Bank erosion has widened the main channel, and the resulting increased tidal prism has led to an expanding network of tidal creeks that feed into the Slough (John Oliver, personal communication). According to Malzone and Kvitek [6], the tidal prism increased by 43% during the last decade and the surface area covered by salt water increased by 48%. Based on aerial surveys, losses to the surrounding wetlands (composed primarily of *Salicornia* marsh) have increased significantly over the past 50 years [7]. Erosion has led to an overall loss in vegetated marsh around the Slough that was most apparent during the first decade following the opening of Moss Landing Harbor.

Many environmental factors such as loss of *Salicornia* marsh, ichthyoplankton abundance, nutrient distributions, phytoplankton distributions, pesticide accumulation, and changes in biodiversity are related directly, or indirectly, to the circulation and physical properties of ES. According to Dyer [8], the physical, chemical, biological, and geological systems within a given estuary are, to a large extent, inseparable. Less is known about the physical environment of ES than perhaps some of its other defining properties. This is due in part to the spatial and temporal complexities of the circulation, and the rate at which physical changes to the system are occurring.

It is our purpose to summarize what is known about the tides, the circulation, and the physical properties of ES, based on a period of data collection that began in 1970 and continued into the early 2000s. In this regard, the manuscript is a period piece that spans a recent ∼30-year period. The work contained herein is based on the work of the first author's students, M.S. theses by some of these students, and, importantly, new observations. The text covers (1) the physical setting of the Slough, (2) the tides, (3), the physical properties, and finally, (4) the conclusions. This manuscript is based primarily on information that was contained in an unpublished report by Broenkow and Breaker [9]. However, a number of significant refinements have been made to that report which are included here for the first time.

2. The setting

ES is located in central California at the eastern side of Monterey Bay mid-way between Monterey and Santa Cruz. Several tributaries (i.e., lesser sloughs) including Bennett, Moro Cojo, and Tembladero Sloughs feed directly into ES or Moss Landing Harbor. Originally, ES was somewhat removed from direct tidal flow and the Salinas River discharged directly into Monterey Bay just north of the entrance to Moss Landing Harbor (**Figure 1**). In the late 1800s, the lands surrounding ES were altered through the construction of ditches and dikes to make the low-lying marshes suitable for agriculture. Around 1900, a 150-ha area near the mouth of the Slough was diked to form evaporative salt ponds. In 1908, the mouth of the Salinas River was diverted about 7 km to the south, removing any residual tidal influence from ES. When the U.S. Army Corps of Engineers created the channel between Monterey Bay and ES in 1946, the old Salinas River channel was dredged to form what is now Moss Landing Harbor (**Figure 2**) and the Slough was opened to full tidal circulation.

ES is about 10 km long, with depths ranging from 8 m at the harbor entrance, to 0.5 m near the head of the Slough (**Figure 1**). The average depth is approximately
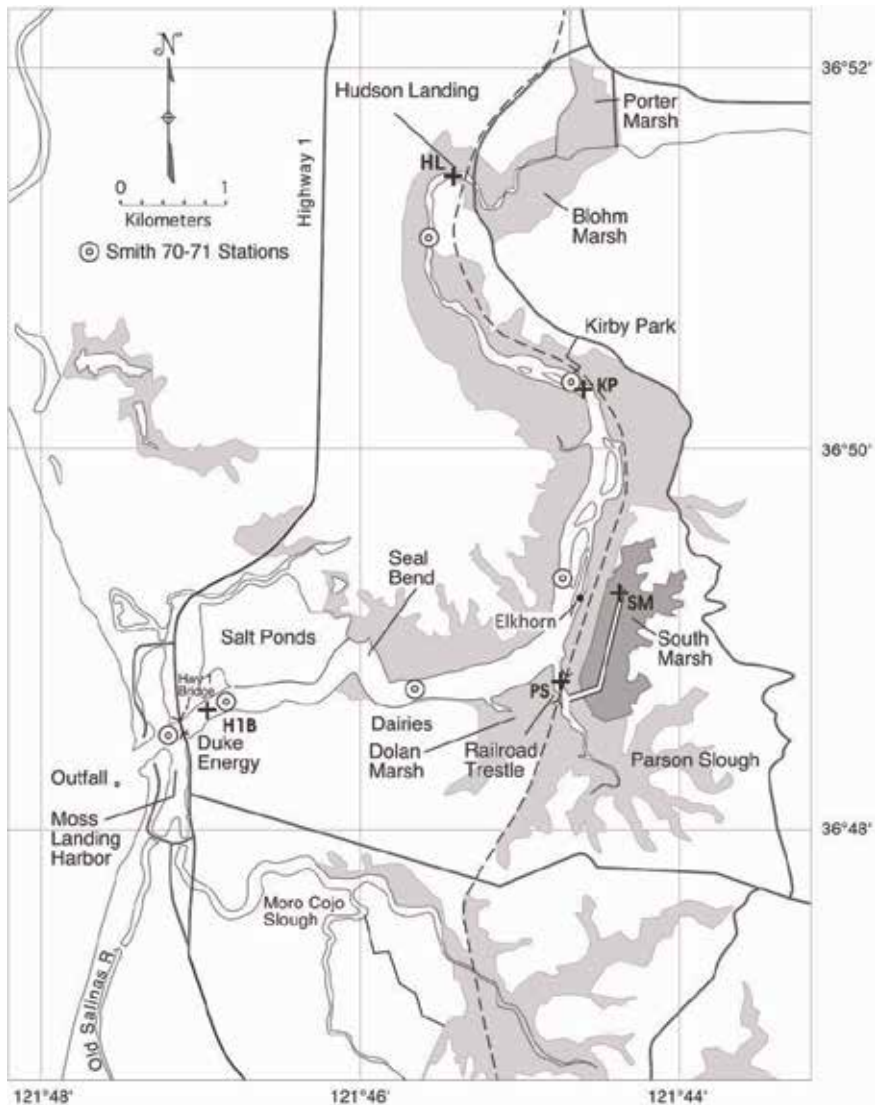
Figure 1.
Elkhorn Slough. This map was originally drawn by John Hansen from aerial photographs in 1971 and has been updated subsequently. Circles show Smith's [10] sampling stations. Crosses show tide stations.

3 m. The main channel has a width of about 200 m landward of the Highway 1 Bridge (H1B), to 90 m near the entrance of Parsons Slough. The ES drainage area is small: 585 km^3 [1], and significant fresh water enters the Slough only during winter months. The sinuous path of ES, with four major bends, has a major impact on its circulation. Because it is a complex, shallow waterway comprised of a main channel, extensive mud flats, *Salicornia* marsh, and small tidal channels, it is difficult to obtain reliable estimates of its volume, tidal prism, surface and cross-sectional areas, and bathymetry. **Figure 1** is a map of ES based on an aerial photograph taken in 1971 (Hansen, personal communication) with recent updates from 1993 aerial photographs. At low tide, the Slough consists essentially of a narrow channel whereas at high tide, waters entering the Slough inundate the surrounding mud flats, greatly increasing the surface area covered by water.

A number of prominent features in the aerial photograph of ES are shown in **Figure 3**: the lower Slough with the entrance cutting across the beach near the
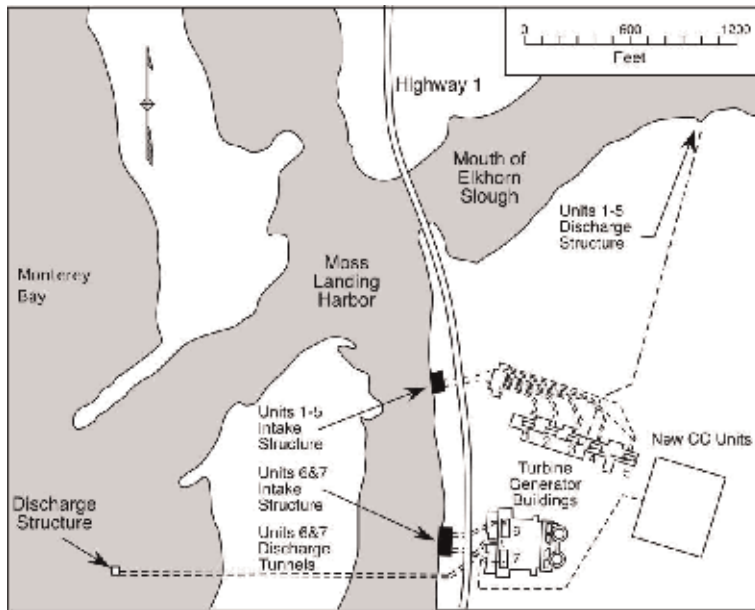
Figure 2.
Moss Landing Harbor, adapted from Duke Energy Moss Landing [10].

center; the Duke Energy Power plant with several reserve fuel storage tanks paralleling the lower slough; the now abandoned National Refractories and Minerals plant with a large tailing waste pond composed of mainly calcium carbonate precipitate, and Moss Landing Harbor with a small fishing fleet and pleasure boat moorings. The Highway 1 Bridge near the Duke power plant has been the site of a number of current meter studies. Near the main northward bend in the channel (**Figures 1** and **3**), a linear strip of land supports the Southern Pacific railroad and separates the main Slough from Parsons Slough and the South Marsh. This relatively large body of water is connected to the Slough through a 50-m wide channel under the railroad trestle. Because Parsons Slough and the South Marsh serve as one body with respect to ES, we will usually refer to them as Parsons Slough from this point on unless there is a reason to refer to them separately.

Figure 3.
A more recent aerial photograph of Elkhorn Slough taken in September 2002, looking eastward from an altitude of 1500 m (courtesy of Scott Benson).

During the past 25 years, major changes have occurred in the Slough's morphology, and these have further altered its tidal response. During the winter months when the Salinas River flows into the bay, a channel is bulldozed across the beach 7 km south of Moss Landing to prevent local flooding in the surrounding towns of Castroville and Moss Landing. The sources of freshwater entering the Slough during this period include rainfall and agricultural runoff from its small drainage basin. Moss Landing Harbor receives a continual supply of low salinity water from agricultural runoff, and before 1982, when the Monterey Regional Outfall began operation, treated sewage discharge from Castroville entered the system via Tembladero Slough south of Moss Landing Harbor. These waters now enter the south harbor at low tide through a tide gate. Recently, another tide gate limiting the flow of waters into Moro Cojo Slough has been removed, and that area is again open to tidal action. Recent changes in bottom depth at one location are readily apparent in the four profiles shown in **Figure 4**. These profiles, taken at the Highway 1 Bridge, show that bottom depth and channel width have both increased significantly since 1972.

The Duke Energy of North America Power Company operates the largest power generation plant (2.5 gW) in California at Moss Landing (**Figures 2** and **3**). Before Duke Energy acquired the plant in 1998, it was operated by the Pacific Gas and Electric Company (PG&E power plant or simply PG&E). At that time, seawater coolant was pumped from the east side of Moss Landing Harbor at a maximum rate of 2.7×10^6 m³/day, with a temperature of 7–10°C above ambient [11]. The original five power generating units (1–5) discharged coolant waters into Elkhorn Slough, while coolant waters from units 6 and 7 were discharged into the head of Monterey Submarine Canyon within 200 m of the harbor entrance. In 1998, discharges into Elkhorn Slough were eliminated. In July 2002, two new 1.1 gW gas turbine generation units became operational and their coolant waters were discharged through the offshore outfall (**Figure 2**). Until recently, the National Refractories and Minerals (NRM) operated a magnesium extraction plant, just south of the Duke Energy
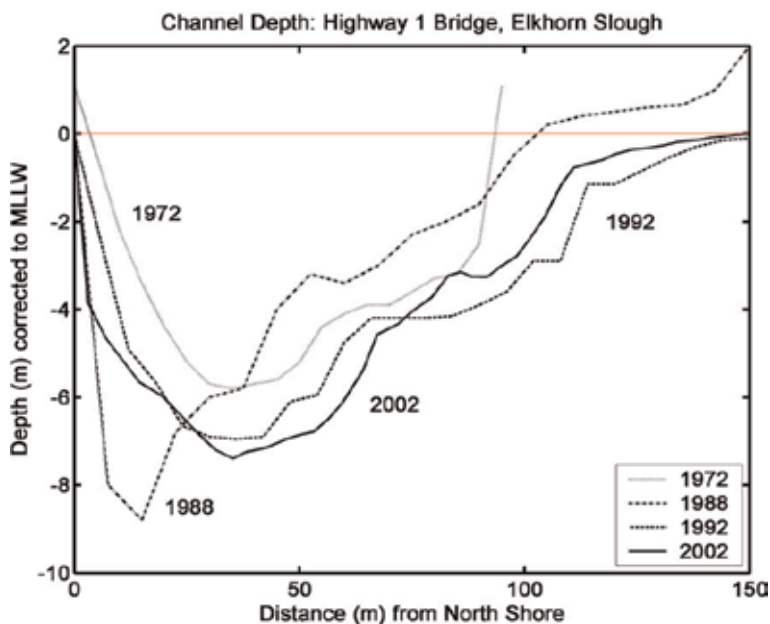
Figure 4.
Bottom profiles at Highway 1 Bridge (H1B). Depths are referenced to MLLW.

plant. The National Refractories plant ceased operation in the year 2000, but the tailing pond of $CaCO_3$ remains.

The last large-scale change to the hydrography of Elkhorn Slough was implemented by the California State Department of Fish and Game in 1983. Dairy pastures of 160 ha (1.6×10^6 m^2) were returned to tidal flooding by digging a channel across former dikes and excavating about 10% of the marsh to a depth of 2 m below MLLW. This area, called the South Marsh, is now part of the Elkhorn Slough National Estuarine Research Reserve (ESNERR). More recently, ES may have been affected by the 1989 Loma Prieta earthquake. Cracks in the surrounding marshlands have been identified that appear to be related to this event (R. Kvitek, personal communication) and there is evidence that the *Salicornia* marsh has settled (G. Greene, personal communication).

3. The tides

3.1 Introduction

The tides in ES are mixed, and thus are similar to those found elsewhere along the California coast. The form ratio for the tides in Monterey Bay is 0.96, indicating that the tides are mainly semidiurnal. A characteristic of the tides in ES is that the greatest tidal range during the tidal day corresponds to the transition *from* MHHW *to* MLLW. This is an important factor that determines in part the relative speeds of the ebb and flood currents. The mean range of the semidiurnal tide for the four principal tidal constituents ($K_1 + O_1 + M_2 + N_2$) at the Highway 1 Bridge (H1B) is about 1.2 m, with a mean diurnal range of 1.7 m. The spring range is about 2.5 m, while the neap range is about 0.9 m [12].

3.2 Tidal constituents

The observed tide is represented as a sum of harmonic constituents, each with its own amplitude and phase. The number of constituents, and their corresponding amplitudes and phases, are specific to a given location. The primary tidal constituents fall into three categories: semidiurnal, with periods of approximately half a day; diurnal, with periods of approximately a day; and long-period, with periods of two weeks, to years. The tidal analyses for Monterey Bay and ES are based on record lengths of a year or less. Consequently, it is not yet possible to resolve the longer period constituents. The M_2, K_1, O_1, S_2, P_1, and N_2 constituents (amplitudes in descending order), are the six most important constituents for Monterey Bay. In addition to these, at least 15 other constituents have been identified in tidal records collected in Monterey Bay by the National Ocean Service and recorded in the Tide Tables they have produced.

To obtain data suitable for predicting tidal height and phase, water levels in ES were measured from June 2002 to August 2003. Our 120-day records for three stations in ES were of sufficient length to separate most of the constituents listed in **Table A1**, which is included in the Appendix A, following the references. However, the tidal amplitudes obtained from these analyses were not directly comparable to those obtained earlier by the National Ocean Service from year-long observations in 1976, because the variability was distributed among slightly different constituents and because the record lengths were different. The data acquired by NOS is included in **Table A2** of the Appendix A. Our record lengths varied from 1 to 14 months (**Table A1**). Although the constituent amplitudes around the diurnal (1 cycle per day [cpd]) and semidiurnal (2 cpd) frequencies for the MB and ES

stations are similar, the appearance of the higher frequency constituents between 2.8 and 3.9 cpd inside ES clearly distinguishes its tidal response from that of Monterey Bay. In addition, overtides were found with periods of 8.3, 6.2, and 4.1 h that correspond to the M_3, M_4, and M_6 constituents, respectively. The 8.3-h M_3 constituent represents one of the lunar terdiurnal components. Because its period is close to the period of the terdiurnal SO_3 compound tide (8.19 vs. 8.28 h), the SO_3 constituent could not be clearly separated from the M_3 tide.

A comparison of the tidal constituents determined from our water level measurements at six locations is shown in **Figure 5** and illustrates the differing character of the tide from MB to the head of ES: Monterey Harbor (a), representative of Monterey Bay, Moss Landing Harbor (b), the H1B (c), the entrance to Parsons Slough (d), Kirby Park (e), and Hudson's Landing (f). Log_{10} of the amplitude in mm is plotted vs. each constituent frequency in cpd. A similar constituent analysis for Monterey Bay was performed 25 years earlier by the National Ocean Service
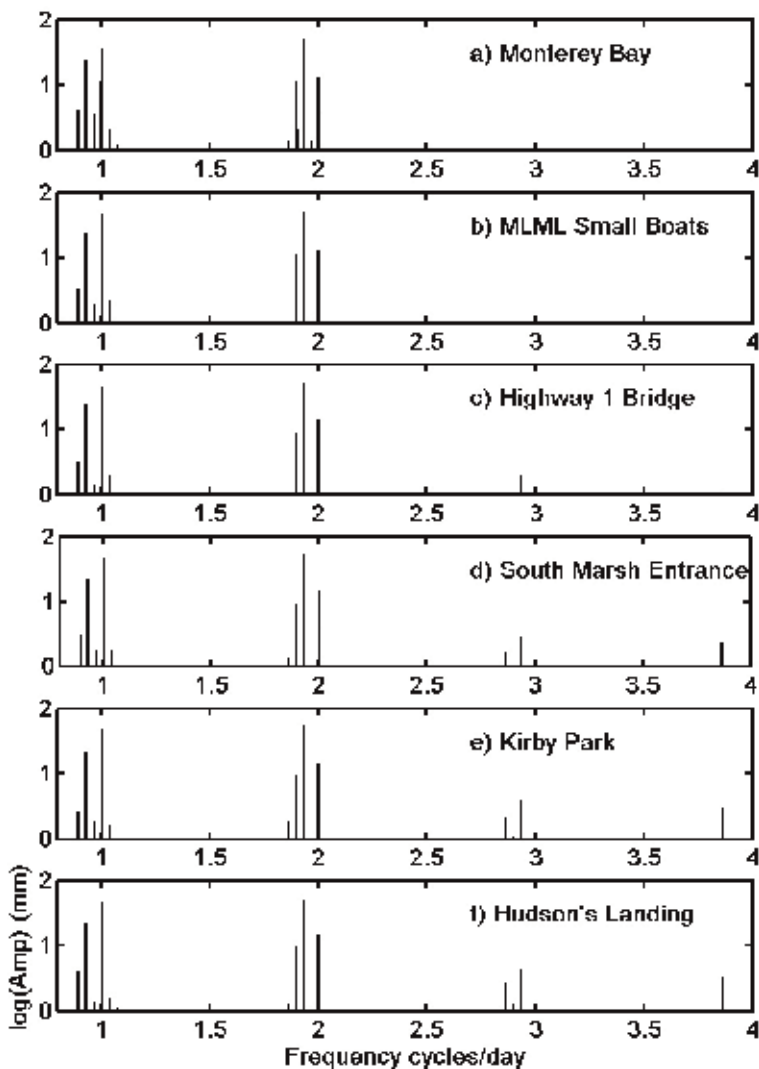
Figure 5.
Log_{10} tidal constituent amplitude vs. frequency for five locations in Elkhorn Slough (**Figure 1**): (a) Monterey Bay (NOS, 1 year); (b) Moss Landing Harbor at MLML Small Boat Dock; (c) Lower Elkhorn Slough 200 m east of Highway 1 Bridge; (d) Railroad Trestle at the entrance to Parsons Slough; (e) Kirby Park; (f) and Hudson Landing.

(NOS) from a 1-year record acquired in 1976 in Monterey Harbor and comparisons with our analysis are constructive.

Our least squares regression results which are summarized in **Table A1** of the Appendix A show large amplitudes for the dominant tidal constituents (M_2, K_1, O_1, S_2, P_1, and N_2) at the ES stations indicated above similar to those obtained earlier by NOS (**Table A2**). Our results in Moss Landing Harbor show insignificant values for the overtides (M_3, M_4, and M_6) and the compound tides (MK_3, $2MK_3$, MN_4, and MS_4). The amplitudes of these constituents increase significantly as we move landward, consistent with similar increases in these constituents obtained by NOS, and consistent with the increasing influence of frictional effects as the bottom depth decreases moving inland. Of particular note, we find a ~25% increase in the 2002 data compared to the 1976 data, suggesting that morphological changes in ES have modified its tidal response noticeably over a period as short as 25 years! In addition, we now include the set of tidal constituents inside the ESNERR South Marsh restoration area in **Table A1**. They demonstrate that South Marsh is not tidally choked (i.e., providing insufficient time for the unrestricted inflow and outflow of the tidal transport over a complete tidal cycle) despite being limited by the 50-m-wide, 4–6-m-deep entrance under the Southern Pacific Railroad Trestle.

Tidal phase differences in ES were estimated by Wong [13] by comparing the times of high and low water at several locations consistent with tidal propagation up the Slough. Between a point 200 m east of the H1B, and 5 km up the Slough near the Parsons Slough entrance, Wong found, on average, that high water occurred 48 min later at Parsons Slough but low water occurred only 18 min later. The large difference between the HHW and LLW phases at these two locations, emphasizes the tidal asymmetry in ES. Wong also compared these values with the NOS tide predictions from 1976 and found that the time for the tide to propagate over this portion of the Slough had increased significantly.

Based on shallow water wave theory, the expected phase speed, $c(x,t)$, for the incoming tide where tidal elevation and water depth are of the same order, is

$$c(x,t) = [\, g(h(x) + \eta(x,t))]^{\frac{1}{2}}, \tag{1}$$

where h is the water depth, η is the tidal elevation, and g is the acceleration of gravity. The tide propagates at 6.3 m/s for a water depth of 4 m with a free surface elevation $\eta(x,t)$ of zero. Integrating $c(x,t)$, the travel times along the Slough from the H1B to Hudson's Landing using channel depths for the diurnal mean tide (high = 1.7 m, low = 0.0 m) are 24 and 31 min. These times change to 23 and 37 min for the greatest observed tidal range (2.0 to −0.6 m).

3.3 Tidal currents

The first measurements of the tidal currents were made in 1970 by Clark [14] in the main channel on the harbor side of the Highway 1 Bridge. We note that since this record was not referenced to a standard tidal datum, the exact depth of these observations is not known but they were acquired at "mid-depth," clearly well above the bottom boundary layer. Clark made a total of five time series measurements with durations of one to two tidal days using a mechanical current meter. A 2-day sample is shown in the first (i.e., top) panel of **Figure 6**, where maximum currents of almost 40 cm/s were observed during the 0.75 m flood tide and 60 cm/s on the following 1.75 m ebb tide. Ebb domination is apparent as the flood tide lasted almost twice as long as the ebb. Clark observed that the tidal currents in ES were approximately standing wave in character because the tidal heights and currents were approximately 90° out of phase.

Wong [13] used an ENDECO 714 current meter set at a height of 1.6 m above the bottom to measure the flow near the H1B for a 2-week period in September 1986 (**Figure 6**—second panel). He found maximum speeds of 80 cm/s during the ebb tide. Because these measurements were made within the bottom boundary layer, he estimated the values to be approximately 20% lower than the corresponding free-stream velocities, assuming a logarithmic velocity distribution in the bottom boundary layer [15]. From measurements made at the H1B during a spring tide, Wong estimated speeds as high as 113 cm/s on ebb and 75 cm/s on the flood. More recent observations at the entrance to Parsons Slough (**Figure 1**) approximately 4 km from the entrance to Moss Landing Harbor indicate maximum flooding and ebbing velocities of 150 and 170 cm/s, respectively. These current speeds are significantly higher than those measured by Wong at the H1B, a result of the narrow entrance to Parsons Slough, and thus are not representative of the flows encountered in the main channel of ES. Wong found that cross-channel velocities were less than 3 cm/s at all locations, consistent with highly channelized flow. Wong's data indicated that velocities near the mouth were approximately 50% greater than Clark's measurements, apparently due to the increase in tidal prism resulting from the addition of the South Marsh to tidal flooding and to the continued effects of erosion over the 16 years between the two sets of measurements [5]. Finally, Wong [13] found that overall, over 90% of the variance in current speed in ES is caused by the tides.

We made current measurements in 1992 with an InterOcean S4 current meter suspended from the H1B, 3 m above the bottom. Again these measurements indicate increasing tidal flows at the H1B where maximum speeds on the ebb tide approaching 120 cm/s were observed (**Figure 6**—third panel). The higher-frequency ripples superimposed on the tidal current record are primarily due to seiche period oscillations in Monterey Bay [16]. Our most recent record (**Figure 6**—bottom panel) shows a 1-month sample from a 14-month time series made with an InterOcean S4 current meter located 1.1 m above the bottom (almost certainly within the bottom boundary layer) in the main channel approximately 250 m east of the H1B. Modulation of the primary diurnal and semidiurnal tidal currents by the spring and neap tides produces maximum ebb currents during the spring tide (105 cm/s) that are three times greater than the maximum ebb currents observed during the neap tide (35 cm/s). Adjusting for boundary layer attenuation, the near surface ebb and flood speeds could reach 125 and 42 cm/s, respectively.

During December 1993, Malzone and Kvitek [6] used an S4 current meter to measure currents near the time of maximum ebb at four locations along the main channel of ES (**Figure 7**). These results show a steady decrease from slightly over 100 cm/s at the mouth, to approximately 50 cm/s at 8.5 km inland. This decrease in current speed is consistent with the reduced tidal prism landward of each measurement location. The large decrease in current speed between 2.2 km and 6.5 km is caused by the addition of waters that drain from Parsons Slough at about 3.5 km from the H1B.

Vertical current profiles in ES have been examined on several occasions. Wong [13] constructed vertical current profiles from observations acquired during May 1987 and April 1988, approximately 200 m from the H1B during peak flow on the ebb tide (**Figure 8**). He found a significant reduction in speed in the deepest 3–4 m with vertical shears as high as ∼10 cm/s/m. His data showed no well-defined core of maximum speed. He made these measurements by lowering and raising a single S4 current meter. Wong used his data to estimate a roughness length for the bottom and a thickness for the bottom boundary layer using standard boundary layer parameterizations. From a logarithmic decay law for the boundary layer, he estimated a bottom roughness length of 6.5 cm. Using this figure, he calculated a
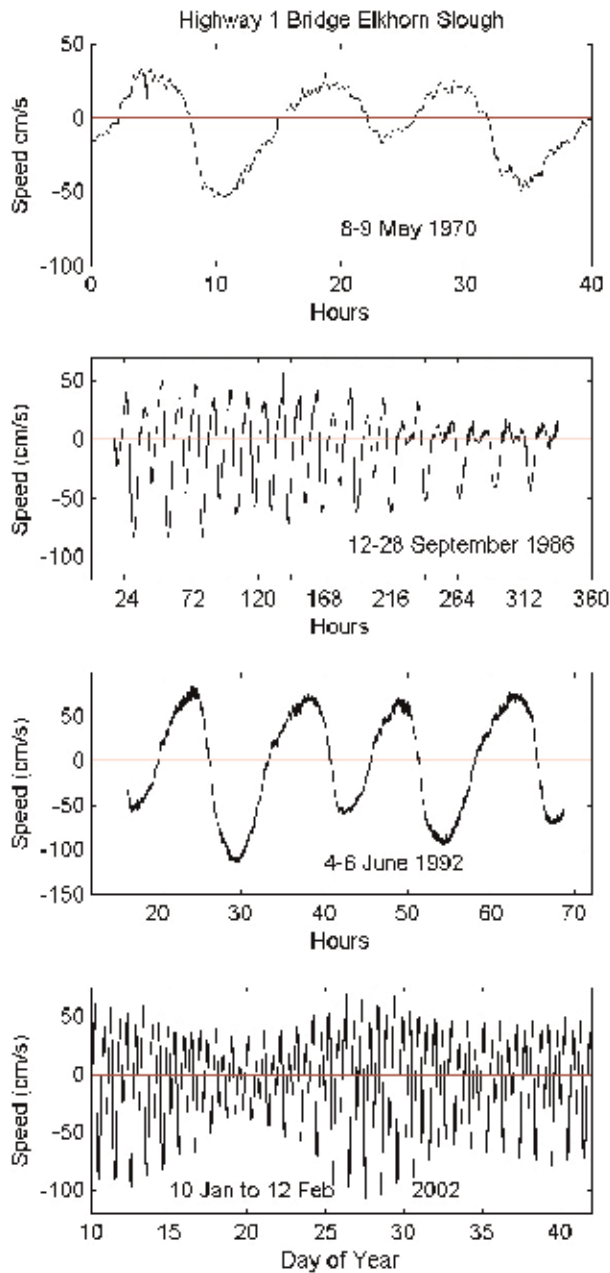
Figure 6.
Current measurements acquired in Elkhorn Slough at or near the Highway 1 Bridge (H1B). The top panel shows Clark's [14] first measurements in ES using a paper recording TSK current meter. In the second panel, Wong's [13] measurements are shown where an S4 meter suspended from the bridge was employed. In the third panel, our 1992 measurements duplicating Wong's method are shown, and finally, in the fourth or bottom panel, our S4 current measurements from January (2002) are shown using a bottom mounted current meter at 1.1 m above the bottom and 200 m east of the H1B.

friction velocity for the bottom, and used the friction velocity to estimate a thickness for the bottom boundary layer of 3.3 m, following Komar [17].

Vertical profiles constructed from current meter data collected closer to the H1B in February 1994 at different stages of the tide [4], indicate less vertical shear in the upper 5 m, but increased shear in the bottom boundary layer where the thickness of the layer itself appeared to be less than 2 m (not shown). These results taken near
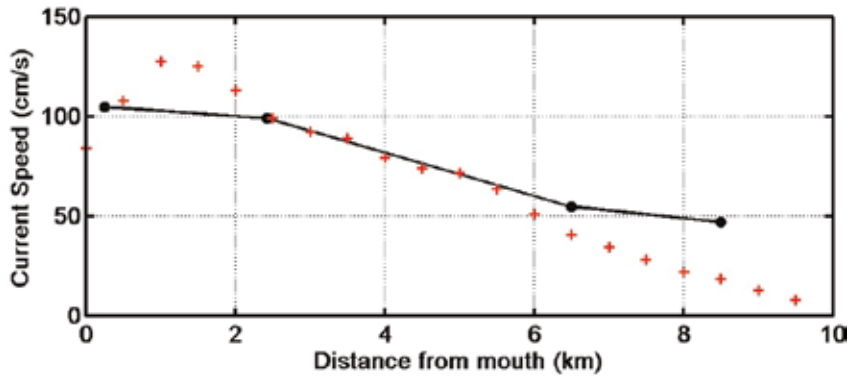
Figure 7.
*The red crosses show main channel current speed measurements made near maximum ebb tide (taken from [6]). The solid black line shows results of the continuity model (redrawn from **Figure 17**). Greatest changes are found inland of the Parsons Slough entrance.*
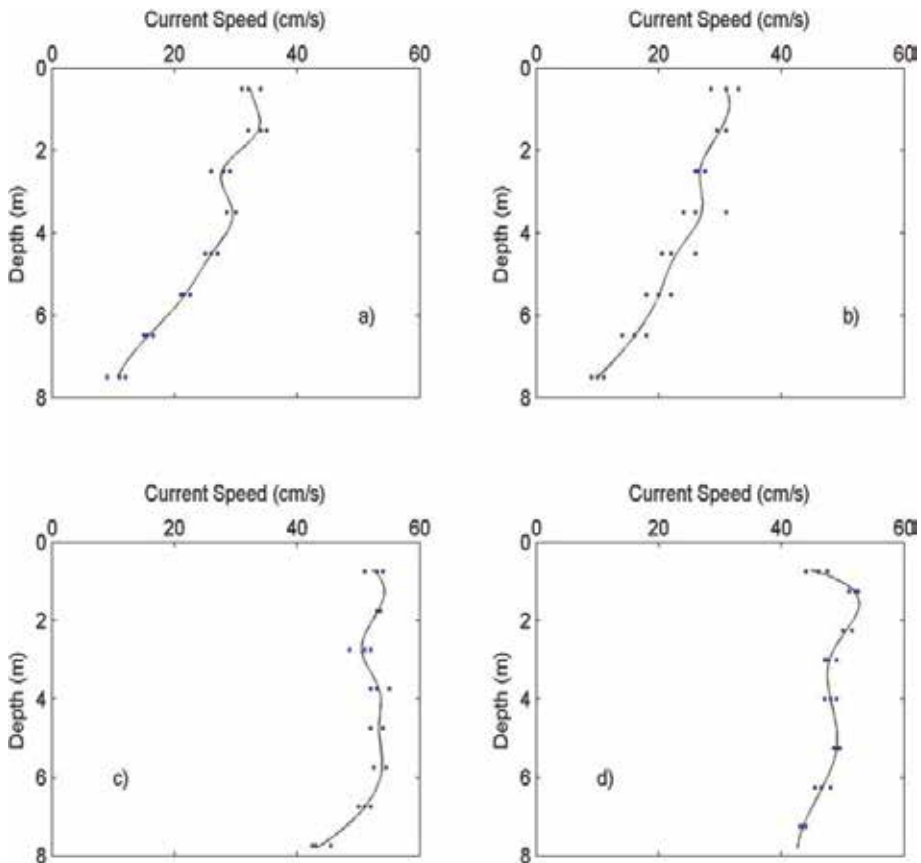
Figure 8.
Vertical current profiles in ES show deceasing current speed in the bottom boundary layer which extends up to 3 m above the bottom [13]. All times are PST + 8 h. (a) 20 May 1987, 22:30; (b) 30 May 1987, 23:00; (c) 9 April 1988, 07:30; and (d) 22 April 1988, 08:30.

the H1B where the primary channel is about 100 m wide, suggest that velocity shear near the bottom may be large enough to mix the entire water column above. Wong's and Malzone's results also demonstrate that tidal current speeds had increased during the 6-year interval between their observations.

Until 2002, no measurements of the tidal currents in and around Parsons Slough and the adjoining South Marsh had been made. This overlooked area contributes at least 30% to the tidal prism of ES, as we discuss in Section 6. As a result, ADP observations of the currents at the entrance of Parsons Slough were acquired on 20 November 2002 over a half-tidal cycle. The results are shown in **Figure 9**. We gauged the ebbing flow from the ESNERR area with nine transects made up of ten stations each spaced about 10 m apart across the 90 m wide channel. Tidal currents during the ebb cycle were acquired with speeds often in excess of 100 cm/s with a maximum speed of 112 cm/s observed during a 2-h period when the ebbing flow was most intense. Ebbing flow in this channel is deflected clockwise (looking in the direction of flow), and maximum speeds were always observed in the 5 m-deep channel close to the southern (right) bank consistent with centripetal acceleration. Horizontal shear near the south bank approached 10 cm/s/m.

Wong [13] observed a large time lag and reduced amplitude between the tide in the ES main channel and the tide in the ESNERR suggesting that the tide was restricted, indicative of tidal choking as encountered by Kjerfve and Knoppers [18] in a coastal lagoon along the U.S. East Coast. Our observations show that the principle tidal range in the ESNERR (**Table A1**) is virtually identical to that observed at the SP railroad trestle, and that HHW in the South Marsh lags that at the SP railroad trestle by only 20 min, not necessarily consistent with tidal choking. These results also indicate that relatively large volumes of water are exchanged between Parsons Slough and ES itself. Clearly, additional measurements of the tidal currents through the entrance of the Parsons Slough/South Marsh area are required to better understand this relatively new and overlooked portion of the Slough.
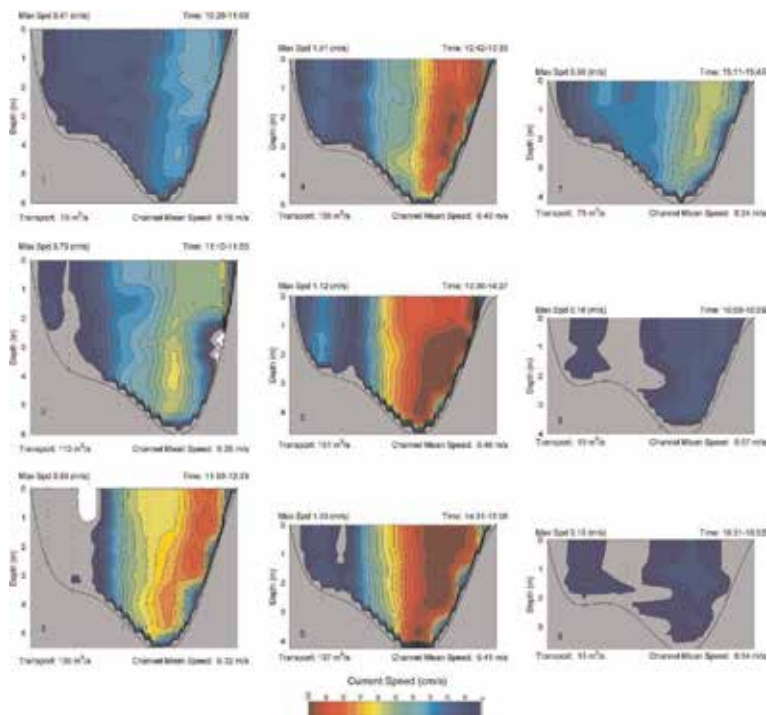
Figure 9.
ADP vertical sections of along-channel currents landward of the SP railroad trestle at the entrance to Parsons Slough. The south shore is on the right. These data were obtained through an ebb tidal cycle 20 November 2002. The integrated transport was 2.4×10^6 m^3.

Figure 10 shows a time series obtained from an S4 current meter deployed close to the location where the ADP measurements were acquired and during the same period. Vigorous tidal flows are observed that approach 100 cm/s during the ebb tide and values that approach 60 cm/s during the flood. Higher frequency oscillations superimposed on the tidal records are due to the natural seiche oscillations of Monterey Bay [16].

All of the current measurements made in Elkhorn Slough until 2003 were acquired at a single location in the cross-slough direction, usually in the main channel. Hence, cross-channel shear had not been measured, although its importance in making volume transport calculations was well recognized. Without some knowledge of cross-channel current variability, it is impossible to obtain even crude estimates of the water volume exchange between the Slough and the Bay over a complete tidal day.

To address this shortcoming and, at the same time, obtain a more reliable estimate of the tidal prism, we made a series of acoustic Doppler profiler (ADP) measurements (Pinkel [19]) at 10 locations across the channel, 250 m east of the H1B on 2 January 2003 (**Figures 1** and **11**). We held a small boat stationary using a mooring line stretched across the 190-m-wide channel of the Slough. The data were binned in 0.25 m increments and averaged for two minutes to reduce Doppler noise to less than 1 cm/s. The lack of vessel motion ensured that high quality data were acquired. We completed six cross-channel profiles during a 6.9-h flood tidal cycle with a tidal range of −0.43 to 1.19 m referenced to MLLW.

At the beginning of the flood cycle, the typically 10–20 cm/s flow was centered over the northern (right) and southern (left) channels (**Figure 11**). As the flow increased, core speeds of 50 cm/s were observed near the mid-channel shoal. At maximum flood, the ~60 cm/s core remained near the center of the channel, and not in the 4.5 m deep channel located near the north bank. As the flow subsided, the current core moved toward the southern channel. The vertical sections in **Figure 11** show a core maximum
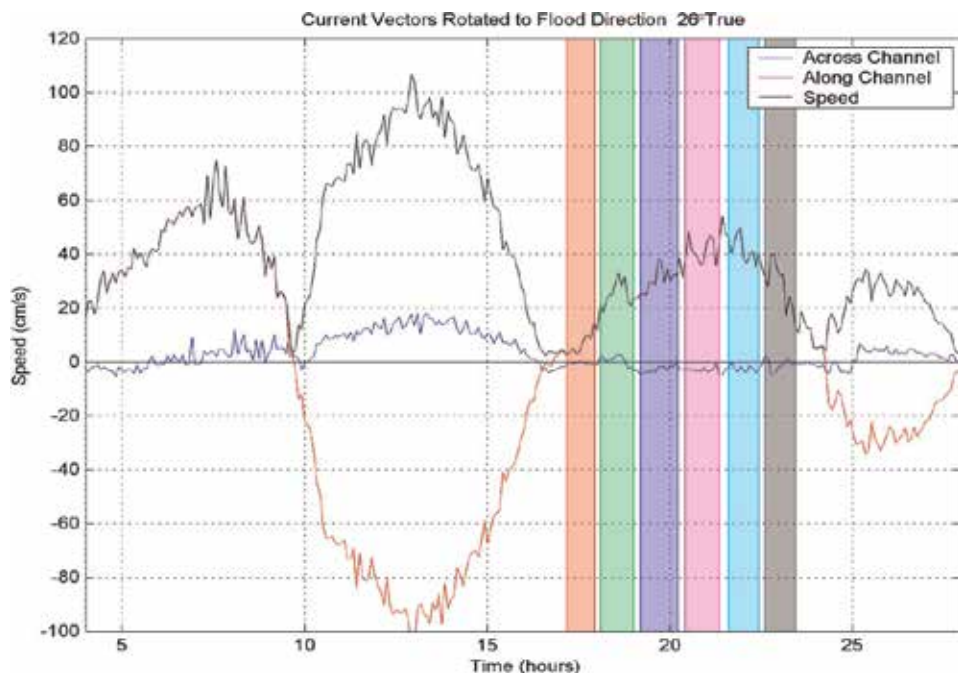
Figure 10.
*S4 Current meter time series acquired on 2 January 2003 during the ADP cross sections shown in **Figure 9**. Shown are the along-channel and cross-channel velocities as well as the total speeds. Note the large variability caused by seiche motions in Monterey Bay. The shaded bars show the periods of the six ADP cross sections.*
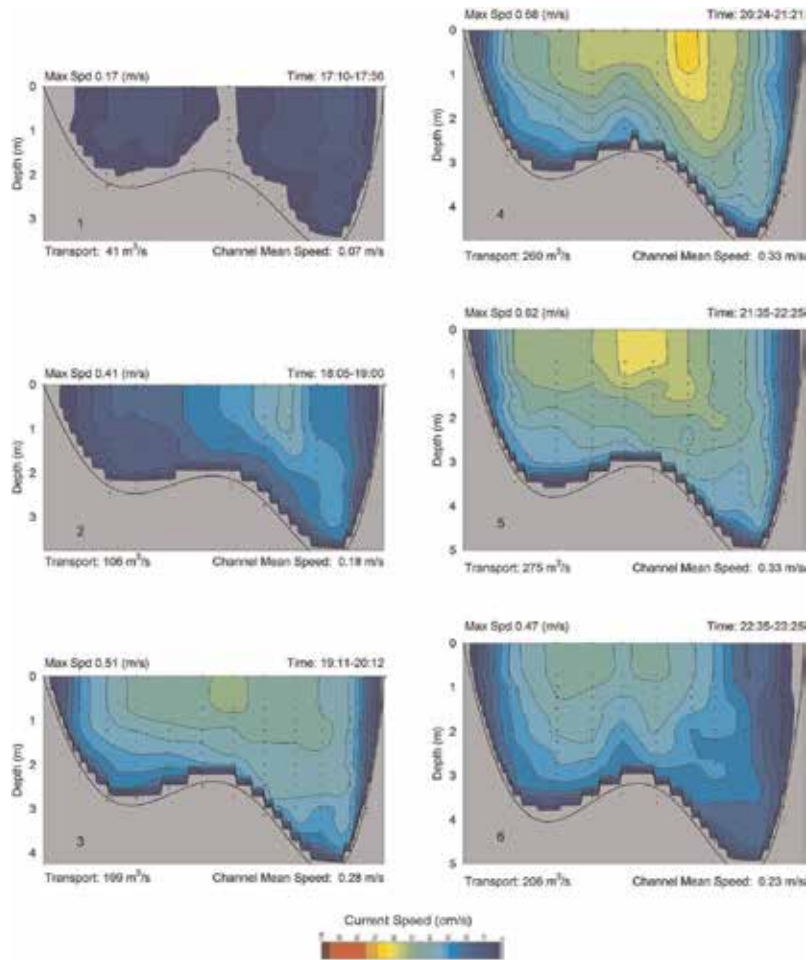
Figure 11.
ADP vertical sections of along-channel currents 250 m east of H1B show vertical and horizontal shear. The north shore is on the right. These data were obtained through a flood tide cycle on 2 January 2003. The integrated transport was 4.9×10^6 m^3.

with near surface speeds of 62 cm/s about midway through the tidal cycle. Greatest horizontal shear occurs between the core and the north shore (right side of **Figure 11**) but does not exceed 2 cm/s/m. Flow at all depths was in the flooding direction. Because of the time required to acquire the data, these profiles were, of course, not synoptic.

4. Estimating the tidal prism

In this section, we address the tidal prism, a crucial factor that essentially determines the tidal currents. The tidal prism is the volume of water exchanged between a bay and its parent body of water over a tidal cycle. Also, the current regime of an estuary is strongly influenced by three factors: morphology, river flow, and tidal forcing. The ratio of river flow to tidal volume characterizes the physical transport of water and other materials through the system. Hence, one of the most important problems is to evaluate the total tidal transport through the Slough.

From the conservation of volume, the average current speed is directly related to the tidal prism and inversely related to the cross-sectional area. This may be expressed as

$$u_{max} = 4/3(rc/2)(A/S)(H/T),\qquad(2)$$

giving the mid-channel maximum tidal current, u_{max}, in an enclosed basin [20]. A is the surface area of the basin inland from the main tidal channel, S is the cross-sectional area through which the current flows, H is the half-tidal range, and T is the half-tidal period. The factor 4/3 represents horizontal shear: the mid-channel current is about 1/3 greater than the cross-sectional mean current, and $rc/2$ relates the mean velocity for the half-tidal period to the maximum half-tidal velocity. Finally, the tidal prism corresponds to the volume AH.

Where the tides are mainly mixed diurnal and semidiurnal, the tidal prism is often taken to represent that volume of water associated with the change in elevation between MHHW and MLLW, but other tidal transitions could be used. To the extent that other sources and sinks of salt and fresh water contribute to the total volume of water in ES, the tidal prism will depart from the total water flux that is exchanged over a tidal cycle. The tidal prism can be estimated in several ways: by metering water fluxes through a vertical section on successive ebb and flood tides, by mapping sea level in the embayment at various tide levels, or by measuring the surface area and thickness of the discharge plume at an appropriate stage of the tide. The tidal prism for ES has been estimated using the first two methods with varying degrees of success, and the differences obtained from these methods provide at least one measure of the uncertainty in estimating this quantity.

During a 1956 survey of tidal inlets on the Pacific coast, Johnson [21] reported a tidal prism of 2.65×10^6 m^3 for ES, but the details of its estimation were not given. Smith [10] constructed a cross-sectional model for ES from which he estimated the tidal prism and the volume of slough waters at different tidal stages. He divided the Slough into three provinces: main channel, mud flats, and marsh. An idealized cross-section for ES, based on this classification scheme, identifies these provinces (**Figure 12**). He observed a predicted tide height of 0.88 m at the mud flat level and 1.45 m at the *Salicornia* marsh level. These heights are referenced to the tidal datum: 0.0 m at MLLW. Using Hansen's map (the basis for **Figure 1**), which was based on aerial photographs, he estimated the areas for each of these surfaces. The volumes obtained using this approach (i.e., the first method above) were then compared with volume transport estimates obtained using the second method, based on Clark's current meter measurements at the H1B. By adjusting the elevations of the mud flats and marsh, Smith showed reasonable agreement between the two methods. Smith's estimate of the tidal prism for HHW to LLW was 4.7×10^6 m^3. Smith used his results to estimate that the tidal prism extended 4.8 km into the Slough, assuming insignificant mixing between the ambient slough water and new
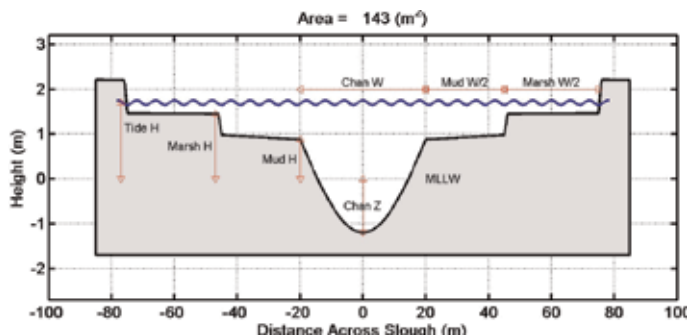
Figure 12.
Idealized cross section of ES. Mean sea level occurs near the edge of the mud flats, and the Salicornia *marsh is about 1.45 m above MLLW. Adapted from Smith [10]. Labeled quantities are used in Smith's volume continuity model of the currents.*

tidal volumes. Of historical note, a foam line produced by waters discharged from the PG&E power plant was often observed 4–5 km inland. Because coolant waters are now discharged directly into Monterey Bay, this foam line is no longer present. Continuing, in 1992, we applied Smith's model to a new aerial photograph that included the ESNERR South Marsh reclamation area, a province of the Slough that did not exist in 1974. The tidal prism from this work was estimated to be 6.2×10^6 m^3 (**Figure 13**).

Clark [14] used observations of u_{max} at the H1B and H/T to form a regression relationship whose intercept provides an estimate of the non-tidal flow, and whose slope provides a measure of A/S, the ratio of the flooded surface area to the cross-sectional area (**Figure 14**). This regression can also be used to estimate maximum tidal flows. Using comparisons of data from different periods, we can illustrate changes in the tidal flow and thus changes in the tidal prism. Using this approach, Wong found an intercept of about 10 cm/s indicating a net non-tidal flow directed out of the Slough. Because the values were relatively small, however, its significance is uncertain. Several factors most likely accounted for the net seaward flow according to Wong, including recent rainfall, agricultural runoff, and the discharge of cooling water into the lower slough from the PG&E power plant which operated the Slough outfall at that time.

U_{max} vs. H/T has been plotted for measurements that were acquired between 1971 and 1992 (**Figure 14**). The increase in regression slopes, based on a linear least squares fit to the data, indicates that maximum currents and thus the tidal prism (by an increase in the surface area, A) have increased by nearly a factor of two since 1971. At least two factors have contributed to increased tidal fluxes. The first was the restoration of formerly diked pasture which led to tidal flooding (**Table 1**). This sudden increase in surface area clearly contributed to Wong's [13] observed increase in tidal currents. However, erosion continues to enlarge the Slough at rates which have been documented on several occasions, e.g., [3–5], and this process continues to enhance the tidal flow, unabated.
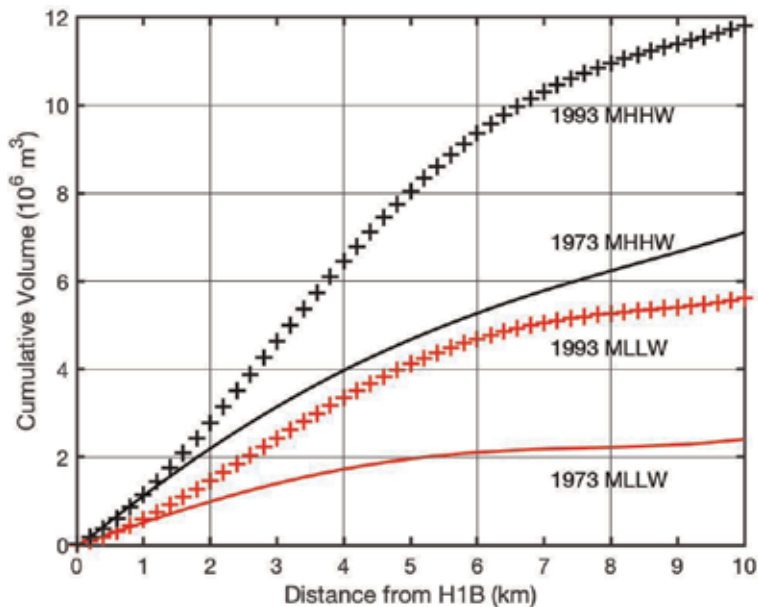
Figure 13.
Cumulative volume of water in ES at MLLW and MHHW from Smith [10] and as re-evaluated in 1993 from more recent aerial photographs. The volume between MLLW and MHHW is defined as the tidal prism, and estimated to be 4.7×10^6 m^3 in 1973 and 6.2×10^6 m^3 in 1993.
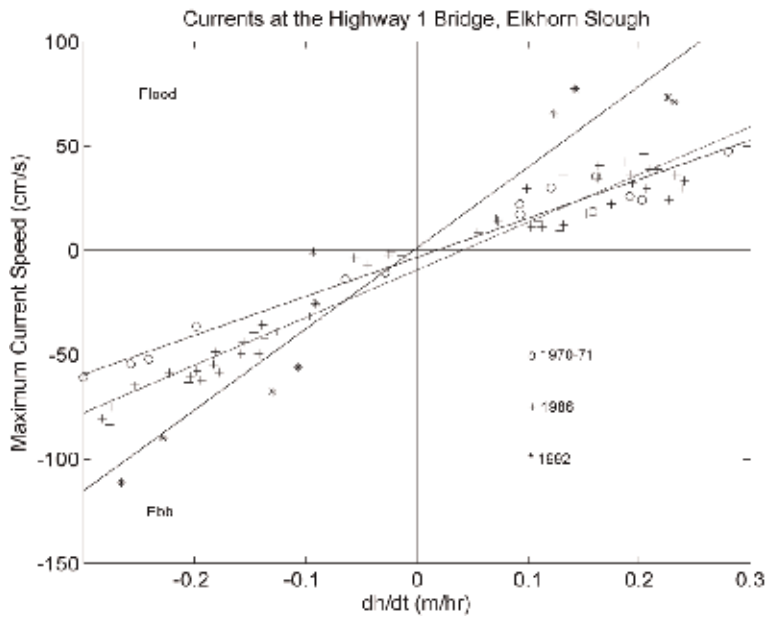
Figure 14.
Summary of current meter observations at the H1B. Y-axis values give smoothed along channel maximum speeds during a single half-tidal cycle. X-axis values are the ratios of the predicted or observed tidal range and half-tidal period (Eq. (2)). The symbols "o" represent Clark's [14] observations, "+" represent Wong's [13] measurements, and "" represent our 1992 data. The least squares regression lines show a systematic increase in time which reflects the increase in tidal prism.*

Location	Date	Surface area		Tidal volume	
		km^2	%	1×10 m^3	%
Parsons Slough and South Marsh	1984	1.8	20	1600	30
North Marsh	1985	0.6	7	53	1
Dolan Marsh	1986	0.3	3	130	2
Salt Ponds	1984–88	0.6	7	510	9
Bloom/Porter Marsh	1989	1	11	22	1

Table 1.
Recent additions to the Elkhorn Slough system that contribute to tidal volume increase and salt water incursion [6].

Our newer estimates of the tidal prism and total volume of water in ES also indicate major increases. The tidal prism from these more recent estimates is approximately 6.2×10^6 m^3 (**Figure 13**), a 32% increase in approximately 20 years. Interpreting recent changes to the water budget in ES is further complicated by the 1989 Loma Prieta earthquake which may have caused subsidence in the upper Slough. In addition to the restoration area discussed earlier, other additions have been made to ES which have increased its volume since the mid-1980s. Man-made alterations to the Slough and the approximate increases in surface area and volume caused by these changes are listed in **Table 1** [6]. The Parsons Slough area (**Figure 1**) is the major contributor to these increases. Also, the bottom depth at the entrance channel to Parsons Slough has increased from about 3 m in 1993 [6] to almost 5 m in August 2002 based on recent measurements.

In addition to water volume, current measurements in ES have been used to estimate several related parameters of interest including non-tidal contributions to

the circulation, and the geometry of the Slough. Using Eq. (2), Clark estimated the ratio *A/S* for Elkhorn Slough. Then, using measurements of the cross-sectional area at the Highway 1 Bridge (**Figure 4**), he estimated the effective surface area of the Slough to be 1.5 and 1.1×10^6 m^2 at high and low tides, respectively. Using a similar approach, Wong [13] obtained estimates of the effective surface area, which were almost twice those obtained by Clark. According to Wong, the increase in surface area was caused primarily by restoration of Parsons Slough, and this lead to accelerated erosion through increased tidal action.

Wong also calculated the tidal volume using the product of the tidal height and the effective surface area. He compared his volume estimates with previous values from Smith [10] who estimated the volume as the product of water height and the areas that covered the channel, the mud flats, and the marsh. Wong found that the mean tidal prism had increased from slightly over 4×10^6 to almost 7×10^6 m^3, and that the total water volume at high tide had increased from approximately 9×10^6 to 10×10^6 m^3. Although the uncertainty associated with these estimates is high, they show a trend toward higher values which we believe is significant. Wong found that the mean diurnal tide flushes roughly 75% of the total volume of water from the Slough. Based on these results and the assumption that the remaining waters in the Slough do not mix with the incoming waters from Monterey Bay, he estimated that the tidal prism would extend almost 5 km inland from the mouth, only slightly larger than the value of 4.8 km obtained by Smith [10].

5. Physical properties and processes

5.1 Distribution of physical properties

Three distinct water types result from the physical processes in ES [10, 22]. The primary water type consists of offshore waters which enter the Slough with the flood tide and is characterized by cool temperatures ranging from 9 to 16°C, and salinities that range from slightly over 33 to almost 34 parts per thousand (ppt). The second water type consists of relatively fresh water mainly derived from agricultural runoff from the Old Salinas River channel through South Moss Landing Harbor. Because this water is of low salinity (<10 ppt), it is less dense than the waters from Monterey Bay and forms a thin surface layer. According to Smith [10], this water did not usually extend its influence beyond the South Harbor basin because pumping by the PG&E power plant was sufficient to maintain a net flow of offshore water into the harbor. As the pumping rates at the power plant have increased, the influence of fresh water entering the Slough from the South Harbor has correspondingly been reduced.

The third water type is formed in the upper Slough. During summer, this water is of higher salinity due to excess evaporation, and during winter, it is usually of lower salinity due to precipitation and runoff. Because this water type is formed in the upper Slough (5–10 km from the mouth), it may lie beyond the inland reach of the tidal prism and was found to have longer residence times than lower slough waters. Although the characteristics of this water type were well-documented from data collected in the 1970s, the properties and extent of this water type may have changed due to the increased tidal prism. For example, the reach of the tidal prism may extend further up the Slough today than it did 30 years ago. Because the volumes of water associated with the second and third water types are small in comparison to the offshore waters, their influence is primarily restricted to where they enter the Slough (South Moss Landing Harbor), or are formed (in the upper Slough). From measurements made over 25-h periods at the H1B and in the upper

Slough during 1971 and 1975, variations in temperature and salinity were highly correlated with tidal forcing at periods of 12 and 24 h [10, 22]. The ratio of the 12 and 24-h salinity amplitudes were similar to the corresponding tidal height amplitudes. The amplitudes for temperature and dissolved oxygen, however, showed a higher correlation at 24 h than at 12 h, suggesting that diurnal variations in heating/ cooling and biological photosynthesis/respiration contributed significantly to these variations. In the lower slough (0 to ~5 km from the mouth), the influence of offshore waters decreased the effect of diurnal heating. As indicated earlier, tidal forcing causes the waters of ES to be well-mixed particularly along the main channel. Vertical profiles of temperature and salinity show little vertical stratification, except during periods of heavy rainfall in the winter [10].

The physical properties of ES vary on a seasonal basis. Seasonal changes in temperature and salinity in the upper slough are due to local influences, whereas seasonal changes in the lower Slough primarily reflect changes that occur in Monterey Bay. In **Figure 15**, temperature (upper panel) and salinity (lower panel) as a function of time and distance from the mouth are shown for the period July 1974 to May 1976. All sampling was done at high tide to remove the large tidal influences. The upper Slough is warmer than the lower Slough during the summer, and temperatures of 22°C have been observed. During winter, temperatures are cooler or about the same as offshore waters. In the upper Slough, temperatures during the winter as low as 12°C have been observed. A 14-month temperature time series (not shown) demonstrates that during the summer spring tide, pulses of relatively warm (>18°C) upper slough waters reach the lower Slough, and during winter, pulses of cool (<12°C) upper slough waters reach the lower Slough. ES, because of its direct connection to the bay, is also affected by El Nino conditions, and higher temperatures (~2 to 4°C) may be observed during these episodes.

In the upper Slough, salinity (**Figure 15**, lower panel) is affected by precipitation, runoff, and evaporation. During late winter, when precipitation is greatest, salinities as low as 17 ppt have been observed. During late summer, when evaporation is maximum, salinities in the upper slough have reached 37 ppt. Thus, the characteristics of the Slough can vary from typically estuarine during periods of heavy precipitation in the winter, to an evaporative basin during the summer. We note that due to the occurrence of recent dry years along the central California coast, characterizing ES as typically estuarine during the winter may be less appropriate than characterizing the upper Slough as an evaporative basin during the summer.

Finally, Smith [10] concluded that the area above the tidal prism, i.e., the upper Slough, was essentially isolated from offshore influence in the lower Slough, and tended to develop a separate physical identity. Although increased tidal action might reduce the contrast between upper and lower slough water masses, recent work on phytoplankton community structure in ES shows that these waters have retained their separate identities (N. Welschmeyer, personal communication).

5.2 Diffusion and mixing

The tides contribute to horizontal as well as vertical mixing in ES. The effects of horizontal mixing can be quantified by estimating the coefficient of eddy diffusivity, K_X. The magnitude of the along-channel diffusivity has been variously estimated using both physical and chemical parameters. When salinity is used to estimate K_X, both fresh water discharge and evaporative fluxes will affect estimates of K_X, if they are significant. Smith [10] estimated eddy diffusivities for ES using salinity data acquired during June and October of 1971, periods with no precipitation. Smith used the one-dimensional advection-diffusion equation balancing the seaward eddy diffusive salt flux with the landward advective salt flux to produce
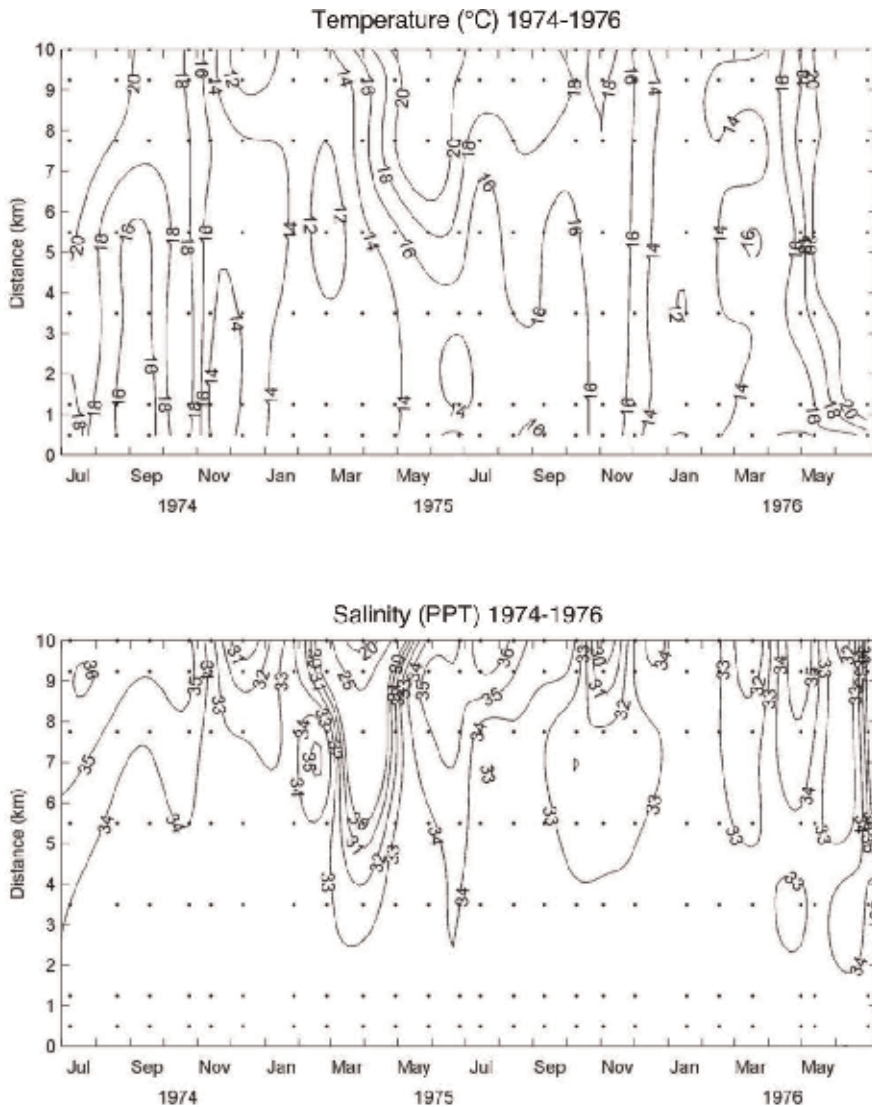
Figure 15.
Seasonal variation in temperature (upper panel) and salinity (lower panel) in ES between 1974 and 1976 (redrawn from Broenkow [22]).

the local time rate of change in salinity. He calculated the non-tidal landward velocity from observed evaporation rates from a nearby reservoir. From his results, the mean diffusivities for the summer can represented by a second-order polynomial as

$$\ln\left(K_X \times 10^{-3}\right) = 0.095 - 1.65X + 9.00X^2, \tag{3}$$

where K_X is the eddy diffusivity (m^2/s) and X is distance from the mouth (km). Smith's table correctly sets the eddy diffusivity at 1 km from the mouth as infinite which is the case when lower slough waters exit the Slough and do not return. Monthly mean K_X values, obtained over the length of the Slough, decreased by almost two orders of magnitude from the lower Slough ($\sim$500 $\times$ 10^3 cm^2/s) to the head of the Slough ($\sim$6 $\times$ 10^3 cm^2/s). These values from Smith are also in good

agreement with similar estimates of K_X obtained in other well-mixed estuaries [23]. The relatively high values of eddy diffusivity in the lower Slough demonstrate the importance of the tides as the dominant forcing mechanism. Because similar results were obtained in successive months, Smith concluded that a balance between evaporation and tidal diffusion provided a satisfactory explanation for the increase in salinity that was observed.

Reilly [24] calculated Reynolds fluxes to estimate eddy diffusivity in the lower Slough. In September 1975, he measured currents and salinity in the main channel at two depths, 1 m above the bottom and 1 m below the surface, based on a 50-hour time series acquired 3 km inland from the H1B. Reilly decomposed observations of salinity and the along-channel component of velocity into mean, periodic, and turbulent components, following Hansen [25]. He then obtained estimates of the salt transport by taking the product of the various components of salinity and velocity, with the cross-sectional area of the channel at the location where the measurements were acquired. Cumulative fluxes of salinity for the periodic (i.e., tidal) and fluctuating (i.e., turbulent) components are shown in **Figure 16**.

The periodic Reynolds fluxes (upper panel) promote a seaward salt flux, whereas the turbulent Reynolds fluxes (lower panel) promote a landward flux. We note that Reilly's estimates of eddy diffusivity compare favorably with those obtained by Smith. However, because Smith's analysis was based on an integral taken over the summer season, his method is to be preferred.

5.3 Residence time

The flushing or residence time of slough waters is of considerable importance regarding the fate of pollutants and other dissolved materials. As indicated earlier, most of the water that leaves the Slough on the outgoing tide does not re-enter on the incoming tide. Thus, the residence time for waters in the lower Slough is short, on the order of a tidal cycle or a few cycles at most. However, the degree to which waters from the upper slough mix with waters from the lower slough is not
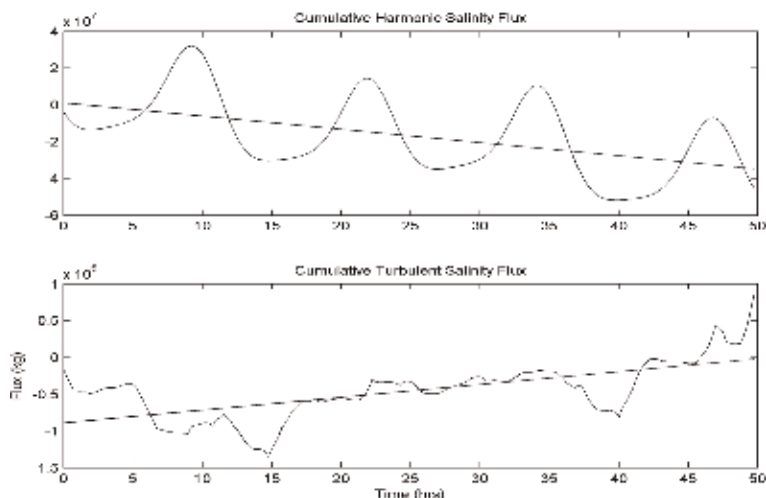
Figure 16.
Cumulative salinity fluxes in ES from Reilly's Reynolds flux calculations are shown [24]. Observations were made over a 50-hour period that were acquired near the "Dairies". Upper panel shows the harmonic salt flux $U_p S_p A$, where U_p and S_p amplitudes are computed from harmonic analysis of the M_2 and K_1 tidal periods. Lower panel shows turbulent salt flux $U'S'A$, where U' and S' are turbulent residuals following harmonic analysis. The trend lines indicate a seaward tidal flux and a landward turbulent flux. Note the different scales used to represent the fluxes.

well-established and is almost certainly seasonally dependent. During summer, the waters in the upper Slough become somewhat isolated from the waters in the lower Slough. In winter, during periods of precipitation, inflows from connecting tributaries and runoff enter the Slough and circulate into the lower Slough where they become part of the tidal prism. Smith [10] estimated that this sequence of events probably took upwards of a month in 1970, following a period of major precipitation. He also used his previously-derived eddy diffusivities (Section 5) to obtain estimates of residence times of about 30 days in the upper Slough during summer.

Because the tidal prism has increased since Smith's work, residence times in the upper slough are likely to have decreased. Near-surface temperature measurements taken across the channel between Parsons Slough and Kirby Park in July 2002 indicate that in areas outside the main channel, temperatures are slightly higher along the banks. This suggests that circulation in wider portions of the Slough may be weaker than flow along the main channel.

6. Discussion

6.1 Tidal asymmetry

The fact that higher high water always precedes lower low water in Elkhorn Slough is one reason that ebb current speeds exceed flood current speeds. The advance of the flood tide and the retreat of the ebb tide are retarded by frictional effects. The mud flats and *Salicornia* marsh areas are large compared to the channel area and they contribute to these frictional effects and thus to the retardation. The retardation, however, is apparently greater on the incoming tide than it is on the outgoing tide and we will say more about this in what follows. According to Wong [13], this retardation contributes to the tidal asymmetry where the duration of the ebb tide is reduced relative to that of the flood tide.

Because the asymmetry between flood and ebb currents is cumulative, the effect on tidal height becomes more pronounced towards the head of the Slough. Distortion of the incoming tidal wave also occurs as a result of the frictional effects associated with the bottom and lateral boundaries and is compounded by the effects of decreasing bottom depth, narrowness of the entrance, and decrease in channel cross section toward the head of the Slough. This distortion produces a number of new shallow water tidal constituents including overtides and compound tides. Overtides arise as the incoming tidal wave runs into shallow water where the trough is retarded more than the crest due to bottom friction and thus the wave loses its simple harmonic form [26]. These frictional effects lead to the production of compound tides which also occur in ES. The existence of overtides and compound tides is clearly evident from the tidal records at Kirby Park, approximately 7 km from the harbor entrance. Finally, because tidal heights and currents have often been found to be roughly 90° out of phase, the tides in ES may approximate a standing wave system.

6.2 Generation of overtides and compound tides

Observations presented in Section 3 revealed the presence of higher frequency tidal constituents in ES. Because of tidal transformations, the tidal regime in ES differs from that of Monterey Bay. Tidal periods of 8.4, 8.3, 8.2, 6.2, and 4.1 h were found that correspond to the $2MK_3$, M_3, MK_3, M_4, and M_6 tidal constituents, respectively. The 8.3-h M_3 lunar terdiurnal tide is not classified as a shallow water constituent [26] and may originate outside the Slough. The 6.2-h M_4 and the 4.1-h

M_6 constituents are overtides that represent the first harmonic of the primary M_2 tide, and the sixth-diurnal tides, respectively. The $2MK_3$ (8.4 h) and the MK_3 (8.2 h) constituents, or terdiurnal components, are compound tides that correspond to the sums ($MK_3 = M_2 + K_1$), or differences ($2MK_3 = 2M_2 - K_1$) of the primary M_2 and K_1 constituents. We find the amplitudes of these constituents to increase monotonically with distance inland. However, the amplitudes of the primary constituents do not decrease significantly with distance up the Slough. M2 increases by 40 mm and K1 is nearly constant. That the M2 amplitude inside ESNERR is only slightly smaller than at the entrance to Parsons Slough clearly suggests that the return flow during ebb at this location is not at the present time choked or partially choked [18].

According to Wong [13] and Clark [14], the time of maximum ebb flow occurred slightly later than or midway through the ebb tide, while the time of maximum flood tide occurs slightly later than midway through the flood tide, towards the time of high water. They attributed this delay during the flood tide to the volume of water that must be transported across the tidal flats which may also contribute to the observed overtides in ES [30]. We have examined this process using a month-long current record from January 2002 (**Figure 6**, bottom panel). From a cross-correlation analysis between the mean corrected pressure (i.e., tidal elevation) and the along-channel current speed, we found that the maximum lag was 3.24 h, which is very close to quadrature for the dominant M_2 tide (12.42 h). Harmonic analysis of these data showed that the phase angle between the dominant semidiurnal and diurnal harmonic constituents for tidal elevation and current speed (M_2 and K_1) were 84° and 88°, respectively, consistent with Clark and Wong's standing wave description of the tidal regime in ES.

Considerable research has been conducted on tidal transformations in well-mixed estuaries, primarily along the U.S. East Coast [27–30]. In many respects, their results should be generally applicable to any well-mixed estuary. However, there is one important difference between the tides along the East Coast and West Coast of the U.S. Along the East Coast, they are semidiurnal, whereas along the West Coast, they are mixed, mainly semidiurnal, and the greatest tidal range occurs from higher high water to lower low water. This characteristic produces initial conditions for tides entering shallow embayments along the West Coast that clearly favor ebb domination prior to any tidal transformation. Once the tide has entered the estuary, shallow water effects produce overtides and compound tides which experience down-channel evolution in amplitude and remain phase-locked to the parent tides throughout the estuary [29]. According to Parker [31], the increase in amplitude of the overtides and compound tides with distance up the Slough occurs at the expense of the fundamental constituents to which they are harmonically related through the nonlinear transfer of momentum and energy. However, we note that our results are not necessarily consistent with Parker's explanation since we found that although the amplitudes of the overtides and compound tides did increase with distance inland, the amplitudes of the primary constituents did not decrease significantly over the same distance.

According to Boon and Byrne [32], distortion of the incoming tide leads to temporal asymmetries in the rise and fall of the surface tide. These, in turn, result in temporal and amplitude asymmetries in the velocity field. Further, these asymmetries cause estuaries to be either flood- or ebb-dominant. According to Friedrichs and Aubrey [30], non-linear tidal distortion has two principal causes, frictional interaction between the tide and the channel bottom which leads to shorter flood tides, and intertidal storage which causes the ebb tides to be shorter. Based on the work of Friedrichs and Aubrey, intertidal storage due to the presence

of the extensive *Salicornia* marsh and mud flats in ES may be a principal factor that contributes to the dominance of the ebb tide in ES.

Basic mathematics can be used to illustrate how certain estuarine tidal transformations arise. First, we show one simple approach that illustrates how both overtides and compound tides can be generated. We assume that shallow-water effects are proportional to the square (or higher power) of tidal sea level, following Pugh [33]. Take two primary constituents such as M_2 and K_1, whose frequencies are ω_2 and ω_1, form their sum, and square the result,

$$
\begin{aligned}
[\eta_{M2}\cos2\omega_2 t + \eta_{K1}\cos2\omega_1 t]^2 = {} & 1/2\left(\eta_{M2}{}^2 + \eta_{K1}{}^2\right) + 1/2\left(\eta_{M2}{}^2\right)\cos4\omega_2 t \\
& + 1/2\left(\eta_{K1}{}^2\right)\cos4\omega_1 t + \eta_{M2}\eta_{K1}\cos2(\omega_1 + \omega_2)t \\
& + \eta_{M2}\eta_{K1}\cos2(\omega_1 - \omega_2)t,
\end{aligned} \tag{4}
$$

where η is the free surface elevation, t is time, $\omega = 2\pi/T$, and T is the constituent period. This expansion contains additional harmonics with frequencies $4\omega_2$ and $4\omega_1$ which represent the overtides.

The last two terms contain the sum and difference frequencies for ω_2 and ω_1 which represent the compound tides. Also, the first term contains the sum, $1/2(\eta_{M2}{}^2 + \eta_{K1}{}^2)$, which corresponds to an increase in mean sea level. Observations in many estuaries have shown an increase in mean sea level for the incoming tide as the head of the estuary is approached [33]. Closer at hand, the NOS tide survey in 1976 [12] shows that mean sea level may increase by as much as 30 mm (0.1 ft) between the H1B and Hudson's Landing.

To illustrate an alternate approach for the generation of overtides, we employ the one-dimensional equations of motion and continuity to illustrate how the relevant hydrodynamics apply to tidal transformations. For the along-channel ("x") momentum equation, we have the following,

$$
\frac{\partial u}{\partial t} + u\frac{\partial u}{\partial x} = -g\frac{\partial \eta}{\partial x} \tag{5}
$$

where x, t, η, and g are distance along the x-axis, time, surface elevation, and the acceleration of gravity, respectively, and u is the along-channel current velocity. The governing equation for continuity which employs the same variables with the addition of H, the bottom depth, can be expressed as,

$$
(H + \eta)\frac{\partial u}{\partial x} + u\frac{\partial \eta}{\partial x} = -\partial\eta/\partial t. \tag{6}
$$

This equation has been modified slightly to take into account the geometry that we often apply to estuaries where the rates of mass transport into and out of a vertical column are equated [34]. These two simultaneous nonlinear differential equations can be solved, as shown in Officer [34], to obtain a solution for $\eta(x,t)$, of the following form,

$$
\eta(x,t) = \eta_o\,\cos\left(kx + \omega t\right) - \left(3gk\eta_o{}^2\omega/4c^3\right)\,x\,\sin\left\{2(kx + \omega t)\right\} \tag{7}
$$

where only terms of order $\eta_o{}^2$ or lower have been retained. η_o is the tidal amplitude at an arbitrary point of origin for x and t, and k is the wave number, $2\pi/L$, where L is the shallow water wavelength, g is the acceleration of gravity, and $c = gH$, the shallow water wave velocity. The second term in (7) captures the essence of overtide generation where $\eta(x,t)$ is seen to be directly proportional to x, the distance in the up-estuary direction. As x increases, H generally decreases which also contributes to

increasing amplitude as the tidal wave propagates inland. The increase in $\eta(x,t)$ clearly reflects the increasing distortion experienced by the incoming tidal wave as it propagates in the up-slough direction. Finally, our tidal observations presented in **Table A1** show a monotonic increase in the M_4 and M_6 overtides and in the MK_3, $2MK_3$, and SO_3 compound tides between the H1B and the head of ES.

With respect to the tides in estuaries, the magnitude and phase of each constituent reflect the hydrodynamic processes that are important. For estuaries where the M_2 tide is dominant, its first harmonic, the M_4 tide, is usually the dominant overtide, as in ES. The phase relationship between the M_2 and M_4 components determines the direction and magnitude of the tidal asymmetry [29]. Ebb-dominance is further enhanced by inefficient water exchange around high water in estuaries with relatively deep channels and extensive intertidal water storage. Low water velocities in intertidal marshes and mud flats cause the high tide to propagate slower than the low tide [30]. At low tide, the marshes and flats are empty while the channels serve to accelerate the flow in the down-channel direction. The extensive mud flats and marshes in ES contribute to weak or sluggish water exchange around the time of high tide, as indicated by the results of Wong [13].

To expand on this topic slightly, we refer back to the idealized cross-section for ES (**Figure 12**). One aspect of this model cross-section is that the mud flats slope downward toward the main channel. We expect these slopes to retard rising water levels on the incoming tide, and accelerate flow back into the main channel on the return tide. This mechanism should contribute to the asymmetry of the tides in ES depending on the magnitude of the slopes and their extent, and, most importantly, helps to explain why the incoming tide experiences greater retardation than the outgoing tide. Thus, intertidal water storage due to sloping muds flats may also be a significant factor that contributes to ebb-dominance in ES.

6.3 Industrial effects

The original PG&E power plant at Moss Landing began operations in 1952 [1]. Intake cooling for seven generators was supplied by water from Moss Landing Harbor (**Figure 2**). Of the original generators two discharged their 40% effluent through a pipe into Monterey Bay just south of the harbor entrance about 200 m offshore. Five of the original generators discharged about 60% of the heated effluent approximately 0.5 km inland from the H1B; however, this was stopped in 1995 when these units were retired. In 1998, Duke Energy assumed operation of the power plant and has upgraded two of the original units and has added two new turbine generators. The mean temperature of the effluent is approximately 11°C higher than the intake temperature. Intake rates increased from the original design rate of 1.4×10^3 m^3/min, to almost 3.0×10^3 m^3/min circa 1980 [11]. Presently, the average and maximum expected intake flow rates for the original units are approximately 1.8 and 2.3×10^3 m^3/min. The two new generators add almost 1.0×10^3 m^3/min to the flow. The effluent is discharged directly at the head of Monterey Submarine Canyon through the existing underground piping.

The power plant intake provides a continuous landward flow independent of the tide. It has no effect on the exchange of waters in ES itself unlike the previous situation through the now abandoned slough outfall. However, it is still interesting to compare the power plant coolant water flow with the tidal prism of ES. For an intake rate of 3.0×10^3 m^3/min, the total volume over a half tidal day (12.4 h) is 2.2×10^6 m^3. If we use our estimate of the tidal prism of 6.2×10^6 m^3 (1993), then the coolant water flow represents 35% of the ES tidal prism. Although the plant intake and discharge has no effect on the Slough, it dominates the water budget of

Moss Landing Harbor. The present intake rate through the harbor entrance with a cross-sectional area of 300 m^2, decreases the ebb current speed by roughly 15 cm/s or about 10% of the observed maximum ebb current speeds under the H1B.

6.4 Tidal prism revisited

To put the various tidal transport results in perspective and because of the continuing physical changes in the channel, mud flats and marsh, including the addition of the restoration area, we have updated Smith's model based on more recent data acquired during 2002 and 2003. ADP current measurements were also acquired as part of this data collection effort. We have used the following approach to obtain updated estimates of the tidal prism for Parsons Slough, for the location near the H1B, and finally, for the entire Slough. Additional details concerning the methods and results can be found in Broenkow and Breaker [9].

Smith's parameterized cross-section model was employed together with a recent bathymetric map from Malzone [4] in conjunction with the volume continuity equation given earlier (Eq. (2)) to estimate the mid-channel tidal currents and the tidal prism. Using the model with a U-shaped channel, sloping mud flats, and level *Salicornia* marsh, we first calculated the updated cross-sectional area. By integrating the cross-sectional area along the length of the Slough, we then obtained a new water volume. Finally, by integrating the channel, mud flat and marsh widths, we obtained updated surface areas. These values were then used in Eq. (2) to estimate the volume transports during a half tidal cycle through the seaward-most sections of Elkhorn Slough and Parsons Slough. The values entering the model were subsequently adjusted within reasonable limits given the uncertainties involved to produce volume transports that were generally consistent with the recently-acquired ADP current measurements.

The computed mid-channel current speeds are shown in **Figure 17a** and indicate values consistently in excess of 150 cm/s over the first 2 km from the entrance of ES. The tidal prism for Parsons Slough was estimated to be 2.4×10^6 m^3 and that for the H1B to be 4.9×10^6 m^3. The results for the entire Slough produce a somewhat larger tidal prism than those predicted by the earlier results (**Figure 17b**). The maximum tidal prism, i.e., the difference between the cumulative high and low tidal volumes, is approximately 7.6×10^6 m^3 and can be inferred directly from **Figure 17b**. The contribution to the cumulative volume from Parsons Slough corresponds to the step increase observed in **Figure 17b** between 2 and 4 km from the entrance to ES. The model estimate for Parsons Slough itself represents over 30% of the tidal prism for the entire Slough.

6.5 Classification

It is difficult to compare ES with some of the more well-known estuaries along the West Coast, such as Puget Sound, the Columbia River, and San Francisco Bay, because its characteristics differ significantly, particularly its spatial scales and recent evolutionary development. One estuary that is similar in some respects, however, is Morro Bay, located approximately 150 km south of ES just north of Pt. Conception. Morro Bay is a bar-built estuary or barrier-lagoon [35]. Like ES, it has a well-defined entrance channel that feeds into the bay itself with a bay interior that is essentially marine-dominated. In summer, salinities increase by several parts per thousand (ppt) inside the bay due to excess evaporation. Although the tidal prism for ES and Morro Bay are similar, the surface area of Morro Bay is almost twice that of ES [21]. Perhaps the largest difference between these estuaries is that while ES is growing rapidly, Morro Bay appears to be filling gradually [36].
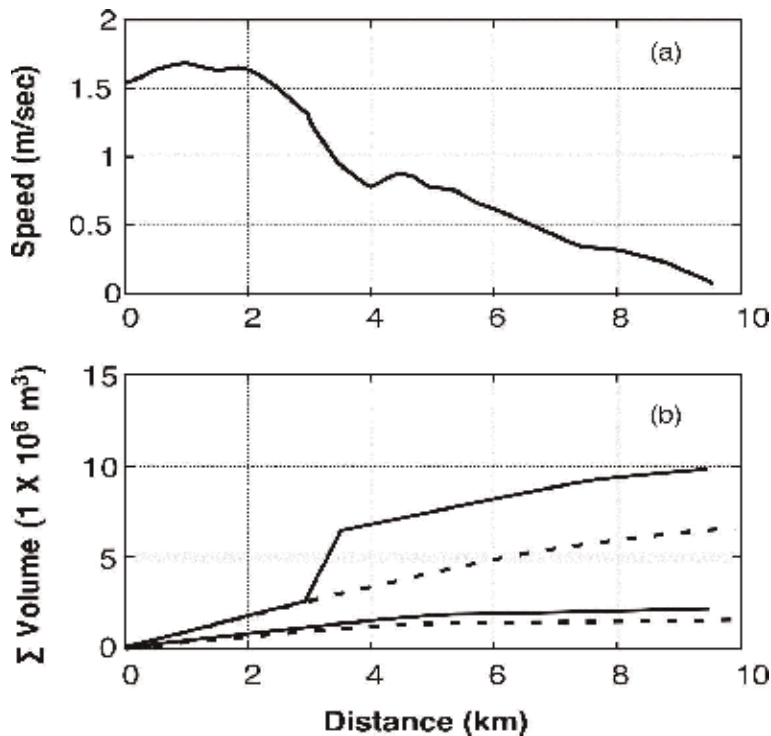
Figure 17.
The upper panel (a) shows the computed mid-channel current speed using the continuity model. The lower panel (b) shows the cumulative tidal volume at given stages of the tide. The tidal prism is the difference between the high and low tide cumulative volumes. The dotted line represents the results from Smith's [10] model.

Formally, a slough is a swamp-like region, inlet, or backwater. According to most accounts, e.g., [1], ES certainly qualified for the name prior to 1946 before the entrance to Moss Landing Harbor was created. However, now the name is inappropriate since its character has changed dramatically through direct tidal exchange between ES and Monterey Bay. However, some of the tributaries that feed into ES are still sloughs in the formal sense. ES appears to be unique in this region because it continues to expand, whereas many other inlets/estuaries appear to be filling in over time. Various terms have been used to describe Elkhorn Slough such as a "seasonal estuary" or as a "tidal embayment." Both terms are appropriate. Because of vigorous tidal forcing, and because density stratification from fresh water discharge occurs only in winter, vertical mixing is intense especially at constrictions such as the H1B and the Parsons Slough railroad trestle. ES is nearly vertically homogeneous in the main channels where most observations have been made. Although ES is vertically well-mixed, it is not necessarily laterally homogeneous. Although the data are few, the observations of temperature and salinity in the Slough, particularly in the wider portions, indicate cross-slough gradients that are consistent with increased warming and higher salinities in these shallower regions. During the summer, ES is a negative estuary because excess evaporation produces higher salinities in the upper slough leading to decreasing salinities toward the mouth. Values greater than 37 ppt have been observed leading to what some authors call "hypersaline" conditions where salinities in this case were higher than salinities in offshore waters. During winter when increased precipitation often occurs, fresh water fluxes increase with additional input from the adjoining sloughs, causing ES to resemble a true estuary with salinities increasing toward the Bay.

7. Conclusions

Elkhorn Slough is unique: unlike estuaries which have evolved over hundreds or thousands of years, this estuary was transformed from a sluggish backwater in 1946 when Moss Landing Harbor was formed, to a vigorous, rapidly growing estuary that has become a habitat for many fish, marine, mammals and sea birds. This transformation has taken place in less than 50 years and continues today.

ES is an ebb-dominated embayment which produces asymmetric tides. The ebb tidal currents are stronger than the flood currents and the duration of the transition from high to low tides is shorter than the reverse. The presence of extensive mudflats and *Salicornia* marsh distorts the incoming tide through water storage on the mudflats and through increased friction. Thus, the mud flats slope downward may be an important factor in contributing to the tidal asymmetry in ES. The distortion experienced by the incoming tidal wave produces a number of shallow water constituents including the M_3, M_4, and M_6 overtides, and the $2MK_3$ and MK_3 compound tides. The degree to which ebb domination is due to the form of the incoming tide, i.e., mixed, mainly semidiurnal, or to the overtides and compound tides that are generated is an open question. Tidal currents are maximum along the main channel and their vertical structure indicates that slough waters are well mixed between the bottom boundary layer and the surface. Tidal currents near the H1B at maximum ebb have increased from approximately 75 to 150 cm/s over the past 30 years. This increase in current speed can be attributed primarily to the increase in tidal prism which has increased from approximately 2.5 to 7.6×10^6 m^3 between 1956 and 2003. The increase in tidal prism is the result of both man-made changes to the Slough, and the continuing process of tidal erosion. We note that these changes are not independent as far as the circulation of ES is concerned. When the man-made effects of increasing the surface area of the Slough occurred in 1983, the corresponding increase in the tidal prism required that the tidal currents increase in accordance with the tidal prism. Thus, that the mud flats slope downward may be an important factor in contributing to the tidal asymmetry in ES.

As in most estuaries, the tidal response in ES shows both standing and progressive wave character. Since the incoming tide is subject to frictional dissipation as it progresses up the Slough, the combined response of both waves consists of a mixture of a standing wave (without amplification) and a progressive wave. From harmonic analysis of the currents in the lower slough, we find that currents lag tidal elevation by 84° and 88° for the M_2 and K_1 constituents, respectively. Thus standing wave behavior appears to dominate, in agreement with Dyer [8] who indicates that most estuaries display characteristics that are consistent with standing wave behavior.

The physical properties of ES vary seasonally and with location. Temperature and salinity in the lower slough reflect primarily the influence of Monterey Bay waters, whereas the temperature and salinity of the waters in the upper slough ($>\sim$5 km from the mouth) tend to reflect the influence of heating and precipitation (or their converses) from the atmosphere. During the summer, both temperature and salinity are higher in the upper slough due to local heating and excess evaporation, respectively. During the winter, salinities can reach values of less than 20 ppt during periods of heavy precipitation.

Our knowledge of the circulation and distribution of physical properties in ES are, to a large extent, based on data collected during the 1970s and 1980s. However, the results presented here show that the Slough is changing rapidly. In the past,

waters in upper ES were distinct from lower ES with the high tide interface located near the entrance to the Parsons Slough and South Marsh additions. As the tidal prism increases, this boundary between upper ES and Monterey Bay waters will move inland, and waters in the lower slough will be more ocean-like. With future observations, we will be able to confirm or reject these ideas.

Few measurements have been made in Parsons Slough and the adjoining South Marsh. This overlooked area contributes over 30% to the tidal prism for ES. From recent observations, we have observed vigorous tidal flows entering ($\sim$60 cm/s) and leaving (>100 cm/s) Parsons Slough through its entrance located under the narrow railroad trestle (**Figures 9** and **10**). Recent current measurements near the entrance indicate that relatively large volumes of water are exchanged between Parsons Slough and ES itself. It is recommended that new observations of water elevation, temperature, and salinity in the South Marsh/Parsons Slough area, and current measurements through the entrance to Parsons Slough be acquired to better understand this relatively new portion of ES and its contribution to the overall water budget of the Slough per se.

The volume of water taken in by the Duke Energy Power Plant on a daily basis is relatively large compared to the tidal prism of ES. For an intake rate of 2.0×10^3 m^3/min, the total volume of water taken in by the power plant is almost 50% of the tidal prism over a tidal day. However, the intake has essentially no effect on the Slough itself, but profoundly affects the circulation of Moss Landing Harbor and increases the current speeds for the incoming tide through the harbor entrance by up to 10 cm/s.

Residence time for waters in the lower slough is relatively short, on the order of a tidal cycle or perhaps several cycles at most. Summertime diffusive residence times for the upper Slough based on data collected in 1973–1974 were of the order of 30 days. Because of the increase in tidal prism in ES since that time, residence times in the upper Slough have almost certainly decreased. New observations in the upper Slough will be required to address this important question.

As of the early 2000s, few if any observations have been made of the ES discharge plume in Monterey Bay. Cursory observations show that the plume is discharged to the southwest and becomes entrained in the circulation of Monterey Bay. At its maximum extent, the plume may extend as far as 3 km offshore. These sediment laden plumes provide further evidence of the erosional processes at work inside the Slough. On daily time scales, the plume provides a clear indication of the sediment erosion that takes place within the Slough. On longer time scales, this erosion eventually contributes to sediment transport through Monterey Submarine Canyon. For sediment, nutrient and water budgets, we must know more about the fate of the plume as it becomes entrained in Monterey Bay waters, and learn more about the pathway taken by waters which enter the Slough and Harbor on the incoming tide.

It is interesting to note that the four estimates of the tidal prism for ES that have been made over the past 47 years show a somewhat linear increase over time (**Figure 18**). However, changes in the tidal prism have often occurred rather abruptly due to human intervention, such as the restoration of Parsons Slough and South Marsh in 1983; as a result, the slope of the trend in **Figure 18** is not constant, as might otherwise be inferred. We believe the accuracy of the tidal prism estimates is about $\pm$ 20%, although more conservative estimates have been reported for other estuaries, e.g., O'Brien, $\pm$15% [37]. In lieu of a better predictor, the slope of the linear trend in **Figure 18** is approximately 0.1×10^6 m^3/year over the 47 years between 1956 and 2003. We also note that although the uncertainty of the individual estimates of the tidal prism may be relatively large, the uncertainty of the slope
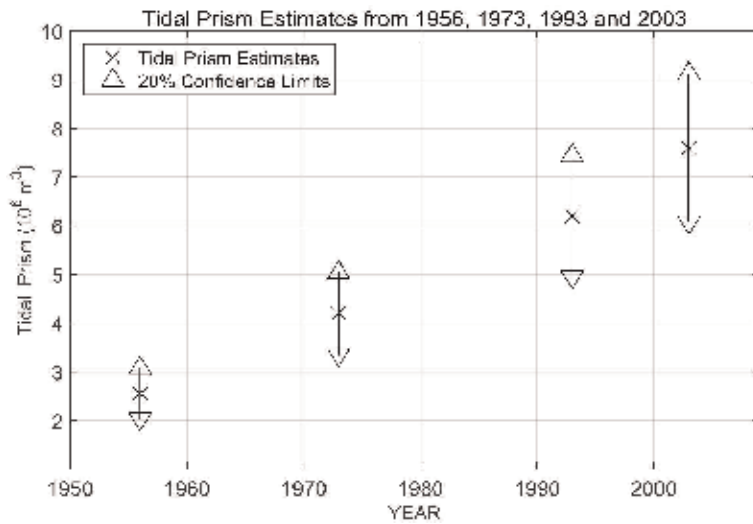
Figure 18.
Elkhorn Slough tidal prism estimates including the estimated uncertainties.

itself should be less uncertain because it is based on four independent estimates. To the extent that the continuing process of tidal erosion is an important mechanism for increasing the tidal prism in ES (vs. abrupt man-made changes), this predictor may be useful.

Acknowledgements

A. Appendix

See **Tables A1** and **A2**.

Name	N	Tidal constituents 2002-2003						
	°/h	Amplitudes (mm)						
		MB	SB	H1B	PS	KP	HL	SM
J1	15.5854	22	18	18	16	16	14	
K1	15.0411	366	359	361	360	361	343	457
K2	30.0821	37	37	40	37	37	37	
L2	29.5285	7	8	6	16	21	28	
M1	14.4967	12	11	12	12	13	12	
M2	28.9841	493	507	484	516	527	531	512
M3	43.4762		3	5	8	10	11	15
M4	57.9682		5	7	23	30	32	23
M6	86.9523		1	2	9	12	14	15
N2	28.4397	112	111	108	111	114	114	
2N2	27.8954	13	15	15	14	13	15	
O1	13.9430	230	232	233	223	222	219	206
OO1	16.1391	11	11	14	15	16	14	
P1	14.9589	114	107	108	116	115	110	
Q1	13.3987	41	38	40	40	39	40	
2Q1	12.8543	5	3	3	3	4	3	
S1	15.0000	10	16	10	19	16	37	
S2	30.0000	130	141	138	147	149	147	111
T2	29.9589	7	7	5	11	11	13	
lmbda2	29.4556	3	4	4	7	8	13	
mu2	27.9682	12	11	10	5	6	9	
nu2	28.5126	22	19	22	21	22	21	
rho1	13.4715	8	5	9	9	10	10	
MK3	44.0252		2	10	21	26	33	36
2MK3	42.9271		3	6	15	20	24	19
MN4	57.4238		2	3	10	12	13	18
MS4	58.9841		1	3	14	17	18	13
Name	N	Tidal constituents 2002–2003						
	°/h	Phase (h)						
		MB	SB	H1B	PS	KP	HL	SM
J1	15.5854	15.0	6.7	7.2	8.0	8.5	9.0	
K1	15.0411	14.6	6.8	6.5	7.3	7.4	7.6	6.6
K2	30.0821	5.7	9.6	9.5	9.8	9.8	9.8	
L2	29.5285	7.5	9.2	9.7	9.2	9.3	9.3	
M1	14.4967	15.6	8.3	9.0	9.0	9.3	9.6	
M2	28.9841	6.2	10.3	10.3	10.7	10.8	10.9	10.9
M3	43.4762		0.5	0.6	1.7	1.9	2.4	2.0
M4	57.9682		5.2	6.0	0.2	0.2	0.5	0.9

Name	N	Tidal constituents 2002–2003						
	°/h	Phase (h)						
		MB	SB	H1B	PS	KP	HL	SM
M6	86.9523		2.0	2.2	1.7	1.7	1.7	1.9
N2	28.4397	5.4	9.6	9.6	10.1	10.2	10.4	
2N2	27.8954	4.4	8.9	8.9	9.1	9.2	9.4	
O1	13.9430	14.6	6.0	6.0	6.5	6.7	6.9	6.5
OO1	16.1391	15.5	7.8	8.2	8.4	8.4	7.7	
P1	14.9589	14.4	6.7	6.4	7.1	7.3	8.0	
Q1	13.3987	14.6	5.7	5.7	6.5	6.8	7.0	
2Q1	12.8543	15.5	11.7	4.5	13.1	15.0	17.7	
S1	15.0000	21.3	1.0	18.4	22.2	22.6	2.8	
S2	30.0000	6.0	10.0	10.0	10.4	10.6	10.6	10.0
T2	29.9589	5.6	9.5	9.3	9.5	9.5	9.5	
lmbda2	29.4556	6.1	9.5	9.5	8.6	8.6	8.5	
mu2	27.9682	4.1	8.7	8.0	11.5	12.1	12.5	
nu2	28.5126	5.7	9.7	9.8	10.2	10.1	10.5	
rho1	13.4715	14.6	4.6	5.5	6.3	6.0	6.3	
MK3	44.0252		5.2	4.3	4.6	4.6	4.9	4.2
2MK3	42.9271		3.8	4.3	4.6	4.8	5.1	5.8
MN4	57.4238		5.1	5.8	6.3	0.1	0.4	0.5
MS4	58.9841		5.5	0.0	0.6	0.6	1.0	1.7
Locations and duration of tide height observations								
MH	9413450 Monterey Harbor 12 months				36.36.3′ N		121. 53.3′ W	
SB	MLML small boat dock Moss Landing Harbor 3 months				36°48.247′ N		121°47.166′ W	
H1B	250 m east of Highway 1 Bridge 14 months				36°48.667′ N		121°46.997′ W	
PS	Near SP Trestle Parson Slough entrance 4 months				36°48.951′ N		121°44.704′ W	
KP	Kirby Park 4 months				36°50.951′ N		121°44.817′ W	
HL	Hudson's Landing head of Elkhorn Slough 3 months				36°51.453′ N		121°45.434′ W	
SM	South Marsh landward of SP trestle 1 month				36°49.209′ N		121°44.259′ W	

Table A1.

Tidal height amplitude in Moss Landing Harbor and Elkhorn Slough determined from 1-month to 14-month observations, beginning in June 2002. N is the constituent speed number in degrees per hour (°/h). The record lengths are: H1B 14-months; SB, PS, KP, HL 3-months; SM 1-month.

Name	N	NOS historical tidal constituents 1976					
	°/h	Amplitudes (mm)					
		OP	GF	PM	ELK	KP	RR
J1	15.5854	16	18	17	17	16	21
K1	15.0411	356	366	361	356	366	348
K2	30.0821	39	35	34	38	35	37
L2	29.5285	6	14	14	9	15	12

Name	N	NOS historical tidal constituents 1976					
	°/h	Amplitudes (mm)					
		OP	GF	PM	ELK	KP	RR
M1	14.4967	6	16	16	15	15	19
M2	28.9841	484	502	508	495	523	522
M3	43.4762	2			9		11
M4	57.9682	3	2	6	15	20	25
M6	86.9523	1	1	1	2	2	4
M8	115.9364	1	1	0	2	2	3
N2	28.4397	105	120	121	109	124	116
2N2	27.8954	14	16	16	15	16	14
O1	13.9430	228	223	218	221	211	217
OO1	16.1391	12	9	9	9	9	17
P1	14.9589	113	121	120	113	121	110
Q1	13.3987	43	43	42	38	41	38
2Q1	12.8543	10	6	6	5	5	4
R2	30.0411	1	1	1	2	1	5
S1	15.0000	5			4		13
S2	30.0000	130	128	126	132	127	134
S4	60.0000	3	2	0	1	2	2
S6	90.0000	1	1	1	1	0	1
T2	29.9589	10	8	7	7	8	10
lmbda2	29.4556	1	3	4	4	4	8
mu2	27.9682	16	12	12	5	12	5
nu2	28.5126	19	23	23	19	24	19
rho1	13.4715	10	9	8	7	8	5
MK3	44.0252	1			18		26
2MK3	42.9271	2			14		25
MN4	57.4238	2			7		12
MS4	58.9841	1			10		16
2SM2	31.0159	4			3		4
Mf	1.0980	25			12		12
MSf	1.0159	10			9		13
Mm	0.5444	3			7		13
Sa	0.0411	96			109		166
Ssa	0.0821	38			43		50
Name	**N**	**NOS historical tidal constituents 1976**					
	°/h	Phase(h)					
		OP	GF	PM	ELK	KP	RR
J1	15.5854	15.3	14.8	14.8	16.1	15.0	16.8
K1	15.0411	14.7	14.9	14.9	15.0	15.1	15.3

Name	N	NOS historical tidal constituents 1976					
	°/h	Phase(h)					
		OP	GF	PM	ELK	KP	RR
K2	30.0821	5.4	6.1	6.1	5.6	6.4	5.9
L2	29.5285	6.6	7.2	7.2	5.6	7.3	5.9
M1	14.4967	16.1	14.9	14.9	17.1	15.1	18.3
M2	28.9841	6.2	6.3	6.4	6.5	6.5	6.6
M3	43.4762	8.2			0.8		0.8
M4	57.9682	5.3	6.1	1.8	2.1	1.9	2.2
M6	86.9523	3.9	1.3	1.5	1.5	0.8	1.4
M8	115.9364	1.1	2.1	2.9	0.4	0.2	0.5
N2	28.4397	5.4	5.5	5.5	5.8	5.7	6.0
2N2	27.8954	4.0	4.6	4.7	5.1	4.9	5.7
O1	13.9430	14.5	14.9	14.9	15.0	15.2	15.4
OO1	16.1391	14.0	14.8	14.8	16.2	14.9	17.1
P1	14.9589	14.6	14.9	14.9	14.6	15.1	15.2
Q1	13.3987	13.8	14.9	15.0	15.3	15.3	15.9
2Q1	12.8543	10.9	15.0	15.0	16.5	15.3	16.1
R2	30.0411	7.2	6.1	6.2	7.1	6.4	8.2
S1	15.0000	22.5			1.0		17.6
S2	30.0000	6.0	6.1	6.2	6.3	6.4	6.6
S4	60.0000	5.6	5.2	4.6	2.0	2.1	3.1
S6	90.0000	0.9	3.5	3.6	1.4	0.5	1.5
T2	29.9589	5.0	6.1	6.2	5.4	6.4	5.3
lmbda2	29.4556	11.0	6.2	6.3	5.0	6.5	4.6
mu2	27.9682	4.5	5.9	5.9	5.4	5.9	7.9
nu2	28.5126	5.4	5.6	5.7	5.9	5.9	6.1
rho1	13.4715	17.9	14.9	15.0	14.9	15.3	16.8
MK3	44.0252	6.8			4.3		4.6
2MK3	42.9271	3.3			4.8		4.9
MN4	57.4238	5.7			1.9		2.0
MS4	58.9841	2.6			2.2		2.3
2SM2	31.0159	10.4			9.9		10.1
Mf	1.0980	116.9			155.9		228.3
MSf	1.0159	173.5			343.4		34.1
Mm	0.5444	59.9			420.1		122.7
Sa	0.0411	5196.2			5033.0		5303.3
Ssa	0.0821	2778.3			2695.5		1883.4
NOS station number and location www.co-ops.nos.noaa.gov							
OP	9413616 Ocean Pier, Moss Landing			36.48.1′ N		121.47.4′ W	
GF	9413617 General Fish Co. Pier ML Harbor			36.48.1′ N		121.47.2′ W	

	NOS station number and location www.co-ops.nos.noaa.gov		
PM	9413624 Pacific Mariculture Dock ES	36.48.8′ N	121.45.5′ W
ELK	9413631 Elkhorn Slough at Elkhorn	36.49.1′ N	121.44.8′ W
KP	9413651 Kirby Park, Elkhorn Slough	36.50.5′ N	121.44.8′ W
RR	9413663 Elkhorn Slough Railroad Bridge	36.51.4′ N	121.45.3′ W

Table A2.
Tidal height amplitude in Moss Landing Harbor and Elkhorn Slough determined from 12-month observations in 1976 by the National Ocean Survey.

Author details

William W. Broenkow and Laurence C. Breaker*
Moss Landing Marine Laboratories, Moss Landing, CA, United States of America

*Address all correspondence to: lbreaker@mlml.calstate.edu

IntechOpen

References

[1] Gordon BL. Monterey Bay Area: Natural History and Cultural Imprints. 3rd ed. Pacific Grove, California: Boxwood Press; 1996

[2] Breaker LC, Broenkow WW. The circulation of Monterey Bay and related processes. Oceanography and Marine Biology: An Annual Review. 1994; **32**(1994):1-64

[3] Crampton TA. Long-term effects of Moss Landing Harbor on the wetlands of Elkhorn Slough [M.S. thesis]. Santa Cruz, California: University of California Santa Cruz; 1994

[4] Malzone CM. Tidal scour and its relation to erosion and sediment transport in Elkhorn Slough [M.S. thesis]. San Jose State University: Department of Geology; 1999

[5] Wasson K, Van Dyke E, Kvitek R, Brantner J, Bane S. Tidal Erosion at Elkhorn Slough, Ecosystem Observations for the Monterey Bay National Marine Sanctuary 2001. Monterey, California: NOAA, Monterey Bay National Marine Sanctuary; 2001. pp. 13-14

[6] Malzone CM, Kvitek R. Tidal scour, erosion, and habitat loss in Elkhorn Slough, California. A Report of the Elkhorn Slough Foundation Pursuant to National Oceanic and Atmospheric Administration Award #NA37OM0523. 1994. 15 pp

[7] Lowe P. Marsh loss in Elkhorn Slough, California: Patterns, mechanisms, and impact on shorebirds [M.S. thesis]. San Jose State University: Moss Landing Marine Laboratories; 1999

[8] Dyer KR. Estuaries: A Physical Introduction. London: John Wiley & Sons; 1972

[9] Broenkow WW, Breaker LC. A 30-year history of tide and current measurements in Elkhorn Slough, California. Scripps Institution of Oceanography Library. Paper 8. 2005. 55 p. Available from: http://repositories.cdlib.org/sio/lib/8

[10] Smith RE. The hydrography of Elkhorn Slough, a shallow California coastal embayment [M.A. thesis]. San Jose, California: Moss Landing Marine Laboratories and Department of Natural Sciences, San Jose State University; 1974

[11] Duke Energy Moss Landing, LLC: Moss Landing Power Plant Modernization Project, Evaluation of Proposed Discharge System with Respect to the Thermal Plan. Final Report. 2000

[12] NOS National Ocean Service: Tide Tables 1994. West Coast of North and South America. Rockville, MD: U.S. Department of Commerce, National Oceanic and Atmospheric Administration; 1993

[13] Wong CS. Observations of tides and tidal currents in Elkhorn Slough, California [M.S. thesis]. San Jose, California: Moss Landing Marine Laboratories, San Jose State University; 1989

[14] Clark LR. Long period wave characteristics in Moss Landing Harbor and Elkhorn Slough [M.A. thesis]. San Jose, California: Moss Landing Marine Laboratories and Department of Natural Sciences, San Jose State University; 1972

[15] Jackson PS. On the displacement height in the logarithmic velocity profile. Journal of Fluid Mechanics. 1981;**111**(1981):15-25

[16] Lynch TJ. Long wave study of Monterey Bay. [M.S. thesis]. Monterey, California: Naval Postgraduate School; 1970

[17] Komar PD. Boundary layer flow under steady unidirectional currents. In: Marine Transport and Environmental Management. New York: John Wiley and Sons; 1976. pp. 91-125

[18] Kjerfve B, Knoppers BA. Tidal choking in a coastal lagoon. In: Tidal Hydrodynamics. New York: John Wiley and Sons; 1991. pp. 169-182

[19] Pinkel R. Acoustic doppler techniques. In: Air-Sea Interaction Instruments and Methods. Vol. 1980. New York and London: Plenum Press; 1980. pp. 171-199

[20] Sverdrup HU, Johnson MW, Fleming RH. The Oceans: Their Physics, Chemistry, and General Biology. New York: Prentice Hall; 1942

[21] Johnson JW. Characteristics and behavior of Pacific coast tidal inlets. Journal of the Waterways, Harbors and Coastal Engineering Division. 1973; **WW3**:325-339

[22] Broenkow WW. Water Chemistry of Elkhorn Slough and Moss Landing Harbor. Ecologic and Hydrographic Studies of Elkhorn Slough, Moss landing Harbor and Nearshore Coastal Waters, July 1974–June 1976. Moss Landing, California: Moss Landing Marine Laboratories; 1977. pp. 388-465

[23] Bowden KF. The mixing processes in a tidal estuary. International Journal of Air and Water Pollution. 1983;7: 343-356

[24] Reilly PT. Phosphate flux in Elkhorn Slough, Monterey, California [M.A. thesis]. San Jose, California: Moss Landing Marine Laboratories and Department of Natural Sciences, San Jose State University; 1978

[25] Hansen DV. Currents and mixing in the Columbia River Estuary. In: Ocean Science and Ocean Engineering: Joint Conference of Marine Technology

Society and the Society of Limnology and Oceanography; Washington, DC. 1965. pp. 943-955

[26] Schureman P. Manual of Harmonic Analysis and Prediction of Tides. Washington, DC: U.S. Govt. Printing Office, U.S. Dept. of Commerce Publication 89; 1958

[27] Aubrey DG, Speer PE. A study of nonlinear tidal propagation in shallow inlet/estuarine systems, part 1: Observations. Estuarine, Coastal and Shelf Science. 1985;**21**:185-205

[28] Speer PE, Aubrey DJ. A study of nonlinear tidal propagation in shallow inlet/estuarine systems, part 2: Theory. Estuarine, Coastal and Shelf Science. 1985;**21**:207-224

[29] Aubrey DG. Hydrodynamics controls on sediment transport in well-mixed bays and estuaries. In: Lecture Notes on Coastal and Estuarine Studies. Berlin: Springer-Verlag; 1986. pp. 254-258

[30] Friedrichs CT, Aubrey DG. Nonlinear tidal distortion in shallow well-mixed estuaries: A synthesis. Estuarine, Coastal and Shelf Science. 1988;**27**:521-545

[31] Parker BB. The relative importance of the various nonlinear mechanisms in a wide range of tidal interactions. In: Tidal Hydrodynamics. New York: John Wiley and Sons; 1991. pp. 237-268

[32] Boon JD, Byrne RJ. On basin hypsometry and the morphodynamic response of coastal inlet systems. Marine Geology. 1981;**40**:27-48

[33] Pugh DT. Tides, Surges and Mean Sea Level. Chichester: John Wiley & Sons; 1987

[34] Officer CB. Physical Oceanography of Estuaries (and Associated Coastal

Waters). New York: John Wiley & Sons; 1976

[35] Orme AR. Evolution of the Morro Bay barrier-lagoon system: A synthesis. In: ASCE Coastal Sediment Conference. Seattle, WA; 1991. pp. 7.3.39-7.3.48

[36] Haltiner J, Thor D. Sedimentation processes in Morro Bay, California. In: Sedimentation and Physical Processes, ASCE Coastal Sediment Conference. Seattle, WA; 1991

[37] O'brien MP. Equilibrium flow areas of tidal inlets on sandy coasts. In: Proceedings of the Tenth Conference on Coastal Engineering. Tokyo, Japan: ASCE; 1967. pp. 676-686

Chapter 2

Tidal Evolution Related to Changing Sea Level; Worldwide and Regional Surveys, and the Impact to Estuaries and Other Coastal Zones

Adam Thomas Devlin and Jiayi Pan

Abstract

Global sea level rise understanding is critical for coastal zones, and estuaries are particularly vulnerable to water level changes. Sea level is increasing worldwide due to several climactic factors, and tidal range may also change in estuaries due to sea level rise and anthropogenic harbor improvements that may modify friction and resonance, increasing risks to population centers. Tidal range changes may further complicate the risks of sea level rise, increasing the frequency of nuisance flooding, and may affect tide-sensitive ecosystems. Higher total water levels threaten to increase flood zone areas in estuarine regions, which can impact the infrastructure, industry, and public health of coastal populations, as well as disrupting sensitive biological habitats. Therefore, it is of critical interest to analyze how tidal range changes under sea level changes. This chapter describes the tidal anomaly correlation (TAC) methodology which can quantify the tidal evolution related to sea level changes. A basin-wide survey of Pacific and Atlantic Ocean tide gauges is detailed, showing that tidal changes due to sea level rise is present at most locations surveyed. A focused regional study of Hong Kong is also described as an example of how tidal evolution can impact high population density coastal zones.

Keywords: ocean tides, tidal variability, sea level rise, coastal flooding, nuisance flooding

1. Introduction

Ocean tides are a manifestation of the response to the gravitational forcing induced by astronomical bodies; namely, the Sun and Moon. The lunar forcing is approximately twice the magnitude of the solar forcing, since the closer distance of the Moon is more important than the larger mass of the Sun, as the universal law of gravitation is directly proportional to mass but inversely proportional to the square of the distance between heavenly bodies. However, there are also interactions between the Sun and Moon that modulate the distance of both bodies, which in turn influences the forcing felt at any point on Earth as a linear combination of tidal

frequencies with forcing frequencies that range from twice-daily to decadal. Thus, though gravitation between two bodies is straightforward and definite, the true expression of tidal forcing experienced on Earth is an example of complex relation known as the "three-body problem" [1], which is only numerically calculable. However, this forcing is well-known, and essentially constant over short timescales.

Logic would dictate that due to this predictable "celestial clockwork", the ocean tides on Earth should be equally predictable at all locations. However, this would only be true if Earth's oceans had a constant depth and simple coastlines, as originally assumed by LaPlace in his tidal equations in the eighteenth century. This, of course, is not the case. Earth has a complex and highly variable ocean depth, with undersea ridges, trenches, plateaus, and valleys. Coastlines are also highly complex. Both factors can modulate the response of tidal forcing, with shallow coastal areas being the most sensitive. Thus, coastal tides are much larger and more variable than those seen in the deep ocean. The tides in coastal regions are also highly sensitive to changes in the shape and depth of shallow water regions. Some semi-enclosed coastal regions can amplify the resonant response of tidal forcing, such as in the Bay of Fundy in Canada, where tides can exceed tens of meters. Changes in local water depth can also influence the response of tides. Since recent decades have experienced the most rapid rise in mean sea levels (MSL) in millennia [2, 3], due to the steric rise of the ocean from ice melt and the thermal expansion of ocean water [4], both due to climate-change induced factors, future tidal range evolution is likely.

The changes in MSL are most pronounced in shallow coastal regions, especially in developed population centers, such as estuaries. Changes in MSL may lead to a change in local water depth in coastal regions, which have a first-order impact to coastal zones as rising background water levels. In turn, changes in water depth can modulate the response of tides as the resonant behavior changes. Small changes in water depth can lead to large changes in tidal range, which leads to a second-order impact to coastal zones. Estuaries are among the most vulnerable areas to these changes, since these regions are where large population centers are located, as well as sensitive ecosystems. Both natural and anthropogenic systems are highly dependent on tides. Biological habitats such as mangrove forests rely on constant tidal range, as do the complex food webs seen in estuarine regions. Consequently, changes in biology and ecology can have serious detrimental effects on human society, as much of the economy and industry of estuarine population may be dependent on stable ecosystems, e.g., fisheries, farming, and tourism. Changes in tidal range, tidal currents and tidal energy distribution can amplify these factors.

There are significant physical risks to estuarine cities and population centers that can be brought about by changing tides related to MSL rise. A large percentage of human settlements are in estuarine regions, as the abundance of fresh water and easy access to the open ocean allows civilization to easily thrive in these regions. Throughout history, estuarine cities have existed at the mercy of both the river and the sea. Extreme floods or extreme droughts can lead to extreme responses of the riverine aspects of estuaries, with implications for local farming and public health factors. On the oceanic side, storm events such as hurricanes and typhoons or tsunamis can be disastrous to estuarine cities, with extensive infrastructure damage and disruption to the local economy. However, both types of extreme events tend to be short-lived, and population centers in estuaries have developed knowing that even though such events can happen anytime, the average properties of the coastal zones, such as mean sea level and local tidal range, remain relatively constant. These assumptions have determined the planning and design of estuarine developments, such as harbors, roads, residence centers, and other infrastructure. Flooding due to inland storms and river surge might be occasionally extreme, but it could be

predicted to only reach certain maximum flood levels. However, under scenarios of sea level rise, and the resultant changes in ocean tides, modern times are now producing changes in this "stable background", and previous assumptions of the worst-case scenarios may no longer be valid, rendering past coastal defense efforts inadequate to resist future extreme events. Changing tides on top of sea-level rise also allow the possibility of nuisance flooding, also known as "sunny-day flooding", in which flood levels can be exceeded at exceptional high tides without the influence of a storm of river surge event [5, 6]. Other impacts possible under rising sea-levels and tidal evolution besides local flooding include disruptions in shipping and other coastal-based logistic factors. Most importantly, the coupled changes in MSL and ocean tides may be occurring rapidly, and across multiple spatial and temporal scales, making it a complex problem to predict with certainty, as each coastal location may experience a much different response.

This chapter will explore the dynamics and details of changing ocean tides. A background will first be given about past research that has identified secular (long-term) non-astronomical changes in ocean tides as well as a summary of past studies of MSL rise. Next will be a description of the methodology of newer efforts that have analyzed the correlated changes in sea levels and ocean tides in the Pacific and Atlantic Oceans, based primarily on the work of Devlin et al. [7–11]. Following this will be a summary of significant results in the Pacific and Atlantic basins, as well as results from a focused study of the Hong Kong region, where some of the strongest magnitude changes have been observed. Next, there will be a discussion section about the implications of coupled MSL and tidal variability for estuaries and coastal zones including effects like nuisance flooding, and finally, conclusions.

2. Background

2.1 Sea level changes

Mean sea level (MSL) is increasing nearly everywhere on Earth, with a globally-averaged rise of $+1.7 \pm 0.2$ mm year^{-1} as estimated from coastal and island tide gauge measurements from 1900 to 2009 [2, 12, 13], and at a rate $+3.4 \pm 0.4$ mm year^{-1} for 1993–2016 as estimated from satellite altimetry (http://sealevel.colorado.edu/; [14]). In the twentieth century, the most rapid increase in MSL over the last three millennia has been observed, based on a semi-empirical estimate of sea-level rise [3], finding that without global warming, the observed increases in global sea levels would have been much less. Furthermore, since ~1970, global mean sea level rise has been dominated by anthropogenic forcing [15]. Some climate models predict that MSL rates will accelerate in future decades via global climate change mechanisms [13] such as ice sheet melt and thermosteric MSL rise; both of these are induced by upper-ocean warming [4, 12, 16–19].

However, there is a wide spatial variability to these rates [3, 20], attributed to the combined effects of spatially variable wind and warming, and different vertical rates of land subsidence. In the Western Pacific, MSL rise often is larger than $+10$ mm year^{-1} in some locations, whereas Eastern Pacific rates are near zero or sometimes slightly negative because of tectonic and weather factors [21]. The anomalously rapid sea level rise observed in the western Pacific tends to be underestimated in many models. This may be because of low variability in tropical zonal wind stress [22]. However, the extreme rate in the Western tropical Pacific is unlikely to persist unabated [23], and a reversal of this Pacific asymmetry may be imminent soon.

2.2 Tidal changes

Ocean tides have classically been considered stationary because of their close relationship to celestial motion of the Moon and Sun [24]. However, many studies have clearly demonstrated that tides are evolving at different rates in different regions of the world, and these changes are not related to astronomical forcing [25–28]. Early studies discovered that long-term tidal changes are present at some stations such as at Brest, France, which has been steadily recording tidal levels for hundreds of years [29, 30]. It has also been shown that tidal changes can be a result of harbor modifications [31–36] through mechanisms such as channel deepening and land reclamation. Alternatively, long-term tidal changes can be due to modulations in the internal tide [37, 38]. Regionally focused studies have discovered changes in the major diurnal and semidiurnal tides in the Eastern Pacific [39], in the Gulf of Maine, [40], in the North Atlantic [26, 41], in China [42, 43], in Japan [44], and at certain Pacific islands [45].

2.3 Coupled changes in tides and MSL

Mean sea levels may influence tidal evolution directly, or it may be correlated with tidal variability through secondary mechanisms in a multitude of ways; some may be acting locally, and others may be active on basin-wide (amphidromic) scales. One way is through changes in water depth (e.g., due to climate-change induced sea level rise), which may influence tides on a large geographic scale via a "coupled oscillator" mechanism between the shelf and the deep ocean [46, 47]. Water depth changes can also modify the propagation and dissipation of tides [48, 49] by directly altering wave speed in shallow areas, or by changing the effect of bottom friction. The warming of the upper ocean [4] may lead to internal changes to stratification properties and a modulation of thermocline depth. Both mechanisms can yield a steric sea level signal which may modify the surface manifestation of internal tides, thus producing a detectable change at tide gauges. Such changes have been observed at the Hawaiian Islands [37]. On a shorter timescale, seasonal tidal variations can be due to rapid changes in water column stratification [50, 51], or by seasonal river flow characteristics [52, 53]. The shifting of the amphidromic points, e.g., as seen around Britain and Ireland [54], is possibly associated with changes in regional tidal properties [55]. In harbors and estuaries, increased water depths can alter the tidal prism, local resonance, and frictional properties [34, 56].

2.4 Dynamical relations of MSL and tides

A tidal constituent amplitude can be expressed as a function of multiple variables:

$$Amp_{tidal} = f(H, r, \Psi_\omega, \dots) \tag{1}$$

Here, H is the water depth (which includes MSL, waves, storm surge, ocean stratification, river discharge, winds, etc.), r represents friction, and Ψ_ω is the frequency-dependent tidal response to astronomical tidal forcing. The " ... " indicates other variabilities not considered here, e.g., wind. For a constituent amplitude to experience change (i.e., ΔAmp_{tidal}) it is necessary that one or more of these variables change, expressed by:

$$\Delta Amp_{tidal} = f(\Delta H, \Delta r, \Delta \Psi_\omega, \dots) \tag{2}$$

Subsequently, each of the variables that can change the tidal amplitudes depend on multiple factors:

$$\Psi_\omega = f(H, r, \dots) \rightarrow \Delta \Psi_\omega = f(\Delta H, \Delta r, \dots) \tag{3}$$

$$H = f(\rho, Q_r, \dots) \rightarrow \Delta H = f(\Delta \rho, \Delta Q_r, \dots) \tag{4}$$

$$r = f(H, \rho, \dots) \rightarrow \Delta r = f(\Delta H, \Delta \rho, \dots) \tag{5}$$

The depth-averaged tidal response function is therefore a function of astronomical forcing, water depth and the local frictional properties. Additionally, water depth may depend on vertical land movement [57], global sea-level rise [2], and other location-dependent environmental factors such as the local water density (ρ), local river discharge, Q_r [52], and local and far field wind forcing [21] effects. The effective frictional damping will be dependent on water depth, stratification, and mixing induced at the boundaries (bottom and surface). Finally, density ρ, as well as changes in buoyancy and stratification, are a function of water temperature, T_w, water salinity, T_s, river discharge, Q_r, and mixing, m_x:

$$\rho = f(T_w, S_w, Q_r, m_x, \dots) \rightarrow \Delta \rho = f(\Delta T_w, \Delta S_w, \Delta Q_r, \Delta m_x, \dots) \tag{6}$$

The chain rule can be applied to Eq. (2), and considering the possible changes of all factors yields a general expression for the variability in tidal amplitudes:

$$\Delta Amp_{tidal} = f(\Delta H, \Delta Q_r, \Delta \rho, \Delta m_x, \Delta r, \Delta \Psi_\omega, \dots) \tag{7}$$

It can be seen from this derivation that many of the variabilities can be correlated to each other. **Figure 1** shows a simple cartoon displaying the possible mechanisms that can affect MSL and tides, based on the derivations and references given above. Hence, the existence of multiple mechanisms, many of which may be
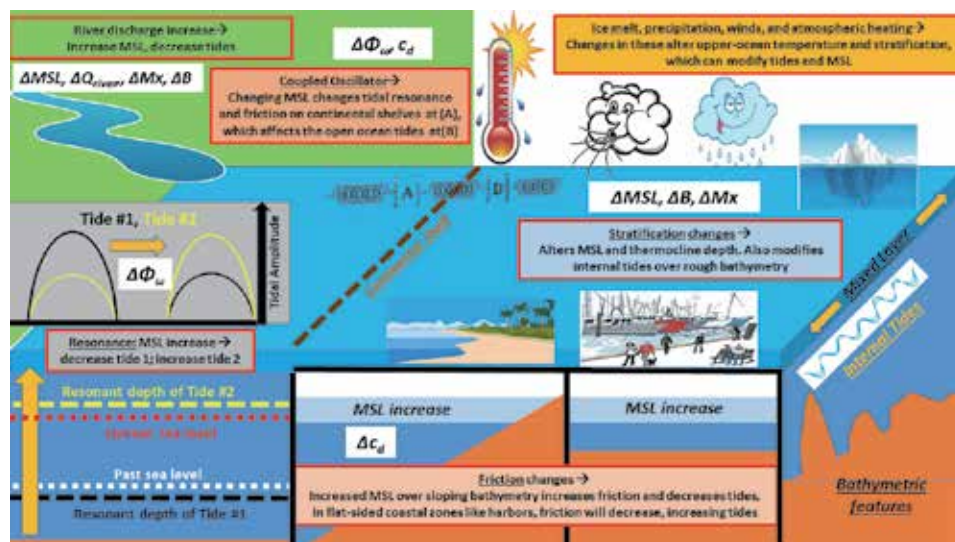
Figure 1.
Schematic cartoon showing some of the mechanisms that can affect MSL and tides. See the text above for complete description of cartoon components.

correlated with each other, can make it difficult to discern the causes of observed variability. Yet, understanding these correlations is still vital, with the best strategy being to consider each location's dominating factors individually instead of relying on globally averaged solutions.

3. Methodology of tidal variability analysis

3.1 Tidal analysis

Recent studies have developed a reliable methodology to analyze tidal variability related to MSL variability [7–11]. These methods have been applied to many tide gauge locations worldwide, with a twofold approach. The first technique involves analyzing individual tidal constituents, while the second involves the consideration of the combination of multiple tides. For any individual tide gauge, water levels are typically recorded hourly as a continuous time series. Harmonic analysis of this data yields individual time series of multiple tidal constituents, each corresponding to an individual component of astronomical motion of the Sun and Moon, and their co-interactions. The largest parts of the tidal energy concentrate in the once-a-day (diurnal) and twice-a day (semidiurnal) frequency bands, with several closely spaced tidal constituents being important in each band. In practice, however, only a small number of these contain most of the tidal energy. For the purposes of our discussions of past studies we will only need to mention a few. The major twice-daily (semidiurnal) tide due to the Moon is denoted M_2, and the twice-daily tide due to the Sun is denoted S_2. Two important lunisolar interaction tides that define the once-a-day (diurnal) tides are denoted K_1 and O_1. Most of the past analyses only consider these four components, however, some of the locations considered (in the Atlantic Ocean) also consider two more semidiurnal components, denoted N_2 and K_2, and two more diurnal components, P_1 and Q_1 (**Table 1**).

3.2 Tidal admittance calculations

Investigations of tidal trends are carried out using a tidal admittance method. An admittance is the unit-less ratio of an observed tidal constituent to the corresponding tidal constituent in the astronomical tide generating force (ATGF) expressed as a potential, V, divided by the acceleration due to gravity, g, to yield a quantity, $Z_{pot}(t) = V/g$, with units of length that can be compared to tidal elevations $Z_{obs}(t)$ on a constituent by constituent basis. Because nodal and other low-frequency astronomical variability is present with similar strength in both the observed tidal record and in V, its effects are eliminated in the yearly analyzed admittance time series. Yearly tidal harmonic analyses are performed at monthly time steps on both the observed tidal records and the hourly $Z_{pot}(t)$ at the same location, using the *r_t_tide* MATLAB package [58], a robust analysis suite based on *t_tide* [59]. The tidal potential is determined based on the methods of Cartwright and Tayler [24], and Cartwright and Edden [60]. The result from a single harmonic analysis of $Z_{obs}(t)$ or $Z_{pot}(t)$ determines an amplitude, A, and phase, θ, at the central time of the analysis window for each tidal constituent, with error estimates. Analyzing the entire tide gauge record produces time-series of amplitude and phase. From amplitude $A(t)$ and phase $\theta(t)$ time series, one can construct complex amplitudes $Z(t)$:

$$\mathbf{Z}(t) = A(t)e^{i\theta(t)} \tag{8}$$

Station name	Country	Lat.(N)	Long. (E)	K_1	(±)	M_2	(±)	δ-HAT	(±)
Northeast Pac.									
French Frigate Sh.	USA	23.87	−166.28	−8.52	4.44	−33.37	9.36	−52.62	16.89
Cabo San Lucas	Mexico	22.88	−109.92	−8.83	3.06	39.78	12.45	57.75	64.52
Kodiak Island, Alaska	USA	57.73	−152.52	12.96	10.03	20.84	7.79	12.27	18.80
Adak, Alaska	USA	51.87	−176.63	47.76	15.62	−11.11	7.46	11.60	17.66
Dutch Harbor, Alaska	USA	53.88	−166.53	−44.37	14.73	−2.59	8.26	−61.00	17.63
Midway	USA	28.22	−177.37	−2.07	5.62	6.03	8.61	−15.74	15.04
Johnston	USA	16.75	−169.52	−32.27	11.78	−29.85	16.25	−116.88	24.45
Honolulu, Hawaii	USA	21.3	−157.87	−9.03	6.53	140.77	23.35	139.51	21.62
Nawiliwilli Bay, Hawaii	USA	21.97	−159.35	−3.63	5.87	61.28	13.80	55.61	12.27
Kahului, Hawaii	USA	20.9	−156.47	2.60	7.52	−43.41	8.79	−13.41	7.19
Hilo, Hawaii	USA	19.73	−155.07	12.90	5.96	131.07	14.35	146.75	12.18
Mokuoloe, Hawaii	USA	21.43	−157.8	38.77	6.45	6.35	14.28	44.24	25.30
Tofino	Canada	49.15	−125.92	6.25	8.01	44.64	8.41	13.39	31.77
Victoria	Canada	48.42	−123.37	−1.66	17.45	−33.09	12.66	−60.30	43.39
San Francisco, California	USA	37.8	−122.47	−70.20	10.99	−80.34	21.57	−146.56	35.20
La Jolla, California	USA	32.87	−117.25	16.03	12.40	28.83	12.57	59.50	34.60
Monterey, California	USA	36.6	−121.88	1.40	10.29	31.79	5.07	27.37	22.30
Crescent City, California	USA	41.75	−124.18	−15.27	10.44	−9.50	11.40	−48.44	12.73
Neah Bay, Washington	USA	48.37	−124.62	4.50	8.21	−11.95	6.26	9.80	14.06
Sitka, Alaska	USA	57.05	−135.35	−20.61	12.37	21.93	15.29	−23.03	39.63
Seward, Alaska	USA	60.12	−149.43	3.27	11.30	5.68	11.70	−8.19	25.83
Seldovia, Alaska	USA	59.43	−151.72	21.69	17.88	−63.71	25.41	−53.76	40.79

Station name	Country	Lat.(N)	Long. (E)	K_1	($\pm$)	M_2	($\pm$)	δ-HAT	($\pm$)
Valdez, Alaska	USA	61.13	−146.37	17.86	19.01	12.24	16.33	52.06	18.79
Port San Luis, California	USA	35.18	−120.77	−10.55	12.57	12.68	6.89	4.49	18.17
Los Angeles, California	USA	33.72	−118.27	−11.03	10.87	−7.38	7.33	−21.39	17.05
San Diego, California	USA	32.72	−117.17	−13.71	7.29	−0.87	7.02	−17.77	17.18
Yakutat, Alaska	USA	59.55	−139.73	−7.87	11.12	2.48	13.54	21.99	41.13
Ketchikan, Alaska	USA	55.33	−131.63	−1.48	11.66	10.32	12.64	21.89	15.73
Astoria, Oregon	USA	46.22	−123.77	−32.65	10.87	−91.81	16.36	−256.81	35.09
Charleston, Oregon	USA	43.35	−124.32	0.64	7.90	−0.08	8.72	−17.47	18.59
Santa Monica, California	USA	34.02	−118.5	−2.46	12.81	−38.31	6.77	−51.72	47.75
Cordova, Alaska	USA	60.57	−145.75	31.25	15.59	10.45	16.29	16.24	14.86
South Beach, Oregon	USA	44.63	−124.05	−18.06	9.08	5.08	8.58	−16.05	40.56
Seattle, Washington	USA	47.6	−122.4	14.68	14.84	−13.26	10.09	−34.64	37.09
Vancouver	Canada	49.29	−123.11	−33.85	32.52	−42.29	32.99	−160.29	53.48
Point Atkinson	Canada	49.34	−123.25	−41.09	44.91	−30.66	44.21	−97.58	232.94
Bella Bella	Canada	52.16	−128.14	−33.68	10.94	15.34	13.91	−35.24	33.36
Queen Charlotte	Canada	53.25	−132.07	7.91	15.64	47.42	49.37	1.47	71.85
Port Hardy	Canada	50.72	−127.49	−33.95	14.16	8.94	23.59	−12.79	36.92
Bamfield	Canada	48.84	−125.14	−7.67	9.78	−3.59	13.20	11.02	26.28
Southeast Pac.									
Baltra	Ecuador	−0.43	−90.28	7.28	4.66	27.08	5.22	26.89	18.15
Papeete (Tahiti)	Fr. Poly.	−17.53	−149.57	−10.12	7.75	−136.07	33.43	−95.29	43.32
Juan Fern Island	Chile	−33.62	−78.83	−4.57	6.50	−16.53	4.92	−28.68	11.47
Easter Island	Chile	−27.15	−109.45	−3.57	6.44	−7.74	8.94	28.73	24.75

Station name	Country	Lat.(N)	Long. (E)	K₁	(±)	M₂	(±)	δ-HAT	(±)
Rarotonga	Cook Is.	−21.2	−159.78	10.79	3.36	16.68	12.11	49.97	20.53
Penrhyn	Cook Is.	−8.98	−158.05	17.77	3.59	27.57	6.00	31.33	18.75
Santa Cruz	Ecuador	−0.75	−90.32	3.16	2.52	−22.93	11.02	−34.78	25.26
San Felix	Chile	−26.28	−80.13	14.34	4.05	45.31	11.31	79.63	36.25
Nuku'alofa	Tonga	−21.13	−175.17	5.44	4.11	−42.04	10.64	−103.31	10.30
Antofagasta	Chile	−23.65	−70.4	−6.79	6.72	1.77	10.92	−33.28	5.49
Valparaiso	Chile	−33.03	−71.63	11.31	10.34	−2.27	22.44	−122.85	38.33
Lobos de Afuera	Peru	−6.93	−80.72	3.46	4.21	38.64	10.79	23.92	16.59
Buena Ventura	Colombia	3.9	−77.1	−14.51	4.14	−8.24	31.63	−81.61	16.93
Caldera	Chile	−27.07	−70.83	40.34	6.74	51.24	10.74	127.40	27.28
La Libertad	Ecuador	−2.2	−80.92	−6.04	3.86	−72.17	19.85	−73.11	16.75
Matarani	Peru	−17	−72.12	−18.57	4.27	−20.16	9.34	−40.29	22.12
Balboa	Panama	8.97	−79.57	−1.38	2.67	−27.46	8.98	−56.77	11.19
Tumaco	Colombia	1.83	−78.73	−3.10	3.14	9.79	19.83	33.97	21.07
Puerto Montt	Chile	−41.48	−72.97	−81.37	16.93	−610.13	99.43	−963.21	107.66
Northwest Pac.									
Chichijima	Japan	27.1	142.18	12.13	10.78	−11.32	13.99	−17.09	20.63
Hong Kong	China	22.3	114.22	308.37	42.97	292.49	50.31	665.44	99.23
Kaohsiung	Taiwan	22.62	120.28	17.19	5.11	−4.74	8.47	−17.48	16.91
Keelung	Taiwan	25.15	121.75	−25.79	8.79	−48.15	13.64	−54.28	53.95
Nakanoshima	Japan	29.83	129.85	−15.68	13.07	53.18	29.44	47.39	36.07
Abashiri	Japan	44.02	144.28	−52.16	17.57	−30.74	6.12	−126.15	47.40
Hamada	Japan	34.9	132.07	45.18	19.21	−26.27	7.07	56.95	83.61

Station name	Country	Lat.(N)	Long. (E)	K_1	(±)	M_2	(±)	δ-HAT	(±)
Toyama	Japan	36.77	137.22	−27.94	14.91	−0.49	6.12	−29.18	37.40
Kushiro	Japan	42.97	144.38	**53.69**	**11.20**	−17.03	8.16	−43.71	22.09
Ofunato	Japan	39.07	141.72	13.39	11.44	**−34.36**	**8.83**	**−78.73**	**32.98**
Mera	Japan	34.92	139.83	**−79.54**	**16.67**	17.51	14.68	**−100.04**	**9.57**
Kushimoto	Japan	33.47	135.78	16.35	9.90	17.82	25.25	−25.03	26.31
Aburatsu	Japan	31.57	131.42	**38.75**	**10.78**	−11.91	15.38	36.18	12.17
Naha	Japan	26.22	127.67	3.88	8.08	1.31	12.50	39.46	18.16
Maisaka	Japan	34.68	137.62	**−71.20**	**12.49**	**−100.99**	**18.78**	**−350.29**	**29.25**
Miyakejima	Japan	34.07	139.48	**−12.04**	**4.10**	**−17.33**	**3.84**	**−55.27**	**8.44**
Naze	Japan	28.38	129.5	−11.61	7.86	**−44.00**	**11.37**	−29.62	29.23
Wakkanai	Japan	45.4	141.68	−30.41	18.19	7.10	10.61	**−108.48**	**22.70**
Nagasaki	Japan	32.73	129.87	−18.21	9.60	**−84.81**	**22.61**	**−85.53**	**28.09**
Nishinoomote	Japan	30.73	131	5.24	8.35	4.67	14.57	14.34	34.65
Hakodate	Japan	41.78	140.73	8.66	14.45	7.66	10.04	11.96	24.16
Ishigaki	Japan	24.33	124.15	**27.59**	**10.49**	**−101.09**	**13.26**	**−85.53**	**17.11**
Hachinohe	Japan	40.53	141.53	**−21.13**	**9.67**	**−20.69**	**7.18**	**−82.28**	**23.08**
Hanasaki	Japan	48.28	145.58	4.92	4.87	−9.99	5.93	**53.59**	**17.67**
Kamaishi	Japan	39.27	141.89	20.34	11.48	−9.73	15.15	−13.60	49.69
Minamizu	Japan	34.63	138.89	−3.59	8.10	**18.81**	**9.24**	−15.73	23.52
Miyako	Japan	39.63	141.97	3.63	8.02	**−34.28**	**10.34**	−18.20	9.85
Nagoya	Japan	35.08	136.88	**−17.08**	**6.58**	**29.19**	**8.22**	2.49	7.05
Omaezaki	Japan	34.6	138.23	9.08	7.29	**−35.90**	**6.80**	−29.21	38.98
Onahama	Japan	36.93	140.92	**24.81**	**11.15**	**−30.12**	**11.23**	−42.33	31.63

Station name	Country	Lat.(N)	Long. (E)	K_1	(±)	M_2	(±)	δ-HAT	(±)
Owase	Japan	34.07	136.22	0.61	6.40	15.47	4.84	−3.58	12.84
Toba	Japan	34.47	136.85	−9.90	7.91	13.56	25.85	−85.16	14.55
Tokyo	Japan	35.67	139.77	−52.32	7.96	−32.71	15.18	−137.30	31.50
Urigami	Japan	33.55	135.9	−18.83	6.86	−35.15	13.16	32.69	18.72
Odomari	Japan	31.02	130.69	−9.46	8.14	−101.22	14.67	−193.72	52.20
Okada	Japan	34.78	139.4	20.32	8.69	78.65	15.14	158.85	20.41
Shimizuminato	Japan	35.02	138.5	−50.66	12.38	−57.18	14.54	−208.53	54.03
Shirihama	Japan	33.68	135.38	13.51	6.39	−47.26	13.33	−38.17	34.38
Tosashimizu	Japan	32.78	132.97	1.62	7.79	1.10	8.35	−81.37	56.50
Southwest Pac.									
Pohnpei	Micronesia	6.98	158.25	21.28	5.37	9.68	15.66	−6.22	14.96
Nauru	Rep of Nauru	−0.53	166.92	−2.33	6.78	−20.22	9.46	−53.89	7.83
Majuro	Rep Marshall Is	7.12	171.37	0.77	7.57	−2.52	16.65	−26.84	20.39
Malakal	Rep of Belau	7.33	134.47	50.30	5.19	−27.23	7.01	4.34	24.61
Yap	Fd St Micronesia	9.52	138.13	24.44	6.77	−39.92	7.01	−57.78	25.15
Honiara	Solomon Islands	−9.42	159.95	4.00	4.23	64.61	4.71	66.79	10.13
Rabaul	Pap. New Guinea	−4.2	152.18	−30.61	3.82	103.43	9.22	30.36	7.86
Christmas Island	Rep of Kiribati	1.98	−157.47	−7.59	3.68	−50.00	8.77	−70.51	8.38
Suva	Fiji	−18.13	178.43	−2.86	4.92	59.61	16.99	71.90	68.46
Noumea	France	−22.3	166.43	27.01	10.82	21.36	38.45	73.12	28.04
Funafuti	Fiji	−8.5	179.22	−8.33	4.16	−27.28	8.38	−26.57	30.14
Saipan	N. Mari. Islands	15.23	145.75	7.19	12.54	34.13	17.96	−5.84	14.93
Kapingamarangi	Fd St Micronesia	1.1	154.78	−21.95	6.02	36.75	8.44	15.71	15.00

Station name	Country	Lat.(N)	Long. (E)	K_1	($\pm$)	M_2	($\pm$)	δ-HAT	($\pm$)
Port Villa	Vanuatu	-17.77	168.3	-11.72	4.86	82.47	19.47	74.19	52.38
Wake	USA	19.28	166.62	2.14	7.14	62.21	24.97	-24.16	31.65
Guam	Guam	13.43	144.65	-26.24	12.26	-8.45	17.93	-115.92	17.85
Kwajalein	Marshall Islands	8.73	167.73	1.07	5.62	12.76	12.49	38.25	12.64
Pago Pago	USA	-14.28	-170.68	14.34	3.64	21.05	17.03	28.16	21.31
Manus Island	Pap. New Guinea	-2.02	147.27	-15.77	10.06	-26.10	13.99	0.36	51.64
Wellington	New Zealand	-41.28	174.78	-7.37	7.82	-17.48	19.95	-39.35	17.88
Cendering	Malaysia	5.27	103.18	-4.83	16.88	-57.34	10.35	-131.72	67.22
Johor Bahru	Malaysia	1.47	103.8	-109.04	28.62	-175.99	27.86	-232.08	36.09
Kuantan	Malaysia	3.98	103.43	-57.48	18.26	-67.71	21.92	-216.82	53.51
Tioman	Malaysia	2.8	104.13	-79.55	20.41	-87.70	27.24	-292.35	48.19
Sedili	Malaysia	1.93	104.12	-118.19	21.58	-74.64	28.15	-215.36	107.81
Kukup	Malaysia	1.33	103.45	-17.17	14.89	-97.15	15.16	-184.56	59.35
Getting	Malaysia	6.23	102.1	-23.03	9.98	-44.19	10.05	-83.72	103.62
Ko Lak	Thailand	11.8	99.82	30.32	26.28	29.16	7.93	-42.28	53.26
Tanjong Pagar	Singapore	1.27	103.85	-140.02	31.09	0.18	32.51	4.46	9.54
Kelang	Malaysia	3.05	101.37	12.01	14.74	-152.54	14.72	-152.29	34.13
Kaling	Malaysia	2.22	102.15	-78.24	14.28	-83.51	9.09	-218.47	57.52
Langkawi	Malaysia	6.43	99.75	-14.33	5.61	-83.03	12.81	-143.79	37.15
Lumut	Malaysia	4.23	100.62	-2.44	12.17	-76.20	7.31	-116.95	42.95
Penang	Malaysia	5.42	100.35	-4.51	7.46	-95.06	11.40	-138.73	29.69
Ko Taphao Noi	Thailand	7.83	98.43	-2.85	4.33	-62.23	14.66	-70.35	32.54
Vung Tau	Vietnam	10.33	107.07	59.30	16.80	-1.71	37.52	108.00	87.06

Station name	Country	Lat.(N)	Long. (E)	K_1	(±)	M_2	(±)	δ-HAT	(±)
Kota Kinabalu	Malaysia	5.98	116.07	−1.72	11.41	**−21.09**	**5.90**	**−67.18**	**23.90**
Bintulu	Malaysia	3.22	113.07	**287.13**	**44.81**	−23.43	13.76	**614.89**	**140.46**
Sandakan	Malaysia	5.82	118.07	**49.54**	**10.99**	**24.79**	**9.18**	**107.56**	**28.17**
Brisbane	Australia	−27.37	153.17	0.40	17.56	−6.46	48.04	**272.56**	**39.62**
Bundaberg	Australia	−24.83	152.35	5.54	5.40	**−18.03**	**7.09**	−13.85	19.94
Ft. Denison	Australia	−33.85	151.23	−0.92	0.28	**−13.98**	**0.35**	−2.46	20.72
Townsville	Australia	−19.25	146.83	−1.52	5.17	6.23	12.47	−11.58	12.32
Spring Bay	Australia	−42.55	147.93	19.69	12.34	**−81.68**	**29.84**	−87.50	80.18
Booby Island	Australia	−10.6	141.92	25.44	24.63	−6.48	15.22	19.60	79.56
Hobart	Australia	−42.88	147.33	−20.13	11.19	19.65	15.83	27.53	23.14
Manila	Philippines	14.58	120.97	33.98	25.32	**−92.68**	**14.56**	−118.76	66.57
Legaspi	Philippines	13.15	123.75	−21.13	7.33	**−146.09**	**21.30**	**−144.79**	**36.48**
Davao	Philippines	7.08	125.63	**191.90**	**22.16**	**−79.66**	**14.90**	68.99	89.72
Lord Howe Island	Australia	−31.52	159.07	4.80	7.23	−7.22	12.74	10.24	27.38
Lautoka	Fiji	−17.6	177.43	4.14	3.07	**23.39**	**10.60**	**53.80**	**19.66**
Cairns	Australia	−16.92	145.77	−1089.03	477.48	109.08	20.28	297.56	1274.52
Gladstone	Australia	−23.85	151.26	−146.62	515.09	36.50	39.90	−40.45	300.49
Williamstown	Australia	−37.86	144.89	**398.57**	**186.07**	9.63	15.64	145.75	568.48

All values are expressed as millimeter change in tide per meter rise in MSL ($mm\ m^{-1}$).
Significant values are in bold text, based on a SNR > 2, and an absolute magnitude of >10 $mm\ m^{-1}$.

Table 1.
Tidal anomaly correlations (TACs) in the Pacific for M_2, K_1 and δ-HAT, along with 95% confidence limits.

Time-series of tidal admittance amplitude (**A**) and phase lag (**P**) for a constituent are formed using Eqs. (9) and (10):

$$\mathbf{A}(t) = abs|\frac{Z_{obs}(t)}{Z_{pot}(t)}| \tag{9}$$

$$\mathbf{P}(t) = \theta_{obs}(t) - \theta_{pot}(t) \tag{10}$$

The harmonic analysis that generates the **A**s and **P**s also provides an MSL time-series. For each resultant dataset (MSL, **A** and **P**), the mean and trend are removed from the time series, to allow direct comparison of their co-variability around the trend. Applying trend removal also reduces the effects of land motions (e.g., glacial isostatic adjustment (GIA), subsidence, and tectonic effects. All of these are assumed linear on the time scale of tidal records) that occur on longer time scales, whereas we are concerned with short-term variability.

3.3 Tidal anomaly correlations (TAC)

Tidal range changes are quantified using tidal anomaly correlations (TACs), the relationships of detrended short-term tidal variability to detrended short-term MSL fluctuations. These are used to determine the sensitivity of individual constituents to a sea-level perturbation, and the result is expressed as a millimeter change in constituent amplitude per meter change in sea-level. The M_2, S_2, K_1, and O_1 tidal constituents are first considered separately, and later in combination as a proxy for the change in the highest astronomical tide (δ-HAT). We assume that the interannual variability captured by TACs can be extrapolated to the longer time scales, subject to the qualification that the changes remain "small-amplitude", meaning a 0.5–1 m change in MSL and a change in tidal amplitude of a few tens of cm. Thus, we report TACs in units of mm m^{-1}. The detrended time series of **A** and **P** can each be compared to detrended MSL, but herein, only the absolute magnitudes of the **A** for major constituents will be considered, because of their direct role in changing high water levels. The slope of the regression between **A** and MSL is the definition of the TA, deemed significant if the signal to noise ratio (found from comparing the magnitude of the TAC to the 95% confidence interval (CI) of the robust fitting error) is greater than 2.0.

3.4 Example of a TAC

The M_2 TAC results at Honiara in the Solomon Islands exhibits one of the clearest signals in our data inventory. **Figure 2** shows the M_2 TAC at Honiara on the island of Guadalcanal (Solomon Islands, 9.4167°S and 159.950°E). The M_2 tide amplitude is relatively small at this location ($\sim$50 mm), but the anomaly correlation is large, +58.9 $\pm$ 3.7 mm m^{-1} (118% of the local M_2 amplitude), and very coherent. Since the trend is reasonably linear over such a large range (>100% in terms of tidal amplitude and $\sim$0.45 m MSL), our analysis approach is demonstrated to be valid, even in cases where the small amplitude assumption is stretched.

3.5 Change in the highest astronomical tide (δ-HAT)

We also consider a combined tidal variability besides the individual TACs. The M_2, S_2, K_1, and O_1 variabilities are summed to produce a combined tidal variability that is compared to MSL (δ-HAT). The δ-HAT is a proxy for the change in the highest astronomical tide, which is estimated by combining the complex time series
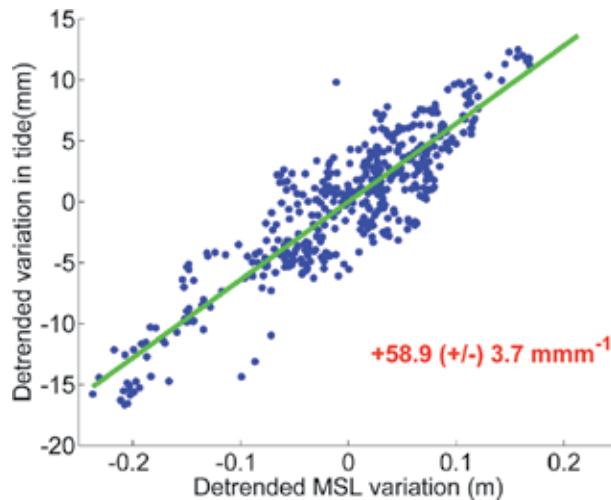
Figure 2.
M_2 TAC relation of detrended absolute tidal amplitude to detrended MSL at Honiara in the Solomon Islands [9]. The green line is a robust linear regression trend, in mmm^{-1}.

of the yearly analyzed M_2, S_2, K_1, and O_1 tides, approximately 75% of the full tidal height. "Complex" means, in this context, that each constituent is considered as a complex number (accounting for both amplitude and phase), the complex vectors are added, and the total amplitude is resolved from the complex sum. The detrended time series of δ-HAT is then compared to the detrended MSL variability. The magnitude of the slope of the regression is the definition of the δ-HAT, and, like the TACs, we report δ-HATs in units of mm m^{-1}. Theoretically, the four constituents will not be exactly in phase more than once during every 18.6-year nodal cycle, though the constituents may be approximately aligned more often; therefore, this summation provides a suitable proxy for the envelope of possible tidal amplitudes. A detailed description of the step-by-step method, with additional figures showing the intermediate steps in the process, are provided in the supplementary materials of Devlin et al. [8]. The δ-HAT analyses performed for the Atlantic tide gauge stations [10] employed an eight-tide combination, which adds the N_2, K_2, P_1 and Q_1 tidal constituents to the δ-HAT sum (**Table 2**).

3.6 Error analysis and autocorrelation handling

Our approach uses one-year harmonic analyses at a one-month step to yield smooth time-series. However, this approach must be taken with caution, as there may be autocorrelation in the regression due to data overlap. Thus, calculations of regressions and associated statistics (i.e., the p-values) are based on a sub-sampled dataset of one determination per year. The definition of the "year window" used for harmonic analysis may influence the value of the TAC or δ-HAT, i.e. calendar year (Jan–Dec) vs. water year (Oct–Sep). Thus, we use an ensemble of TACs and δ-HATs using 12 distinct year definitions (i.e., Jan–Dec, Feb–Jan, ...). We take the average of this set as the magnitude of the TAC or δ-HAT. For an estimate of the confidence interval of the trend, the interquartile range (middle 50% of the set range) is used. We consider correlations to be significant if they have a p-level of <0.05, the trend is greater than the interquartile range by at least a factor of 1.5, and the magnitude is greater than ±10 mm m^{-1} for individual TACs, and greater than ±50 mm m^{-1} for the δ-HATs. Some determinations had unexpected errors or grossly insignificant statistics (especially for the shorter records) that made them

Station	Country	Lat (N)	Long(E)	M₂ TAC	IQR	K₁ TAC	IQR	δ-HAT	IQR
Charlotte Amalie	USA	18.34	−64.92	**25.7**	**2.9**	9.2	5.5	15.0	7.8
Magueyes Island	USA	17.97	−67.05	−10.3	8.6	**14.5**	**8.0**	−56.0	7.9
San Juan	USA	18.47	−66.12	**35.7**	**2.7**	39.6	13.8	177.7	23.8
Cristobal	Panama	9.36	−79.92	**−27.1**	**6.2**	6.7	5.8	−1.9	13.7
Cartagena	Columbia	10.38	−75.53	−1.8	8.9	27.7	18.8	−19.5	41.3
Port Isabel, Texas	USA	26.06	−97.22	−8.6	1.9	1.6	10.0	−31.1	27.6
Corpus Christi, Texas	USA	27.58	−97.22	3.1	3.4	4.9	8.8	14.5	24.0
Rockport, Texas	USA	28.02	−97.05	−3.8	1.9	0.5	6.5	−0.2	11.1
Freeport, Texas	USA	28.95	−95.31	**−12.6**	**7.2**	10.4	22.5	−17.8	35.9
Galveston Pl. Pier, Texas	USA	29.29	−94.79	−0.1	6.6	7.9	16.9	−5.7	48.3
Galveston Pier 21, Texas	USA	29.31	−94.79	**−57.6**	**8.6**	9.0	13.7	**−116.4**	**49.5**
Sabine Pass N, Texas	USA	29.73	−93.87	**−25.1**	**8.9**	−1.0	12.9	−49.9	37.2
Grand Isle, Louisiana	USA	29.26	−89.96	0.1	3.8	**25.8**	**6.4**	39.4	9.3
Dauphin Island, Alabama	USA	30.25	−88.08	−1.6	18.1	**33.3**	**21.8**	47.8	50.8
Pensacola, Florida	USA	30.40	−87.21	9.0	4.7	**32.0**	**12.2**	**112.5**	**24.3**
Panama City Beach, Florida	USA	30.21	−85.88	**12.2**	**2.8**	0.8	22.7	**109.5**	**59.7**
Apalachicola, Florida	USA	29.73	−84.98	**12.7**	**6.0**	**−53.9**	**19.7**	**−74.5**	**33.1**
Saint Petersburg, Florida	USA	27.76	−82.63	**102.4**	**23.3**	**36.3**	**21.5**	**296.5**	**70.6**
Naples, Florida	USA	26.13	−81.81	**49.3**	**29.3**	−14.2	16.2	**139.0**	**53.2**
Key West, Florida	USA	24.55	−81.81	−4.9	9.9	−1.1	14.3	−6.9	39.1
Settlement Point	Bahamas	26.72	−78.98	**189.6**	**30.8**	−5.4	5.4	**323.1**	**33.7**
Virginia Key, Florida	USA	25.73	−80.16	**21.4**	**5.8**	**−42.1**	**17.4**	−48.3	29.4
Port Canaveral, Florida	USA	28.42	−80.59	−15.0	23.0	−10.7	9.9	**−56.8**	**41.8**
Fernandina Beach, Florida	USA	30.67	−81.47	**−54.7**	**5.9**	4.6	10.6	**−91.6**	**9.2**
Fort Pulaski, Georgia	USA	32.03	−80.90	**−87.9**	**14.0**	−10.4	8.0	**−132.5**	**61.0**
Charleston, S. Carolina	USA	32.78	−79.93	**−107.6**	**5.6**	**−11.7**	**6.0**	**−157.7**	**30.3**
Springmaid, S. Carolina	USA	33.66	−78.92	**−42.0**	**20.3**	**27.5**	**3.5**	4.5	10.7
Wilmington, N. Carolina	USA	34.23	−77.59	**−211.4**	**60.5**	**−38.0**	**12.1**	**−413.3**	**141.2**
Duck Pier, N. Carolina	USA	35.18	−75.75	**−12.6**	**3.5**	**−18.9**	**6.3**	−13.4	39.5
Sewells Point, Virginia	USA	36.95	−76.33	**−21.7**	**1.6**	**−30.2**	**6.2**	−50.6	29.2
Chesapeake BBT, Virginia	USA	36.97	−76.11	−10.1	5.7	**−33.5**	**8.2**	−39.0	18.0
Kiptopeke, Virginia	USA	37.17	−75.99	**55.8**	**7.5**	**−32.2**	**11.9**	86.0	25.7
Cambridge II, Maryland	USA	38.57	−76.07	**31.1**	**9.7**	−2.9	26.7	70.6	55.7

Station	Country	Lat (N)	Long(E)	M₂ TAC	IQR	K₁ TAC	IQR	δ-HAT	IQR
Washington, DC	USA	38.87	−77.02	**−78.4**	**25.0**	**−16.4**	**8.6**	−91.8	42.8
Annapolis, Maryland	USA	38.98	−76.48	2.3	17.4	**−27.0**	**9.9**	6.0	45.8
Baltimore, Maryland	USA	39.27	−76.58	**35.2**	**5.6**	**−25.5**	**16.1**	**68.7**	**36.5**
Lewes, Delaware	USA	38.78	−75.12	3.4	10.9	−2.6	7.0	**79.7**	**29.6**
Cape May, New Jersey	USA	38.97	−74.96	19.9	29.1	1.6	13.9	**104.3**	**15.1**
Reedy Point, Maryland	USA	39.56	−75.57	**97.6**	**48.4**	−3.9	17.1	**142.8**	**62.2**
Philadelphia, Pennsylvania	USA	39.93	−75.14	17.5	24.5	−6.5	10.1	**72.6**	**41.5**
Atlantic City, New Jersey	USA	39.36	−74.42	**−20.5**	**6.0**	−6.0	18.5	**−59.7**	**21.3**
Sandy Hook, New Jersey	USA	40.47	−74.01	**23.4**	**13.7**	**−36.0**	**7.5**	**54.1**	**35.1**
New York City, New York	USA	40.70	−74.01	**50.3**	**26.0**	−0.8	18.7	**57.3**	**36.2**
Montauk, New York	USA	41.05	−71.96	4.9	6.1	**−14.6**	**15.4**	**13.8**	**16.4**
Bridgeport, Connecticut	USA	41.17	−73.18	**−39.7**	**20.1**	**−43.7**	**9.6**	−10.2	53.0
New London, Connecticut	USA	41.36	−72.09	**15.0**	**3.2**	**−23.3**	**12.1**	14.5	22.5
Newport, Rhode Island	USA	41.51	−71.33	−0.1	9.5	−13.0	22.9	33.2	31.7
Providence, Rhode Island	USA	41.81	−71.40	−4.7	8.1	−4.6	13.4	2.5	21.4
Nantucket, Massachusetts	USA	41.29	−70.10	8.0	13.1	−2.3	4.6	**130.7**	**17.0**
Woods Hole, Massachusetts	USA	41.52	−70.67	**38.6**	**7.6**	−7.3	8.8	**69.2**	**34.4**
Boston, Massachusetts	USA	42.36	−71.05	**−48.8**	**14.9**	**−18.2**	**5.8**	**86.6**	**28.6**
Portland, Maine	USA	43.66	−70.25	**−79.6**	**43.6**	**−30.0**	**11.0**	−3.9	50.9
Bar Harbor, Maine	USA	44.39	−68.21	**62.4**	**16.0**	0.9	12.4	**243.0**	**63.2**
Eastport, Maine	USA	44.90	−66.98	**−145.8**	**16.7**	**−23.1**	**8.2**	27.2	46.9
Saint John	Canada	45.25	−66.06	**−258.7**	**35.2**	−2.0	5.5	**−378.0**	**39.0**
Yarmouth	Canada	43.83	−66.12	−7.0	56.5	−11.0	11.8	55.2	96.6
Halifax	Canada	44.67	−63.58	25.1	27.7	−11.3	8.3	**71.6**	**12.0**
Charlottetown	Canada	46.23	−63.12	**53.3**	**12.6**	**−71.0**	**16.1**	−47.4	20.3
North Sydney	Canada	46.22	−60.25	−3.6	7.3	**−30.1**	**17.4**	26.3	48.6
Lower Escuminac	Canada	47.08	−64.88	**−18.7**	**10.9**	**−77.8**	**27.2**	**−94.1**	**18.6**
Port-aux-Basques	Canada	47.57	−59.13	**−23.9**	**6.7**	**−19.8**	**7.2**	**−92.8**	**29.9**
Argentua	Canada	47.30	−53.98	−15.9	13.2	**−54.2**	**3.6**	−19.5	8.6
St. Johns	Canada	47.57	−52.72	−3.5	3.3	−5.2	3.8	−26.5	19.6
Churchill	Canada	58.78	−94.20	16.3	100.7	7.5	8.1	51.3	272.4
Reykjavik	Iceland	64.15	−21.94	−14.9	17.8	0.8	8.2	**−118.2**	**43.6**
Ny-Aelsund	Norway	78.93	11.95	**−10.4**	**3.0**	−5.5	3.7	**64.5**	**29.6**

Station	Country	Lat (N)	Long(E)	M$_2$ TAC	IQR	K$_1$ TAC	IQR	δ-HAT	IQR
Vardo	Norway	70.33	31.10	−0.7	13.7	5.0	8.1	−3.2	25.7
Honningsvaag	Norway	70.98	25.97	**−20.2**	**13.2**	−10.9	13.1	−108.3	**44.9**
Andenes	Norway	69.32	16.15	−8.4	5.5	−1.4	12.7	−14.1	13.5
Rorvik	Norway	64.87	11.25	**−23.2**	**5.7**	**−16.2**	**7.9**	**−60.5**	**23.2**
Heimsjoe	Norway	63.43	9.10	**−20.2**	**5.8**	**−12.4**	**7.5**	**−82.2**	**27.0**
Maaloey	Norway	61.93	5.11	1.3	17.1	4.7	9.8	−21.1	48.0
Wick	UK	58.44	−3.09	8.7	11.8	**15.0**	**8.5**	47.0	86.8
Kinlochbervie	UK	58.46	−5.05	**−14.3**	**6.3**	−6.2	7.3	**−105.8**	**64.4**
Stornoway	UK	58.21	−6.39	**−43.4**	**19.5**	5.7	12.1	**−110.8**	**51.6**
Aberdeen	UK	57.14	−2.07	−8.6	4.1	−5.3	3.2	−43.3	41.8
Leith (Edinburgh)	UK	55.99	−3.18	−46.2	35.0	28.5	33.5	−48.2	147.7
North Shields	UK	55.01	−1.44	2.9	10.5	−2.3	7.4	**166.7**	**43.6**
Whitby	UK	54.49	−0.61	10.3	17.0	**−59.2**	**27.8**	32.9	128.3
Immingham	UK	53.63	−0.19	**48.0**	**26.5**	2.9	7.8	84.4	69.7
Cromer	UK	52.94	1.30	**29.2**	**9.3**	−7.8	7.0	**148.0**	**18.8**
Lowestoft	UK	52.47	1.75	**46.4**	**27.8**	12.9	28.0	**293.6**	**69.1**
Felixstowe	UK	51.96	1.35	**−80.0**	**54.9**	**−28.1**	**12.0**	**−203.4**	**55.1**
Sheerness	UK	51.44	0.74	**−46.3**	**83.9**	**−11.7**	**2.6**	**−109.9**	**20.5**
Dover	UK	51.12	1.32	**−135.7**	**80.4**	18.0	7.5	**−276.5**	**87.2**
Newhaven	UK	50.78	0.06	**−100.5**	**28.9**	**−21.5**	**12.1**	**−212.6**	**69.0**
Portsmouth	UK	50.80	−1.11	**−23.2**	**5.5**	−4.4	6.7	**−157.5**	**65.7**
Bournemouth	UK	50.71	−1.87	−2.0	40.9	**33.1**	**12.5**	−8.4	132.0
Weymouth	UK	50.61	−2.45	**−57.5**	**17.4**	−1.8	11.1	−42.7	59.7
Devonport	UK	50.37	−4.19	**−38.4**	**20.6**	**30.5**	**16.2**	−48.7	170.3
Newlyn	UK	50.10	−5.52	**−52.7**	**23.7**	17.1	22.6	80.8	146.7
St. Mary's	UK	49.92	−6.32	−11.5	18.2	5.4	13.6	**−108.4**	**33.6**
Ilfacombe	UK	51.21	−4.11	**−23.2**	**9.7**	**−12.6**	**5.0**	**112.7**	**38.9**
Hinkley Point	UK	51.22	−3.13	−5.6	91.1	11.0	22.8	−12.8	105.3
Avonmouth	UK	51.51	−2.71	**92.7**	**22.6**	**−26.1**	**11.5**	**255.5**	**88.9**
Newport	UK	51.55	−2.99	**187.6**	**93.8**	−3.6	11.5	48.4	175.9
Mumbles	UK	51.57	−3.98	**−76.1**	**42.3**	−12.2	14.7	**−434.1**	**98.7**
Milford Haven	UK	51.70	−5.01	**−41.0**	**17.3**	−3.7	8.5	**−142.2**	**99.8**
Fishguard	UK	52.01	−4.98	**−77.2**	**10.6**	**14.0**	**4.5**	**81.6**	**31.6**
Barmouth	UK	52.72	−4.05	−7.3	29.4	3.3	10.9	−22.3	69.6
Holyhead	UK	53.31	−4.63	**−27.9**	**10.4**	**−11.6**	**8.8**	**−120.3**	**40.9**
Llandudno	UK	53.33	−3.83	−17.2	56.8	−12.1	24.1	**−427.7**	**235.4**
Liverpool	UK	53.45	−3.02	**59.5**	**16.9**	**−23.6**	**4.2**	**−94.3**	**22.2**
Heysham	UK	54.03	−2.92	**56.4**	**15.8**	**17.2**	**8.1**	**385.1**	**56.7**
Port Erin	UK	54.09	−4.77	−5.0	15.0	**−38.6**	**12.1**	**−229.8**	**42.8**
Workington	UK	54.65	−3.57	**−69.8**	**35.1**	**−29.5**	**7.8**	**−435.4**	**239.3**
Portpatrick	UK	54.84	−5.12	−34.1	34.9	3.9	19.3	−24.6	135.3

Station	Country	Lat (N)	Long(E)	M_2 TAC	IQR	K_1 TAC	IQR	δ-HAT	IQR
Millport	UK	55.75	−4.91	21.9	23.9	19.1	25.4	**341.7**	**108.3**
Port Ellen (Islay)	UK	55.63	−6.19	−9.5	14.3	**−14.8**	7.7	**−100.4**	**13.2**
Portrush	Ireland	55.21	−6.66	2.4	18.5	**47.7**	**19.2**	−37.3	196.2
Malin Head	Ireland	55.37	−7.33	**−38.7**	**24.8**	8.4	4.1	−44.0	40.7
Tregde	Norway	58.00	7.57	**−17.3**	**4.9**	*	*	−14.1	23.2
Oslo	Norway	59.91	10.73	**−41.6**	**11.2**	*	*	**−107.2**	**36.6**
Kungsvik	Sweden	59.00	11.13	**−30.1**	**11.5**	*	*	−44.7	25.9
Smogen	Sweden	58.35	11.22	**−34.6**	**18.6**	*	*	−47.6	65.2
Stenungsund	Sweden	58.09	11.83	−3.5	16.0	*	*	−10.8	22.3
Goteburg-Torshamnen	Sweden	57.68	11.79	**−20.6**	**6.0**	*	*	−3.3	35.3
Ringhals	Sweden	57.25	12.11	−17.6	18.4	*	*	−13.1	46.6
Viken	Sweden	56.14	12.58	**−18.2**	**6.7**	*	*	−17.5	62.2
Hornbaek	Denmark	56.10	12.47	**−16.9**	**7.4**	*	*	20.7	23.6
Esbjerg	Denmark	55.47	8.43	12.1	16.8	−9.9	16.3	56.0	60.6
Cuxhaven	Germany	53.87	8.72	**134.9**	**25.8**	−1.3	10.0	**218.1**	**36.6**
Delfzijl	Netherlands	53.33	6.93	11.7	35.9	27.6	23.2	**140.9**	**51.7**
Den Helder	Netherlands	52.97	4.75	**63.3**	**27.9**	**−49.0**	**26.7**	**139.3**	**38.6**
Hoek van Holland	Netherlands	51.98	4.12	27.3	22.7	**−62.1**	**21.1**	−4.7	51.5
Dunkurque	France	51.05	2.37	**−142.9**	**39.5**	**−28.9**	**14.7**	**−340.1**	**87.5**
Le Havre	France	49.48	0.11	**−39.6**	**22.7**	0.3	6.2	29.2	45.6
Cherbourg	France	49.65	1.64	−10.2	9.6	−4.8	6.0	40.7	14.5
St. Helier (Jersey)	UK	49.18	−2.12	**−145.7**	**70.8**	8.6	18.9	**−475.2**	**163.6**
Saint Malo	France	48.64	−2.03	**−141.9**	**20.8**	−2.3	12.4	**−408.3**	**49.1**
Roscoff	France	48.72	−3.97	**−56.6**	**21.3**	−0.1	8.1	39.0	46.0
Le Conquet	France	48.36	−4.78	−2.3	41.8	10.9	11.6	**138.6**	**62.7**
Brest	France	48.38	−4.50	**−74.0**	**17.1**	3.7	12.1	**−166.8**	**42.6**
Port Tudy	France	47.64	−3.45	**−24.1**	**13.5**	**−15.8**	**4.9**	−19.1	24.2
Donges	France	47.31	−2.09	**−26.2**	**8.4**	−7.1	6.7	−4.3	31.1
Cordemais	France	47.28	−1.89	**−409.2**	**113.3**	**−19.6**	**4.6**	**−589.5**	**146.3**
Le Pellerin	France	47.21	−1.77	**−625.0**	**27.6**	**−12.8**	**3.1**	**−983.0**	**55.6**
Nantes-Usine-Brulee	France	47.19	−1.63	**−663.0**	**9.4**	**−11.8**	**2.2**	**−1009.9**	**32.8**
Saint-Gildas	France	47.14	−2.25	**57.6**	**33.5**	2.1	18.9	40.2	89.2
Les Sables d'Olonne	France	46.50	−1.79	**−17.2**	**9.7**	−0.5	7.3	−44.1	66.3
Bayonne Boucau	France	43.53	−1.51	**−21.6**	**11.8**	3.4	3.8	−13.9	15.3
Saint Jean de Luz	France	43.40	−1.68	−9.5	17.3	−1.2	8.0	**−52.1**	**25.0**
Bilbao	Spain	43.36	−3.05	−3.3	18.8	11.5	10.9	**120.6**	**37.0**
Gijon	Spain	43.56	−5.70	2.3	10.0	**10.4**	**5.4**	**82.1**	**29.5**
La Coruna	Spain	43.37	−8.40	**28.2**	**17.3**	2.9	7.5	**200.6**	**62.5**
Vigo	Spain	42.24	−8.73	−6.4	9.2	2.5	9.6	44.2	16.2
Huelva	Spain	37.13	−6.83	10.7	14.4	**−33.5**	**21.9**	−14.3	113.0

Station	Country	Lat (N)	Long(E)	M$_2$ TAC	IQR	K$_1$ TAC	IQR	δ-HAT	IQR
Bonanza	Spain	36.80	−6.34	−7.9	14.1	−11.4	14.1	−43.6	27.8
Cadiz	Spain	36.53	−6.28	**75.8**	**12.8**	4.6	2.6	**247.3**	**84.1**
Tarifa	Spain	36.00	−5.60	8.4	13.6	**14.2**	**3.7**	−3.6	9.0
Funchai	Portugal	32.64	−16.91	**124.1**	**9.5**	6.4	2.8	**166.0**	**18.1**
Gran Canary	Spain	28.14	−15.41	**26.3**	**12.0**	7.4	13.2	**106.3**	**21.2**
Tenerife	Spain	28.48	−16.24	−11.4	15.4	5.3	24.5	**−73.9**	**28.1**
Barseback	Sweden	55.76	12.90	−22.9	29.7	*	*	**−80.6**	**48.0**
Klagshamn	Sweden	55.52	12.89	**−25.0**	**12.4**	4.3	17.6	−2.1	26.1
Skanor	Sweden	55.42	12.83	**−14.4**	**5.9**	6.1	10.2	21.1	56.7
Gedser	Denmark	54.57	11.93	−0.6	8.5	16.8	16.6	41.3	29.5
Simrishamn	Sweden	55.56	14.36	−1.1	7.8	−0.8	7.0	30.6	28.5
Stockholm	Sweden	59.33	18.08	0.3	3.9	−4.6	5.8	0.2	21.0
Hanko	Finland	59.82	22.98	−1.8	8.0	3.1	5.7	−8.0	16.5
Helsinki	Finland	60.15	24.96	2.1	3.7	**17.3**	**6.9**	30.4	29.2
Hamina	Finland	60.56	27.18	−2.7	7.3	**20.1**	**9.2**	30.8	17.1
Ceuta	Spain	35.90	−5.32	7.0	13.1	−5.6	10.8	45.1	42.4
Algeciras	Spain	36.12	−5.43	**21.0**	**12.8**	11.4	13.0	**93.0**	**40.8**
Gibraltar	UK	36.13	−5.35	3.3	6.3	0.9	2.6	3.1	8.1
Malaga	Spain	36.72	−4.42	9.8	6.1	4.6	3.6	27.3	15.9
Venezia	Italy	45.42	12.43	**−39.8**	**21.4**	−28.3	21.3	**−108.7**	**65.2**
Trieste	Italy	45.65	13.75	**29.0**	**7.8**	−2.8	19.6	**82.8**	**38.4**
Bakar	Croatia	45.30	14.53	**−11.2**	**5.7**	**−32.1**	20.2	−64.1	67.9

The TAC magnitude is determined by the ensemble average of 12 monthly determinations, and the confidence interval on the determined trend is given by the interquartile range (IQR) of the ensemble. Significant determinations are given in bold text. Entries marked with an '*' indicate locations where analyses failed due to small tidal amplitudes. Units of the TACs and IQRs are in mm m^{-1}.

Table 2.
TAC results for M$_2$ and K$_1$ and δ-HAT results at all Atlantic locations.

unreliable. These were not included in averaging process, though at all locations, a minimum of eight of 12 determinations was required to deem a result significant. For more detailed descriptions of the TAC and δ-HAT determinations, please refer to Devlin et al. [10], and the supplementary material of Devlin et al. [8, 9].

4. Selected results

4.1 Data inventory and sources

We now present some of the best results from past studies. Pacific Ocean locations were analyzed in Devlin et al. [9] for individual TACs, whereas Devlin et al. [8] analyzed the combined tidal variability of the δ-HATs, 152 total locations were analyzed in both Pacific studies. Locations are shown in **Figures 3** and **4** (Eastern Pacific and Western Pacific, respectively) with major water basins labeled. The Atlantic Ocean was analyzed in Devlin et al. [10], which calculated both TACs

and δ-HATs, considering a total of 170 locations. Atlantic locations are displayed in **Figure 5** and major basins are labeled. Most of the hourly tide gauge records in the Pacific and Atlantic are obtained from the University of Hawaii's Sea Level Center
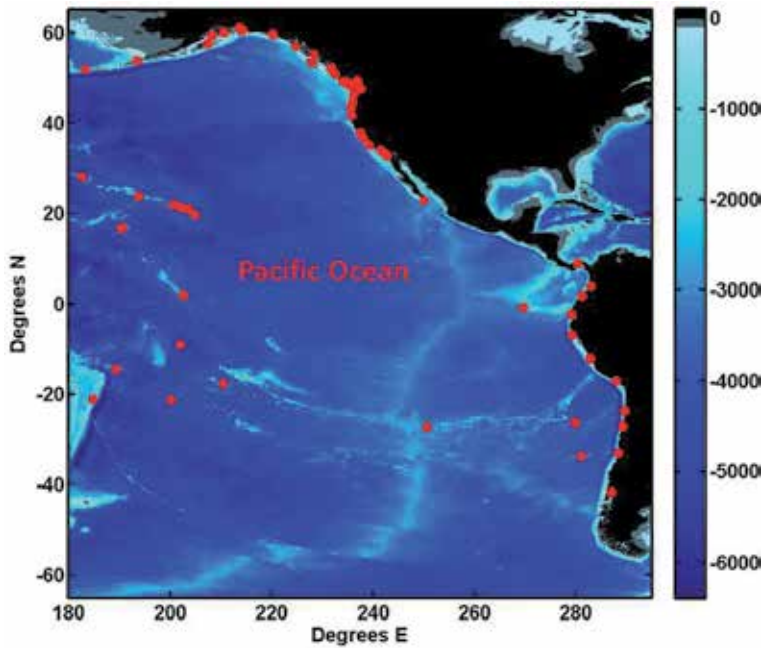
Figure 3.
Red dots indicate gauge locations in the Eastern Pacific [9]. Color bar indicates water depth, in meters. Areas with a depth less than 100 m are shaded gray, and land is black.
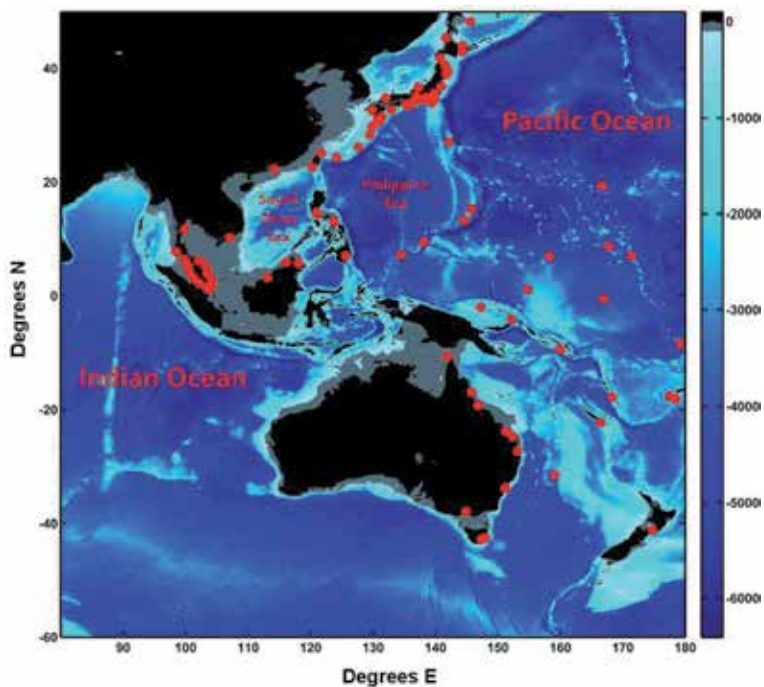
Figure 4.
Red dots indicate gauge locations in the Western Pacific [9]. Color bar indicates water depth, in meters. Areas with a depth less than 100 m are shaded gray, and land is in black.

(UHSLC), with additional data from the following agencies: The Japanese Oceanographic Data Center (JODC); Canada's Fisheries and Ocean office (FOC); Australia's National Tidal Center (AuNTC), and the remainder from the Global Extreme Sea Level Analysis dataset, 2nd edition (GESLA [61]; www.gesla.org), an archiving project that has gathered high-frequency water level data into a single standardized data format from multiple worldwide monitoring agencies. Finally, a close regional study of the tidal variability (individual and combined) of the Hong Kong tide gauge network (12 gauges) was performed in Devlin et al. [11]; this data was obtained from the Hong Kong Observatory (HKO) and the Hong Kong Marine Department (HKMD); locations are shown in **Figure 6**. For the Pacific and Hong Kong studies, the four largest tidal constituents (M_2, S_2, K_1, and O_1) and their combinations (δ-HAT) were considered. The Atlantic study also considered four more tides (N_2, K_2, P_1, and Q_1), and the combined δ-HAT considered here involved all eight components. However, for the sake of brevity in this chapter, only the largest semidiurnal (M_2) and diurnal (K_1) tide results will be discussed, along with δ-HAT determinations.

In all Pacific plots, the magnitude of the TACs or δ-HATs are indicated by the color intensity of the dots according to the scale shown in the legend; positive TACs are in shades of red, negative TACs are in shades of blue. For a gauge with an insignificant TAC (signal-to-noise ratio less than 2.0), the dots are white. In the Atlantic and Hong Kong results, red markers indicate positive TACs and blue markers indicate negative TACs, with magnitudes proportional to marker size, as shown in the legend, and insignificant results are shown as black dots. These values provide a measure of the tidal response, normalized to a 1 m MSL rise. In the TAC plots, the green and yellow background fields show the mean value of tidal
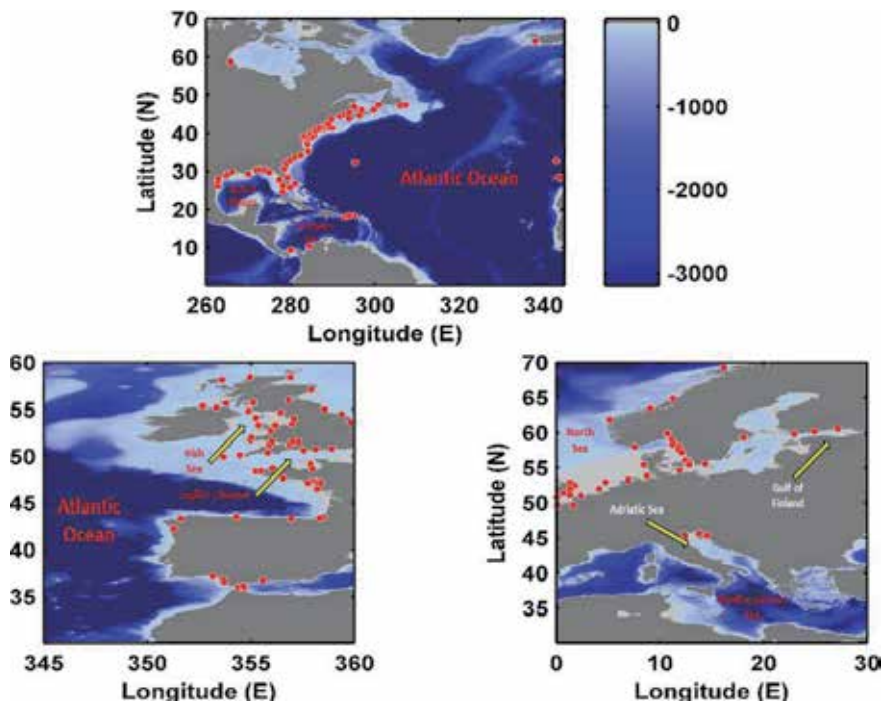
Figure 5.
Gauge locations analyzed in the Atlantic Ocean. The colored background shows water depth, in units of meters [10].
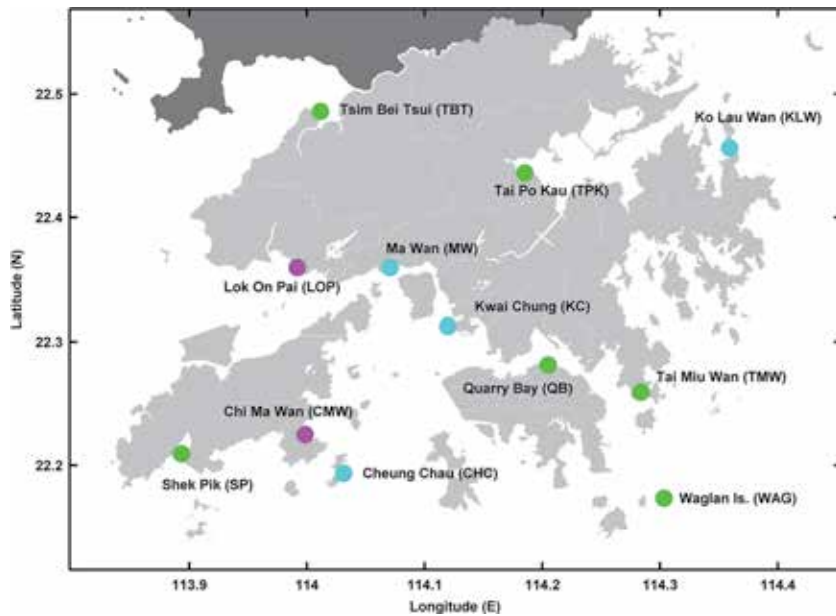
Figure 6.
Tide gauge locations in Hong Kong used in this study [11]. Green markers indicate active gauges provided by the Hong Kong Observatory (HKO), light blue markers indicate gauges provided by the Hong Kong marine department (HKMD), and red markers indicate historical gauges (once maintained by HKO) that are no longer operational.

amplitudes over the satellite altimetry record (1993–2014), using a tidal solution from the TPXO7.2 tide model [62, 63].

4.2 Pacific results

4.2.1 Pacific M_2 TACs

The M_2 TACs do not reveal any coherent basin-wide patterns of variability, however, there are localized features of interest. In the Eastern Pacific (**Figure 7**), river-influenced gauges, such as San Francisco, California, Astoria, Oregon (labeled as "SF" and "AST" on the map) exhibit strong negative TACs. Strongly positive M_2 TACs are observed at many Hawaiian and Alaskan gauges. Other locations show only weak or isolated correlations. At one gauge of note, Puerto Montt in far southern Chile (labeled as "PM" in **Figure 7**), there is an exceptionally large negative M_2 TAC, greater than -500 mm m^{-1}. There are a higher number M_2 TACs in the Western Pacific than in the Eastern Pacific, but again the relevant variability is local (**Figure 8**). M_2 TACs are negative for the majority of Japan and Taiwan, some exceeding -100 mm m^{-1}. However, some large positive M_2 TACs are at isolated locations, such as at Okada (labeled as "OKA" in **Figure 8**) and in Tokyo harbor ("TOK"). At Hong Kong ("HK"), one of the largest positive M_2 TACs is found (discussed in further detail below). Most significant positive TACs are south of the equator, and most negative TACs are north of the equator. The correlations at nearly all gauges in Malaysia (-40 to -150 mm m^{-1}) and in the Philippines (-80 to -145 mm m^{-1}) are strongly negative. Finally, Honiara ("HON") in the Solomon Islands and Rabaul, Papua New Guinea ("RAB") have small mean M_2 amplitudes ($\sim$50 mm) but display large relative correlations.
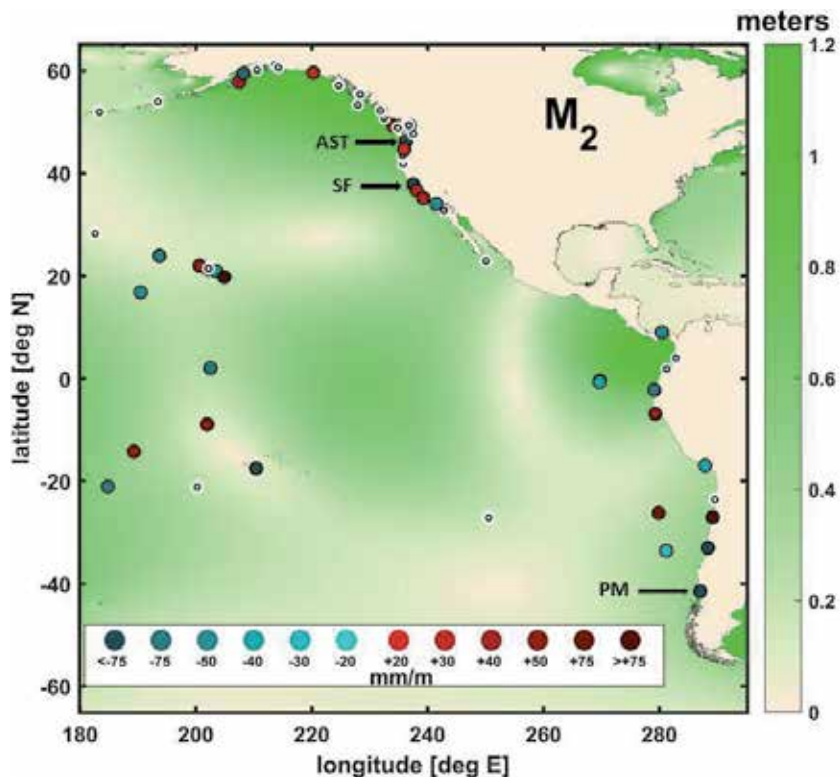
Figure 7.
M₂ TAC map in the Eastern Pacific [9], showing changes in amplitude (per m MSL rise). Map background shows mean tidal amplitudes (meters, green color scale) from the ocean tidal model of TPXO7.2 [62, 63]. Red and blue colored markers show positive and negative TACs, respectively. The magnitudes are indicated by color intensity, as shown by legend at the bottom, in units of mm of tidal change per meter of sea level rise (mm m⁻¹). TACs are only plotted if the ratio of the 95% confidence limit of the trends has a signal-to-noise ratio of >2.0. Statistically insignificant values are indicated by white circles. Maps were generated using MATLAB version R2011a (www.mathworks.com).

4.2.2 Pacific K_1 TACs

K_1 tidal anomaly correlations also reveal some regions of regionally coherent behavior but no basin-scale patterns. In the Eastern Pacific (**Figure 9**), the river-influenced gauges of San Francisco, California (labeled "SF" in **Figure 9**), and Astoria, Oregon ("AST") show TACs that are strongly negative, as was true for M_2. However, slightly negative or insignificant K_1 TACs are observed along the rest of the US west coast (**Figure 9**). Fewer significant K_1 TACs are observed in Alaska and Hawaii than was seen for M_2. In South America, Puerto Montt, Chile ("PM") shows a very strong negative K_1 TAC, like M_2. A larger number of significant K_1 TACs are found in the Western Pacific (**Figure 10**). As with M_2, most coastal Japan gauges exhibit negative TACs, and there is a very large positive TAC in Hong Kong (labeled "HK" in **Figure 10**). In the Southwest Pacific, large positive TACs occur at both island and shelf stations, while significant negative TACs are mainly observed at island gauges, and in Malaysia and Thailand. Almost all significant negative TACs are north of ~10 degrees South.

4.2.3 Pacific δ-HATs

In the Eastern Pacific (**Figure 11**), significant δ-HATs are isolated. San Francisco, California (labeled "SF" in **Figure 11**) and Astoria, Oregon ("AST")
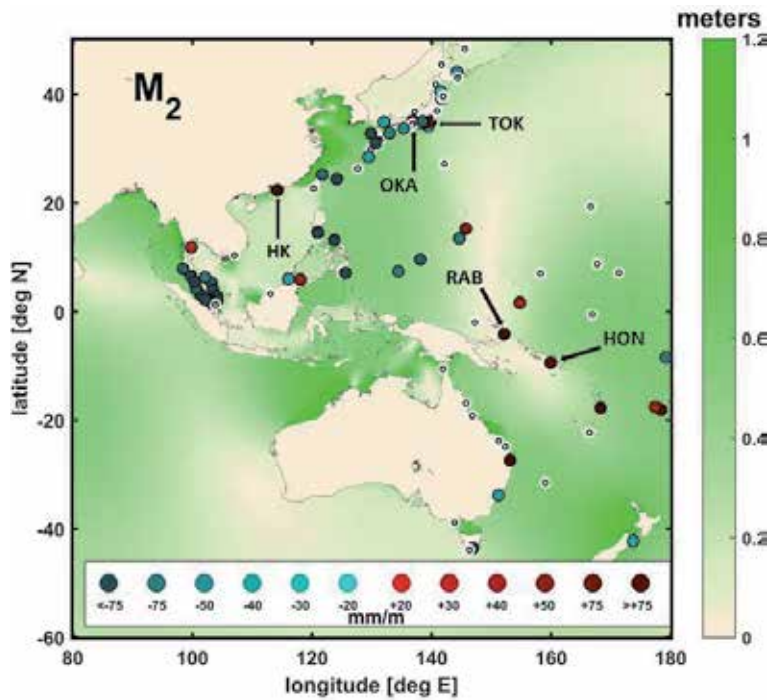
Figure 8.
*M_2 TAC map in Western Pacific [9] showing changes in amplitude anomaly trends (for a 1-meter MSL rise); symbols and backgrounds are as in **Figure 7**; units of red and blue markers are mmm^{-1}, and units of the backgrounds are meters. Maps were generated using MATLAB version R2011a (www.mathworks.com).*
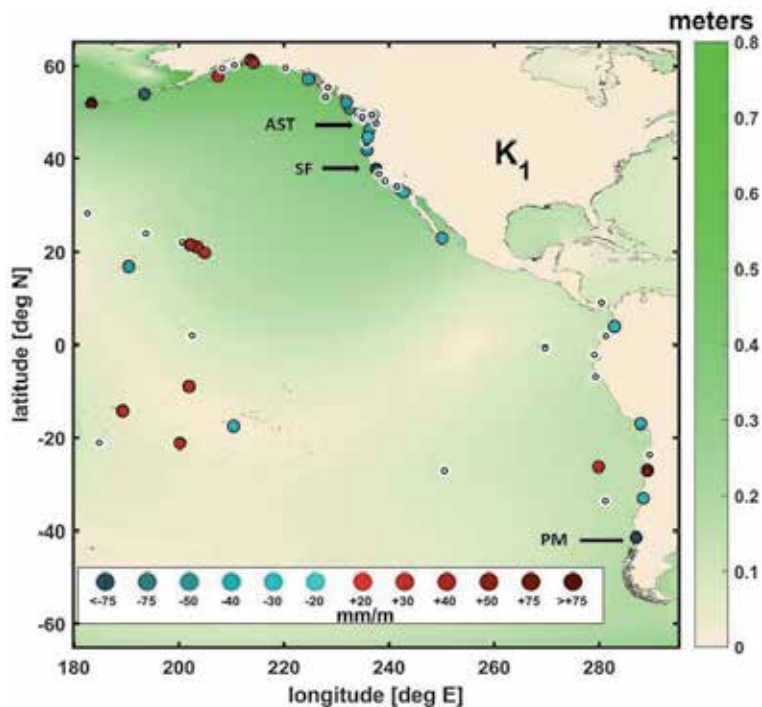
Figure 9.
*K_1 TAC map in Eastern Pacific [9] showing changes in amplitude anomaly trends (for a 1-m MSL rise); symbols and backgrounds are as in **Figure 7**; units of red and blue markers are mmm^{-1}, and units of the backgrounds are meters. Maps were generated using MATLAB version R2011a (www.mathworks.com).*
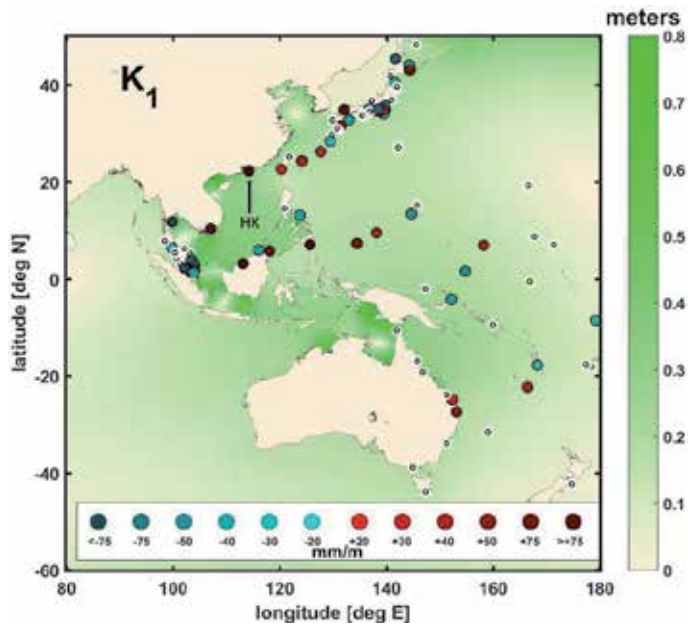
Figure 10.
*K_1 TAC map in Western Pacific [9] showing changes in amplitude anomaly trends (for a 1-m MSL rise); symbols and backgrounds are as in **Figure 7**; units of red and blue markers are mm m^{-1}, and units of the backgrounds are meters. Maps were generated using MATLAB version R2011a (www.mathworks.com).*
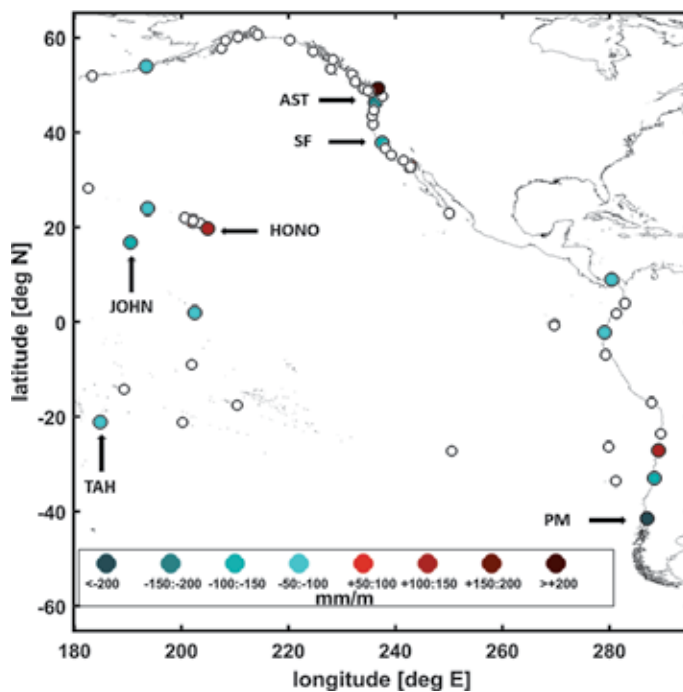
Figure 11.
Color scale map of the eastern Pacific δ-HAT determinations (in mm m^{-1}), based on the combined M_2, S_2, K_1, and O_1 detrended tidal variations [8]. Red and blue colored markers show positive and negative δ-HATs, respectively. Un-colored, open circles indicate that the calculated δ-HATs was not significant (p > .05). Maps were generated using MATLAB version R2011a (www.mathworks.com).
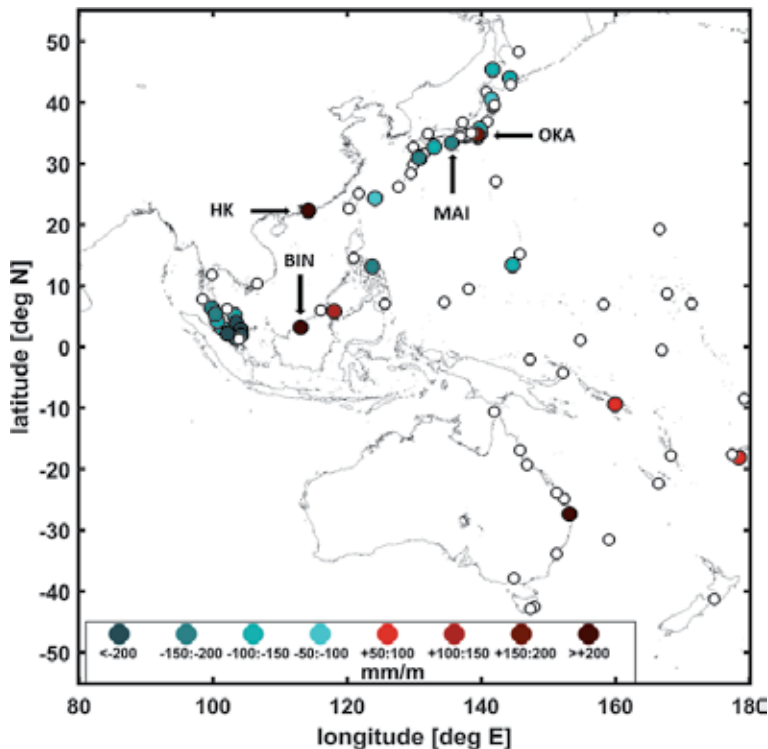
Figure 12.
Color scale map of the Western Pacific δ-HAT determinations (in mm m⁻¹), symbols and colors as in
Figure 11 *[8]. Maps were generated using MATLAB version R2011a (www.mathworks.com).*

exhibit δ-HAT values of −146- and −257-mm m^{-1}, respectively. Honolulu ("HONO") and Hilo, Hawaii have positive values of +139- and +147-mm m^{-1}, respectively. Along the coast of South America, there is an anomalously large negative anomaly correlation at far-southern Puerto Montt, Chile ("PM"), with a δ-HAT value of −963 mm m^{-1}. Elsewhere in the Eastern Pacific of note, Johnston Island ("JOHN") and Papeete on the island of Tahiti ("TAH"), exhibit large negative δ-HATs of −117 mm m^{-1} and −95 mm m^{-1}, respectively.

The δ-HAT correlations are more significant in the Western Pacific (**Figure 12**). Eleven gauges in Japan show negative δ-HATs, seven of which are greater than −100 mm m^{-1}, with a maximum negative value of −351 mm m^{-1} occurring at Maisaka (labeled "MAI" in **Figure 12**). Only two significant positive δ-HATs are observed in Japan, at Okada ("OKA") with a value of +159. At Western Pacific islands, results are mixed, with moderate positive δ-HATs and moderate negative δ-HATs both observed. Within the South China Sea, the distribution of δ-HATs is complex. An anomalously large positive δ-HATs is observed at Hong Kong ("HK"; +665 mm m^{-1}) and at Bintulu, Malaysia ("BIN"; +615 mm m^{-1}). Both sides of the Malay peninsula exhibit strongly negative δ-HATs. The Malacca Strait on the west side of the peninsula has δ-HATs of approx. −70 to −220 mm m^{-1}, and the Gulf of Thailand on the eastern side shows δ-HATs of approx. −130 to −290 mm m^{-1}; a common feature is that both sides show gradual increases in magnitude from the northern reaches to the southern tip of the Malay Peninsula.

4.3 Atlantic results

4.3.1 Atlantic M_2 TACs

Figure 13a–c show the M_2 results. In North America (**Figure 13a**), the M_2 TACs show a dipole-like pattern. Both sides of the Florida Peninsula show TACs that are consistently positive. However, they are moderately negative in the Western Gulf of Mexico. Farther north along the US Atlantic coast, a strong concentration of negative TACs are seen from the Florida panhandle to Virginia in the Sargasso Sea, with the strongest correlation in Wilmington, North Carolina (-211 mm m^{-1}; labeled "WIL" in **Figure 13**). Positive TACs are seen in the Chesapeake and Delaware Bays, New York City, New York ("NYC"), and Bar Harbor, Maine ("BH"). Finally, TACs in the Gulf of Maine and into the Bay of Fundy are strongly negative, reaching a magnitude of -259 mm m^{-1} at St. John, Canada ("STJ"). In Europe, the TAC patterns are somewhat more consistent (**Figure 13b, c**). Negative TACs are seen in most of the English Channel and the Irish Sea, and in the eastern parts of the North Sea. Conversely, positive TACs are found at inland semi-enclosed locations in England such as the Severn estuary; being largest at Avonmouth ("AVON"), farther north at Liverpool ("LIV"), and along the southern coast of the North Sea.

4.3.2 Atlantic K_1 TACs

Diurnal components are generally smaller than semidiurnal constituents in the Atlantic, and TACs are also generally lower magnitude (usually $< \pm 100$ mm m^{-1})
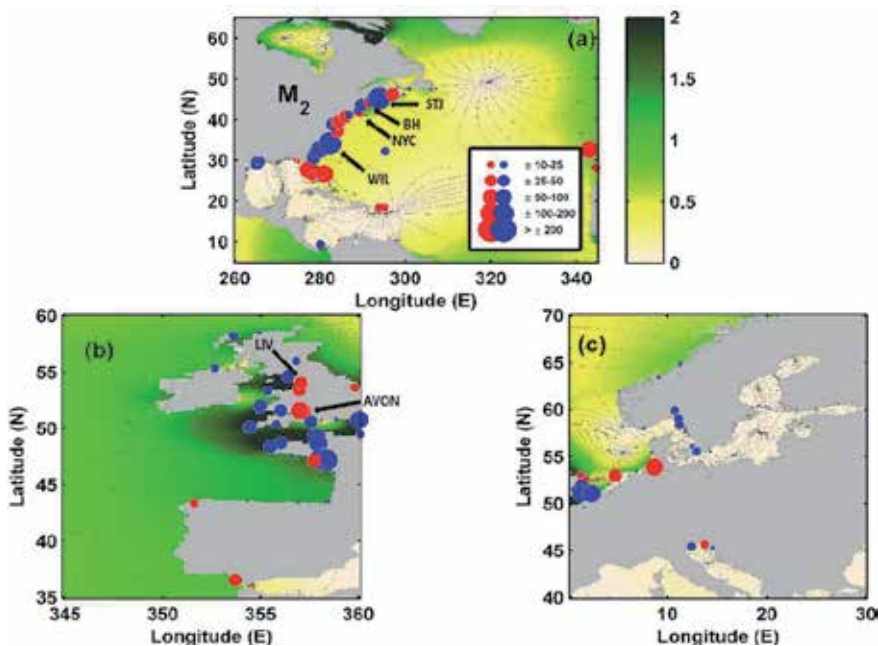
Figure 13.
M_2 TAC Atlantic Ocean maps [10]. North American locations are shown in (a), Western Europe and United Kingdom locations are shown in (b), and Eastern Europe locations are shown in (c). Red markers indicate positive TACs and blue markers indicate negative TACs, with magnitudes proportional to marker size, as shown in the legend in (a). Black markers indicate insignificant results. Green-and-yellow background maps show the global tidal solutions overs the satellite era, taken from the TPXO7.2 solution [62, 63], with green and yellow colors giving the tidal amplitudes, and black lines showing tidal phases. Maps were generated using MATLAB version R2011a (www.mathworks.com).
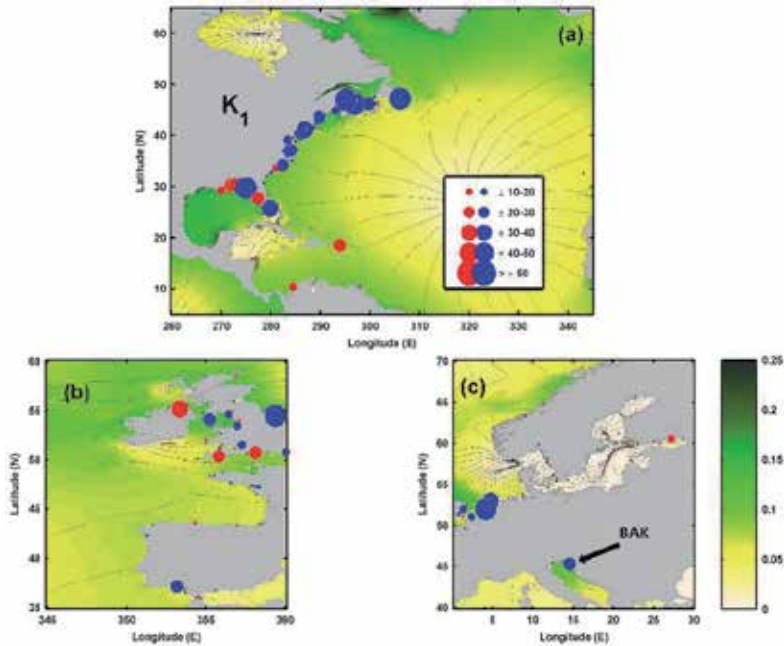
Figure 14.
*K₁ TAC Atlantic Ocean maps [10]. North America locations are shown in (a), Western Europe and United Kingdom locations are shown in (b), and Eastern Europe locations are shown in (c). Markers and background maps are as described in **Figure 13**. Maps were generated using MATLAB version R2011a (www.mathworks.com).*
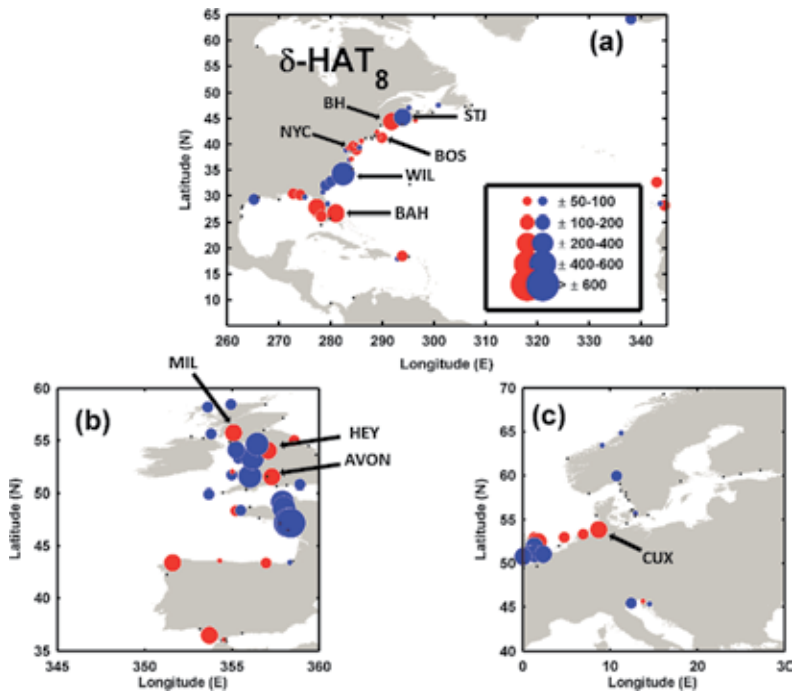
Figure 15.
*δ-HAT Atlantic Ocean maps [10], showing combined variability of eight largest gravitational tides (M₂ + S₂ N₂ + K₂ + K₁ + O₁ + P₁ + Q₁). North American locations are shown in (a), Western Europe and United Kingdom locations are shown in (b), and Eastern Europe locations are shown in (c). Markers are as described in **Figure 13**. Maps were generated using MATLAB version R2011a (www.mathworks.com).*

and less often significant. However, there are still some regions of interest. The K_1 tide (**Figure 14a**) has TACs that are consistently negative along the North American coast from Florida through maritime Canada. However, the TACs in the Gulf of Mexico are mainly positive, as well as in the Caribbean. K_1 has some isolated positive TACs in Europe in the western English Channel, while the eastern Channel has a concentration of negative TACs (**Figure 14b**). There is a negative TAC at Bakar, Croatia (labeled "BAK" in **Figure 14**) at the end of the Adriatic Sea, where a large diurnal amplification occurs, and a small positive TAC at the end of the Gulf of Finland, where a diurnal amplification of the otherwise small Baltic tides also occurs (**Figure 14c**).

4.3.3 Atlantic δ-HATs

The calculation of the δ-HATs in the Atlantic use an eight-tide combination instead of the four-tide combination used in the Pacific, as detailed in Devlin et al. [10]. Results in North America (**Figure 15a**) are generally positive in the eastern Gulf of Mexico, Puerto Rico, and a large magnitude δ-HAT is seen in the Bahamas (+323 mm m^{-1}; labeled "BAH" in **Figure 15**). New York City, New York ("NYC"), Boston, Massachusetts ("BOS"), Bar Harbor, Maine ("BH"), and parts of the Delaware Bay also are strongly positive. Strong negative δ-HATs are found from Florida to Wilmington, North Carolina (−413 mm m^{-1}; "WIL"), and at St. John at the head of the Bay of Fundy (−378 mm m^{-1}; "STJ"). In Europe (**Figure 15b, c**), strong positive δ-HATs are found in the southern North Sea at Cuxhaven, Germany (+219 mm m^{-1}; "CUX") and in the Netherlands. Three locations within semi-enclosed regions of the Irish Sea show the strongest positive δ-HATs; at Avonmouth located at the head of the Severn Estuary (+256 mm m^{-1}; "AVON"), and at Heysham ("HEY") and Millport ("MIL"; +385 and +341 mm m^{-1}, respectively). However, there are mainly negative δ-HATs seen in the rest of the UK, including most of the English Channel.
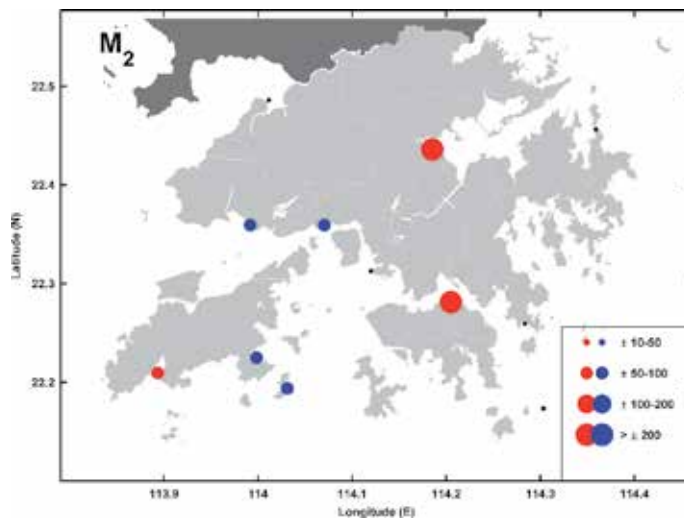
Figure 16.
Tidal anomaly correlations (TACs) of detrended M_2 amplitude to detrended MSL in Hong Kong [11], with the marker size showing the relative magnitude according to the legend, in units of mm m^{-1}. Red/blue markers indicate positive/negative TACs, and black markers indicate TACs which are not significantly different from zero. Maps were generated using MATLAB version R2011a (www.mathworks.com).

4.4 Hong Kong results

4.4.1 TAC and δ-HAT results

We now move from basin-wide surveys to a more tightly focused regional analysis of the Hong Kong waters, where 12 closely spaced tide gauges are available. For gauge names and locations, the reader is directed to refer to **Figure 6**.
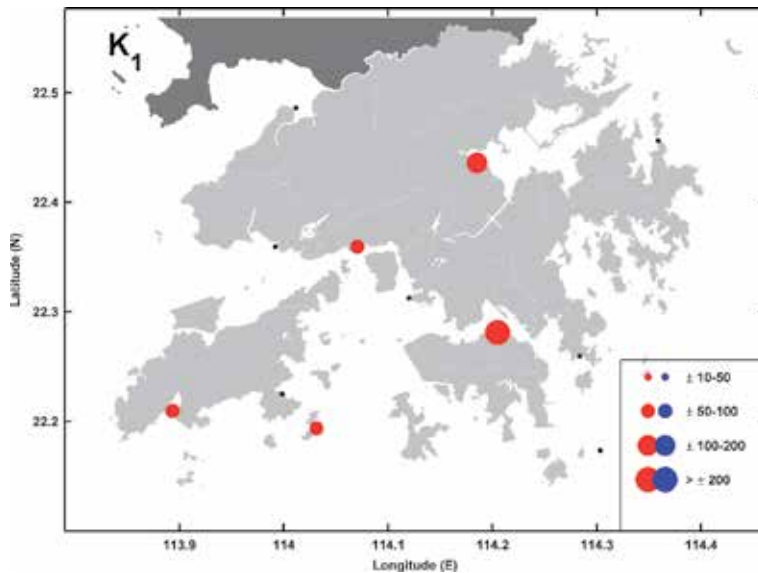
Figure 17.
Tidal anomaly correlations (TACs) of detrended K_1 amplitude to detrended MSL in Hong Kong [11], with the marker size showing the relative magnitude according to the legend, in units of mm m^{-1}. Markers are as in **Figure 16**. *Maps were generated using MATLAB version R2011a (www.mathworks.com).*
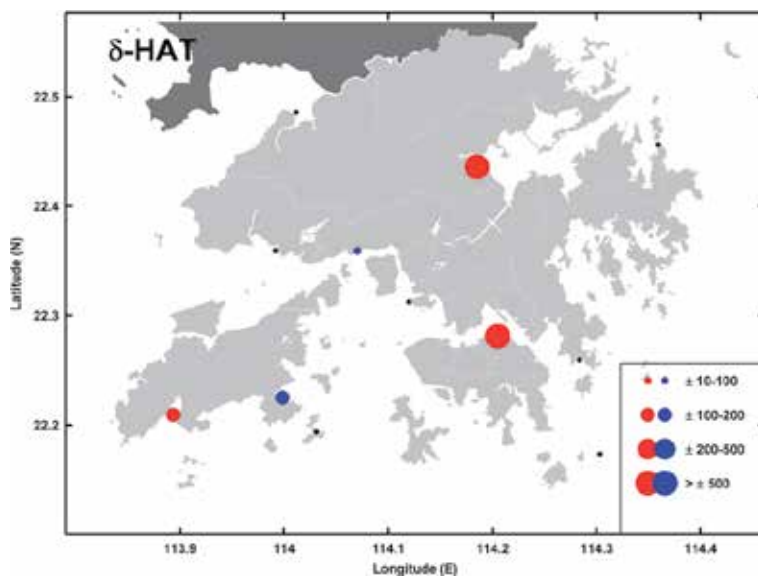
Figure 18.
δ-HAT map in Hong Kong [11], with the marker size showing the relative magnitude according to the legend, in units of mm m^{-1}. Markers are as in **Figure 16**. *Maps were generated using MATLAB version R2011a (www.mathworks.com).*

The strongest positive M_2 TACs are seen at Quarry Bay (+218 mm m^{-1}), and at Tai Po Kau (+267 mm m^{-1}), with a smaller positive TAC seen at Shek Pik (**Figure 16**). In the waters west of Victoria Harbor, all gauges except Kwai Chung exhibit moderate negative TACs. The diurnal TACs in Hong Kong generally exhibit a larger-magnitude and more spatially coherent response than semidiurnal TACs. Like M_2, the strongest K_1 values in Hong Kong (**Figure 17**) are seen at Quarry Bay (+220 mm m^{-1}) and Tai Po Kau (+190 mm m^{-1}).

The TACs are widely observed in Hong Kong, but the δ-HATs are only of significance at a few locations (**Figure 18**). Five stations exhibit significant δ-HAT values, with Quarry Bay and Tai Po Kau having very large positive magnitudes (+665 mm m^{-1} and +612 mm m^{-1}, respectively), and Shek Pik having a lesser magnitude of +138 mm m^{-1}. Conversely, Ma Wan and Chi Ma Wan exhibit moderate negative δ-HAT values (approx. −100 mm m^{-1}). The remainder of gauges (which are mainly open-water locations) have statistically insignificant results for the combined tidal amplitudes, even where some large individual TACs were observed. This shows that the combined tidal amplitude effect as expressed by the δ-HATs is most important in semi-enclosed harbors.

5. Summary and discussions

5.1 Summary of results

We have presented the salient features of several past studies, covering nearly all the global ocean, in efforts to understand the nature of tidal variability associated with mean sea level variability. Here, we will present a quick summary of the results, and then discuss some similarities of all results.

In the Pacific Ocean, out of 152 tide gauges considered, M_2 TACs are significant at 89 gauge, and K_1 TACs are significant at 76 gauges. For the combined tidal variability of these four tides, 54 stations (∼35%) are significantly correlated to variations in sea-level, with δ-HATs $> \pm 50$ mm m^{-1} (i.e., $> \pm 5\%$ of the sea level perturbation). In the Atlantic Ocean, 104 gauges have significant TACs, and for K_1, 62 locations exhibit TACs that are significant. For the combination of the eight largest tides, there is a near even mix in the Atlantic of positive (40) and negative (47) δ-HATs. Finally, in Hong Kong, mixed results were seen for individual TACs, but δ-HATs were only important at a few semi-enclosed harbor locations, namely Quarry Bay (Victoria Harbor), and Tai Po Kau, where the largest positive feedbacks worldwide were seen.

5.2 TAC and δ-HAT distributions and patterns

There are a few commonalities seen in both the Pacific and Atlantic basins. First, the yearly averaged response of the tides due to correlated MSL changes (TACs) show an overall mixed pattern of positive and negative responses. There is no apparent ocean-wide pattern that might suggest a single cause to the variability, but some regionally coherent patterns of variability are apparent. While many gauges show an increase in tidal amplitudes with increasing MSL (positive TAC), many exhibit a decrease (negative TAC), which suggests a variety of mechanisms may be at play. Second, individual TACs are more widespread, being significant at a larger number of tide gauges, but δ-HATs are only significant at a smaller number of locations. This is because some individual TACs can be partially canceled out by other individual TACs, yielding an overall tidal variability that is less intense. However, some locations do see a reinforced trend when considering all major tidal

constituents, yielding strong δ-HATs, and both positive and negative combinations are observed. Third, the largest δ-HATs tend to be located in coastal locations and not at open-ocean island locations. Many estuarine regions see the largest δ-HATs and most of the strongest individual TACs, as can be seen from the results in Hong Kong, which is located in the Pearl River Delta, and had the largest magnitude results. Other locations of note that are in estuarine environments include gauges in or near the Severn estuary in England, the Loire estuary in France, Astoria, Oregon, in the Columbia River Delta, and San Francisco Bay, California, which is fed by the Sacramento River.

There are some isolated locations do not fit this generalization, such as Hawaii, where the large significant positive values of δ-HATs at Honolulu and Hilo are mainly due to the M_2 TAC, but this is likely related to the changing phase of the internal tide [37]. On the western side of the South China Sea, gauges in Malaysia exhibit large negative δ-HATs related to the seasonal variability in tides due to stratification, seasonal monsoon winds and water depth [64]. In other shallow, semi-enclosed regions, such as the North Sea, increasing sea-level has amplified tides on the German/Dutch coast over the past 50 years due to reduced frictional effects [65].

The regional case of Hong Kong is particularly interesting. Only a few locations showed strong δ-HATs, and these are in sensitive harbor locations. Hong Kong has had a long history of land reclamation to accommodate an ever-growing infrastructure and population, including the building of a new airport island (Chep Lap Kok), new land connections, channel deepening to accommodate container terminals, and many bridges, tunnels, and "new cities", built on reclaimed land. All of these may have changed the resonance and/or frictional properties of the region. Tai Po Kau has also had some land reclamation projects that have changed the coastal morphology and may have modulated the tidal response. Other locations in Hong Kong did not show such extreme variations, so these variations appear to only be amplified in harbor areas.

5.3 Importance of combined tidal variability and nuisance flooding

The individual TACs reveal valuable information about the complex frequency-dependent response of the ocean. However, the metric that is most important for coastal planning is how all tidal components can combine and interact under changing MSL to increase local flood frequency and intensity. The δ-HATs provide an effective parameter to measure the full effect of changing tides, as they incorporate multiple tidal variabilities simultaneously. It is therefore of the greatest interest for the future of coastal flooding to find where all tides can change in the same direction, and the occurrence of the largest δ-HATs are likely dominated by local effects, such as a combination of natural and human-induced water level changes in sensitive harbor areas. If regional or amphidromic scales were dominant, then more coherent regional changes would be observed in the δ-HATs. If the changes in a local environment are favorable, all major tides can be enhanced and reinforced, and this may be via changes in tidal velocity and phase that better "tune" the response to yield higher water levels.

The impact of large δ-HATs on coastal and estuarine locations as sea level rises may be best demonstrated via the concept of nuisance flooding. Nuisance flooding refers to minor flooding events that happen at high tide without a strong storm surge, also called "sunny day flooding" [66]. Such events may also be induced by minor storm tides, Rossby waves [67] or pluvial flooding [68]. Nuisance floods are usually non-destructive individually, yet frequent occurrences can cause cumulative financial and societal impacts to coastal regions. Roads may flood more,

disrupting logistics and supply chains [69]. Sewers and drainage systems may overflow [70], increasing public health risks [71]. Flood probabilities and cumulative hazards are likely to further increase under future sea level rise scenarios, with an increased effect seen during El Nino events [5, 6, 72]. Most previous examinations of nuisance flooding only consider a changing MSL and a static tidal range, but some studies have demonstrated the importance of tidal changes leading to increased inundation, such as at Boston [73]. In some locations, secular changes to tidal range far outpace sea-level rise (e.g., Wilmington, North Carolina; [35]), and help drive flood risk. Moreover, since storm surge is a long wave, factors affecting tides can also alter storm surge [34, 74].

Figure 19 shows a simple representation of nuisance flooding with four cases presented. In the past when MSL was stable, it would take a storm surge (dark blue) to surpass local flooding levels (situation [a]), but under higher MSL conditions of the present day with unchanged tides, inundation can occur at high tide, especially on higher spring tides (situation [b]). If tides are not stationary with MSL rise, two additional situations are possible. If MSL increase leads to a slightly dampened high tide, then nuisance flooding will still happen, but will not be as extreme (situation [c]). However, if there is an additional increase of tidal range as MSL rises, then flooding will be more extreme, both with storm surge and without (situation [d]).

If tidal evolution related to MSL variability is present, then flood risk cannot accurately be assessed via superposition of present-day tides and surge onto a higher baseline sea-level, as such predictions would be insufficient at locations with a high tidal sensitivity to water levels. Long-term trends of tides and MSL can give a picture of the "slow and steady change" that will be most relevant for the future of coastal health, such as the unrecoverable loss of low-lying population zones such as estuaries under higher baseline MSL. On the other hand, short-term variabilities can indicate where "quick and sudden change" is important, which may increase the intensity of major storms as well as increasing the frequency of lower-impact yet more frequent high-water events (such as nuisance flooding) that can yield a
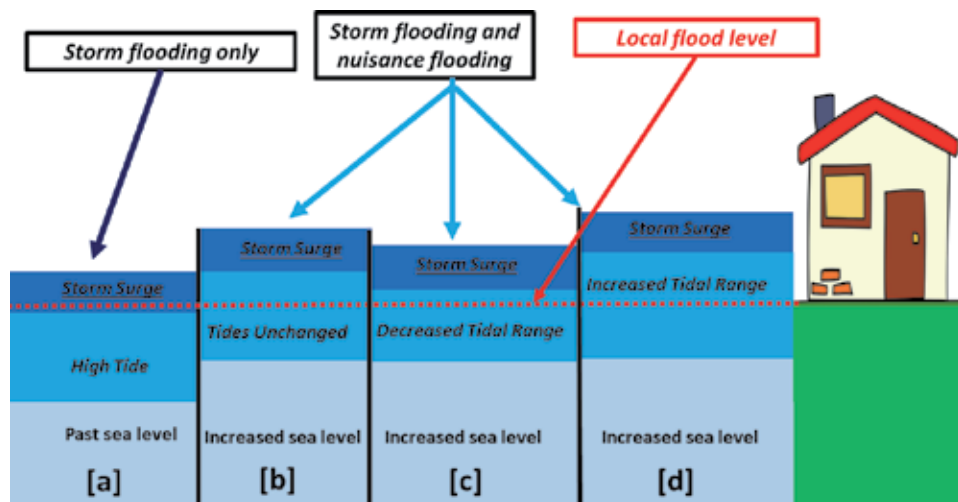
Figure 19.
Simple cartoon showing the effect of nuisance flooding under four situations [9]. In the past, when sea levels were lower, it would take a large storm surge to cause nuisance flooding (situation [a]), but more recently, as sea levels have risen, nuisance flooding may happen at high tide (situation [b]). If tidal range are damped as MSL rises, then situation [c] will arise, where nuisance flooding is still present, but not as much as in situation [b]. If tidal amplitudes also increase as MSL increases, then flooding will be particularly extreme (situation [d]). The red dashed line indicates the local flood level, which is only exceeded by storm surge in the past (situation [a]), but under modern MSL conditions is exceeded to varying degrees in situations [b], [c], and [d].

cumulative degradation of coastal areas. Therefore, both tides and MSL should be considered to fully quantify future water level changes in coastal areas, and a regional-to-local approach is prescribed.

6. Conclusions

This chapter has strived to summarize the salient features of a suite of past studies [7–11] that have analyzed the issue of changing tidal evolution that is correlated with MSL variability, both of which are likely related to climate-change related factors. It has been demonstrated that these tidal changes are likely to have the greatest effect on coastal locations, especially estuarine regions, which are often highly developed, densely populated, and environmentally sensitive. Overall, in both the Pacific and Atlantic, over 90% of all locations surveyed show a significant TAC in at least one tidal constituent, and around one-third of all locations have a significant δ-HAT.

In general, coastal inundation is associated with peak water level, not mean sea level, and depends on the combined effects of tides, storm surge, sea-level variability, inland precipitation, river flow, and other factors which may lead to increases in extreme water level exceedance probabilities. MSL rise can affect the tidal dynamics directly, or the reasons for the observed changes can be related to secondary mechanisms, including, but not limited to: river flow, changing bed friction due to harbor development and other causes, barotropic friction effects, heat content, buoyancy, stratification, mixing and eddy viscosity, ocean currents, waves, storm surge, and indeed, any source of water or energy input.

Here, the effects of tidal evolution, and the impacts of these changes on nuisance flooding have been described. Identifying connections and correlations between tidal range and MSL is critical for making reliable predictions of coastal water levels and inundation risk. When combined with storm surge, larger tides and higher MSL may amplify flood risk, coastal inundation, damage to infrastructure, and population displacement. Even without the consideration of storm surge, changes in tides and sea-levels may lead to more occurrences of nuisance flooding.

Author details

Adam Thomas Devlin* and Jiayi Pan
School of Geography and Environment, Jiangxi Normal University, Nanchang, Jiangxi, China

*Address all correspondence to: atdevin@jxnu.edu.cn; phlux1@gmail.com

IntechOpen

References

[1] Gutzwiller MC. Moon-Earth-Sun: The oldest three-body problem. Reviews of Modern Physics. 1998;**70**(2):589

[2] Church JA, White NJ. Sea level rise from the late 19th to the early 21st century. Surveys in Geophysics. 2011;**32** (4–5):585-602. DOI: 10.1007/s10712-011-9119-1

[3] Kopp RE, Kemp AC, Bittermann K, Horton BP, Donnelly JP, Gehrels WR, et al. Temperature-driven global sea-level variability in the Common Era. Proceedings of the National Academy of Sciences. 2016;**113**(11):E1434-E1441

[4] Domingues CM, Church JA, White NJ, Gleckler PJ, Wijffels SE, Barker PM, et al. Improved estimates of upper-ocean warming and multi-decadal sea level rise. Nature. 2008;**453**(7198):1090. DOI: 10.1038/nature07080

[5] Moftakhari HR, AghaKouchak A, Sanders BF, Matthew RA. Cumulative hazard: The case of nuisance flooding. Earth's Future. 2017;**5**(2):214-223. DOI: 10.1002/2016EF000494

[6] Moftakhari HR, AghaKouchak A, Sanders BF, Feldman DL, Sweet W, Matthew RA, et al. Increased nuisance flooding along the coasts of the United States due to sea level rise: Past and future. Geophysical Research Letters. 2015;**42**(22):9846-9852. DOI: 10.1002/2015GL066072

[7] Devlin AT, Jay DA, Talke SA, Zaron E. Can tidal perturbations associated with sea level variations in the western Pacific Ocean be used to understand future effects of tidal evolution? Ocean Dynamics. 2014;**64**(8):1093-1120. DOI: 10.1007/s10236-014-0741-6

[8] Devlin AT, Jay DA, Zaron ED, Talke SA, Pan J, Lin H. Tidal variability related to sea level variability in the Pacific Ocean. Journal of Geophysical Research-Oceans. 2017;**122**(11):8445-8463. DOI: 10.1002/2017JC013165

[9] Devlin AT, Jay DA, Talke SA, Zaron ED, Pan J, Lin H. Coupling of sea level and tidal range changes, with implications for future water levels. Scientific Reports. 2017;**7**(1):17021. DOI: 10.1038/s41598-017-17056-z

[10] Devlin AT, Pan J, Lin H. Extended spectral analysis of tidal variability in the North Atlantic Ocean. Journal of Geophysical Research-Oceans. 2019;**124** (1):506-526

[11] Devlin AT, Pan J, Lin H. Tidal variability in the Hong Kong region. Ocean Science. 2019;**15**(4):853-864

[12] Church JA, White NJ. A 20th century acceleration in global sea-level rise. Geophysical Research Letters. 2006;**33**(1). DOI: 10.1029/ 2005GL024826

[13] Nicholls RJ, Cazenave A. Sea-level rise and its impact on coastal zones. Science. 2010;**328**(5985):1517-1520. DOI: 10.1126/science.1185782

[14] Nerem RS, Chambers DP, Choe C, Mitchum GT. Estimating mean sea level change from the TOPEX and Jason altimeter missions. Marine Geodesy. 2010;**33**(S1):435-446. DOI: 10.1080/ 01490419.2010.491031

[15] Slangen AB, Church JA, Agosta C, Fettweis X, Marzeion B, Richter K. Anthropogenic forcing dominates global mean sea-level rise since 1970. Nature Climate Change. 2016;**6**(7):701-705. DOI: 10.1038/nclimate2991

[16] Dangendorf S, Marcos M, Wöppelmann G, Conrad CP, Frederikse T, Riva R. Reassessment of 20th century global mean sea level rise. Proceedings of the National Academy of Sciences. 2017;**114**(23):5946-5951

[17] Woodworth PL, White NJ, Jevrejeva S, Holgate SJ, Church JA, Gehrels WR. Evidence for the accelerations of sea level on multi-decade and century timescales. International Journal of Climatology: A Journal of the Royal Meteorological Society. 2009;**29**(6): 777-789. DOI: 10.1002/joc.1771

[18] Jevrejeva S, Grinsted A, Moore JC, Holgate S. Nonlinear trends and multiyear cycles in sea level records. Journal of Geophysical Research: Oceans. 2006;**111**(C9)

[19] Sallenger AH Jr, Doran KS, Howd PA. Hotspot of accelerated sea level rise on the Atlantic coast of North America. Nature Climate Change. 2012;**2**(12): 884-888

[20] Merrifield MA, Merrifield ST, Mitchum GT. An anomalous recent acceleration of global sea level rise. Journal of Climate. 2009;**22**(21):5772-5781. DOI: 10.1175/2009JCLI2985.1

[21] Merrifield MA. A shift in western tropical Pacific Sea level trends during the 1990s. Journal of Climate. 2011;**24**(15):4126-4138. DOI: 10.1175/2011JCLI3932.1

[22] Peyser CE, Yin J. Interannual and decadal variability in Tropical Pacific Sea level. Water. 2017;**9**(6):402. DOI: 10.3390/w9060402

[23] Bromirski PD, Miller AJ, Flick RE, Auad G. Dynamical suppression of sea level rise along the Pacific Coast of North America: Indications for imminent acceleration. Journal of Geophysical Research. 2011;**116**: CO7005. DOI: 10.1029/2010JC006759

[24] Cartwright DE, Tayler RJ. New computations of the tide-generating potential. Geophysical Journal of the Royal Astronomical Society. 1971;**23**:45-74. DOI: 10.1111/j.1365-246X.1971. tb01803.x

[25] Haigh ID, Wijeratne EMS, MacPherson LR, Pattiaratchi CB, Mason MS, Crompton RP, et al. Estimating present day extreme water level exceedance probabilities around the coastline of Australia: tides, extra-tropical storm surges and mean sea level. Climate Dynamics. 2014;**42**(1–2): 121-138

[26] Müller M, Arbic BK, Mitrovica JX. Secular trends in ocean tides: Observations and model results. Journal of Geophysical Research-Oceans. 2011; **116**(C5). DOI: 10.1029/2010JC006387

[27] Woodworth PL. A survey of recent changes in the main components of the ocean tide. Continental Shelf Research. 2010;**30**(15):1680-1691. DOI: 10.1016/j. csr.2010.07.002

[28] Mawdsley RJ, Haigh ID, Wells NC. Global secular changes in different tidal high water, low water and range levels. Earth's Future. 2015;**3**(2):66-81

[29] Cartwright DE. Secular changes in the oceanic tides at Brest, 1711–1936. Geophysical Journal International. 1972; **30**(4):433-449. DOI: 10.1.1.867.2468

[30] Proudman J, Doodson AT. V. The principal constituent of the tides of the North Sea. Philosophical Transactions of the Royal Society of London. Series A, Containing Papers of a Mathematical or Physical Character. 1924;**224**(616-625): 185-219

[31] Amin M. On perturbations of harmonic constants in the Thames Estuary. Geophysical Journal of the Royal Astronomical Society. 1983;**73**(3): 587-603. DOI: 10.1111/j.1365-246X.1983. tb03334.x

[32] Bowen AJ, Gray DA. The tidal regime of the River Thames; long-term trends and their possible causes. Philosophical Transactions of the Royal Society of London A. 1972;**272**(1221): 187-199. DOI: 10.1098/rsta.1972.0045

[33] Vellinga NE, Hoitink AJF, van der Vegt M, Zhang W, Hoekstra P. Human impacts on tides overwhelm the effect of sea level rise on extreme water levels in the Rhine–Meuse delta. Coastal Engineering. 2014;**90**:40-50. DOI: 10.1016/j.coastaleng.2014.04.005

[34] Chernetsky AS, Schuttelaars HM, Talke SA. The effect of tidal asymmetry and temporal settling lag on sediment trapping in tidal estuaries. Ocean Dynamics. 2010;**60**:1219-1241. DOI: 10.1007/s10236-010-0329-8

[35] Familkhalili R, Talke SA. The effect of channel deepening on tides and storm surge: A case study of Wilmington, NC. Geophysical Research Letters. 2016;**43**(17):9138-9147. DOI: 10.1002/2016GL069494

[36] Jay DA, Leffler K, Degens S. Long-term evolution of Columbia River tides. ASCE Journal of Waterway, Port, Coastal, and Ocean Engineering. 2011;**137**:182-191. DOI: 10.1061/(ASCE)WW.1943- 5460.0000082

[37] Colosi JA, Munk W. Tales of the venerable Honolulu tide gauge. Journal of Physical Oceanography. 2006;**36**(6):967-996. DOI: 10.1175/JPO2876.1

[38] Müller M, Cherniawsky JY, Foreman MGG, Storch JS. Global M_2 internal tide and its seasonal variability from high resolution ocean circulation and tide modeling. Geophysical Research Letters. 2012;**39**(19). DOI: 10.1029/2012GL053320

[39] Jay DA. Evolution of tidal amplitudes in the eastern Pacific Ocean. Geophysical Research Letters. 2009;**36**:L04603. DOI: 10.1029/2008GL036185

[40] Ray RD. Secular changes of the M_2 tide in the Gulf of Maine. Continental Shelf Research. 2006;**26**(3):422-427. DOI: 10.1016/j.csr.2005.12.005

[41] Ray RD. Secular changes in the solar semidiurnal tide of the Western North Atlantic Ocean. Geophysical Research Letters. 2009;**36**(19). DOI: 10.1029/2009GL040217

[42] Feng X, Tsimplis MN. Sea level extremes at the coasts of China. Journal of Geophysical Research-Oceans. 2014;**119**(3):1593-1608. DOI: 10.1002/2013JC009607

[43] Feng X, Tsimplis MN, Woodworth PL. Nodal variations and long-term changes in the main tides on the coasts of China. Journal of Geophysical Research-Oceans. 2015;**120**(2):1215-1232. DOI: 10.1002/2014JC010312

[44] Rasheed AS, Chua VP. Secular trends in tidal parameters along the coast of Japan. Atmosphere-Ocean. 2014;**52**(2):155-168. DOI: 10.1080/07055900.2014.886031

[45] Zaron ED, Jay DA. An analysis of secular change in tides at open-ocean sites in the Pacific. Journal of Physical Oceanography. 2014;**44**(7):1704-1726. DOI: 10.1175/JPO-D-13-0266.1

[46] Arbic BK, Karsten RH, Garrett C. On tidal resonance in the global ocean and the back-effect of coastal tides upon open-ocean tides. Atmosphere-Ocean. 2009;**47**(4):239-266. DOI: 10.3137/OC311.2009

[47] Skiba AW, Zeng L, Arbic BK, Müller M, Godwin WJ. On the resonance and shelf/open-ocean coupling of the global diurnal tides. Journal of Physical Oceanography. 2013;**43**(7):1301-1324. DOI: 10.1175/JPO-D-12-054.1

[48] Arbic BK, Garrett C. A coupled oscillator model of shelf and ocean tides. Continental Shelf Research. 2010;**30**(6):564-574. DOI: 10.1016/j.csr.2009.07.008

[49] Pugh DT. Tides, Surges and Mean Sea Level: A Handbook for Engineers and Scientists. Chichester: Wiley; 1987. 472pp. ISBN: 978-0471915058

[50] Müller M. The influence of changing stratification conditions on barotropic tidal transport and its implications for seasonal and secular changes of tides. Continental Shelf Research. 2012;**47**:107-118. DOI: 10.1016/j.csr.2012.07.003

[51] Kang SK, Chung JY, Lee SR, Yum KD. Seasonal variability of the M2 tide in the seas adjacent to Korea. Continental Shelf Research. 1995;**15**(9): 1087-1113

[52] Guo L, van der Wegen M, Jay DA, Matte P, Wang ZB, Roelvink D, et al. River-tide dynamics: Exploration of nonstationary and nonlinear tidal behavior in the Yangtze River estuary. Journal of Geophysical Research-Oceans. 2015;**120**(5):3499-3521. DOI: 10.1002/2014JC010491

[53] Hoitink AJF, Jay DA. Tidal river dynamics: Implications for deltas. Reviews of Geophysics. 2016;**54**(1): 240-272

[54] Pugh DT. Changing sea levels. In: Effects of Tides, Weather and Climate. Cambridge, UK: Cambridge University Press; 2004. 280pp. ISBN: 978-0521532181

[55] Pickering MD, Wells NC, Horsburgh KJ, Green JAM. The impact of future sea-level rise on the European Shelf tides. Continental Shelf Research. 2012;**35**:1-15

[56] Holleman RC, Stacey MT. Coupling of sea level rise, tidal amplification, and inundation. Journal of Physical Oceanography. 2014;**44**(5):1439-1455. DOI: 10.1175/JPO-D-13-0214.1

[57] Holgate SJ, Woodworth PL. Evidence for enhanced coastal sea level rise during the 1990s. Geophysical Research Letters. 2004;**31**(7)

[58] Leffler KE, Jay DA. Enhancing tidal harmonic analysis: Robust (hybrid L1/

L2) solutions. Continental Shelf Research. 2009;**29**(1):78-88. DOI: 10.1016/j.csr.2008.04.011

[59] Pawlowicz R, Beardsley B, Lentz S. Classical tidal harmonic analysis including error estimates in MATLAB using T_TIDE. Computers and Geosciences. 2002;**28**(8):929-937. DOI: 10.1016/S0098-3004(02)00013-4

[60] Cartwright DE, Edden AC. Corrected tables of tidal harmonics. Geophysical Journal International. 1973; **33**(3):253-264. DOI: 10.1111/j.1365-246X.1973.tb03420.x

[61] Woodworth PL, Hunter JR, Marcos M, Caldwell P, Menéndez M, Haigh I. Towards a global higher-frequency sea level dataset. Geoscience Data Journal. 2016;**3**(2):50-59. DOI: 10.1002/gdj3.42

[62] Egbert GD, Erofeeva SY. Efficient inverse modeling of barotropic ocean tides. Journal of Atmospheric and Oceanic Technology. 2002;**19**(2):183-204. DOI: 10.1175/1520-0426(2002)019 <0183: EIMOBO>2.0.CO

[63] Egbert GD, Erofeeva SY. OTIS: The OSU Tidal Inversion Software TPXO7. 2. College of Oceanic and Atmospheric Sciences, Oregon State University. 2010. Available from: http://volkov.oce.orst. edu/tides/otis.html

[64] Devlin AT, Zaron ED, Jay DA, Talke SA, Pan J. Seasonality of tides in Southeast Asian waters. Journal of Physical Oceanography. 2018;**48**(5): 1169-1190

[65] Mudersbach C, Wahl T, Haigh ID, Jensen J. Trends in high sea levels of German North Sea gauges compared to regional mean sea level changes. Continental Shelf Research. 2013;**65**:111-120. DOI: 10.1016/j.csr.2013.06.016

[66] Sweet WV, Park J. From the extreme to the mean: Acceleration and tipping points of coastal inundation

from sea level rise. Earth's Future. 2014;**2**(12):579-600

[67] Calafat FM, Wahl T, Lindsten F, Williams J, Frajka-Williams E. Coherent modulation of the sea-level annual cycle in the United States by Atlantic Rossby waves. Nature Communications. 2018;**9**(1):2571

[68] Moftakhari HR, AghaKouchak A, Sanders BF, Allaire M, Matthew RA. What is nuisance flooding? Defining and monitoring an emerging challenge. Water Resources Research. 2018;**54**(7):4218-4227

[69] Suarez P, Anderson W, Mahal V, Lakshmanan TR. Impacts of flooding and climate change on urban transportation: A systemwide performance assessment of the Boston Metro Area. Transportation Research Part D: Transport and Environment. 2005;**10**(3):231-244. DOI: 10.1016/j.trd.2005.04.007

[70] Cherqui F, Belmeziti A, Granger D, Sourdril A, Le Gauffre P. Assessing urban potential flooding risk and identifying effective risk-reduction measures. Science of the Total Environment. 2015;**514**:418-425. DOI: 10.1016/j.scitotenv.2015.02.027

[71] Ten Veldhuis JAE, Clemens FHLR, Sterk G, Berends BR. Microbial risks associated with exposure to pathogens in contaminated urban flood water. Water Research. 2010;**44**(9):2910-2918. DOI: 10.1016/j.watres.2010.02.009

[72] Vandenberg-Rodes A, Moftakhari HR, AghaKouchak A, Shahbaba B, Sanders BF, Matthew RA. Projecting nuisance flooding in a warming climate using generalized linear models and Gaussian processes. Journal of Geophysical Research-Oceans. 2016;**121**(11):8008-8020

[73] Ray RD, Foster G. Future nuisance flooding at Boston caused by

astronomical tides alone. Earth's Future. 2016;**4**(12):578-587. DOI: 10.1002/2016EF000423

[74] Arns A, Dangendorf S, Jensen J, Bender J, Talke SA, Pattiaratchi C. Sea level rise induced amplification of coastal protection design heights. Nature Scientific Reports. 2017;7:40171. DOI: 10.1038/srep40171

Chapter 3

Linear and Nonlinear Responses to Northeasters Coupled with Sea Level Rise: A Tale of Two Bays

Stephen Moore, Huijie Xue, Neal R. Pettigrew and John Cannon

Abstract

This study aimed at dissecting the influence of sea level rise (SLR) on storm responses in two bays in the Gulf of Maine through high-resolution, three-dimensional, hydrodynamic modeling. Saco Bay, an open bay characterized by gentle coastal slopes, provided a contrast to Casco Bay that has steep shorelines and is sheltered by barrier islands and peninsulas. The Finite-Volume Coastal Ocean Model (FVCOM) was implemented for Saco Bay and Casco Bay to simulate the February 1978 northeaster and an April freshwater discharge event in 2007 following the Patriots Day storm. Both events were repeatedly simulated under SLR scenarios ranging from 0 to 7 ft. Modeled storm responses were identified from the 1978 Blizzard simulations and were tracked across SLR scenarios. By comparing changes in inundation, storm currents, and salinity distribution between the two bays, freshwater discharge and bathymetric structure were isolated as two determining factors in how storm responses change with the rising sea level. The steplike bottom relief at the shoreline of Casco Bay sets up nonlinear responses to SLR. In contrast, storm responses in Saco Bay varied significantly with SLR due to alterations in river dynamics attributed to SLR-induced flooding.

Keywords: storm response, sea level rise, Saco Bay and Casco Bay, the Gulf of Maine, simulation, coastal ocean model

1. Introduction

The influence of sea level rise (SLR) on coastal storm responses is highly complex and not well understood. It has been shown that the impact of SLR on storm tide and surge can vary greatly over small spatial scales [1, 2] though the causes of these variations, likely regionally specific, have not been thoroughly explored. Due to the limited understanding of small-scale uncertainties, linear relationships between SLR and storm response patterns are commonly assumed when modeling SLR scenarios for risk management. This study is aimed at investigating the variability of storm responses sensitive to SLR along the coastline of Saco Bay and Casco Bay in the Gulf of Maine through the application of a hydrodynamic coastal ocean model. The coastline across these two bays varies greatly in topography and intertidal characteristics, which has been shown to be a major factor affecting the impact of SLR on storm surge [3]. Furthermore, coastal flooding caused by northeasters

along the New England coastline is a common occurrence during the cool seasons when cyclogenesis is driven by dynamic atmospheric forcing associated with the jet stream. This makes accurate predictions of storm response of great importance to the coastal communities.

During the October–April period, the extratropical storms affecting this domain are characterized by large, synoptic-scale cyclones, heavy precipitation, and strong wind and are accompanied by wave run-up and sea level setup. As a result, northeasters in this region often result in significant damages including loss of life and property, as well as environmental impacts such as beach erosion. The latter is particularly notable in Saco Bay in northern New England, where beach erosion has been a major issue for several decades. Conversely, in the same area, tropical cyclones are often smaller and move faster, resulting in less time for storm surges to develop over these shallow areas [4], and typically transition into extratropical cyclones before landfall. As such, this study will primarily focus on major extra-tropical storm events. Scarcity of real-time observation data during these storms has led to an increased reliance on numerical model results for storm forecasts along the coastline [4]. Testing the developed hydrodynamic model against these extreme events across varying SLR scenarios will also help ensure the model's capability in modeling future events.

This study was designed to quantify the relationship between sea level rise and coastal storm responses in Saco Bay and Casco Bay. In doing so, improved forecasts can be provided to coastal communities in preparation for future storm events. To accomplish these goals, a predictive storm response model was developed, building upon the Finite-Volume Coastal Ocean Model (FVCOM) [5]. Inputs for this model were derived from the Northeast Coastal Ocean Forecast System (NECOFS, http://www.smast.umassd.edu:8080/thredds/catalog/models/fvcom/NECOFS/Archive/catalog.html) and the United States Geological Survey (USGS, https://waterdata.usgs.gov/nwis). Validation of the resultant model was carried out with data collected from NOAA buoys and stations, the University of Maine buoy deployments, and the Sustainable Ecological Aquaculture Network (SEANET). Buoy records and tidal station data along with the validated model simulation were used to establish a baseline assessment of the bays. Storm simula-tions were then analyzed to identify and dissect storm responses to be tracked across a range of sea level rise scenarios.

The present investigation differentiates itself from past studies in three promi-nent ways. First, no hydrodynamic model study has been conducted over this domain at the high-resolution used herein. By simulating storms with the minimum 10-m resolution nearshore, we can identify very-small-scale features and provide more accurate dynamic inundation and storm response predictions than what is currently available. Additionally, the methodology of tracking modeled storm responses under elevating SLR scenarios has not yet been applied to the Gulf of Maine, a region particularly vulnerable to the impacts of northeasters. Finally, this study provides a comparison of storm responses and SLR vulnerability in two adjacent bays, distinct from each other in geomorphological and hydrodynamic characteristics.

The following section provides a review of studies contributing to the understanding of SLR storm response interactions and includes a brief overview of the Saco and Casco domain and of the storm events being examined. The rest of the paper is organized as follows. The design, configuration, and validation of the model are discussed in Section 3, followed by an analysis in Section 4 to depict the modeled storm responses. Section 5 looks at the modeled responses in the events of sea level rise, including inundation and circulation patterns. Finally, Section 6 provides a summary of the findings revealed by this study.

2. Background

2.1 Prior understanding of interactions between storm responses and SLR

The relationship between SLR and storm response is still not well understood, as was made clear by Woodruff et al. in a review of studies up to 2012 aimed at dissecting the relationship between SLR and flooding caused by tropical cyclones [6]. Of interest in Woodruff's review were two studies mentioned earlier which applied modeling techniques to investigate storm surge in hurricane conditions under SLR scenarios [1, 2]. Smith et al. [1] was the first to show quantitatively that the relationship between SLR and storm surge is not necessarily linear. In areas with high surge under present conditions, the increase in storm surge under the relative sea level rise (RSLR) scenarios remained linear, with RSLR defined as the cumulative change in vertical height of both land and water [7], but the amplification of surge in areas that typically saw low surge heights was increased by a much larger factor under heightened RSLR scenarios. While not explored in depth by the authors, another important conclusion was a potential plateau effect on the relative impact of SLR on storm surge in certain areas.

Interest in researching the impacts of global SLR and risk management has increased significantly since the NOAA 2012 National Climate Assessment (https://scenarios.globalchange.gov) wherein 100-year projections of SLR scenarios were produced for the coastal United States. The assessment report acknowledged the uncertainties regarding the relationship between ocean warming, ice sheet and glacier loss, and SLR, and in doing so provided four different SLR projections, with final endpoints ranging from 0.2 to 2.0 m of coastal SLR by 2100. This range formed the basis for the SLR scenarios chosen for many subsequent investigations, including the present Saco and Casco model study. Some recent studies have acknowledged the uncertainties in the 2012 assessment, illustrating the benefits of analyzing the acceleration of flooding, which appeared to be a more precise calculation than measuring acceleration of SLR [3, 8]. These studies assumed zero acceleration of SLR, linearly generalizing the predicted rise to the entire Gulf of Maine.

The most recent modeling efforts of coastal responses to storms have largely focused on risk management and damage estimation under potential SLR scenarios, such as changes in land cover due to increased storm surge resulting from SLR [9]. Passeri et al. offered a good review of such studies looking at changes in coastal structure estimated from secondary SLR impacts, such as increased surge morphing the landscape in shallow areas [10]. The proposed structural impacts of SLR tie back into the efforts to estimate RSLR, as the generalized linear SLR projections did not account for changes in vertical land height or coastal slopes.

Looking specifically at the Saco and Casco domain, groups local to the region have been focusing on the global SLR projections, as RSLR projections, such as those for NYC and Louisiana, are not readily available. Peter Slovinsky of the Maine Geological Survey incorporated the global projections made by these earlier studies into a presentation for the 2015 State of the Bay Conference [11], in which he outlined the steps that coastal communities have been taking in anticipation of future SLR impacts, including ordinance changes, vulnerability assessments, coastal modeling efforts, public outreach, and infrastructure remodeling. He also pointed out how SLR trends in Portland, Maine, such as those discussed by Ezer and Atkinson [3], may indicate accelerated SLR over the past few decades, which would increase the 2100 SLR projections for Portland to be closer to the higher estimates offered by NOAA [12]. At present, focus continues to rest on risk mitigation and community actions in preparation for worst-case scenario future projections. The Saco and Casco storm response study was devised to support this continued effort through

the simulation of two major storm events: The Blizzard of 1978 and the Patriots Day storm in 2007.

2.2 Saco Bay and Casco Bay

Though situated next to each other, Saco Bay and Casco Bay differ significantly in terms of geography (**Figure 1**). Saco Bay is a 10-mile wide embayment containing the Saco Estuary, Goose Fare Brook tidal inlet, and Scarborough marshes that are fed by Nonesuch River. The mean tidal range of the bay is 2.7 m. During a storm study of Saco Bay, bottom current velocities measured at Higgins Beach and a mooring located just offshore of East Grand Beach reached a maximum of 1.09 m/s across six storm events monitored between January 23 and March 7, 2001 [13]. Many of these hydrodynamic features of Saco Bay have been partially explained by the sheltering of the bay from southerly waves by Biddeford Pool in the south and the presence of the Richmond Island headland in the north acting as a barrier to sediment transport [14]. Much of Saco Bay is very shallow and thus highly sensitive to rises in sea level, in contrast to the steeper shores of Casco Bay.

In this text, Casco Bay is split into northern and southern Casco Bay at the Chebeague Island. As is the case with Saco Bay, the M2 semidiurnal lunar tide is the primary tidal constituent for Casco Bay [14]. The primary freshwater input into the bay is considered as the combined discharge of the Presumpscot and Royal rivers, averaging roughly 40 m^3/s [15]. A salinity gradient is also present in the northern Casco Bay due to the input from the Kennebec [16], a river system comprised of the Kennebec and Androscoggin rivers that has been observed to discharge upward of 4000 m^3/s of freshwater during the spring.

2.3 Historical storms

Two storm events were chosen for this study. The Blizzard of 1978, herein referred to as the 1978 event, was selected for the peak sea levels recorded at
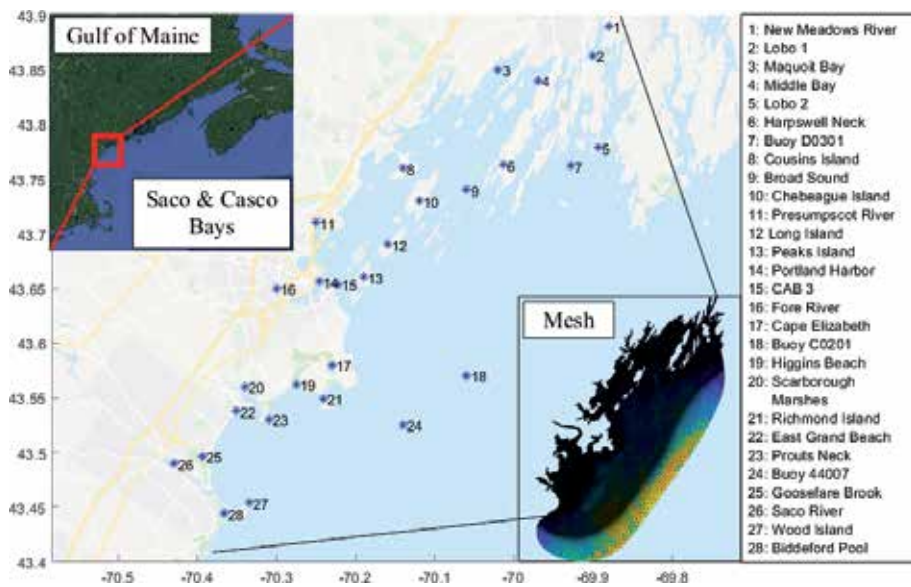
Figure 1.
Points of interest in Saco Bay and Casco Bay. In this study, the model domain south of point 17 (Cape Elizabeth) is considered "Saco Bay," while all points north of 17 are considered to be within "Casco Bay." The mesh designed for the Saco-Casco model is shown in the bottom right.

Portland Station, identified as a 100-year event. The Patriots Day storm, herein referred to as the 2007 event, was chosen for the peak freshwater discharge that occurred following the storm, offering an opportunity to relate the dynamics of river flooding to SLR.

First identified as an extratropical cyclone on February 5, the 1978 event reached a low pressure of 984 mbar as it retrograded from well off the mid-Atlantic coast to Long Island, moving northward toward the New England coastline [17]. On February 7, northeasterly wind gusts of 83 and 92 mph were reported in Boston and Cape Cod, respectively, along with sustained hurricane force winds [17]. The record surge resulting from the cyclone makes it a focal point for this study, as sea level heights reached their 100-year maximum during this event both in Portland, Maine, and in Boston. Specifically looking at Portland, historical archives report 14.17 ft. (equivalent to 4.32 m) above the MLLW as the peak water level ever recorded [4].

The 2007 event was initially reported on April 15 as a low pressure in the southeastern United States before it traveled north along the coastline. NOAA records indicate a barometric low of 972 mbar and wind gusts up to 59 mph over Portland [18]. The Portland Harbor tide gauge reported a peak water level of 13.28 ft. during this event [4]. Rainfall totaled 5.6 inches in Portland, Maine. River flooding was severe with near record levels reported for the Presumpscot River. This provides an effective case study of rainfall vs. snowfall effects on bay responses between this storm and the 1978 event, as icing resulted in decreased river flow following the 1978 event, whereas a surge in freshwater discharge resulted from the precipitation during the 2007 event. The National Weather Service (NWS) Storm Events Database (SED) and the National Centers for Environmental Information (NCEI) database also reported that the Patriots Day storm destroyed two homes due to flooding, and significant flooding was reported along with high levels of coastal erosion along the bays' coastlines.

Northeasterly coastal winds associated with the northeaster events were captured by the NECOFS model simulation (**Figure 2**). The storm window of the 2007 event over the Saco and Casco domain was defined as April 16, 01:00, when the upward climb of observed winds at buoy C0201 exceeded the maximum winds prior to the storm, to April 19, 20:00, when winds dropped below the monthly mean winds for April 2007. The NECOFS output wind fields for April 2007 differed
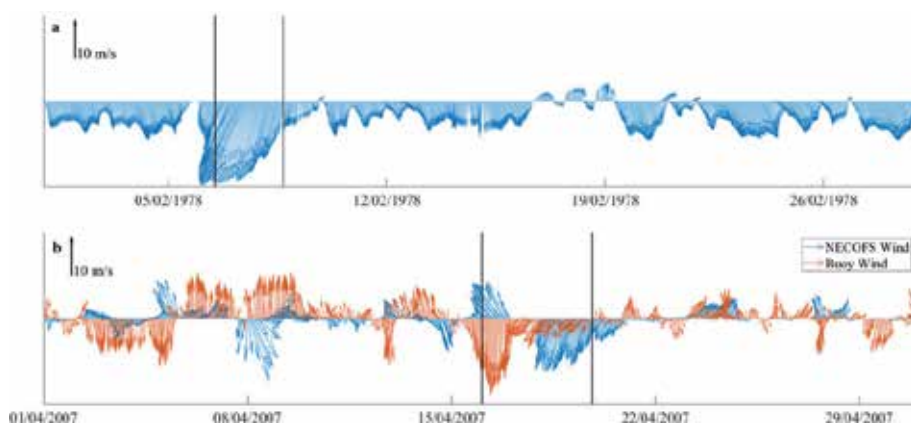
Figure 2.
Wind velocities during February 1978 (a) and April 2007 (b) at buoy C0201. Observed winds, available only for the latter period, are shown in red, while NECOFS-predicted winds are shown in blue. Storm windows are indicated by vertical black lines. The black arrow in the top left of each plot indicates velocity scale.

significantly in magnitude and direction from buoy observations. At buoy C0201, NECOFS-modeled storm winds were initially directed in nearly the opposite direction from observed winds, with roughly half the speed. Saco River discharge rates increased rapidly from an estimated minimum of ~60 m^3/s to an estimated peak of ~500 m^3/s on April 16 at 22:00 and remained high for the remainder of the month due to spring freshet. For the 1978 event, no such observations were available, so its storm window was defined purely from NECOFS wind output as Feb 6, 12:00, to Feb 8, 16:00, when storm winds rose above the maximum February 1978 winds not associated with the storm.

3. The Saco and Casco model

3.1 Model setup

The Saco-Casco model was an implementation of FVCOM that was developed to model complex coastal systems [5]. The finite-volume method takes the advantage of both the finite-element and finite-difference methods. It calculates the transport between elements by evaluating the integral form momentum and mass conservation equations along each element's boundaries [5, 19]. The three-dimensional unstructured grid is specified as the two-dimensional mesh coupled with the terrain-following layers in the sigma coordinate in the vertical. By performing calculations across an unstructured grid, FVCOM allows for high-resolution modeling along complex coastlines that would otherwise be difficult to accurately simulate [5].

The domain defined for the Saco and Casco model covers the coastal waters, including intertidal areas, from Kennebunkport in the south to Sebasco in the north in the Gulf of Maine (see the lower right inset in **Figure 1**). Saco Bay was discretized to the highest resolution of 10 m in areas shallower than 2 meters below the mean sea level, while equivalent depths in Casco Bay were set to 100-m resolution. Resolution in the rest of the domain was determined by depth, expanding to a maximum resolution along the open boundary to match that of NECOFS Gulf of Maine 3 (GOM3) mesh.

The 1/3 arc-second NOAA digital elevation model (DEM) for Portland, Maine [20], was used to specify the bathymetry for Saco Bay and Casco Bay. Through Aquaveo's Surface Modeling Software, the 10-m-resolution DEM was interpolated onto the unstructured triangular mesh developed for this study. Prior to interpolation, the DEM was converted from mean high water (MHW) to MSL to match the rest of the input data for the FVCOM model setup. Additional iterations of the Saco and Casco mesh were developed by integrating LiDAR bathymetry data from the NOAA digital coast system [21]. Specifically, the 2010 USACE NCMP Topobathy and 2014 USACE NAE Topobathy datasets were used, covering the Saco Bay coastline and Scarborough marsh with vertical accuracies of 20 and 10 cm and horizontal accuracies of 75 and 100 cm, respectively.

The Saco, Fore, Presumpscot, and New Meadows rivers were incorporated in the Saco and Casco model mesh. Two USGS gauges in the Saco and Casco domain were used for estimating discharge rates from rivers. Station 01064118 at Westbrook, Maine, for the Presumpscot River provides 15-minute discharge rates and gauge heights recorded from October 2016 and 2007 to present, respectively. Fifteen-minute discharge rates and gauge heights for the Saco River are available from station 01066000 at Cornish, New Hampshire, from October 1989 and 2007 to present, respectively.

Discharge rates for the 2007 event from station 01066000 were applied directly to the model's river forcing for the Saco River. Estimations of freshwater discharge had to be made in all other cases. Regressions were developed between gauge height and discharge rates for stations 01064118 and 01066000 using monthly datasets for February and April in years when both variables were available. Numerous iterations on these relationships were implemented, using a past study on the plume structure of Saco River [22] as a guide to adjust the regression coefficients. The results discussed herein reflect model simulations using the most stable freshwater discharge forcing, with the Saco and Nonesuch rivers using simplified discharge rates of 5.94 and 2.97*Gh, respectively, where Gh is the observed gauge height in feet at site 01064118. For the Fore, Presumpscot, and New Meadows rivers, discharge rates were estimated at 2.97, 1.48, and 2.97*Gh, respectively. Only gauge 01064118 was used for the final 1978 simulations, as the regressions built from gauge 01066000 indicated lower than reasonable estimations. For the 2007 event, Gh for these three rivers was also taken from site 1016600, as site 01064118 has no available data for April 2007 and there was no suitable proxy to capture the freshwater discharge event. As gauge heights for 1978 were unavailable, February 2017 observed gauge heights were used as a proxy, as a northeaster occurred at roughly the same time of the year in 2017 as in 1978.

At the time of writing, estimated hindcast discharge rates have been made available at site 01064118 from October 1975 to present and at site 01066000 from May 1916 to present. In comparing our estimated discharge rates to those presented by USGS, the same trends are depicted. Furthermore, the baseline (0 ft. SLR) model has since been rerun upon release of these datasets, which confirms that no noticeable changes are detected when using the modeled discharge vs. USGS predictions.

The Saco-Casco model was initialized and forced at the open boundary with hourly outputs from NECOFS hindcasts gom3_197802.nc and gom3_200704.nc (http://www.smast.umassd.edu:8080/thredds/catalog/models/fvcom/NECOFS/ Archive/Seaplan_33_Hindcast_v1/catalog.html). The NECOFS, supported by the Northeastern Regional Association of Coastal and Ocean Observing Systems (NERACOOS) to complement the ocean observing system, is an FVCOM-based ocean model covering the domain between Long Island and Nova Scotia [23]. The NECOFS was configured using the third iteration of FVCOM coupled with the SWAN model, using the output from a larger-scale Weather Research and Forecasting (WRF) model for meteorological forcing. Data from the National Data Buoy Center buoys, NOAA C-MAN stations, river discharge statistics, and satellites were collected to support the development and testing of the NECOFS model. The NECOFS hindcasts used a mesh, labeled the GOM3, which has a peak resolution of 0.3–1.0 km in coastal areas, including the full Saco and Casco domain.

3.2 Model validation

In situ observations from multiple sources were used to validate the model. Data from the NOAA-operated tidal stations (http://tidesand currents.noaa.gov/) were used for the sea surface height and water temperature validation. The University of Maine Physical Oceanography Group initiated the development of the Gulf of Maine Ocean Observing System (GoMOOS) in 2001 [24]. The moored buoys designed for this project were equipped with sensors specific to their installation site in addition to a standard set of instruments allowing for the collection and archive of wind speed and direction, visibility, air temperature, wave parameters, water temperature, and conductivity at 1-m depths and current velocity at 2-m depths [25]. For the Saco and Casco modeling project, data were collected from

the University of Maine Mooring C0201, Maine EPSCoR Mooring D0301 as well as Lobo 1 and Lobo 2 (http://umaine.edu/epscor/seanet/), and NOAA National Data Buoy Center Buoy 44007 (http://www.ndbc.noaa.gov) (see **Figure 1**). These datasets were used for the validation of additional test runs performed over the deployment periods of the buoys.

Time series validation of selected model output variables was performed. Only one station 8418150 (Portland, Maine) existed within the Saco and Casco domain with water level data for these two historic events. Tidal analyses were conducted using the "UTide" Matlab package to assess the model's ability at capturing tides and tidal residuals. **Figure 3a** and **d** compares the modeled SSH with the observations at the Portland station. **Figure 3b** and **e** compares the reconstructed tidal signals with UTide, which were removed from the raw signals to calculate the residuals (**Figure 3c** and **f**). After correcting for a constant negative bias of 2 feet detected between buoy records and NECOFS output, the modeled water level was able to capture the observed storm surge for the February 1978 event. However, the storm water level was lower than the observation in the first half of the storm window for the 2007 event. This was likely caused by the weaker predicted storm in the first half of the storm window wind seen in **Figure 2b**.
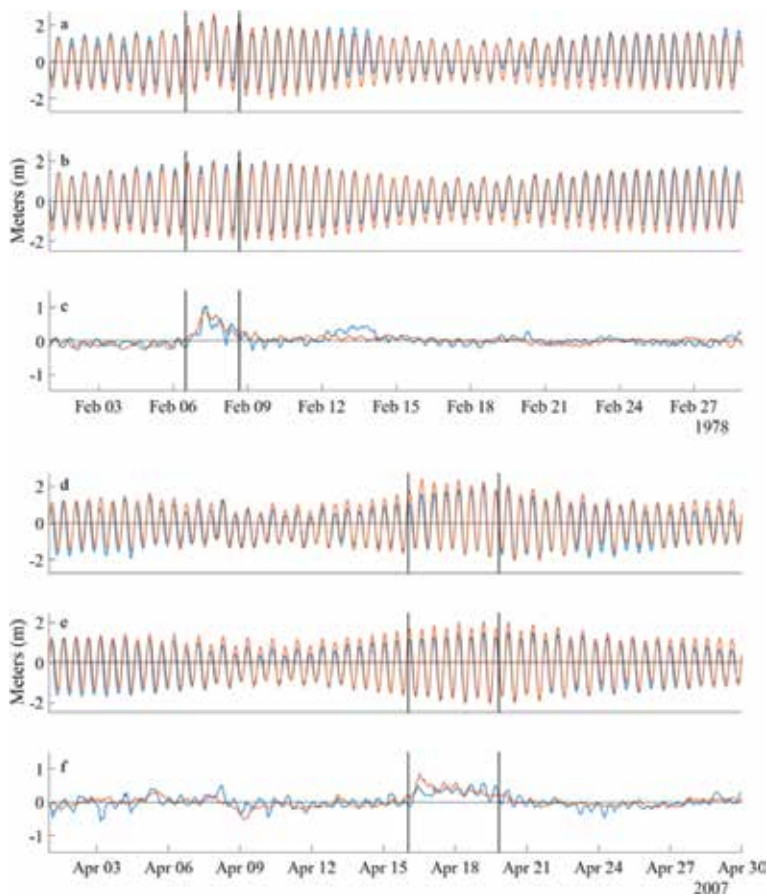
Figure 3.
Comparison of the water level for the baseline simulation of the 1978 event (a–c) and the 2007 event (d–f) for the raw signals (a and d), tidal harmonics (b and e), and tidal residuals (c and f). Tidal constituents used in UTide include M2, N2, S2, K1, O1, NU2, and T2. Storm windows are indicated by vertical black lines.
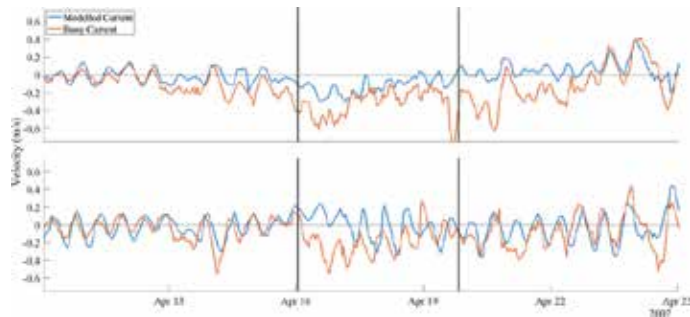
Figure 4.
Comparisons of near-surface currents observed at buoy C0201 and modeled current for the April 2007 event. Negative velocities indicate westward (top) or southward (bottom) currents. The storm window is indicated by vertical black lines.

Furthermore, current data was available at buoy C0201 for the 2007 event (**Figure 4**). The increase in westward velocity was revealed by the model, but at about half of the magnitude. The southward tendency was completely missed in the first half of the storm window again due to the errors in NECOFS-predicted wind direction. Discrepancies in modeled current output were examined by modifying the wind forcing. When the model run was repeated using the buoy-observed wind (red vectors in **Figure 2** and spatially uniform), the southward velocity in the first half of the storm window was improved, but the simulated currents deteriorated before and after the storm (not shown). Therefore, in this study we still used the simulations with NECOFS-predicted winds for the consistency between the surface and lateral boundary conditions because the open boundary condition adopted from the NECOFS was produced with the same set of meteorological forcing. As such, the 2007 event cannot be confidently referred to as a "storm scenario" with regards to modeled currents. However, the high discharge rates and availability of discharge data allowed us to utilize the April 2007 model runs as SLR simulations of a freshwater discharge event.

4. Bay response to northeasters

Responses in this study were defined as deviations from the typical circulation patterns seen during non-storm conditions. A storm window (see Section 2.3 above) was chosen for each storm event wherein anomalies were detected and collected for further analysis.

4.1 Casco Bay

Following the path of the storm winds, we first examine the surface currents entering the model domain from the northeast corner of the model's open boundary. **Figure 5** depicts frames of surface currents during flood and ebb tides prior to and within the1978 event's storm window. From this figure, we can see typical flooding and ebbing currents as strong flows in and out of the bay through the Broad Sound and the passage between the Peaks Island and Long Island. Outflow from the New Meadows River is visible in the upper reach of the estuary during ebb tides. As storm winds reached their peak magnitude, the surface current velocities in New Meadows River, measured at the sites of Lobo 1 and Lobo 2, increased sharply in the southward direction during ebb tides, increasing the reach of the New Meadows river plume into Casco Bay. The most apparent change was the
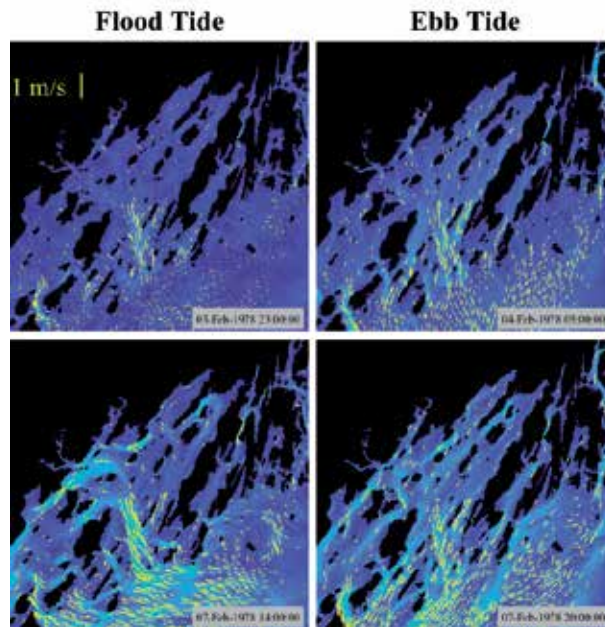
Figure 5.
Frames of modeled surface currents in northern Casco Bay for the 1978 event before (top) and during (bottom) the storm window during flood (left) and ebb (right) tides. The yellow arrow in the top left panel indicates velocity scale.

increased northward surface current during flood tides within the storm window, which flowed into the Broad Sound along the east coast of Chebeague Island, circulating counterclockwise around Cousins Island.

Continuing southward (**Figure 6**), the flood tide entered southern Casco Bay mostly through the passage between Long Island and Peaks Island, which circulated counterclockwise to enter Portland Harbor and keep the Fore River plume inside the estuary. During ebb, the Presumpscot River and Fore River plumes joined the outgoing tidal flows to form a strong southward current extending from Portland Harbor to south of Cape Elizabeth. Southward ebbing tidal currents were also strong in the passage between Long Island and Peaks Island. Albeit the flows were strengthened, the general patterns remained during the 1978 events except that the Presumpscot plume was more restricted during flood by the impeding tidal plus storm currents.

Briefly comparing the northern and southern halves of Casco Bay, the more open segment in the north, including Broad Sound and Maquoit Bay and Middle Bay, was less susceptible to storm forcing. The southern Casco Bay showed more noticeable storm responses in Portland Harbor, where the Presumpscot River and Fore River plumes were altered significantly by storm winds.

4.2 Saco Bay

Surface currents increased sharply as they continued south of Casco Bay, colliding with the northern coastline of Cape Elizabeth (**Figure 7**). The increase in current velocity was most evident during ebb tides when storm currents and tidal currents aligned but was also visible during flood tides, overpowering the typical tidal currents. Water carried by the southwestward storm currents was directed clockwise around Cape Elizabeth to split to the north and south of Richmond Island. Even though only a small percentage of the water passed to the north of
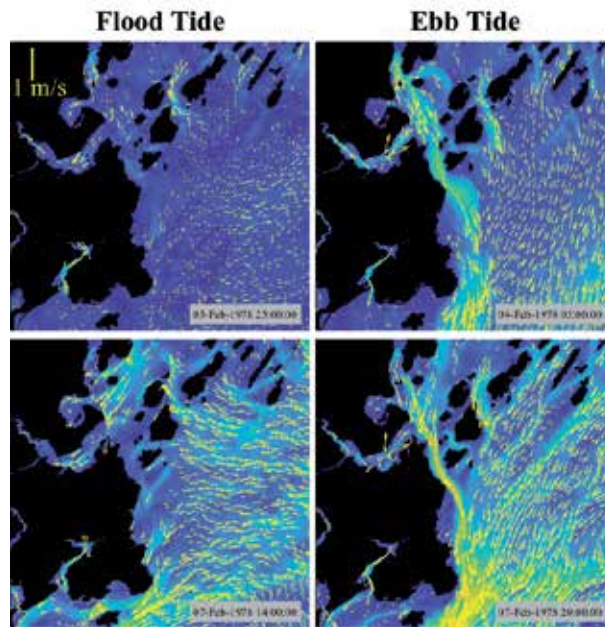
Figure 6.
*Similar to **Figure 5** but for southern Casco Bay.*
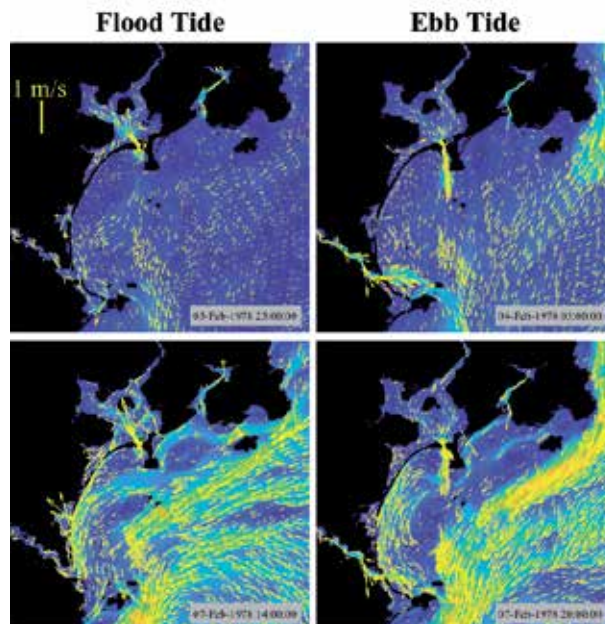
Figure 7.
*Similar to **Figure 5** but for Saco Bay.*

Richmond Island, it was enough to cause a reversal in current velocities there compared to the prestorm flood and ebb tides.

Moving on to Saco Bay itself, under calm conditions, currents formed a clockwise circulation with slow northward flows nearshore and southward flows near the opening. Under storm conditions, circulation in Saco Bay was comprised of a complex relationship between storm winds, tidal currents, and freshwater plume

dynamics. During flood tides, storm currents turning around Cape Elizabeth surged into the bay, generating a persistent southward flow along the Saco Bay shoreline. This southward flow exited the bay primarily through flooded areas in Biddeford Pool, with some merging back with the open-water southward storm currents via a small channel between Biddeford Pool and Wood Island. During ebb tides, the same southward coastal flow was present, but tidal currents increased the velocity of the Saco River and Nonesuch River plumes, which acted as partial barriers against the storm currents from Cape Elizabeth. As flooding in Biddeford Pool decreased, storm currents exiting the bay increased in the channel between Biddeford Pool and Wood Island.

4.3 Comparison of bay responses

It is important to note the diversity of storm responses along the shoreline of the Saco and Casco Bays. Saco Bay was greatly impacted by storm currents extending from the open boundary, resulting in a far more sensitive system. Surface currents during flood tides were heavily dominated by storm currents to result in a reversed flow nearshore, while during ebb tide discharges from the Saco River and Nonesuch River were strong enough to fend off part of the storm currents from the northeast. In contrast, Casco Bay remained largely controlled by normal tidal signals and river discharge rates, except for Portland Harbor, which saw more dramatic responses to storm-induced alterations to the Presumpscot River and Fore River plumes. In northern Casco Bay, the New Meadows estuary experienced minor increases in mixing and a slightly extended reach of the river plume, reducing the incoming reach of tides during peak storm winds. As for deeper waters in each bay, results were as expected; Casco Bay's barrier islands protected it from most open-water storm currents, allowing for tidal currents to remain dominant. In the following section, it will be shown how sensitivity of the bays to these storm currents played a significant role in determining the effects of SLR experienced by each bay.

5. Bay responses to sea level rise

The 1978 and 2007 events were simulated repeatedly under varying sea level rise scenarios. In each run, the open boundary and initial sea surface heights were increased in 1-foot increments from the baseline scenario to a 7-foot scenario to emulate potential water levels. Utilizing the wetting and drying module of FVCOM, mesh cells in Saco Bay and Casco Bay were classified as either "dry," "intertidal," or "wet." The former (latter) were defined as cells in the mesh, which never became wet (dry) throughout the model's runtime. Intertidal areas were cells that alternated between wet and dry.

5.1 Impact of SLR on bay structure

To quantify the impact modeled SLR had on the storm responses, a baseline understanding of how SLR impacted the shapes of Saco Bay and Casco Bay had to be established. As such, inundation maps were generated for the both storm cases under each SLR scenario, where "inundation zone" refers to the subset of the intertidal zone where bathymetric data indicated that the cell had a digital ground relief value above the MHW. **Figure 8** depicts such inundation zone coverage under the baseline (0 ft) and 7-ft. SLR scenarios.

Saco Bay was particularly vulnerable to flooding in response to SLR, specifically in the Scarborough marshes and around the mouth of Saco River. Every beach along
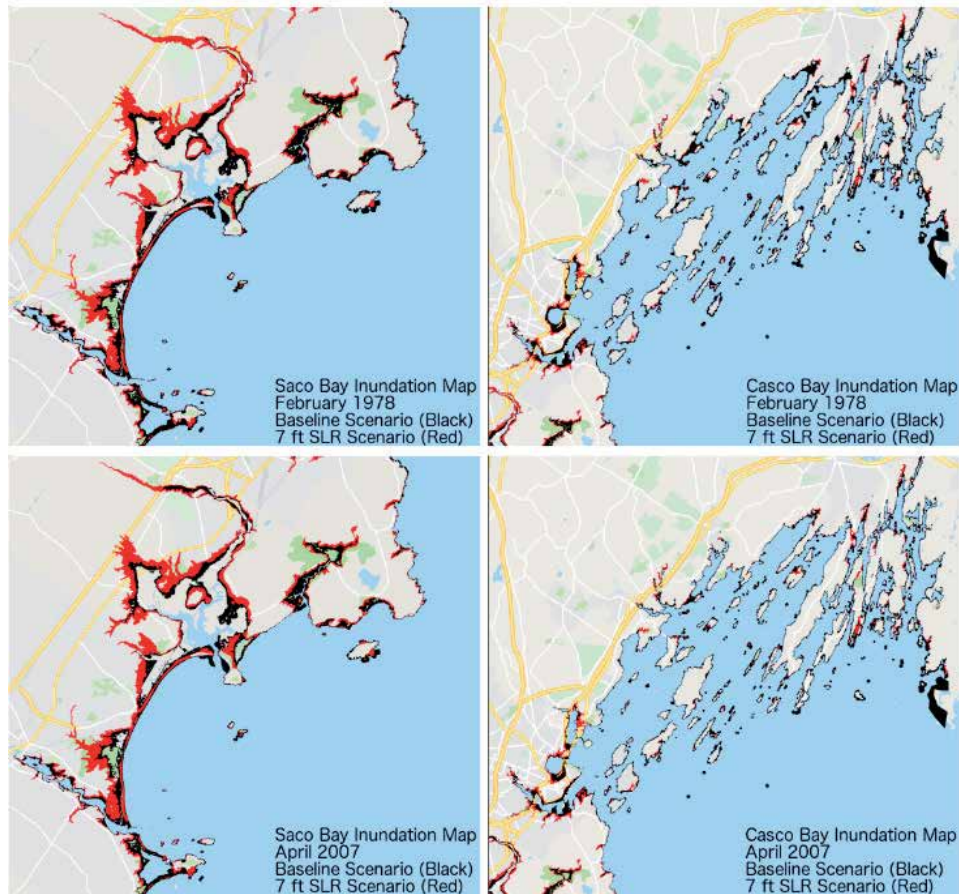
Figure 8.
Inundation maps for the Saco Bay and Casco Bay. Baseline scenario flooding (black) is overlaid by flooding measured in the modeled 7-ft. SLR scenario (black). Inundation cells were identified as the modeled intertidal zone above 0 m MHW.

the bay was completely flooded by 7 ft. of SLR in both storm events, along with the marshes and communities around Goosefare Brook. In contrast, Casco Bay saw less change in inundation zone coverage (relative to the size of the bay) between the baseline and 7-ft. SLR scenarios, primarily isolated to the localized flooding around Portland, where storm-induced flooding spread most noticeably around the mouths of the Fore River and Presumpscot River. The trends of inundation zone expansion can be seen in **Figure 9**, along with the trends of each cell type (dry, wet, and intertidal) against SLR.

It was expected that the inland expansion of the intertidal zone during the 2007 event would mirror that of the 1978 event with a 1-foot "lag" in SLR scenario, as the peak sea level during the 2007 event was roughly 1 foot lower than that of the 1978 event. This lag is clearly visible in the inundation and dry cell trends in both Saco Bay and Casco Bay. Looking closer at the inundation and dry cells, both bays saw a net increase of roughly 20 km^2 in inundation zone coverage from the baseline scenario to the 7-ft. SLR scenario, reflecting an identical drop in dry cell coverage. This 20-km^2 change corresponded to an 18.2% reduction in Casco Bay's dry cell coverage versus a 57.1% reduction in Saco Bay's dry cell coverage. Furthermore, these reductions were not the result of continuously linear trends.

Casco Bay saw a linear drop in dry cell coverage from the baseline to 4-ft. SLR scenario for the 1978 event (baseline to 5-ft. SLR for the 2007 event), before
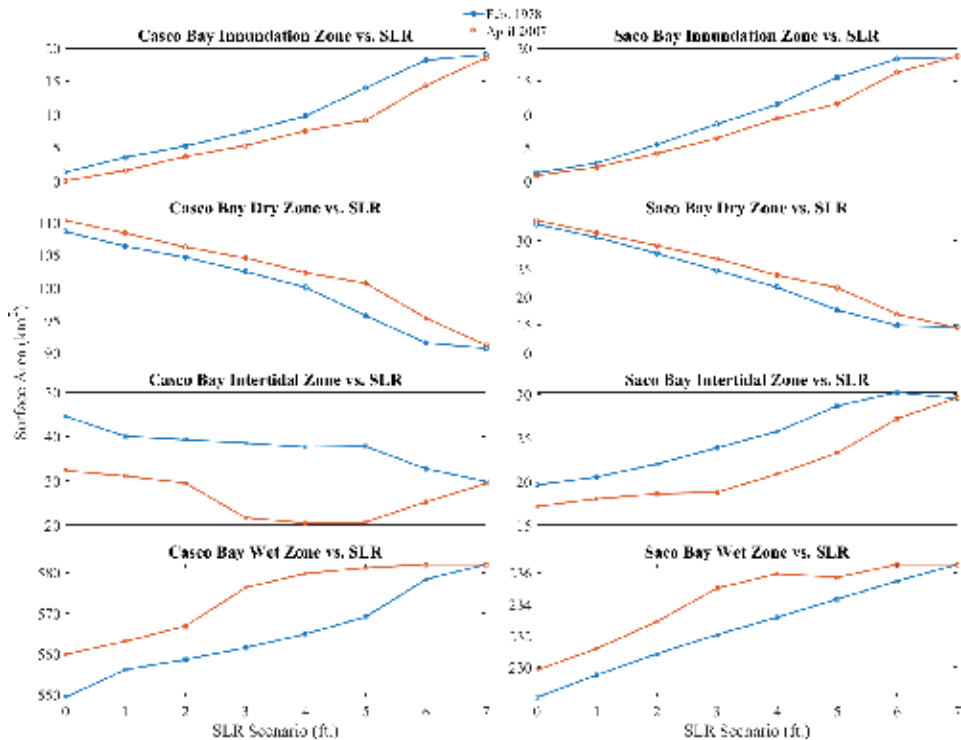
Figure 9.
Cell-state distribution from the FVCOM wetting/drying module vs. SLR during the 1978 and 2007 events in Saco Bay and Casco Bay. Mesh limits were reached in the 7-ft. SLR scenario, causing the zonal distributions in both events to converge.

dropping at a significantly higher rate until the mesh limitations were reached in the 6-ft. SLR scenario (7-ft. SLR for the 2007 event). This "drop off" point was a result of the peak sea level exceeding roughly 13 ft. above MSL, at which point many of the steep coastal slopes in Casco Bay, mainly around Portland Harbor, were overcome, yielding significantly increased flooding. In contrast, Saco Bay's inundation increased at a slightly exponential rate before slowing down following the 4-ft. SLR scenario (5-ft. SLR scenario for the 2007 event).

The intertidal and wet cells of each bay saw far more complex changes in response to SLR. In Casco Bay, there was a significant difference in behavior of the intertidal zone during the 1978 event when compared to the 2007 event. In the 1978 event, after an initial drop of ~5 km^2, the intertidal zone in Casco Bay saw very little change in size until the 5-ft. SLR scenario, at which point the intertidal zone decreased in size by roughly 5 km^2 per 1 ft. of SLR. These drops in intertidal zone coverage were reflected by spikes in wet cell coverage in the 1-ft. SLR and 6-ft. SLR scenarios, resulting from low tides rising above 7.25 and 12.25 ft. above MSL, respectively. For the 2007 event, the wet zone expanded greatly between 2- and 3-ft. SLR, which was accompanied by a sharp decrease in the intertidal zone. The intertidal areas stayed mostly the same between 3- and 5-ft. SLR despite the slight increase of wet zone, which was compensated by the decrease of dry zone. However, between 5- and 7-ft. SLR, the intertidal area expanded largely at the expense of contracting dry zone.

This complex relationship can be better visualized in **Figure 10**. As Casco Bay's coastal slopes are largely characterized by short steps formed by tall shelves, the lower tidal ranges of the 2007 event resulted in low tides being constrained by these
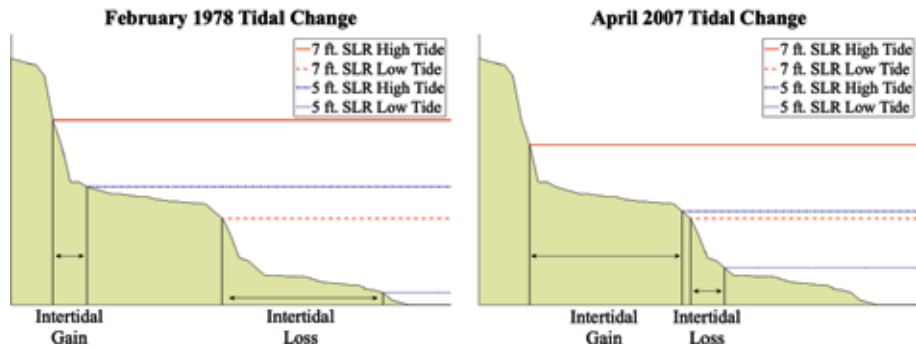
Figure 10.
Sketch of intertidal zones of Casco Bay under the 5- and 7-ft. SLR scenarios. Due to larger tidal ranges in the 1978 event, there was a net loss in intertidal zone coverage, in contrast to a net gain between these scenarios for the 2007 event.

stairs, limiting the change in wet cell coverage across SLR scenarios. In simulations of the 2007 event, the change in wet cell coverage plateaued after the 3-ft. SLR scenario, while dry cell coverage decreased steeply following the 5-ft. SLR scenario, yielding an overall increase in intertidal zone coverage between the 5- and 7-ft. SLR scenarios. In contrast, simulations of the 1978 event yielded far lower low tides, allowing wet cell coverage to increase following the 5-ft. SLR scenario, resulting in a decrease in intertidal zone coverage.

In Saco Bay, wet cell coverage simply increased linearly alongside SLR for the 1978 event, and the intertidal zone also expanded allowed by the much faster rate of decrease of the dry cell coverage. However, the behavior of the wet cell coverage was more dynamic during the 2007 event, largely explained by the relationship between freshwater discharge and sea level around the Scarborough marshes and Nonesuch River. Referring quickly back to the inundation maps (**Figure 8**), one key distinction between the 1978 and 2007 events was that even though the 2007 had lower peak sea level at Portland, the baseline scenario flooding around the Nonesuch River was higher during the 2007 event than that of the 1978 event, suggesting a positive relationship between discharge from the Nonesuch River and localized flooding along the river's edge. Another anomalous behavior occurred after the 4-ft. SLR scenario, where wet cell coverage in the 2007 event slightly decreased by ~1 km^2, contrary to any expected results. This small drop occurred in the Nonesuch River and is likely attributed to a decrease in minimum sea level in the Nonesuch River following an expansion of the channel between Prouts Neck and East Grand Beach during high tides. To explain further, to stabilize the FVCOM model, a limit of 1.5 m/s had to be placed on currents flowing along this channel, which resulted in elevated sea levels during low tide in the Scarborough marshes and Nonesuch River, as the water was unable to empty out from the marsh during ebb. Once the channel was widened following the 4-ft. SLR scenario, the total volume of water carried under the limited currents was increased enough to lower minimum local water level during low tide. The complexity of the relationship between SLR, estuarine dynamics, and intertidal zone structure highlighted by these results further underscores the limitations of generalized predictions on the effects of SLR on a coastline.

5.2 Impact of SLR on bay circulation

Given the dynamic changes SLR yielded on the structure of the two bays, it was reasonable to expect consequential changes in nearshore circulation. Looking first at the storm currents themselves, **Figure 11** depicts the rate of change of vertically

averaged mean current speed at points of interest for each storm across SLR scenarios. Temporal means of currents at all 24 sigma layers were taken within the storm windows and then averaged to produce the values reflected in these plots. Negligible changes to storm currents were witnessed in northern Casco Bay with the exception of a slight increase in slow storm currents at Buoy D0301 during the 2007 event (**Figure 11d**), so the other five chosen points of interest reflect impacts of SLR on storm currents affecting the four freshwater plumes in southern Casco Bay and Saco Bay.

Starting in Portland Harbor (**Figure 11a**), storm currents consistently increased alongside SLR in both storm events, albeit at different rates. The CAB 3 site was chosen to observe trends in both the Presumpscot River and Fore River plumes, as the southward flux of freshwater into the bay from Portland Harbor was located in this channel (**Figure 6**). The 1978 event, while yielding far less freshwater discharge than the 2007 event, saw greater southward storm currents at the CAB 3 site throughout the storm window due to extreme wind speeds. These currents initially decreased in response to the localized increase in flooding around Portland Harbor from the baseline to the 1-ft. SLR scenario, as was discussed earlier (**Figure 9**). Following this drop, as Casco Bay's coastline resisted additional flooding, storm currents began to increase with the higher volumes of water directed through this channel in higher SLR scenarios, though this effect was nonlinear and plateaued quickly. The storm currents at the CAB 3 site in the 2007 event saw a smaller, more linear rise alongside SLR, as storm currents were largely dominated by high discharge rates which remained constant in the SLR simulations.

Moving southward, the storm currents turning around Cape Elizabeth saw a proportionate rise in velocity across SLR (**Figure 11b**), pulling greater volumes of freshwater out of Portland Harbor. This increase in current speed was mostly linear and consistent from the 1- to 7-ft. SLR scenarios for the 1978 event, matching the linear rise from the 3- and 7-ft. scenarios in the April 2007 event. Further offshore to the southeast of Cape Elizabeth at the site of buoy 44007 (**Figure 11c**), the 1978 storm currents saw a more complex response to SLR, while the 2007 event saw no changes at all. The minor (<0.01 m/s) change in current speed from 0- to 4-ft. of SLR in the 1978 event was identified as a small response to the sudden drop in current speed from Portland Harbor following the initial flooding in southern Casco Bay. The increase in storm currents at site 44007 from 4- to 6-ft. of SLR resulted from an increase in southward currents between the barrier islands throughout Casco Bay. This rise was followed by a plateau effect as these islands began to flood, decreasing the effect of SLR on currents within the channels. Following the storm currents into Saco Bay, SLR had a much stronger effect on the dynamics of the Saco River (**Figure 11e**) and the Nonesuch/Scarborough River (**Figure 11f**).

Saco River behaved as expected as SLR increased. The sides of the river flooded rapidly as sea levels rose, resulting in drops in the current speed exiting the mouth of the river. Interestingly, during the low-discharge 1978 event, this drop was largely linear following a small initial spike of 0.01 cm/s, while the 2007 event saw an exponential decay in storm currents as SLR increased, suggesting a nonlinear relationship between river discharge and SLR as factors influencing estuarine storm currents. Nonesuch river, which is renamed to Scarborough River as it enters the Scarborough marshes along the western shore of Prouts Neck (see **Figure 1**), saw the most dynamic changes in response to SLR.

Prouts neck and the beaches around the mouth of the Scarborough River proved to be the most resilient land to flooding in Saco Bay, resulting in few changes to the structure of the river until SLR increased from 3 to 4 ft. for the 1978 event (4 to 5 ft. for the 2007 event). Because of this delayed response, water built up in the Scarborough marshes as SLR increased, negating any potential expected drop in
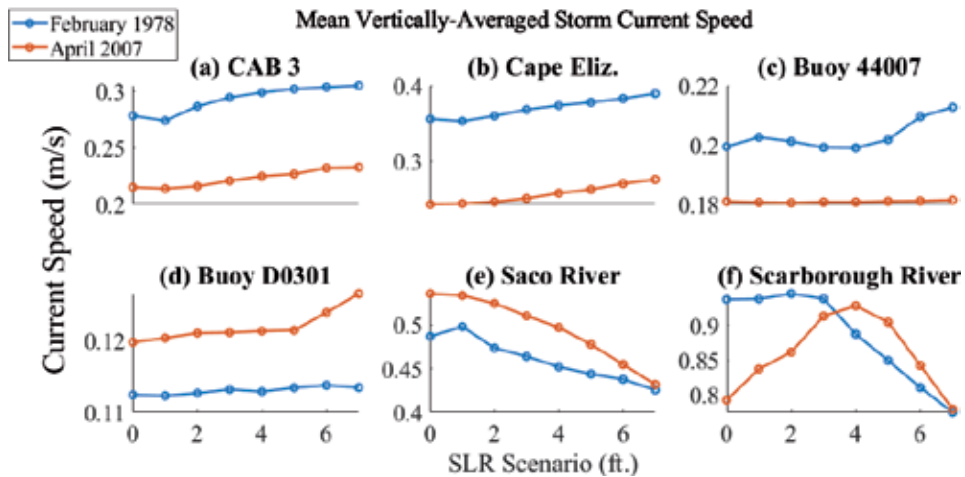
Figure 11.
*Vertically averaged mean current speed vs. SLR within the storm windows at selected sites (see **Figure 1** for locations) for the 1978 and 2007 events. Temporal averages throughout either storm window reflect the impact of SLR on storm-induced plume dynamics.*

current speeds in the 1978 event and resulting in an increase in current speeds aligning with heightened discharge in the 2007 event. Once these shores started to flood, current speed decreased rapidly with SLR, as the constriction point for discharge from the Nonesuch River widened greatly. To fully explain how these differences in storm current response to SLR impacted circulation in the bays, one must look at the resultant changes to plume dynamics following either storm.

Figure 12 was created to show the change in minimum surface salinity (ΔS) between the baseline and 7-ft. SLR scenarios. By plotting minimum surface salinities, we were able to analyze the maximum reach of each river plume and how that reach was affected by SLR. In Casco Bay, the increase in mean storm currents exiting the Fore River and Presumpscot River resulted in further extensions of the combined Fore River and Presumpscot River plumes northeastward toward Broad Sound and southward around Cape Elizabeth for the 1978 event in the 7-ft. SLR simulation. For the 2007 event, flux out of these two rivers due to river discharge decreased dramatically with SLR, as the widened rivers allowed storm currents to dominate freshwater discharge. The end result was a net increase in salinities throughout the Portland Harbor area, as the offshore water was mixed higher up the rivers by storm winds under heightened SLR scenarios.

Saco Bay saw even greater variations in minimum salinity in response to SLR between the two storms, attributable mostly to the icing vs. flooding states of the Saco River and Nonesuch River. For the 1978 event, the inundation zones present in higher SLR scenarios were comprised primarily of offshore high-salinity waters, resulting in a net increase in salinity for the floodwater across the beaches of Saco Bay and large parts of Scarborough marshes except in the Nonesuch River plume. The resiliency of the modeled Nonesuch River was largely influenced in these simulations by mesh limitations; due to an instability issue with FVCOM, the mesh boundaries had to be restricted to 2 m above MSL around this river. Because of this limitation, the model likely underpredicted the full-range up-river mixing of higher-salinity waters into the Nonesuch River.

The stronger river discharge estimated for the April 2007 event resulted in plume water around Prouts Neck, more so in the higher SLR scenarios, as flooding allowed plume waters to flow southward to the eastern shore of Prouts Neck. Interestingly, despite the freshwater discharge from the Saco River being higher in
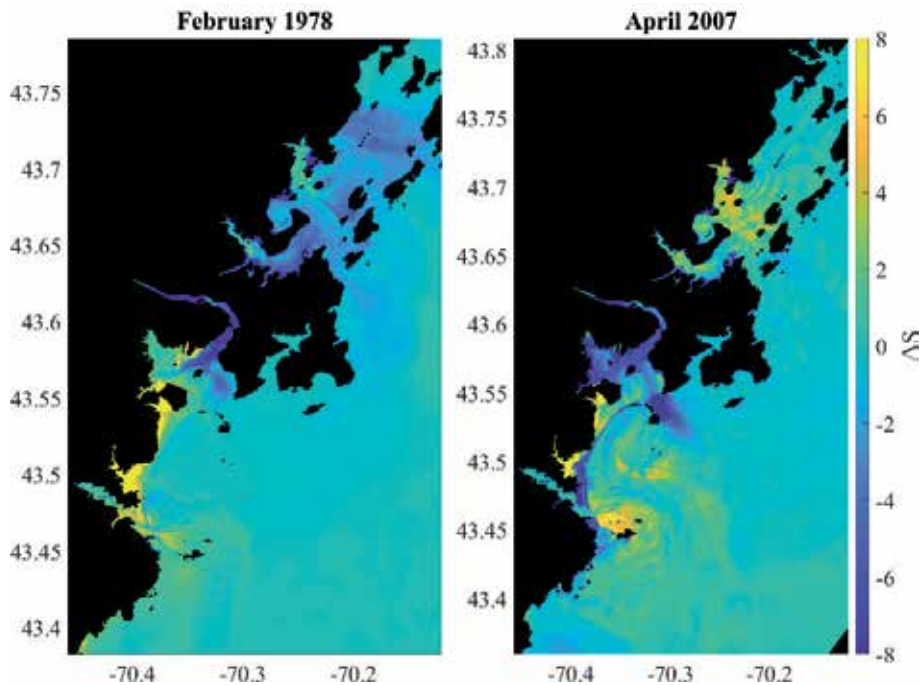
Figure 12.
Map of changes in minimum salinity in response to SLR during the storm windows for the 1978 and 2007 events. Darker colors indicate a decrease in minimum salinity, implying a greater concentration of freshwater with the 7-ft. SLR than the baseline simulation.

the 2007 event than in the 1978 event, the waters just north of Biddeford Pool and around Wood Island saw a large increase in minimum salinity as SLR increased. The reason for this change was the increased SLR resulted in a more northward shift of the Saco River plume that flooded around the mouth of Saco River and the beaches to the north, while the eastward current velocities directed toward Wood Island and Biddeford Pool decreased (**Figure 11e**), hence the higher minimum salinity for the 2007 event at 7-ft. SLR.

6. Conclusions

This study aimed at evaluating the impact SLR would have on responses to major storm events in Saco Bay and Casco Bay in the western Gulf of Maine. A hydrodynamic model was developed to simulate the Blizzard of 1978 and the Patriots Day storm in 2007 under varying SLR scenarios to identify and track modeled storm responses. Inundation maps generated from the model results indicated a nonlinear relationship between SLR and inundation zone coverages, as the diverse slopes of the shoreline played the dominant role in determining the rate of change in inundation. Additionally, shifting circulation patterns and morphing of intertidal zones in response to SLR caused changes where river plumes were directed.

The modeled storm responses in Saco Bay and Casco Bay were primarily influenced by freshwater discharge, storm winds, and coastal structure. The percentage of inundated area changed significantly in Saco Bay under increased SLR scenarios and to a lesser degree in Casco Bay. While total inundated surface area increased in response to increased SLR, the results presented in this model study show that inundation maps generated simply from bathymetry alone do not fully capture the complexities of how SLR will impact the structure of a coastline, since they are

unable to reflect changes in circulation due to such factors as freshwater discharge. Consequently, the relationship between SLR and storm responses adopts the complex interactions between freshwater forcing, wind-induced circulation, and coastal morphology, as the dynamic structural changes experienced by the bays impact the severity of storm responses in a major way.

Many of the past studies reviewed in this paper utilized point-sourced tidal data to generalize the impact of SLR over large areas, but the results of the Saco and Casco model study suggest that there is too much variability in coastal responses to SLR to make such generalizations. Through this study, we have shown how generalizations regarding SLR miss out on the small-scale alterations in coastal structure visible in higher-resolution hydrodynamic modeling. By applying high-resolution 3D modeling techniques to this storm response study, we were able to analyze how morphological changes to a coastline induced by SLR have a direct impact on shallow water circulation and river plumes. In turn, the interactions between river plumes and storm winds were altered, producing dynamic changes in the pattern and magnitude of storm currents.

In effect, this study serves to illustrate that to properly forecast how any estuary will respond to storms under projected sea levels, it will be necessary to incorporate more complex, high-resolution, 3D hydrodynamic models than have been applied in the past. Future studies would also need to simulate more complex shallow water dynamics, such as proper wave propagation along the shoreline, to fully analyze how flood zones would change in response to SLR-induced changes in circulation patterns.

Acknowledgements

Author details

Stephen Moore[1], Huijie Xue[1*], Neal R. Pettigrew[1] and John Cannon[2]

1 University of Maine, Orono, ME, USA

2 NOAA—National Weather Service, Gray, ME, USA

*Address all correspondence to: hxue@maine.edu

IntechOpen

References

[1] Smith JM, Cialone MA, Wamsley TV, McAlpin TO. Potential impact of sea level rise on coastal surges in southeast Louisiana. Ocean Engineering. 2010;**37**(1):37-47

[2] Lin N, Emanuel K, Oppenheimer M, Vanmarcke E. Physically based assessment of hurricane surge threat under climate change. Nature Climate Change. 2012;**2**(6):462

[3] Ezer T, Atkinson LP. Accelerated flooding along the US east coast: On the impact of sea-level rise, tides, storms, the Gulf Stream, and the North Atlantic oscillations. Earth's Future. 2014;**2**(8):362-382

[4] Cannon JW. Northern New England coastal flooding. In: 22nd Conference on Weather Analysis and Forecasting, Park City, UT, Amer. Meteor. Soc., J3A.7A; 2007. Available from: http://ams.confex.com/ams/pdfpapers/123261.pdf

[5] Chen C, Liu H, Beardsley RC. An unstructured grid, finite-volume, three-dimensional, primitive equations ocean model: Application to coastal ocean and estuaries. Journal of Atmospheric and Oceanic Technology. 2003;**20**(1):159-186

[6] Woodruff JD, Irish JL, Camargo SJ. Coastal flooding by tropical cyclones and sea-level rise. Nature. 2013;**504**(7478):44

[7] Cahoon DR. Estimating relative sea-level rise and submergence potential at a coastal wetland. Estuaries and Coasts. 2015;**38**(3):1077-1084

[8] Zervas C. Sea Level Variations of the United States 1854-2006. NOAA Technical Report NOS CO-OPS 053; 2009. 78 pp

[9] Ferreira CM, Irish JL, Olivera F. Quantifying the potential impact of land cover changes due to sea-level rise on storm surge on lower Texas coast bays. Coastal Engineering. 2014;**94**:102-111

[10] Passeri DL, Hagen SC, Medeiros SC, Bilskie MV, Alizad K, Wang D. The dynamic effects of sea level rise on low-gradient coastal landscapes: A review. Earth's Future. 2015;**3**(6):159-181

[11] Slovinsky P. Adapting Maine's Coastal Communities to Sea Level Rise and Storm Surge (2015 State of the Bay Presentation). 2015. https://digitalcommons.usm.maine.edu/cbep-presentations/22

[12] Parris AS, Bromirski P, Burkett V, Cayan DR, Culver ME, Hall J, et al. Global Sea Level Rise Scenarios for the United States National Climate Assessment. NOAA Technical Report OAR CPO-1; 2012. 29 pp

[13] Hill HW, Kelley JT, Belknap DF, Dickson SM. The effects of storms and storm-generated currents on sand beaches in Southern Maine, USA. Marine Geology. 2004;**210**(1-4):149-168

[14] Kelley JT, Barber DC, Belknap DF, FitzGerald DM, van Heteren S, Dickson SM. Sand budgets at geological, historical and contemporary time scales for a developed beach system, Saco Bay, Maine, USA. Marine Geology. 2005;**214**(1-3):117-142

[15] Janzen CD, Churchill JH, Pettigrew NR. Observations of exchange between eastern Casco Bay and the western Gulf of Maine. Deep Sea Research Part II: Topical Studies in Oceanography. 2005;**52**(19-21):2411-2429

[16] Xue H, Du Y. Implementation of a wetting-and-drying model in simulating the Kennebec–Androscoggin plume and the circulation in Casco Bay. Ocean Dynamics. 2010;**60**(2):341-357

[17] Brown HE, Olson DA. Performance of NMC in forecasting a record-breaking winter storm, 6-7 February 1978. Bulletin of the American Meteorological Society. 1978;**59**(5):562-575

[18] Zou Q, Xie D. Tide-surge and wave interaction in the Gulf of Maine during an extratropical storm. Ocean Dynamics. 2016;**66**(12):1715-1732

[19] Chen C, Huang H, Beardsley RC, Xu Q, Limeburner R, Cowles GW, et al. Tidal dynamics in the Gulf of Maine and New England shelf: An application of FVCOM. Journal of Geophysical Research, Oceans. 2011;**116**:C12010. DOI: 10.1029/2011JC007054

[20] Portland M. and DOC/NOAA/ NESDIS/NCEI; National Centers for Environmental Information, U.S. 2019. Portland, Maine 1/3 arc-second MHW Coastal Digital Elevation Model—Data. gov. Catalog.data.gov. Available from: https://catalog.data.gov/dataset/ portland-maine-coastal-digital-elevation-model

[21] Coast.noaa.gov. 2019. Digital Coast Home. Available from: https://coast. noaa.gov/digitalcoast

[22] Tilburg CE, Gill SM, Zeeman SI, Carlson AE, Arienti TW, Eickhorst JA, et al. Characteristics of a shallow river plume: Observations from the Saco river coastal observing system. Estuaries and Coasts. 2011;**34**(4):785-799

[23] Qi J, Chen C, Beardsley RC. FVCOM one-way and two-way nesting using ESMF: Development and validation. Ocean Modelling. 2018;**124**:94-110

[24] Pettigrew NR, Xue H, Irish JD, Perrie W, Roesler CS, Thmoas AC, et al. The Gulf of Maine ocean observing system: Generic lessons learned in the first years of operation (2001-2008). MTS Journal. 2008;**42**(3):91-102

[25] Wallinga JP, Pettigrew NR, Irish JD. The GoMOOS moored buoy design. In Oceans 2003. Celebrating the Past... Teaming Toward the Future (IEEE Cat. No. 03CH37492). IEEE; 2003 Sep 22 (Vol. 5, pp. 2596-2599)

Coastal Altimetry: A Promising Technology for the Coastal Oceanography Community

Xi-Yu Xu, Ke Xu, Ying Xu and Ling-Wei Shi

Abstract

Satellite altimetry has been one of the most important implements for physical oceanographers. The conventional altimeter is best performed over open ocean surface, yet there are many attempts to exploit the potential of altimetry in coastal zone in the last decade. To achieve a high performance for coastal altimetry is a multi-fold effort: the more sophisticated instrument concepts, the smarter onboard trackers, the more expert data editing criteria, the more specific retracking algorithms, the more advanced error correction methods, etc. In this chapter, each of the above aspects is described in detail, and some representative works in the altimetry community are reviewed. Particularly, the coastal altimetry offshore Hong Kong is addressed as a case study to demonstrate the potential of the new technology. In the conclusive session, some prospects for the coastal oceanography community are presented.

Keywords: coastal zone, altimetry, retracker, error correction, Hong Kong

1. Introduction

Coastal altimetry has been one of the key remote sensing technologies in the coastal zone where the effects of a changing climate are most severely felt. For over a quarter century, satellite altimetry technology has been used to routinely monitor sea level changes over the global open ocean, but was largely unexploited in the coastal areas. Indeed, satellite altimetry was originally designed to precisely measure the sea level of the open ocean, yet it has drawn much attention from the coastal community over the past decade.

This chapter addresses the improvements of this intriguing technology. In Section 2, the principles of satellite altimetry and the recent advances of coastal altimetry technology are reviewed, highlighting the coastal-oriental altimetry products which might attract the attention of the coastal oceanographers. In Section 3, a case study is presented at Hong Kong coast to demonstrate the potential of the new technology. This chapter ends with a brief conclusive and prospective section.

2. A brief review of the advances in coastal altimetry

Coastal altimetry has come on to the central stage of the altimetry community. Coastal altimetry workshops (CAWs) are regularly organized (once every 1 or 2

years) for peers to present their recent researches. A book entitled "Coastal Altimetry" was published in 2011 [1], and significant improvements have been made since then. This section attempts to review some important advances in this field.

2.1 Principles of satellite altimetry

"Coastal altimetry" might be much more familiar for the altimetry community than for the coastal community. A very brief background introduction of satellite altimetry would be presented here, and interested readers are encouraged to refer to the elaborate books such as [2, 3].

The concept of the satellite altimetry is straightforward. A nadir-pointing spaceborne radar transmits short pulses and receives the echoes from the earth (usually, sea) surface. The sea level parameters (range between the satellite and sea surface, significant wave height, and backscatter coefficient) are extracted from the echoes via a process called "retracking". The altimetric range can be extremely precisely measured in this way. Meanwhile, the satellite orbit can also be precisely determined. After carefully compensating for a variety of error sources, the surface height relative to an absolute datum (usually the reference ellipsoid) can be accurately retrieved, within no more than few centimeters over open ocean surface.

While the satellite altimetry can be dated back to the 1960s [4], one must admit that the Topex-Poseidon satellite launched in 1992 is a benchmark [5]. Thanks to its unprecedented accuracy, it remolded the knowledge scene of many fields in oceanography, such as ocean circulation, ocean tide, El-Nino, and global climate change. Its successors, Jason series satellites, have been extending the high-quality sea level record incessantly [6–8]. Space agencies of Europe, China, and India are also handling altimetry missions, such as ERS-1, ERS-2, Envisat, Saral, and HY-2 [9–12]. Now a constellation of complementary altimetry satellites (with different orbit sampling strategy) have been formed and abundant data are worthy of exploiting. Nowadays, altimetry is not only a fundamental tool for oceanographers and geodesists, but also an attracting resource for those who research into the fields of coastal zone, Cryosphere and inland waters, etc.

2.2 Difficulties in coastal altimetry

Coastal altimetry is not an easy task. There are a couple of difficulties when extending altimetry technology to coastal zone. Firstly, in the coastal band a few kilometers wide (comparable to the altimeter footprint size), radar echoes are severely contaminated by the nearby land surface, leading to complex waveforms significantly departing from that of open ocean. Things are further complicated by the fact that the geographic and environmental characteristics of the coast (e.g., coastline direction, relief, bathymetry, and rain rate) are extremely diverse throughout the world, and altimetric mission (orbit configuration, on-board tracker, flight direction, etc.) are also different. **Figure 1** shows two examples of waveforms, one over the open ocean (a) and the other over a coastal zone (b). Therefore, a specific process called 'retracking' is widely employed to extract the sea level parameters from these nonstandard waveforms.

Another difficulty is related to the various corrections applied to the altimeter measurements that are usually less accurate at the coast. The most suffered corrections are wet tropospheric delay, ocean tide correction, dynamic atmospheric correction (DAC), and sea state bias. Consequently, most altimeter data near land are flagged as invalid and eliminated from the standard products.
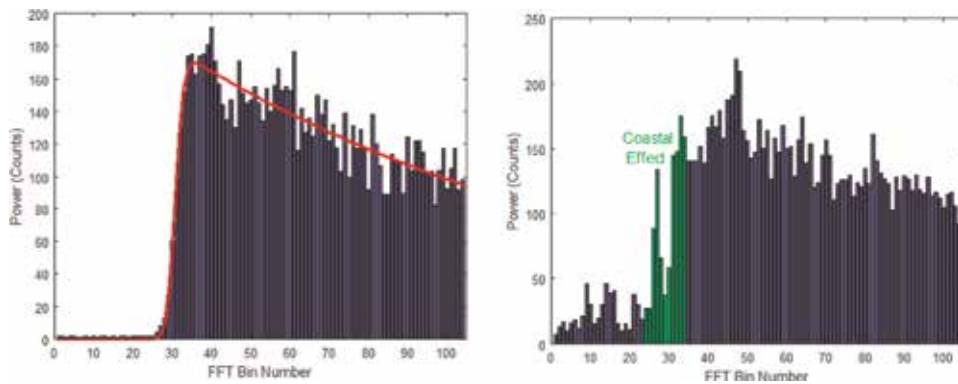
Figure 1.
Examples of typical open ocean waveform (left, the red line corresponds to the fitted Brown model) and coastal ocean waveform (right).

2.3 Review of the current coastal altimetry products

For about a decade, many efforts have been paid by the altimetry community to overcome the above difficulties and exploit altimetry information near the coast. A number of coastal altimetry products were distributed to the community. For the Jason-2 altimeter, the most popular products are (1) X-TRACK developed by LEGOS (Laboratoire d'Etudes en Géophysique et Océanographie Spatiales, France), (2) PISTACH (Prototype Innovant de Système de Traitement pour l'Altimétrie Côtière et l'Hydrologie, Mercier et al. [15]) developed by CLS (Collecte Localisation Satellites, France), and (3) ALES (Adaptive Leading Edge Sub-waveform, Passaro et al. [14]) developed by NOC (National Oceanography Centre, UK). PEACHI (the Prototype for Expertise on Altimetry for Coastal, Hydrology and Ice, PEACHI) is a sister product of PISTACH while it currently focuses on the Saral/Altika. Corresponding coastal altimetry products are based on dedicated analysis of the nonstandard waveforms and/or sophisticated coastal geophysical corrections [13–15].

X-TRACK is a relatively concise product but does not apply waveform retracking, while ALES and PISTACH are extended products to SGDR (Sensor Geophysical Data Record which includes the waveform distributed by AVISO officially), applying waveform retracking, conserving the official SGDR terms, and annexing new parameters (retracking results and geophysical corrections). ALES does not provide improved geophysical correction, while PISTACH provides 2–3 candidate solutions for almost every geophysical correction term.

X-TRACK is a level 3 (L3) product: using the GDR data and state-of-the-art altimetry corrections, along-track sea level time series projected onto reference tracks (points at same locations for every cycle) are computed at 1-Hz (∼6 km along-track resolution). It is simple to use and is based on improved geophysical corrections near the coast (see [6] for details), but its current version only includes the Jason-2 official retracker dedicated to open ocean conditions.

For the geophysical corrections, the advantages of X-TRACK are (1) a more robust median-based editing criterion for the ionosphere correction. (2) A Loess filter (locally weighted scatter plot smoother using a quadratic polynomial model) for the sea state bias correction. (3) A new set of tide solution based on empirical harmonic analysis of the altimetry data.

PISTACH outperforms its counterparts in waveform classification and wet troposphere correction. The decontaminated wet troposphere correction approach is based on the corrected brightness temperature of the on-board radiometer. Another

improvement of PISTACH may be the dedicated sea state bias correction algorithm at the coast, albeit not very reliable due to limited dataset.

ALES simply focuses on the design of an adaptive retracker that can be applied to a variety of waveforms and reduces inconsistence derived from the bias among different retrackers.

The schemes of the three main state-of-the-art coastal altimetry products for Jason-2 satellite altimeter are tabulated in **Table 1**.

2.4 Altimeter waveform processing

The essential part of the altimetry processing is the so-called "waveform retracking". "Waveform", as shown in **Figure 1**, records the amplitude of the earth surface echo as a function of time delay. Due to the difference of contexts or traditions, the x-axis of a waveform can be time, frequency, or range, but the three items above can be transformed to each other by simple scaling factors. "Retracking" is the process of extracting useful parameters (range, amplitude, and sometimes significant wave height) from the waveform. The coastal waveforms show very diverse pattern, and it is impractical to find a unique retracker that performs best for every waveform, so it is necessary to classify the waveforms before retracking.

2.4.1 Waveform classification

The classification methodology either relies on statistical characteristic analysis, or on machine learning skills such as neutral network. One of the earliest works on

Product	X-TRACK	ALES	PISTACH
Affiliation	LEGOS-CTOH	NOC (UK)	CLS
Reference	Birol et al. [13]	Passaro et al. [14]	Mercier et al. [15]
Style	Concise	Similar to SGDR (CGDR)	Similar to SGDR (IPC)
Coastline model	GSHHS & R. P. Stumpf	GSHHS	GSHHS
Waveform classification	NO	NO	16 classes
Land cover	NO	NO	GLOBCOVER (but seems all with default value)
Waveform retracking	NO	ALES Algorithm	ICE1 + ICE3 + OCE3 + RED3
Ocean tide	FES12 + 73 empirical harmonic constants	=GDR	GDR + GOT 4.7
Wet troposphere	composite correction (ECMWF)	=GDR	composite correction or decontaminated correction
Sea state bias	Loess filtering + missed data interpolating	=GDR	=GDR or New OCE3 model
Geoid	NO	No	GDR + EGM2008
Mean sea surface	MSS CLS01V1	DTU10	GDR + GOCINA
Mean topography	CLS09 (be updated soon)	No	Rio 05 + Rio07 over MedSea
Bathymetry	NO	No	DTM2000.1 + WebTide, Etopo2v2

Table 1.
Review of the three main coastal altimetry products for Jason-2 satellite altimeter [13–15].

waveform classification was carried out by Berry et al. [16]. They set up an expertise system to classify the ERS-1 geodetic mission waveforms over ocean, coast, ice, desert, forest, and land. Their interests lied in the land and forest and their objective was to set up a digital elevation model (DEM) with accuracy from one meter (over plain or desert) to several meters (over plateau).

The official Envisat altimeter ground segment classifies the waveform into four types: ocean, ice sheet, glacier, and sea ice. There is no coastal-oriented retracker, but coastal waveforms are regarded as certain ice types. PISTACH product classifies the waveform into 16 classes, including a "doubt" class (see **Figure 2**). For each class, a certain retracker is assigned [15].

Maybe the most complex classification strategy is the one carried out by Schwatek et al. [17]. They classified the waveform into more than 50 classes. Even over the open ocean they have a dozen of classes. It may be somewhat unnecessarily complicated. Anyway, waveform classification and retracking should be a complete suite of solution for waveform processing.

2.4.2 Waveform retracking

The current waveform retrackers can be split into two groups: the model-based ones and model-free ones.

2.4.2.1 Model-based retrackers

In model-based retrackers, the parameters of interest (range between satellite and sea surface, significant wave height, and backscatter coefficient) are estimated by fitting the waveform to a certain model via a maximum likelihood estimation (MLE) approach. What really counts is the choice of the model.
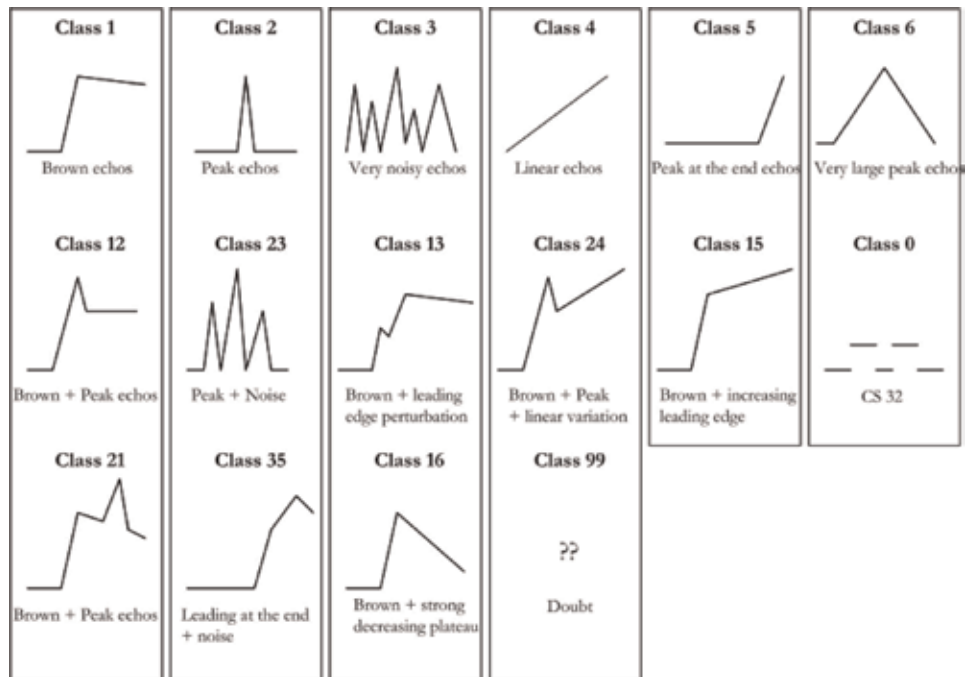
Figure 2.
Schematic representation of the waveform classes within the PISTACH processing [15].

Although the Brown [18] or Hayne [19] model is pretty successful over open ocean surface, there is little theoretic echo model elsewhere. Maybe the most universal coastal waveform model is the one proposed by Enjolras et al.:

$$P_r(t) = A \left[\iint\limits_{S \in water} S_r\left(t - \frac{2h}{c}\right) \frac{G^2(\theta)}{h^4} \sigma_{water}(\theta) dS + \iint\limits_{S \in land} S_r\left(t - \frac{2h}{c}\right) \frac{G^2(\theta)}{h^4} \sigma_{land}(\theta) dS \right] + P_0$$

(1)

In the model the return power is expressed as the weighting average of the water surface echo and land surface echo. This model is not very practical: the geometry of the coastline, the relief, the nature of the terrain, etc., in a word, all characteristics of the coast that are extremely diverse all over the world. Therefore, it is difficult to determine the a priori parameters in the model.

There are also a couple of models, initially developed for ice surface, which are popularly used in coastal retrackers, such as the so-called 5β model [20] and E model [21], with the following expressions:

$$P_r(t) = \beta_1 + \beta_2 \Phi\left(\frac{t - \beta_3}{\beta_4}\right)(1 + \beta_5 Q) \text{ 5β model}$$

(2)

$$P_r(t) = \beta_1 + \beta_2 \Phi\left(\frac{t - \beta_3}{\beta_4}\right) \exp\left(-\beta_5 Q\right) \text{ E model}$$

(3)

where:

$$Q = \begin{cases} 0 & t < \beta_3 + \beta_4/2 \\ t - \beta_3 - \beta_4/2 & t > \beta_3 + \beta_4/2 \end{cases}$$

(4)

The two models are both reduced forms of Brown model, except permitting a negative mispointing angle. When $\beta_5 Q << 1$, the two models are essentially the same. The official Envisat ICE2 retracker is based on a simplified version of 5β model, where β_5 is always set to 0. Obviously, their physical mechanisms are based on open ocean surface and are often not suitable for coastal waveforms.

Hamili et al. [22] proposed a "Brown + Gaussian peaky (BGP)" model for the surface where a strong land scatter is presented in a Brown background. This model is suitable for the coastal zone with vertical structures behaving like corner reflectors.

As have been noted, the most cumbersome problem in coastal waveform is the contamination of land in the radar footprint. Fortunately, usually the contamination does not present in the entire waveform. One can retrack a portion of the waveform bins which are free from land contamination (this portion is called sub-waveform, e.g. [23–25]). After rejecting the contaminated bins one can still retrieve useful information.

In applying the sub-waveform technology, the most important issue is to determine the extent of a sub-waveform. The algorithms designed by PISTACH (RED3 and ICE3 [15]) define a sub-waveform with a fixed range: from the 22nd to the 52nd bins. Therefore no more than 1/3 of the 104 bins (for Jason-2) or 128 bins for (Envisat and HY-2A) are included in the retracker. Consequently, for the land-free waveforms, the precision is worse than the traditional retrackers such as MLE3 and MLE4. ALES can be regarded as an improved version of RED3, in which the

sub-waveform extent is dependent on the significant wave height (SWH). As a consequence, under high sea state conditions, the sub-waveform can cover almost the entire waveform and is difficult to eliminate the contaminated bins.

In Xu et al. [26], a new strategy was proposed in which the extent of the sub-waveform was identified by the "differential spectrum". For the Brown waveforms, the neighboring bins are unlikely to change rapidly except for the leading edge, so if there are land-contaminated bins, the corresponding differential spectrum will show a peaky pattern. The neighboring bins can thus be flagged as invalid ones in the retracking procedure. This strategy has been tested on HY-2A altimeter waveforms and has made significant improvement.

2.4.2.2 Model-free retrackers

The model-free retrackers (or empirical retrackers) do not assume a priori surface features. It can provide robust estimator regardless of physical background. The most famous model-free retracker is the OCOG (Offset Center Of Gravity) retracker that was proposed by Wingham et al. [27]. The idea is to approximate the waveform envelope to a rectangle shape, to find the center of gravity of the rectangle, and to subtract the half of the rectangle width (**Figure 3**) from the center of gravity:

$$t_{COG} = \frac{\sum_{i=1}^{N} i V_i^2}{\sum_{i=1}^{N} V_i^2} \quad A = \sqrt{\frac{\sum_{i=1}^{N} V_i^4}{\sum_{i=1}^{N} V_i^2}} \quad W = \frac{\left[\sum_{i=1}^{N} V_i^2\right]^2}{\sum_{i=1}^{N} V_i^4} \quad t_0 = t_{COG} - W/2 \qquad (5)$$

Another retracker is the simple threshold retracker. Finding the bin with the maximum power, say, M, and finding the first bin whose power exceeds $M^*p\%$, where $p\%$ is a threshold percentage.

OCOG retracker is the most robust retracker, but it has been shown that OCOG retracker usually has relatively large bias (even larger than the simple threshold retracker). On the other hand, the threshold retracker can generate unexplainable results occasionally. The modified threshold retracker adopts the advantages of both retrackers. It uses A in Eq. (5) rather than M as the maximum bin power. The modified threshold retracker is the most widely used model-free retracker. The official Envisat ICE1 retracker and PISTACH ICE1 and ICE3 retrackers all belong to modified threshold retrackers.

Although it is pretty easy to implement, the most troublesome issue of the (modified) threshold retracker is to determine the value of $p\%$. Apparently 50% is reasonable, but various studies gave different values. Tseng et al. [29] pointed that
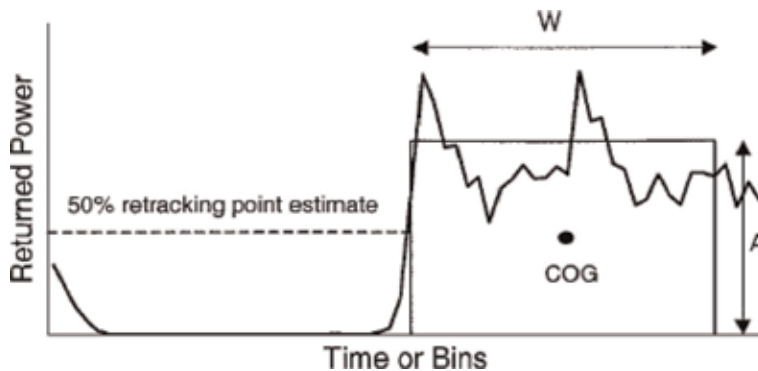
Figure 3.
Principle of an OCOG algorithm (from [28]).

20% is better, and the PISTACH ICE retrackers preferred p = 30% [15]. It seems that the threshold somewhat depends on the characteristics of the study area.

Another model-free algorithm is the curve spline interpolation. It has been mentioned briefly by a couple of authors without details. The idea is to interpolate between neighboring bins when implementing the threshold retracker. It can unlikely bring significant difference from the threshold retracker.

2.4.2.3 Retracking strategy

Scientists have been debating for many years on the retracking strategy. Someone insisted that applying one single algorithm for all kinds of waveforms is a better choice. For instance, ALES developers use their retracker even over open ocean surface, and their analysis shows that the precision of ALES is not substantially worse than the official MLE4 over open ocean surface. On the other hand, PISTACH carried out a waveform classification before retracking. The classification is primarily dependent on the waveform pattern and secondarily on auxiliary information such as land cover model. Different retrackers are implemented for different waveform classes.

Our opinion is that a classification may be preferable because the waveforms have a large variety. A specialized algorithm for a certain waveform would improve the retracker precision significantly. There may be bias between different retrackers and inconsistency in the retracker transition. If the bias between retrackers is not compensated, there might be unexplained jumps in the sea level measurements, and this is the reason why some researchers are inclined to use one unique retracker. We hold that this problem can be solved either by simulative analysis or by calibration.

2.5 Geophysical corrections at the coast

The geophysical corrections near the coast also need specific considerations. Many terms of the geophysical corrections have larger uncertainty at the coast than over the open ocean.

2.5.1 Atmospheric propagation corrections

The most uncertain error source comes from the wet tropospheric correction because the onboard radiometer suffers severely from land contamination in the coastal area. A simple but effective approach is to extrapolate a model-based correction (using, for example, atmospheric reanalysis data from the European Center for Medium-Range Weather Forecasts, ECMWF), but the corresponding spatial resolution is relatively low for coastal applications. Other approaches include an improved radiometer-based correction accounting for the land contamination effect [30], or the computation of GNSS-derived Path Delay (GPD, Fernandes et al. [31]).

Concerning the ionospheric correction, the imperfect coastal altimeter range measurements lead to significant errors, generating outliers in the correction values. The median + MAD (mean absolute bias) criterion is more preferable than the mean + standard deviation criterion, because the outliers are easier to detect and remove. The along-track profile of ionospheric corrections is further spatially low-pass filtered with a cutoff frequency of 100 km.

2.5.2 Sea state bias

Another important correction is the sea state bias (SSB). The SSB depends on the retracking algorithm, because it contains the tracker bias. A careful analysis showed

that for Jason-2 GDR products, the SLAs obtained from MLE3 and MLE4 retrackers have large bias. From a statistical analysis using cycles 1–238 for a couple of altimeter passes over the open ocean, we obtained: $SLA_{MLE3} - SLA_{MLE4}$ = +2.3 cm. Near the coast, this bias appeared to be even larger and even more critical as it is not constant. **Figure 4** shows both MLE3 and MLE4 SSB corrections as a function of SWH for an arbitrary pass (cycle 16, pass #153). MLE3 SSB has a clear bias (∼+3 cm) relative to MLE4 SSB. Moreover, MLE3 SSB seems to have more outliers, in particular near the coast. The bias observed between MLE3 and MLE4 sea level estimates mainly corresponds to a bias in the SSB corrections.

Deeper investigation showed that the MLE3 SSB outliers are often related to large altimeter waveform-derived off-nadir angle estimation values [32], which probably suffer from errors given the good attitude control of Jason-2 satellite. For this reason, we adopted the MLE4 SSB in the computation of all SLAs, resulting in a relative bias <1 cm for all retrackers.

2.5.3 Ocean tide and DAC

The coastal ocean tide corrections, provided by global models, are also far from accurate. There are two families of tide solutions in most altimetry products: the family of the Goddard Ocean Tide (GOT) models developed by Ray et al. [33], and the family of the Finite Element Solution (FES) models developed by Lyard et al. [34].

Ray compared different tide solutions against 196 shelf-water tide gauges and 56 coastal tide gauges. Their accuracy was characterized by the RSS (root sum square) error of the eight main tidal constituents (Q1, O1, P1, K1, N2, M2, S2, and K2). For the shelf-water gauges, the accuracy of GOT4.8 was 7.04 cm (European coasts) or 6.11 cm (elsewhere), while the accuracy of FES2012 was 4.82 cm (European coasts) or 4.96 cm (elsewhere). For the coastal tide gauges, the accuracy of GOT4.8 and FES2012 was 8.46 and 7.50 cm, respectively [35]. In comparison, the accuracy of GOT4.7 and FES2004 in shelf-water was 7.77 and 10.15 cm, respectively. These results illustrate the significant improvement in coastal ocean tide solution during the last decade.
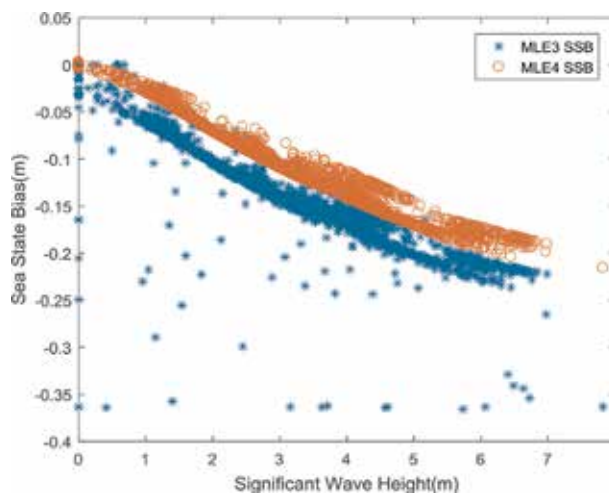
Figure 4.
SSB difference with respect to the significant wave height (SWH).

3. Case study offshore Hong Kong

In this section, Hong Kong coastal zone is chosen as an example to demonstrate the methodology and potential of the coastal altimetry technology. We focus on Jason-2 data here, and other altimetry missions like HY-2 can also be assimilated to achieve denser coverage and cross validation. To exploit the potential of the current endeavors in coastal altimetry, the three products aforementioned are merged and evaluated.

3.1 Study area

Hong Kong (HK) is located just south of the Tropic of Cancer. The climate displays clear seasonal variations. The southwesterly/northeasterly monsoon results in warm wet summers and cool dry winters. HK also frequently suffers from typhoons. On the western side of the HK island flows the Zhujiang River (Pearl River), which brings abundant freshwater, giving rise to a high salinity (hence, sea water density) gradient. All these factors impact significantly on the regional sea level variations.

The HK coast has an extremely complex geomorphology. As shown in **Figure 5**, many tiny islands lie within the altimeter footprints. Therefore, the corresponding altimeter and radiometer measurements are severely contaminated by land effects. This makes this area particularly relevant for analyzing the performances of coastal altimetry data.

The HK coastal topography is more than irregular. Despite a narrow band between 21.8°N and 22°N, where the depth is steeply falling down to ~ -60 m, the study area has very shallow waters. We can thus expect complex local tides and currents, which can influence sea level variations.

3.2 Data sets

3.2.1 Jason-2 altimetry products

The time span in this study covers 6.5 years: from July 2008 to December 2014. The coastal Jason-2 products analyzed in this study are X-TRACK, ALES, and PISTACH.

The retrackers available in the different L2 products are summarized in **Table 2**. The standard GDRs include two solutions: MLE3 and MLE4. The mechanisms of these two retrackers are similar: fitting the waveform to a Brown model [18] based on the MLE (essentially, nonlinear least squares) techniques. MLE3 estimates three parameters: epoch (i.e., altimetric range), significant wave height (SWH), and amplitude (i.e., backscatter coefficient), while MLE4 also retrieves the square of off-nadir angle. The PISTACH products provide four retrackers: OCE3, RED3, ICE1, and ICE3 [15]. OCE3 is essentially the same as the MLE3. ICE1 is a modified threshold retracker. RED3 and ICE3 are the sub-waveform counterparts of OCE3 and ICE1, respectively. ALES is an improved version of RED3, in which the sub-waveform length can vary from 39 bins (for SWH = 1 m) to 104 bins (i.e., the entire waveform, for SWH ≥17 m).

In PISTACH and X-TRACK, state-of-the-art geophysical corrections other than those of the official GDR are provided. For X-TRACK, the ocean tide solution and the DAC are provided individually, while in PISTACH, two to three values are given for each correction. Different sets of correction terms obviously lead to different coastal sea level estimates.
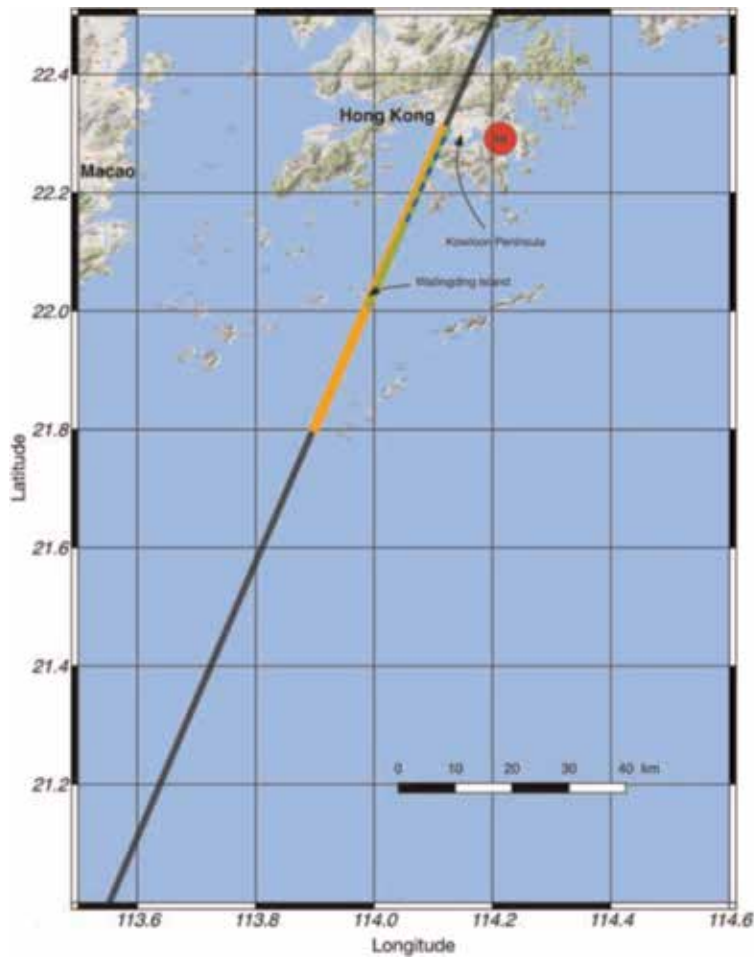
Figure 5.
Map showing the study area, the selected Jason-2 pass 153 (black and colored line) and the Quarry Bay tide gauge (red circle) located ~10 km away from the Jason-2 pass.

Retracker	Product	Idea	Sub-waveform	Comments
MLE4	(S)GDR	Brown model	No	Official standard retracker.
MLE3	(S)GDR	Brown model	No	
OCE3	PISTACH	Brown model	No	Same as MLE3
RED3	PISTACH	Brown model	Fixed: bins: t_0 + [−10:20]	Simplified version of ALES
ALES	ALES	Brown model	Adaptive to the SWH	Two-pass retracker
ICE1	PISTACH	Modified threshold	No	
ICE3	PISTACH	Modified threshold	Fixed: bins: t_0 + [−10:20]	

Table 2.
Overview of different retrackers applied in different altimetry products.

3.2.2 Tide gauge data

The Quarry Bay tide gauge (located at 114.22°E, 22.28°N) regularly measures sea level with an accuracy of ≤1 cm and is well calibrated every other year [36]. The

tide gauge lies near the northern coast of the HK Island, separated from the Kowloon Peninsula by the Victoria Harbor (see **Figure 5**), where ~95% of the shoreline is shaped by human activity [37]. Thus, sea level on this area is expected to be intensively influenced by anthropogenic activities. Hourly tide gauge data are archived and distributed by the Sea Level Center of the University of Hawaii (https://uhslc.soest.hawaii.edu).

A harmonic analysis was first applied to the tide gauge data in order to remove the tidal signals from the sea level time series. A bias (defined as the time-averaged sea level value) was also removed to make the sea level anomaly (SLA) consistent with the altimetry data. Finally, the hourly tide gauge data were interpolated to the Jason-2 satellite overhead time. The tide gauge-based sea level time series interpolated to the closest Jason-2 observations is shown in **Figure 6**. A large seasonal cycle due to the monsoon can be observed, modulated by high-frequency variations up to several tens of cm. A peak in the tide gauge sea level time series can be noticed at cycle 228. It is caused by a storm surge associate d with the Typhoon Kalmaegi that angrily attacked on the HK coast before sunrise on 16 September 2014. The Jason-2 altimeter flew over the HK area at 3:45 am (local time) on that day, and the peak captured the typhoon event. Although it would be quite valuable for the storm surge investigation, in our analysis this peak was eliminated as an outlier.

3.3 Methodology

3.3.1 Altimetry data processing

As indicated above, current coastal altimetry products differ in terms of content. Therefore, in the beginning of the processing the different data sets were merged to obtain homogeneous variables for further comparison. Because there is no waveform data in PISTACH, we used the waveforms provided in ALES and merged PISTACH and ALES using the measurement time common to all products. We also projected all the along-track, cycle-by-cycle L2 data onto the X-TRACK 1-Hz reference grids to benefit from the X-TRACK improved corrections.

Once all the propagation and geophysical corrections are removed, the sea surface height (SSH, i.e., the sea level referred to a reference ellipsoid) can be deduced from the altimeter range. If we further remove a mean sea surface in order to
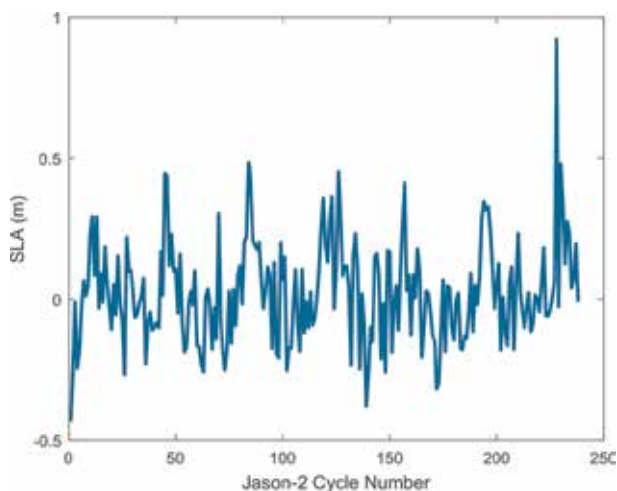
Figure 6.
HK tide gauge sea level time series (in meters) interpolated to Jason-2 observations.

eliminate the influence of the geoid undulation, the sea level anomaly (SLA) can be obtained. In this study, we use SLA data, computed as follows:

$$SLA = H - R - \Delta R_{iono} - \Delta R_{dry} - \Delta R_{wet} - \Delta R_{ssb} - \Delta R_{tide} - \Delta R_{DAC} - MSS \quad (6)$$

In Eq. (6), H is the satellite height, R is the altimeter range, ΔR_{iono}, ΔR_{dry}, and ΔR_{wet} are the ionospheric, dry, and wet tropospheric corrections, respectively, ΔR_{ssb} is the sea state bias, ΔR_{tide} is the tide correction (sum of the ocean tide, pole tide, and solid Earth tide), ΔR_{DAC} is the dynamic atmospheric correction, and MSS is mean sea surface.

At the coast, R is often not directly available, so it can be derived as follows:

$$R = T + E \times (c/2) + D + M + 0.180 \quad (7)$$

where T is the onboard tracking range, E is the retracked offset (with time dimension), "$c/2$ (c being the light velocity)" is the scaling factor from time to range, D is the Doppler correction, M is the instrument imperfection bias [38, 39], and 0.180 is a bias (in meters) due to wrong altimeter antenna reference point [40].

In this study, SLA time series are computed using the altimeter ranges by six retrackers: ALES, MLE3, MLE4, RED3, ICE1, and ICE3. Eq. (7) was used to compute R in the first step, and then Eq. (6) was applied to derive the SLA. To validate our calculation method, we compared our MLE4 SLA with the equivalent official "ssha" parameter in the GDRs and found a very good consistency.

3.3.2 Sea level data analysis

After generating the SLA time series, useful oceanography information can be retrieved. Because of the presence of monsoon, the annual and semi-annual signals are both significant near the HK coast. Therefore, to the first order, SLA variations can be modeled as follows:

$$
\begin{aligned}
SLA(t) = {} & a_1 \cos\left(2\pi t / T_{year}\right) + a_2 \sin\left(2\pi t / T_{year}\right) \\
& + a_3 \cos\left(4\pi t / T_{year}\right) + a_4 \sin\left(4\pi t / T_{year}\right) + a_5 t + a_6 + \varepsilon(t)
\end{aligned}
\quad (8)
$$

where T_{year} = 365.2425 days, $\varepsilon(t)$ is the residual SLA, and a_1 to a_6 are the regression coefficients to be estimated. The estimation uncertainty of the coefficients can be determined from the square root of the diagonal elements in the covariance matrix of the coefficient vector. The linear trend can be inferred from a_5 annual/semi-annual amplitude, and phase can be deduced from a_1 to a_4:

$$A_{annual} = \sqrt{a_1^2 + a_2^2}; \quad A_{semi-annual} = \sqrt{a_3^2 + a_4^2} \quad (9)$$

$$\Phi_{annual} = arctan(a_2/a_1); \quad \Phi_{semi-annual} = arctan(a_4/a_3) \quad (10)$$

3.4 Results

Some results are reported here, in which the sea level for a certain cycle is the average of all the valid measurements within ≤10 distance from the coast. Interested readers can refer to [41] for more details.

3.4.1 Solutions derived from the different Retrackers

For each retracker, we computed a spatially averaged 20-Hz SLA time series as well as the associated 20-Hz noise level (defined as the standard deviation of

the 20-Hz SLA series). ALES solution provides the lowest noise level after editing, and MLE4 is slightly less noisy than MLE3. Concerning the three experimental retrackers used in PISTACH, ICE3 has the lowest noise level, and RED3 is slightly less noisy than ICE1.

Sea level trends of are summarized in **Table 3** (except for OCE3 in PISTACH, which is the same as MLE3). As a reference, after correcting for VLM, we find a trend of +5.5 ± 2.0 mm/yr. at the tide gauge site.

MLE3 and ALES trends are both close to the tide gauge trend (within 0.5 mm/yr). The trends estimated from MLE4 are slightly lower than for ALES and MLE3 but the difference is within the error bar. The trends deduced from the PISTACH retrackers disagree significantly with the tide gauge trend: both ICE3 and RED3 show unrealistic large values (>+5 cm/yr), while ICE1 shows a negative trend of −2 cm/yr. The ICE1 retracker may be inherently not accurate enough to derive trends, but ICE3 and RED3 data surprisingly display large jumps of about +20 cm. This would severely influence the corresponding sea level trend estimates. In the remaining part of the study, we concentrate on MLE3, MLE4, and ALES which, in the context of our study, appear to be the best available retrackers for Jason altimetry.

3.4.2 Coastal seasonal signal along the Jason-2 pass

The amplitude and phase of the seasonal signal are also computed for all sea level time series. The results are shown in **Table 4**. The altimetry annual phases lie around 340° and are significantly larger than the tide gauge-based phase. Amplitudes are also slightly larger. The semiannual phases lie around 240° and are very close to the tide gauge-based phase. Amplitudes are slightly smaller. We cannot exclude the possibility that there is some local seasonal signal at the tide gauge site.

3.4.3 Relative performances of MLE4, MLE3, and ALES near Hong Kong

The sea level residuals obtained after removing the trend and seasonal signal are shown in **Figure 7** for MLE3, MLE4, ALES, and the tide gauge data. A 3-month low pass filter was applied to the different SLA time series to reduce the intrinsic 59-day erroneous signal discovered in Jason altimetry missions [42, 43]. The standard deviations of the altimetry SLA residuals with respect to the tide gauge residuals,

Retracker	ALES	MLE3	MLE4	ICE1	ICE3	RED3
Linear trend and uncertainty (mm/yr)	+5.9 ± 1.5	+5.0 ± 1.6	+4.2 ± 1.6	−29.1 ± 2.4	+57.5 ± 2.3	+55.3 ± 2.1

Table 3.
Estimated linear trend and associated uncertainty (mm/yr) as a function of sea level data source and case.

Data source	Annual	Semiannual
ALES	13.05/344	6.03/235
MLE3	13.29/338	6.17/241
MLE4	12.96/339	6.02/236
Tide gauge	11.46/311	7.62/236

Table 4.
Estimated annual/semiannual amplitude (cm) and phase (degree) as a function of sea level data source and case.
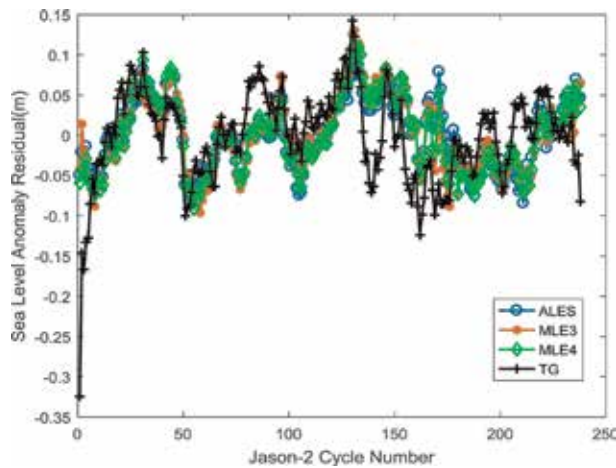
Figure 7.
Detrended and deseasoned SLA time series based on ALES, MLE3, and MLE4, with 3-month smoothing (tide gauge SLA—Noted TG—Is shown as reference).

SLA series	ALES	MLE3	MLE4
Agreement	5.12	4.82	4.88

Table 5.
Deseasoned and detrended SLA standard deviation w.r.t. tide gauge sea level (cm).

before and after the 3-month smoothing, are given in **Table 5**. The improvement due to the smoothing is significant, the standard deviations decreasing by more than 50%. The consistency between the altimetry and tide gauge residuals is about 5 cm, which is encouraging given that the study area is quite complex. ALES SLA has a slightly larger standard deviation with respect to tide gauge sea level.

4. Conclusions and prospective

In this paper, a promising technology: coastal altimetry is described in many facets. The advances in the last decade are reviewed, especially on the coastal waveform processing. In the Hong Kong offshore case study, we find that the coastal sea level trend is about twice as much as the one observed further offshore (which can be inferred as +2.7 mm/yr. from the ESA Sl_CCI product [41]). It suggests that in the Hong Kong region, the short-term sea level trend significantly increases when approaching the coast. Scientists worldwide have discovered many new features in different coastal regions (e.g., the Mediterranean coast, the Australia coasts, the coasts of the United States, West African coast, etc. [44]), and the technology would be further exploited in the future benefiting from the new conceptual altimeters.

Delay Doppler Altimeter (DDA), or Synthetic Aperture Radar (SAR) altimeter, is one of the most exciting advances in altimetry [45]. The along-track resolution is significantly improved by an order magnitude (from several kilometers to a few hundred meters), which is particularly useful to capture the small scale features. Cryosat-2 is the first satellite to demonstrate the DDA approach, and Sentinel-3 satellites operate in DDA mode all the time [46, 47]. China and other countries are also planning to launch altimeters of this type. A few investigations have been

reported to show the potential of the DDA technology, and solid contribution would be made to the coastal community if more dedicated waveform processing and geographic corrections approaches are developed and validated.

Acknowledgements

Author details

Xi-Yu Xu[1]*, Ke Xu[1], Ying Xu[2] and Ling-Wei Shi[1]

1 The Key Laboratory of Microwave Remote Sensing, National Space Science Center, Chinese Academy of Sciences, Beijing, China

2 National Satellite Ocean Application Service, Beijing, China

*Address all correspondence to: xuxiyu@mirslab.cn

IntechOpen

References

[1] Vignudelli S, Kostianoy AG, Cipollini P, Enveniste J, editors. Coastal Altimetry. Berlin Heidelberg: Springer-Verlag; 2011. 576p

[2] Fu LL, Cazenave A, editors. Satellite Altimetry and Earth Science. International Geophysics Series. Vol. 69. San Diego: Academic Press; 2000. 463p

[3] Stammer D, Cazenave A, editors. Satellite Altimetry over Oceans and Land Surfaces. CRC Press; 2017. ISBN: 978-1-4987-4345

[4] Kaula W, editors. NASA (Williamstown report): The Terrestrial Environment, Solid-Earth and Ocean Physics, Application of Space and Astronomic Techniques. Report of a Study at Williamstown, MA, NASA; 1969

[5] Fu L, Christensen E, Yamarone C, et al. TOPEX/POSEIDON mission overview. Journal of Geophysical Research. 1994;**99**:24369-24381

[6] Menard Y, Fu LL, Escudier P, et al. The Jason-1 mission. Marine Geodesy. 2003;**26**:131-146

[7] Lambin J, Rosemary M, Fu LL, et al. The Jason-2 / OSTM mission. Marine Geodesy. 2010;**33**:4-25

[8] Dumont JP, et al. Jason-3 Products Handbook. CNES: SALP-MU-M-OP-16118-CN; 2017

[9] Benveniste J. Towards more efficient use of radar altimeter data. ESA Bulletin. 1993;**76**

[10] Benveniste J, Roca M, Levrini G, et al. The radar altimetry mission: RA-2, MWR, DORIS, and LRR. ESA Bulletin. 2001;**106**:67

[11] Verron J, Sengenes P, Lambin J, et al. The SARAL/AltiKa altimetry

satellite mission. Marine Geodesy. 2015; **38**:2-21

[12] Xu K, Jiang JS, Liu HG. HY-2A radar altimeter design and in flight preliminary results. In: Proceedings of the IEEE International Geoscience and Remote Sensing Symposium. Melbourne; 2013. pp. 1642-1644

[13] Birol F, Fuller N, Lyard F, Cancet M, Niño F, Delebecque C, et al. Coastal applications from nadir altimetry: Example of the X-TRACK regional products. Advances in Space Research. 2017;**59**:936-953. DOI: 10.1016/j. asr.2016.11.005

[14] Passaro M, Cipollini P, Vignudelli S, Quartly GD, Snaith HM. ALES: A multimission adaptive subwaveform retracker for coastal and open ocean altimetry. Remote Sensing of Environment. 2014;**145**:173-189

[15] Mercier F, Rosmorduc V, Carrere L, Thibaut P. Coastal and Hydrology Altimetry Product (PISTACH) Handbook; CLS-DOS-NT-10-246. Paris, France: CNES; 2010

[16] Berry PAM, Jasper A. Retracking ERS-1 Land Altimeter Data Using an Expert System. Southampton: U.K. Geophysical Assembly; 1997

[17] Schwatke C, Dettmering D. Mission-independent classification of altimeter waveforms for applications in the Open Ocean, at the coastal zone and over land. In: 10th Coastal Altimetry Workshop. Florence; 2017

[18] Brown G. The average impulse response of a rough surface and its applications. IEEE Transactions on Antennas and Propagation. 1977;**25**: 67-74

[19] Hayne GS. Radar altimeter mean return waveforms from near-normal–

incidence ocean surface scattering. IEEE Transactions on Antennas and Propagation. 1980;**28**(5):687-692

[20] Martin TV, Zwally HJ, Brenner AC, Bindschadler RA. Analysis and Retracking of continental ice sheet radar altimeter waveforms. Journal of Geophysical Research. 1983;**88**: 1608-1616

[21] Anzenhofer M, Shum CK, Rentsh M. Coastal Altimetry and Applications. Ohio State University Geodetic Science and Surveying Technical Report No. 464; 1999. 36p

[22] Halimi A, Mailhes C, Tourneret J-Y, Thibaut P, Boy F. Parameter estimation for peaky altimetric waveforms. IEEE Transactions on Geoscience and Remote Sensing. 2013;**51**(3):1568-1577

[23] Hwang C, Guo J, Deng X, Hsu H-Y, Liu Y. Coastal gravity anomalies from retracked Geosat/GM altimetry: Improvement, limitation and the role of airborne gravity data. Journal of Geodesy. 2006;**80**:204-216

[24] Bao LF, Lu Y, Wang Y. Improved retracking algorithm for oceanic altimeter waveforms. Progress in Natural Science. 2009;**19**:195-203. DOI: 10.1016/j.pnsc.2008.06.017

[25] Yang L, Lin MS, Liu Q, Pan DL. A coastal altimetry retracking strategy based on waveform classification and subwaveform extraction. International Journal of Remote Sensing. 2012;**33**: 7806-7819

[26] Xu XY, Xu K, Birol F, Yang SB. HY-2A satellite altimetry advanced waveform processing offshore Hong Kong. In: Proceedings of the IEEE International Geoscience and Remote Sensing Symposium.Valencia; 2018. pp. 7668-7671

[27] Wingham DJ, Rapley CG, Griffiths H. New techniques in satellite tracking systems. In: Proceedings of the IEEE International Geoscience and Remote Sensing Symposium; 1986. pp. 1339-1344

[28] Deng X, Featherstone WE, Hwang C, Berry PAM. Estimation of contamination of ERS-2 and POSEIDON satellite radar altimetry close to the coasts of Australia. Marine Geodesy. 2002;**25**:249-271

[29] Tseng KH, Shum CK, Yi Y, et al. The improved retrieval of coastal sea surface heights by retracking modified radar altimetry waveforms. IEEE Transactions on Geoscience and Remote Sensing. 2014;**52**(2):991-1001

[30] Brown S. A novel near-land radiometer wet path-delay retrieval algorithm: Application to the Jason-2/ OSTM advanced microwave radiometer. IEEE Transactions on Geoscience and Remote Sensing. 2010; **48**:1986-1992

[31] Fernandes MJ, Lázaro C, Ablain M, Pires N. Improved wet path delays for all ESA and reference altimetric missions. Remote Sensing of Environment. 2015;**169**:50-74. DOI: 10.1016/j.rse.2015.07.023

[32] He-Guang L, Xi-Yu X, Le Y. Analysis of the dependence on retrackers of the Jason satellites altimetry products. In: Proceedings of the IEEE International Geoscience and Remote Sensing Symposium. Valencia; 2018. pp. 7672-7675

[33] Ray RD, Egbert GD, Erofeeva SY. Tide predictions in shelf and coastal waters: Status and prospects. In: Vignudelli S, Kostianoy AG, Cipollini P, Benveniste J, editors. Coastal Altimetry. Berlin: Springer; 2011. Chapter 7

[34] Lyard F, Lefevre F, Letellier T, Francis O. Modelling the global ocean tides: Modern insights from FES2004. Ocean Dynamics. 2006;**56**:394-415

[35] RayR. Status of modeling shallow-water ocean tides: Report from Stammer international model comparison project. In: Proceedings of the NASA/CNES Surface Water and Ocean Topography (SWOT) Science Definition Team (SDT) Meeting; 26–28 June 2014; Toulouse, France; 2014

[36] Chan YW. Tide reporting and applications in Hong Kong, China. 2006. Available from: www.glosssealevel.org/publications/documents/hong_kong 2006.pdf

[37] Lai WS, Matthew JP, Ho KY, et al. Hong Kong's marine environments: History, challenges and opportunities. Regional Studies in Marine Science. 2016;**8**:259-273

[38] Thibaut P, Amarouche L, Zanife LOZ, Stunou N, Vincent P, Raizonville P. Jason-1 altimeter ground processing look-up correction tables. Marine Geodesy. 2004;**27**:409-431

[39] Xu XY, Xu K, Wang ZZ, Liu HG, Wang L. Compensating the PTR and LPF features of the HY-2A satellite altimeter utilizing look-up tables. IEEE Journal of Selected Topics in Applied Earth Observations and Remote Sensing. 2015;**8**:149-159

[40] Dumont JP, Rosmorduc V, Carrere L, et al. OSTM/Jason-2 Products Handbook (Issue: 1 rev 11); SALP-MU-M-OP-15815-CN; 2017

[41] Xu XY, Birol F, Cazenave A. Evaluation of coastal sea level offshore Hong Kong from Jason-2 altimetry. Remote Sensing. 2018;**10**(2):282

[42] Masters D, Nerem RS, Choe C, et al. Comparison of global mean sea level time series from TOPEX/Poseidon, Jason-1, and Jason-2. Marine Geodesy. 2012;**35**:20-41

[43] Chambers DP, Cazenave A, Champollion N, et al. Evaluation of the global mean sea level budget between 1993 and 2014. Surveys in Geophysics. 2017;**38**:309-327

[44] Ablain M, Legeais JF, Prandi P, Marcos M, Fenoglio-Marc L, Dieng HB, et al. Satellite altimetry-based sea level at global and regional scales. Surveys in Geophysics. 2017;**38**:7-31

[45] Raney RK. The delay/Doppler radar altimeter. IEEE Transactions on Geoscience and Remote Sensing. 1998;**36**(5):1578-1588

[46] Wingham D, Francis CR, Baker S, et al. CryoSat: A mission to determine the fluctuations in Earth's land and marine ice fields. Advances in Space Research. 2006;**37**(4):841-871

[47] Donlon C, Berruti B, Frerick J, et al. The sentinel-3 mission overview. In: Proceedings of the 2011 EUMETSAT Meteorological Satellite Conference; 5–9 September; Oslo, Norway; 2011

Section 2

Observation and Analysis of Coastal Waters and Estuaries

Structure and Dynamics of Plumes Generated by Small Rivers

Alexander Osadchiev and Peter Zavialov

Abstract

The total share of small rivers in the influxes of fluvial water and suspended matter to the world ocean is estimated at between 25 and 40%. On a regional scale, this contribution can be even more significant for many coastal regions. In this chapter, we show that dynamics of small river plumes is significantly different from that of plumes generated by large rivers. Spatial structure of small plumes is generally characterized by sharper horizontal and vertical gradients. As a result, small plumes exhibit more energetic temporal variability in response to external forcing. In this chapter, we address several dynamical features typical for small plumes. We describe and discuss the response of small plumes to wind forcing and river discharge variability, the interaction between neighboring small plumes, and the generation of high-frequency internal waves in coastal ocean by small rivers. We also substantiate the Lagrangian approach to numerical modeling of small river plumes.

Keywords: river plumes, small rivers, plume dynamics, wind forcing, plume interaction, internal waves, Lagrangian modeling

1. Introduction

River discharges inflow to sea and form buoyant river plumes at coastal areas in many world regions. The total surface area and volume of river plumes are relatively small as compared to the saline ambient sea. However, river plumes govern land-ocean fluxes of fluvial water, sediments, nutrients, and pollutants and, thus, significantly influence many physical, biological, and geochemical processes on the continental shelf [1–6]. Structure, dynamics, and variability of river plumes are key factors for understanding mechanisms of advection, convection, transformation, accumulation, and dissipation of fluvial discharge as well as suspended and dissolved river-borne constituents in the coastal sea [7–9].

Two groups of factors govern the processes of formation, spreading, and mixing of river plumes. Immanent characteristics of local landscapes, namely shoreline and sea bottom features, morphology of river mouths, and latitude, which define the local magnitude of the Coriolis force, define the first group of factors [10–13]. The second group consists of variable external forcing conditions, which include river discharge, local wind, coastal circulation, tides, waves, and stratification of the ambient ocean [14–21]. The structure and dynamics of a river plume also strongly depend on its spatial scale. Sizes of river plumes vary from meters to hundreds of kilometers due to large ranges of freshwater discharge rate among world river

systems. Also, spatial scales of many river plumes have large variability within a year caused by seasonal changes in river discharge rates. It results in diverse patterns of formation, spreading, and mixing of a river plume on intra-annual time scale [22–25].

General aspects of the structure and dynamics of river plumes as well as their regional features were addressed in many previous studies. Nevertheless, these works were mostly focused on large river plumes, while small rivers plumes received relatively little attention. This is presumably caused by small influence of individual small plumes on coastal sea as compared to large plumes. Also, most of the world's small rivers are not covered by regular hydrological and discharge measurements, which result in a lack of information about their runoff volume and variability [26, 27].

The total share of small rivers in the influxes of fluvial water and suspended sediments to the world ocean is estimated at about 25 and 40%, respectively [28, 29]. Furthermore, this contribution is much more significant on a regional scale for many coastal regions. Under certain terrain and climatic conditions, the cumulative discharge from small rivers can greatly increase in response to heavy rains and become comparable to or even exceed the runoff of large rivers [30–33]. Flash floods at small rivers caused by active precipitation events can strongly influence the land-ocean buoyancy fluxes, heat, terrigenous sediments, nutrients, and anthropogenic pollutants. Many studies showed that they can affect coastal dynamics of certain world regions [13, 28, 34–37].

In this chapter, we focus on specific features of structure and dynamics of small river plumes, which are not typical for large plumes. In Section 2, we address spatial structure and temporal variability of small river plumes and analyze general aspects of difference between small and large plumes. In Section 3, we describe the Lagrangian numerical model that was specifically designed for simulation of spreading and mixing of small river plumes and the associated transport of river-borne suspended matter. Section 4 provides description and analysis of several important dynamical features of small plumes including the response of small plumes to wind forcing and river discharge variability (Section 4.1), the interaction between neighboring small plumes (Section 4.2), and the generation of high-frequency internal waves in small plumes by river discharge (Section 4.3). The conclusions are given in Section 5.

2. Structure of small river plumes

The process of transformation of freshwater discharge as a result of its interaction with saline sea water can be considered and analyzed on different spatial and temporal scales. Initially, river discharge inflows to sea from a river mouth and forms a sub-mesoscale or mesoscale water mass commonly referred as a river plume, where salinity is significantly lower than of surrounding sea water. Buoyancy force plays an important role in spreading and mixing of this freshened water mass; therefore, dynamics of river plumes and ambient sea is different because of salinity differences. Thus, salinity is the main characteristic that is used to distinguish river plumes and sea water, i.e., define the mixing zone where river plume ends and sea water starts.

A river plume is generally formed by one or multiple distinct sources. Structure and dynamical characteristics within a river plume are strongly nonhomogenous. In particular, salinity and velocity field in vicinity of freshwater source/sources are significantly different as compared to outer parts of a plume [9, 16]. A river plume is spreading and mixing with adjacent sea water, which results in transformation of

a river plume, but also influences physical, biological, and geochemical characteristics of ambient sea. Strength and extent of this influence mainly depend on volume of freshwater discharge and varies from negligible impact of small plumes formed by rivers with low discharge rates on coastal sea [20, 24, 38] to formation of stable freshened water masses in the upper sea layer on wide coastal and shelf areas [11, 39–41]. The latter water masses, commonly referred as regions of freshwater influence (ROFI), are characterized by more homogenous structure, significantly as greater spatial scales and lower temporal variability, as compared to river plumes.

We regard river plumes as water masses formed as a result of transformation of freshwater discharge in coastal sea on diurnal to synoptic time scales, while ROFI reproduce transformation of freshwater discharge on seasonal to annual time scales. River plume embedded into ROFI reproduces a continuous process of transformation of freshwater discharge and, therefore, cannot be distinctly distinguished. On the other hand, river plumes and ROFI have strongly different thermohaline characteristics and dynamics. Therefore, interaction between river plumes and surrounding ROFI significantly influences spreading dynamics and mixing of river plumes on synoptic time scale [5, 25, 31–33].

In this chapter, we focus on small river plumes; therefore, we need to determine characteristic properties of small plumes to distinguish them from large plumes. We define small plumes as plumes that do not form ROFI; i.e., residence time of freshened water in a small river plume is equal to hours and days. Dissipation of freshened water as a result of mixing of a small plume with subjacent saline sea limitedly influence ambient sea and does not result in accumulation of freshwater in adjacent sea area. As a result, small plumes are characterized by sharp salinity and, therefore, density gradient at their boundaries with ambient sea. This density gradient hinders vertical energy transfer between a small plume and subjacent sea.

This feature strongly affects spreading dynamics of a small plume due to following reasons. First, the majority of wind energy transferred to sea remains in a small plume, because vertical momentum flux diminishes at density gradient between a plume and subjacent sea. Thus, wind stress is concentrated in a shallow freshened surface layer that causes higher motion velocity and more quick response of dynamics of a small plume to variability of wind forcing, as compared to ambient sea [42, 43]. Second, circulation of adjacent sea limitedly affects spreading dynamics of a small plume, because density gradient hinders upward momentum flux from subjacent sea to a small plume [44]. It results in wind-driven dynamics of small plumes, which is characterized by very energetic temporal variability of their positions, shapes, and areas [45–47]. Spreading pattern of a small plume can dramatically change during several hours that is regularly registered by in situ and satellite data. High temporal variability of small plumes and their small vertical sizes often result in large inhomogeneity of their horizontal structure.

3. Lagrangian modeling of small river plumes

An important role of buoyancy force and density gradients are key features of dynamics of small river plumes, which is substantially different from dynamics of ambient sea. Small plumes are characterized by sharp spatial gradients and high temporal variability, while ambient sea has more stable and homogenous structure. Thus, an Eulerian approach denoted by state equations for a fixed point of space is suitable for modeling of complex dependences and feedbacks of sea dynamics, but exhibits certain difficulties if applied for modeling of small plumes. On the other
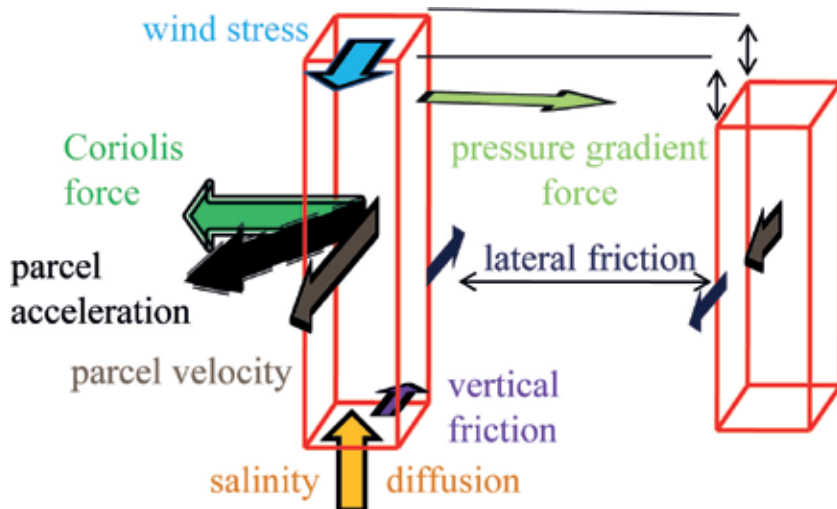
Figure 1.
Schematic of the forces applied to an individual parcel of a river plume.

hand, a Lagrangian approach denoted by state equations for a moving parcel of substance is more efficient for modeling of dynamically active processes and coherent structures typical for small plumes.

We developed a Lagrangian model called Surface-Trapped River Plume Evolution (STRiPE) for simulating the spreading of small river plumes and the associated transport of river-borne suspended sediments [45, 48]. STRiPE represents a river plume as a set of Lagrangian parcels or homogeneous water columns extending from the surface down to the boundary between the plume and the subjacent sea, while their horizontal sizes are presumed to be relatively small. These parcels are initially released from the river mouth and represent river runoff inflowing to sea. The subsequent motion of a parcel is determined by the momentum equation applied to this specific parcel. The overall set of parcels represents the river plume at every step of the model. Thus, the temporal evolution of the plume is simulated. We presume that the buoyant plume remains confined to the surface layer; therefore, the model describes the 2D motion of the parcels, although all parcels exhibit vertical mixing with subjacent sea water. Salinity and density of an individual parcel change in time until it eventually dissipates.

Motion equations, which are applied to an individual parcel, reproduce the main forces that determine river plume dynamics, namely, the Coriolis force, the pressure gradient force, the wind stress force, the friction at the lower boundary of the plume, and the lateral friction (**Figure 1**). At every step of the computation, the model reads the corresponding values from the input time series of river discharge rate, wind stress, and ambient sea current velocity data. Then, the model calculates the acceleration components (a_x, a_y) and the resulting velocity components (u, v) for the whole set of parcels. The STRiPE model tracks individual parcels and, therefore, does not use any spatial grid for solving the motion equations. However, an auxiliary horizontal grid with the respective increments Δx and Δy in zonal and meridional directions is used to calculate the spatial derivatives necessary for parameterizing the pressure gradient force and lateral friction applied to the parcel. Continuous fields of velocity, depth, and density within the plume are obtained by extrapolating the respective values from the overall set of parcels.

The momentum equations for an individual parcel are the following:

$$a_x^{i+1} = fv_{x,y}^i + \frac{\tau_x^i}{\rho_{x,y}^i h_{x,y}^i} - \frac{\mu_v^i}{h_{x,y}^i} \frac{u_{x,y}^i - u_{sea}^i}{h_{x,y}^i}$$

$$+ \frac{\mu_h}{h_{x,y}^i} \left(\frac{\left(u_{x+\Delta x,y}^i - u_{x,y}^i\right) - \left(u_{x,y}^i - u_{x-\Delta x,y}^i\right)}{\Delta x} + \frac{\left(u_{x,y+\Delta y}^i - u_{x,y}^i\right) - \left(u_{x,y}^i - u_{x,y-\Delta y}^i\right)}{\Delta y} \right)$$

$$- g \frac{h_{x+\Delta x,y}^i \rho_{x+\Delta x,y}^i \left(\rho_{sea} - \rho_{x+\Delta x,y}^i\right) - h_{x-\Delta x,y}^i \rho_{x-\Delta x,y}^i \left(\rho_{sea} - \rho_{x-\Delta x,y}^i\right)}{2\Delta x \rho_{sea} \rho_{x,y}^i},$$

$$a_y^{i+1} = -fu_{x,y}^i + \frac{\tau_y^i}{\rho_{x,y}^i h_{x,y}^i} - \frac{\mu_v^i}{h_{x,y}^i} \frac{v_{x,y}^i - v_{sea}^i}{h_{x,y}^i}$$

$$+ \frac{\mu_h}{h_{x,y}^i} \left(\frac{\left(v_{x+\Delta x,y}^i - v_{x,y}^i\right) - \left(v_{x,y}^i - v_{x-\Delta x,y}^i\right)}{\Delta x} + \frac{\left(v_{x,y+\Delta y}^i - v_{x,y}^i\right) - \left(v_{x,y}^i - v_{x,y-\Delta y}^i\right)}{\Delta y} \right)$$

$$- g \frac{h_{x,y+\Delta y}^i \rho_{x,y+\Delta y}^i \left(\rho_{sea} - \rho_{x,y+\Delta y}^i\right) - h_{x,y-\Delta y}^i \rho_{x,y-\Delta y}^i \left(\rho_{sea} - \rho_{x,y-\Delta y}^i\right)}{2\Delta y \rho_{sea} \rho_{x,y}^i},$$

$$(1)$$

where $\left(u_{x,y}, v_{x,y}\right)$ are the interpolated velocity components at the (x, y) grid node, f is the Coriolis parameter, $\left(\tau_x, \tau_y\right)$ are the wind stress components, ρ is the density of water in the parcel, h is the height of the parcel, $\rho_{x,y}$ is the interpolated density at the (x, y) grid node, $h_{x,y}$ is the interpolated height at the (x, y) grid node, μ_h, μ_v are the horizontal and vertical eddy viscosity coefficients, (u_{sea}, v_{sea}) are the ambient sea currents velocity components, ρ_{sea} is the ambient sea water density, and g is the gravity acceleration. The superscripts denote the model time steps. The first term in Eq. (1) denotes the Coriolis force, the second term stands for the wind stress, the third and fourth terms denote the bottom and lateral friction, and the fifth term stands for the pressure gradient force. After the acceleration components $\left(a_x, a_y\right)$ are obtained from the momentum equations, the final velocities (u, v) for the period $(t, t + \Delta t)$ are calculated from kinematic formulas:

$$u^{i+1} = u^i + a_x^{i+1}\Delta t,$$
$$v^{i+1} = v^i + a_x^{i+1}\Delta t.$$

$$(2)$$

In order to simulate the small-scale horizontal turbulent mixing, the deterministic approach described above was complemented by the random-walk Monte Carlo method [49]:

$$x^{i+1} = x^i + u^{i+1}\Delta t - \frac{a_x^{i+1}\Delta t^2}{2} + \sqrt{2D_h^i \Delta t}\, \eta_x,$$

$$y^{i+1} = y^i + v^{i+1}\Delta t - \frac{a_y^{i+1}\Delta t^2}{2} + \sqrt{2D_h^i \Delta t}\, \eta_y,$$

$$(3)$$

where (x, y) are the coordinates of an individual parcel, Δt is the time step, D_h is the horizontal diffusion coefficient depending on the velocity field as specified below, and η_x, η_y are the independent random variables with standard normal

distribution. The horizontal diffusion coefficient used above was calculated from the Smagorinsky formula [50]:

$$D_h^i = \zeta_h \Delta x \Delta y \sqrt{ \left(\frac{u_{x+\Delta x,\,y}^i - u_{x-\Delta x,\,y}^i}{\Delta x}\right)^2 + \frac{1}{2}\left(\frac{v_{x+\Delta x,\,y}^i - v_{x-\Delta x,\,y}^i}{\Delta x} + \frac{u_{x,\,y+\Delta y}^i - u_{x,\,y-\Delta y}^i}{\Delta y}\right)^2 + \left(\frac{v_{x,\,y+\Delta y}^i - v_{x,\,y-\Delta y}^i}{\Delta y}\right)^2 },$$

where ζ_h is the scaling coefficient.

The simulation of the vertical dissipation of a plume parcel is based on the salinity diffusion equation and assumption that density depends linearly on salinity:

$$\frac{\partial \rho}{\partial t} = D_v \frac{\partial^2 S}{\partial z^2}, \tag{4}$$

or, in a discrete form,

$$\rho^{i+1} = \rho^i + \frac{D_v^i}{h_t}\frac{\rho_{sea} - \rho^i}{h^i}\Delta t. \tag{5}$$

where D_v is the vertical diffusion coefficient and h_t is the vertical turbulence scale. Hence, as the saline water from the subjacent sea is entrained into the plume gradually replacing the freshwater, the density of water in the parcel increases, while its height decreases according to the following linear equation:

$$\frac{\partial h}{\partial t} = -\frac{D_v^i}{h_t}, \tag{6}$$

or, in a discrete form,

$$h^{i+1} = h^i - \frac{D_v^i}{h_t}\Delta t. \tag{7}$$

The vertical diffusion coefficient divided by the vertical turbulence scale used above was calculated using the following parameterization based on Richardson number [51]:

$$\frac{D_v^i}{h_t} = \zeta_v \mu_v^i \left(1 - \min\left(1, Ri^i\right)^2\right)^3, \tag{8}$$

where ζ_v is the scaling coefficient, $Ri^i = \frac{N^{i2}}{S^{i2}}$ is the Richardson number, $N^i = \sqrt{\frac{g}{\rho^i}\frac{\rho_{sea}-\rho^i}{h^i}}$ is the buoyancy frequency, and $S^i = \frac{\sqrt{\left(u^i - u_{sea}^i\right)^2 + \left(v^i - v_{sea}^i\right)^2}}{h^i}$ is the vertical shear.

Transport and settling of fine suspended sediments discharged from the river mouth is also simulated by STRiPE. In horizontal direction, sediment particle is defined as a passive tracer of a river plume; i.e., the horizontal movement of a

sediment particle is defined by velocity fields calculated within a plume at every modeling step. Vertical movement is calculated individually for every sediment fraction, which have different sizes of particles. For this purpose, we use a combination of a deterministic component defined by sinking of a particle under the gravity force and a stochastic random-walk scheme that reproduces influence of small-scale turbulent mixing. Sediment particles are initially released from the river mouth with river water. During its motion, a particle sinks within the river plume until it reaches the mixing zone between the river plume and the subjacent sea water. After the particle descends beneath the lower boundary of the plume, it is regarded as settled to ambient sea and is stopped to be simulated by STRiPE. The STRiPE is intended to simulate transport of relatively small particles with diameter less than 10^{-4} m; therefore, gravity-induced vertical motion is determined by

Stokes' law, and particle settling velocity w_s is calculated as follows: $w_s = \frac{gd^2(\rho_s - \rho^i)}{18\mu\rho^i}$, where d is the sediment particle diameter, ρ_s is the sediment particle density, and μ is the dynamic water viscosity.

The total vertical displacement of a sediment particle determined by gravitational sinking, vertical advection, and turbulent mixing was parameterized by the random-walk Monte Carlo method, which represents features of spatially nonuniform turbulent mixing:

$$\Delta z = \left(w_s + \frac{\partial K}{\partial z} \right) \Delta t + \sqrt{\frac{2}{3} K_v \left(z + \frac{1}{2} \frac{\partial K_v}{\partial z} \Delta t \right) \Delta t} \eta, \tag{9}$$

where Δz is the vertical displacement of a particle, K_v is the vertical diffusion coefficient, and η is a random process with standard normal distribution.

The main advantage of STRiPE lies in its computational efficiency in simulating spreading and mixing of river plumes as compared to Eulerian models. However, STRiPE does not reproduce any influence of a river plume on the ambient ocean, which is an important issue for large river plumes. Thus, STRiPE should be applied for simulation of spreading and mixing of small river plumes that limitedly influence the ambient sea.

4. Dynamics of small river plumes

In this section, we address dynamical features of small river plumes using the case study of the Mzymta plume and other small river plumes formed along the Russian coast of the Black Sea (RCBS) between the city of Novorossiysk and the city of Sochi (**Figure 2**). The drainage basin of RCBS is a narrow area (10–40 km wide) limited by the Greater Caucasus range at the east and the sea coast at the west. Steep gorges of this range form the drainage basins of several dozens of rivers that discharge to the sea at RCBS. Watershed basin areas of these rivers are relatively small, and the total freshwater runoff from the study region to the sea is estimated as 7 km^3 in a year [52].

Multiple buoyant plumes are formed along the coast of the study area. The largest plume is generally formed by the Mzymta River, which is the largest river of RCBS with mean monthly discharge equal to 20–120 m^3/s. The area of the Mzymta does not exceed 10 km^2 under average climatic discharge conditions. However, it can increase up to 50 km^2 during spring and summer freshet periods. Areas of the other river plumes of RCBS are even smaller except for rain-induced flash flooding
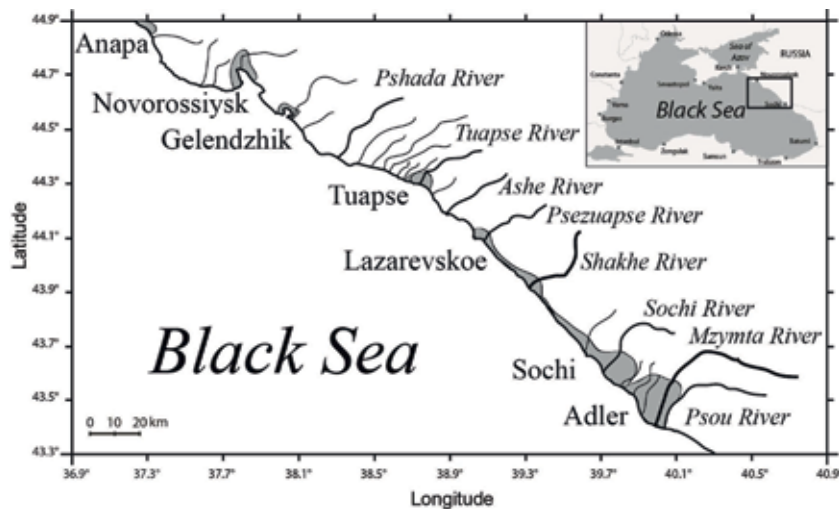
Figure 2.
Location of the largest rivers and cities of the Russian coast of the Black Sea.

periods. The rivers of the study region are significantly more turbid, as compared to sea water, due to elevated concentrations of terrigenous suspended sediments. As a result, surface salinity and turbidity show good correlation within the river plumes. Thus, optical satellite imagery can be effectively used to detect river plumes of RCBS [45, 46]. Both in situ and satellite measurements revealed high spatial and temporal variability of the river plumes of RCBS. Their areas, positions, and shapes can significantly change during several hours in response to variations of river discharge and local wind forcing [42, 43, 45].

4.1 Wind forcing and small river plumes

We used near-simultaneous ocean-color satellite imagery from NASA's Landsat 8 and ESA's Sentinel-2 missions to reconstruct surface currents along RCBS and study spreading dynamics of small river plumes formed in this area [53]. Several times a year, Landsat 8 and Sentinel-2 satellites both pass over the study area within a time interval of less than 10 minutes. The obtained near-simultaneous ocean-color composites can be used to reconstruct surface sea currents. In particular, they can be applied for detection of motion of frontal zones of river plumes, which are visible in optical satellite images. We used an optical flow algorithm applied to near-simultaneous Landsat 8 and Sentinel-2 images to reconstruct surface currents within the Mzymta plume. The obtained results reveal significant differences in wind-driven dynamics of the Mzymta plume and large plumes [12, 16, 54–58].

The main features of the dynamics of the Mzymta plume reconstructed from the satellite imagery are the following. First, the near-field part of the Mzymta plume is smaller than it is estimated by relevant parameterizations based on river discharge parameters designed for large plumes. Second, under low-wind-forcing conditions, the mid-field plume, i.e., a recirculating bulge adjacent to the river mouth, is not formed. The near-field freshwater jet directly transitions to the far-field part of the plume near the Mzymta mouth. Finally, during upwelling, onshore, and offshore wind-forcing periods, the wind-induced Ekman transport within the Mzymta plume occurs at a wide range of angles to the wind direction. It changes from values of 60–80° near the Mzymta mouth to 30–40° at the far-field part of the plume.

We presume the following physical interpretation of dynamical features of a small plume described above. The Mzymta River has a rapid flow (1–2 m/s), but is relatively shallow (1–1.5 m) in its mouth. Thus, relatively small volume of fresh water inflows to sea from the Mzymta River mouth at a relatively high speed. This jet is then abruptly decelerated by the vertical friction with the subjacent sea and the initial inertia of the jet decays in vicinity of the river mouth. Thus, according to the reconstructed surface velocity fields, size of the inertia-governed near-field part of the Mzymta plume is relatively small (1–2 km). It is of one order of magnitude less than, first, was reported by in situ measurements for river plumes formed by rivers with similar discharge rates but lower river inflow velocities [24, 38, 59, 60], and, second, theoretical values of near-field part of a plume numerically estimated by formulae described by [12, 54].

The near-field jet abruptly decelerates and forms a sharp pressure gradient in vicinity of the river mouth, which is directed seaward. As a result, anticyclonic recirculation flow directed to the river mouth is hindered by the pressure gradient force. Thus, the large river inflow velocity and low river discharge volume are the limiting factors for formation of an anticyclonic bulge under low wind-forcing conditions. On the other hand, in case of low velocity and/or a large volume of river inflow, it is not abruptly decelerated in vicinity of the river mouth, and strong velocity and pressure gradients are not formed.

Strong nonuniformity of motion patterns of different parts of the far-field plume in response to wind forcing are revealed by the reconstructed surface velocity fields. Upwelling, onshore, and offshore winds induce spreading of the most stratified parts of the plume adjacent to the Mzymta mouth at an angle of up to 80° to the direction of wind forcing. On the other hand, this angle diminishes to 30–40° at the less stratified outer parts of the plume. This effect is presumed to be caused by inhomogeneity of Ekman layer depth due to strong variability of stratification of the Mzymta plume. These results are supported by numerical experiments focused on relation between parameters of Ekman transport and river plume stratification [61].

Dynamical features of the Mzymta plume described above significantly influence its structure, spreading patterns, and the associated transport of suspended and dissolved river-borne constituents. First, freshwater discharge does not accumulate at the small near-field part of the Mzymta plume, which is not the case for large rivers [9, 15, 55]. As a result, freshwater discharge is mainly accumulated at the far-field part of the Mzymta plume. Winds cause spreading of a far-field plume along the direction of Ekman transport till it is limited by a coastline. Thus, location of a restraining coastline defines two stable states of a plume, which are generally indicated by downstream/upstream location of a sharp plume front. First, an alongshore downstream current is formed if spreading of a small plume is limited by a downstream coastline. Second, a small plume is arrested near its estuary if its spreading is restrained by an upstream coastline.

The observed large angles between surface flow and wind-forcing directions at the strongly stratified part of the Mzymta plume causes significantly different wind-govern spreading patterns of a small plume, as compared to large plumes (**Figure 3**). Upstream spreading of large river plumes is caused by upwelling wind forcing [22, 62, 63], while upstream spreading and accumulation of a small plume was observed only during onshore winds. On the opposite, upwelling wind forcing induced intense offshore spreading of a small plume, while largest cross-shore scales of large plumes were registered during offshore wind-forcing conditions [64, 65]. Downstream spreading of a small plume as an alongshore coastal current during downwelling wind-forcing conditions is similar to spreading patterns observed for large plumes [22, 62, 66–68].

4.2 Interaction between small river plumes

The Mzymta River has a drought period from late summer to the end of winter and a freshet period in spring and early summer caused by snow melting. All other rivers of the study region are mainly rain-fed and are prone to regular flash floods that provide the majority of their total annual runoff. These flash floods are characterized by sharp rises and falls of discharge due to small sizes (<900 km^2) and steep relief of the drainage basins and their high drainage densities (0.85–1.05). It results in quick response of discharge of these rivers on precipitation events, which can significantly increase during several hours after a heavy rain [69].

Under average climatic discharge conditions, plumes formed by small rivers at RCBS are distinctly separated because their spatial scales do not exceed the distances between the river estuaries. However, during rain-induced floods, the areas of the river plumes significantly increase, and the plumes can collide and coalesce with neighboring plumes (**Figure 4**). As a result, the point-source spread of continental discharge dominated by several large rivers under average climatic conditions can change to the line-source discharge from numerous small rivers situated along the coast in response to heavy rains. We studied interaction between these river plumes using a nested combination of the INMOM [70, 71] and the STRiPE numerical models [25]. The Eulerian model INMOM reproduced general ocean
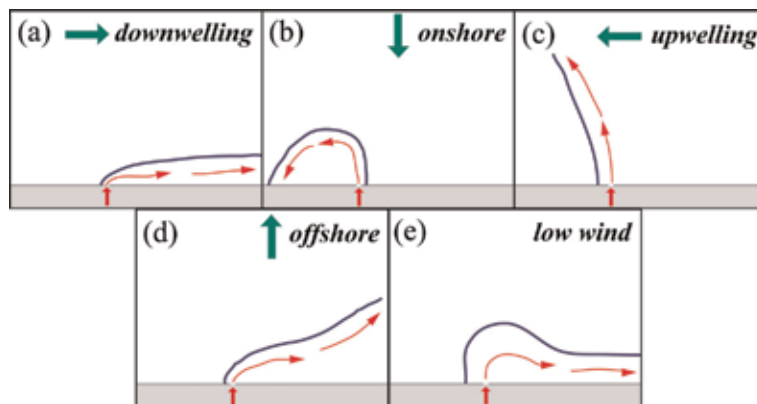
Figure 3.
Schematic of spreading patterns of a small river plume and the related locations of sharp frontal zones of a plume under (a) downwelling, (b) onshore, (c) upwelling, (d) offshore, and (e) low wind-forcing conditions.
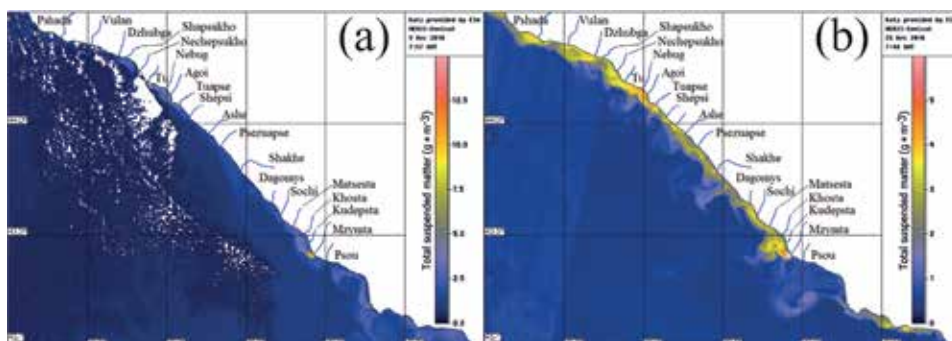
Figure 4.
Satellite-derived surface TSM distribution at the Russian coast of the Black Sea before (a) and after (b) a heavy rain, illustrating collision and coalescence of multiple small plumes at RCBS in response to rain-induced flooding event.

circulation at the northeastern part of the Black Sea and provided boundary conditions for the Lagrangian model STRiPE, which was used for simulating the dynamics of river plumes.

Numerical experiments showed that short-term rain-induced flooding events significantly influence sediment transport and deposition patterns at RCBS. Under average climatic discharge conditions, the total runoff of fluvial water and terrigenous sediments in the study area is dominated by several largest rivers. Discharge of fresh water and terrigenous sediments from the small rivers is relatively low. As a result, plumes formed by small rivers have small sizes, small water residence time, and their influence on coastal sea is almost negligible. Thus, river discharges affect local water quality and sediment accumulation only near the estuaries of several largest rivers. Heavy rains can induce a rapid and substantial increase in discharge of fresh water and terrigenous sediments from the small rivers of the study region. During these flash flooding periods, areas of small plumes substantially increase, neighboring plumes coalesce, and strips of freshened water masses can be formed along large segments of the seashore.

Numerical modeling revealed that interaction between river plumes significantly influence their structure and dynamics. During flash flooding periods, alongshore strips of freshened and turbid water are formed in the study region and their total length can exceed 200 km. The resulting line-source discharge pattern induces switch in dynamics of river plumes and transport pathways of river-borne suspended and dissolved matters at RCBS. The mixing intensity between the plumes and the adjacent strips of freshened and turbid water is relatively low due to the decrease of salinity gradient. As a result, the river plumes exhibit slower dissipation, have larger spatial scales, and have larger water residence time, as compared to point-source discharge conditions. Moreover, line-source discharge conditions induce alongshore geostrophic currents of turbid and freshened water. These currents induce the intense alongshore transport of river-borne sediments in a northwestern direction. This process strongly affects local water quality and causes active sediment accumulation along large segments of the sea shore at the study region, as compared to point-source discharge conditions.

4.3 Generation of high-frequency internal waves

High-frequency internal waves propagating offshore in small river plumes are regularly observed in satellite imagery in many world regions. In particular, Landsat 8 and Sentinel-2 ocean-color composites regularly reveal surface expressions of high-frequency internal waves propagating in small river plumes of RCBS [72]. Sources of these internal waves are small areas (100–200 m long and 25–100 m wide) adjacent to river mouths and elongated in directions of river inflows (**Figure 5a**). These waves propagate offshore from their source areas, and their surface expressions are distinctly observed at optical satellite imagery only within river plumes. These waves dissipate within river plumes at a distance of order of several kilometers from the river mouths or at lateral boundaries of river plumes, if size of a river plume is less than the decay distance of the internal waves. Ranges of wavelengths, phase speeds, and periods of internal waves reconstructed at multiple river plumes of the study region using satellite imagery are equal to 30–60 m, 0.45–0.65 m/s, and 65–90 s, respectively.

We presume the following mechanism of generation of internal waves described above by discharges of small and rapid rivers (**Figure 5b**). Velocity of a river runoff is of one order of magnitude higher than velocity of coastal circulation. It causes abrupt deceleration of a freshened flow, increase of its depth, and formation of a hydraulic jump. The resulting switch of flow conditions from supercritical to
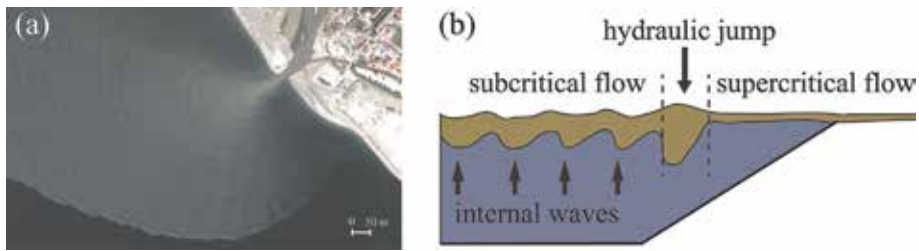
Figure 5.
WorldView-3 ocean color composite of the Mzymta plume from April 4, 2017 illustrating the formation and propagation of internal waves with high spatial resolution (a). Schematic of formation of a hydraulic jump and generation of internal waves by river discharge (b).

subcritical state causes generation of high-frequency internal waves. These waves propagate offshore in a stratified layer between the river plume and the subjacent saline sea. If the internal waves reach lateral boundary of a river plume, they abruptly dissipate due to relatively low stratification in the ambient sea. Thus, energy of internal waves is transformed to turbulence and increase mixing between the river plume and the subjacent sea.

A hydraulic jump described above is formed by river runoff under certain conditions that depend on properties of a river flow, ambient sea water, and a local topography. First, a supercritical freshened flow in vicinity of a river mouth is formed only if a river current is fast enough. At the same time, a freshened flow is abruptly decelerated by friction with ambient sea only if its kinetic energy, i.e., river discharge rate, is relatively low. Second, transformation of kinetic energy of a river flow to potential energy of a hydraulic jump depends on local salinity anomaly. Therefore, ambient sea salinity has to be high enough, which occurs in absence of intense freshwater accumulation in vicinity of a river mouth. Third, depth of a plume has to be smaller than sea depth near a river mouth. In this case, a river plume does not exhibit friction with sea bottom, which can hinder formation of a hydraulic jump.

Many small and rapid mountainous rivers that inflow to deep coastal sea areas correspond to the conditions listed above. These rivers have small but steep drainage basins that result in high flow velocities and small discharge rates. Steep coastal bathymetry typical for mountainous coasts provides quick renewal of sea water in vicinity of river mouths by coastal circulation. Discharges of such rivers form hydraulic jumps and generate internal waves in many world coastal regions (New Guinea, New Zealand, Mexico, Peru, Chile, Taiwan, etc.), which is regularly observed by satellite imagery. Moreover, many of these regions have regular flash flooding events on small rivers during rainfall [25, 30, 73]. The resulting simultaneous generation of high-frequency internal waves from multiple and closely spaced river mouths was registered in several of the mountainous regions listed above.

The processes of generation, propagation, and dissipation of internal waves described above induce transformation of river flow kinetic energy to turbulence in frontal zones of a river plume. As a result, these processes increase mixing in bottom and lateral boundaries of a plume and reduce freshwater volume accumulated in a river plume. This pattern of energy transform observed for small rivers of RCBS is significantly different from those that are typical for larger rivers and/or rivers with less rapid currents, which discharges form recirculating bulges in vicinity of river mouths instead of hydraulic jumps [9, 15, 56]. As a result, a kinetic energy of a river flow transforms to pressure gradient potential energy and kinetic energy of a bulge anticyclonic flow. In this case, increase in a kinetic energy of a

river flow increases freshwater accumulation rate within a bulge and decreases mixing between a river plume and ambient sea [9, 15]. Therefore, generation of internal waves is an important feature of river plumes formed by small and rapid rivers, which strongly affects their structure and dynamics.

5. Conclusions

In this chapter, we described specific features of structure and dynamics of small river plumes, which are significantly different from those typical for large plumes. Small river plumes are river plumes with small residence time of freshened water (hours and days), which mixing with ambient sea limitedly influences its salinity. Small plumes have sharp salinity gradients at their boundaries with ambient sea, which hinders vertical energy transfer between a small plume and subjacent sea. As a result, small plumes are mainly wind driven, while the role of circulation of ambient sea in their dynamics is negligible.

Small plumes are characterized by energetic temporal variability and inhomogeneous horizontal structure. Position, shape, and area of a small plume can significantly change during several hours in response to variability of wind forcing and river discharge rate. Small plumes have very small near-field part and do not form a recirculating bulge adjacent to river mouths due to efficient deceleration of inflowing river runoffs and quick decay of their initial inertia. The wind-induced Ekman transport within a small plume occurs at a wide range of angles to the wind direction during upwelling, onshore, and offshore wind-forcing periods with the largest values in the near-field part of a plume. Interaction between neighboring small plumes can strongly influence their structure and dynamics. Collision and coalescence of multiple small plumes in response to rain-induced flooding events results in the decrease of mixing intensity within small plumes and intensification of their alongshore spreading.

Finally, high-frequency internal waves are generated in certain small plumes formed by rivers with high flow velocity. Such a river inflows to coastal sea, abruptly decelerates, and forms a hydraulic jump in vicinity of a river mouth. Formation and relaxation of a hydraulic jump induces generation of high-frequency internal waves that propagate offshore. These internal waves strongly influence turbulence and mixing at a stratified layer between a buoyant river plume and subjacent ambient sea.

Acknowledgements

Conflict of interest

The authors declare that they have no conflict of interests.

Author details

Alexander Osadchiev* and Peter Zavialov
Shirshov Institute of Oceanology, Russian Academy of Sciences, Moscow, Russia

*Address all correspondence to: osadchiev@ocean.ru

IntechOpen

References

[1] Emmett RL, Krutzikowsky GK, Bentley P. Abundance and distribution of pelagic piscivorous fishes in the Columbia River plume during spring/early summer 1998–2003: Relationship to oceanographic conditions, forage fishes, and juvenile salmonids. Progress in Oceanography. 2006;**68**:1-26. DOI: 10.1016/j.pocean.2005.08.001

[2] Milliman JD, Lin SW, Kao SJ, Liu JP, Liu CS, Chiu JK, et al. Short-term changes in seafloor character due to flood-derived hyperpycnal discharge: Typhoon Mindulle, Taiwan, July 2004. Geology. 2007;**35**:779-782. DOI: 10.1130/G23760A.1

[3] Zhou MJ, Shen ZL, Yu RC. Responses of a coastal phytoplankton community to increased nutrient input from the Changjiang (Yangtze) River. Continental Shelf Research. 2008;**28**:1483-1489. DOI: 10.1016/j.csr.2007.02.009

[4] Huang WJ, Cai WJ, Wang Y, Lohrenz SE, Murrell MC. The carbon dioxide system on the Mississippi River-dominated continental shelf in the northern Gulf of Mexico: 1. Distribution and air-sea CO2 flux. Journal of Geophysical Research, Oceans. 2015;**120**:1429-1445. DOI: 10.1002/2014jc010498

[5] Osadchiev AA, Izhitskiy AS, Zavialov PO, Kremenetskiy VV, Polukhin AA, Pelevin VV, et al. Structure of the buoyant plume formed by Ob and Yenisei River discharge in the southern part of the Kara Sea during summer and autumn. Journal of Geophysical Research, Oceans. 2017;**122**:5916-5935. DOI: 10.1002/2016JC012603

[6] Zavialov PO, Pelevin VV, Belyaev NA, Izhitskiy AS, Konovalov BV, Krementskiy VV, et al. High resolution LiDAR measurements reveal fine internal structure and variability of sediment-carrying coastal plume. Estuarine, Coastal and Shelf Science. 2018;**205**:40-45. DOI: 10.1016/j.ecss.2018.01.008

[7] O'Donnell J. The dynamics of estuary plumes and fronts. In: Valle-Levinson A, editor. Contemporary Issues in Estuarine Physics. Cambridge: Cambridge University Press; 2010. pp. 186-246

[8] Hetland RD, Hsu T-J. Freshwater and sediment dispersal in large river plumes. In: Bianchi TS, Allison MA, Cai W-J, editors. Biogeochemical Dynamics at Large River-Coastal Interfaces: Linkages with Global Climate Change. New York: Springer; 2013. pp. 55-85

[9] Horner-Devine AR, Hetland RD, MacDonald DG. Mixing and transport in coastal river plumes. Annual Review of Fluid Mechanics. 2015;**47**:569-594. DOI: 10.1146/annurev-fluid-010313-141408

[10] Chao SY, Boicort WG. Onset of estuarine plumes. Journal of Physical Oceanography. 1986;**16**:2137-2149. DOI: 10.1175/1520–0485(1986)016<2137:OOEP>2.0.CO;2

[11] Simpson JH. Physical processes in the ROFI regime. Journal of Marine Systems. 1997;**12**:3-15. DOI: 10.1016/s0924-7963(96)00085-1

[12] Horner-Devine AR, Fong DA, Monismith SG, Maxworthy T. Laboratory experiments simulating a coastal river discharge. Journal of Fluid Mechanics. 2006;**555**:203-232. DOI: 10.1017/s0022112006008937

[13] Warrick JA, Farnsworth KL. Coastal river plumes: Collisions and coalescence. Progress in Oceanography. 2017;**151**:245-260. DOI: 10.1016/j.pocean.2016.11.008

[14] O'Donnell J. The formation and fate of a river plume: A numerical model. Journal of Physical Oceanography. 1990; **20**:551-569. DOI: 10.1175/1520-0485 (1990)020<0551:TFAFOA>2.0.CO;2

[15] Fong DA, Geyer WR. Response of a river plume during an upwelling favorable wind event. Journal of Geophysical Research. 2001;**106**: 1067-1084. DOI: 10.1029/2000jc900134

[16] Fong DA, Geyer WR. The alongshore transport of freshwater in a surface-trapped river plume. Journal of Physical Oceanography. 2002;**32**: 957-972. DOI: 10.1175/1520-0485(2002) 032<0957:tatofi>2.0.co;2

[17] Avicola G, Huq P. The characteristics of the recirculating bulge region in coastal buoyant outflows. Journal of Marine Research. 2003;**61**:435-463. DOI: 10.1357/ 002224003322384889

[18] Yankovsky AE, Hickey BM, Munchow AK. Impact of variable inflow on the dynamics of a coastal buoyant plume. Journal of Geophysical Research, Oceans. 2001;**106**:19809-19824. DOI: 10.1029/2001jc000792

[19] Whitney MM, Garvine RW. Wind influence on a coastal buoyant outflow. Journal of Geophysical Research. 2005;**110**:C03014. DOI: 10.1029/ 2003jc002261

[20] Korotenko KA, Osadchiev AA, Zavialov PO, Kao R-C, Ding C-F. Effects of bottom topography on dynamics of river discharges in tidal regions: Case study of twin plumes in Taiwan Strait. Ocean Science. 2014;**10**:865-879. DOI: 10.5194/os-10-863-2014

[21] Yuan Y, Horner-Devine AR, Avener M, Bevan S. The role of periodically varying discharge on river plume structure and transport. Continental Shelf Research. 2018;**158**:15-25. DOI: 10.1016/j.csr.2018.02.009

[22] Geyer WR, Hill P, Milligan T, Traykovski P. The structure of the Eel River plume during floods. Continental Shelf Research. 2000;**20**:2067-2093. DOI: 10.1016/S0278-4343(00)00063-7

[23] Thomas A, Weatherbee RA. Satellite-measured temporal variability of the Columbia River plume. Remote Sensing of Environment. 2006;**100**: 167-178. DOI: 10.1016/j.rse.2005.10.018

[24] Ostrander CE, McManus MA, DeCarlo EH, Mackenzie FT. Temporal and spatial variability of freshwater plumes in a semi-enclosed estuarine– bay system. Estuaries and Coasts. 2008; **31**:192-203. DOI: 10.1007/s12237-007- 9001-z

[25] Osadchiev A, Korshenko E. Small river plumes off the northeastern coast of the Black Sea under average climatic and flooding discharge conditions. Ocean Science. 2017;**13**:465-482. DOI: 10.5194/os-13-465-2017

[26] Vorosmarty C, Askew A, Grabs W, Barry RG, Birkett C, Doll P, et al. Global water data: A newly endangered species. Eos, Transactions of the American Geophysical Union. 2001;**82**:54-58. DOI: 10.1029/01eo00031

[27] Hrachowitz M, Savenije HHG, Bloschl G, McDonnelld JJ, Sivapalan M, Pomeroyg JW, et al. A decade of predictions in ungauged basins (PUB)— A review. Hydrological Sciences Journal. 2013;**58**:1198-1255. DOI: 10.1080/ 02626667.2013.803183

[28] Milliman JD, Syvitski JPM. Geomorphic-tectonic control of sediment discharge to the ocean: The importance of small mountainous rivers. Journal of Geology. 1992;**100**:525-544. DOI: 10.1086/629606

[29] Milliman JD, Farnsworth KL, Albertin CS. Flux and fate of fluvial sediments leaving large islands in the East Indies. Journal of Sea Research.

1999;**41**:97-107. DOI: 10.1016/
s1385-1101(98)00040-9

[30] Mertes LAK, Warrick JA. Measuring
flood output from 110 coastal
watersheds in California with field
measurements and SeaWiFS. Geology.
2001;**29**:659-662. DOI: 10.1130/
0091-7613(2001)029<0659:
mfofcw>2.0.co;2

[31] Wheatcroft RA, Goni MA, Hatten
JA, Pasternack GB, Warrick JA. The role
of effective discharge in the ocean
delivery of particulate organic carbon by
small, mountainous river systems.
Limnology and Oceanography. 2010;**55**:
161-171. DOI: 10.4319/lo.2010.55.1.0161

[32] Kniskern TA, Warrick JA,
Farnsworth KL, Wheatcroft RA, Goni
MA. Coherence of river and ocean
conditions along the US West Coast
during storms. Continental Shelf
Research. 2011;**31**:789-805. DOI:
10.1016/j.csr.2011.01.012

[33] Saldias GS, Largier JL, Mendes R,
Perez-Santos I, Vargas CA, Sobarzo M.
Satellite-measured interannual
variability of turbid river plumes off
central-southern Chile: Spatial patterns
and the influence of climate variability.
Progress in Oceanography. 2016;**146**:
212-222. DOI: 10.1016/j.pocean.
2016.07.007

[34] Meybeck M, Laroche L, Durr HH,
Syvitski JPM. Global variability of daily
total suspended solids and their fluxes in
rivers. Global and Planetary Change.
2003;**39**:65-93. DOI: 10.1016/s0921-8181
(03)00018-3

[35] Brodie J, Schroeder T, Rohde K,
Faithful J, Masters B, Dekker A, et al.
Dispersal of suspended sediments and
nutrients in the Great Barrier Reef
lagoon during river-discharge events:
Conclusions from satellite remote
sensing and concurrent flood-plume
sampling. Marine and Freshwater

Resources. 2010;**61**:651-664. DOI:
10.1071/MF08030

[36] Hilton RG, Galy A, Hovius N,
Horng M-J, Chen H. Efficient transport
of fossil organic carbon to the ocean by
steep mountain rivers: An orogenic
carbon sequestration mechanism.
Geology. 2011;**39**:71-74. DOI: 10.1130/
g31352.1

[37] Bao H, Lee TY, Huang JC, Feng X,
Dai M, Kao SJ. Importance of oceanian
small mountainous rivers (SMRs) in
global land-to-ocean output of lignin
and modern biospheric carbon.
Scientific Reports. 2015;**5**:16217. DOI:
10.1038/srep16217

[38] Romero L, Siegel DA, McWilliams
JC, Uchiyama Y, Jones C. Characterizing
storm water dispersion and dilution
from small coastal streams. Journal of
Geophysical Research, Oceans. 2016;
121:3926-3943. DOI: 10.1002/
2015JC011323

[39] Geyer WR, Beardsley RC, Lentz SJ,
Candela J, Limeburner R, Johns WE,
et al. Physical oceanography of the
Amazon shelf. Continental Shelf
Research. 1996;**16**:575-616. DOI:
10.1016/0278-4343(95)00051-8

[40] Schiller RV, Kourafalou VH, Hogan
P, Walker ND. The dynamics of the
Mississippi River plume: Impact of
topography, wind and offshore forcing
on the fate of plume waters. Journal of
Geophysical Research, Oceans. 2011;
116:C06029. DOI: 10.1029/
2010JC006883

[41] Denamiel C, Budgell WP, Toumi R.
The Congo River plume: Impact of the
forcing on the far-field and near-field
dynamics. Journal of Geophysical
Research, Oceans. 2013;**118**:964-989.
DOI: 10.1002/jgrc.20062

[42] Korotkina OA, Zavialov PO,
Osadchiev AA. Submesoscale variability
of the current and wind fields in the

coastal region of Sochi. Oceanology. 2011;**51**:745-754. DOI: 10.1134/s0001437011050109

[43] Korotkina OA, Zavialov PO, Osadchiev AA. Synoptic variability of currents in the coastal waters of Sochi. Oceanology. 2014;**54**:545-556. DOI: 10.1134/s0001437014040079

[44] Osadchiev AA, Zavialov PO. Lagrangian model of a surface-advected river plume. Continental Shelf Research. 2013;**58**:96-106. DOI: 10.1016/j.csr.2013.03.010

[45] Zavialov PO, Makkaveev PN, Konovalov BV, Osadchiev AA, Khlebopashev PV, Pelevin VV, et al. Hydrophysical and hydrochemical characteristics of the sea areas adjacent to the estuaries of small rivers if the Russian coast of the Black Sea. Oceanology. 2014;**54**:265-280. DOI: 10.1134/s0001437014030151

[46] Osadchiev AA. A method for quantifying freshwater discharge rates from satellite observations and Lagrangian numerical modeling of river plumes. Environmental Research Letters. 2015;**10**:085009. DOI: 10.1088/1748-9326/10/8/085009

[47] Osadchiev AA. Estimation of river discharge based on remote sensing of a river plume. Proceedings of SPIE. 2015;**9638**:96380H. DOI: 10.1117/12.2192672

[48] Osadchiev AA, Korotenko KA, Zavialov PO, Chiang W-S, Liu C-C. Transport and bottom accumulation of fine river sediments under typhoon conditions and associated submarine landslides: Case study of the Peinan River, Taiwan. Natural Hazards and Earth System Sciences. 2016;**16**:51-54. DOI: 10.5194/nhess-16-41-2016

[49] Ross ON, Sharples J. Recipe for 1-D Lagrangian particle tracking models in space-varying diffusivity. Limnology and Oceanography: Methods. 2004;**2**:289-302. DOI: 10.4319/lom.2004.2.289

[50] Smagorinsky J. General circulation experiments with the primitive equation. 1. The basic experiment. Monthly Weather Review. 1963;**91**:99-165. DOI: 10.1175/1520-0493(1963)091<0099:GCEWTP>2.3.CO;2

[51] Large WG, McWilliams JC, Doney SC. Oceanic vertical mixing: A review and a model with a nonlocal boundary layer parameterization. Reviews of Geophysics. 1994;**32**:363-403. DOI: 10.1029/94RG01872

[52] Jaoshvili S. The rivers of the Black Sea. In: Chomeriki I, Gigineishvili G, Kordzadze A, editors. European Environmental Agency, Technical Report No. 71. 2002. Available from: https://www.eea.europa.eu/publications/technical_report_2002_71/at_download/file [Accessed: 15 April 2019]

[53] Osadchiev AA, Sedakov RO. Spreading dynamics of small river plumes off the northeastern coast of the Black Sea observed by Landsat 8 and Sentinel-2. Remote Sensing of Environment. 2019;**221**:522-533. DOI: 10.1016/j.rse.2018.11.043

[54] Yankovsky AE, Chapman DC. A simple theory for the fate of buoyant coastal discharges. Journal of Physical Oceanography. 1997;**27**:1386-1401. DOI: 10.1175/1520-0485(1997)027<1386:astftf>2.0.co;2

[55] Nof D, Pichevin T. The ballooning of outflows. Journal of Physical Oceanography. 2001;**31**:3045-3058. DOI: 10.1175/1520-0485(2001)031<3045:tboo>2.0.co;2

[56] MacDonald DG, Goodman L, Hetland RD. Turbulent dissipation in a near-field river plume: A comparison of control volume and microstructure with a numerical model. Journal of Geophysical Research. 2007;**112**:C07026. DOI: 10.1029/2006JC004075

[57] Chant RJ, Wilkin J, Zhang W, Choi B-J, Hunter E, Castelao R, et al.

Dispersal of the Hudson River plume in the New York Bight: Synthesis of observational and numerical studies during LaTTE. Oceanography. 2008; **21**:148-161. DOI: 10.5670/oceanog. 2008.11

[58] Liu Y, MacCready P, Hickey BM, Dever EP, Kosro PM, Banas NS. Evaluation of a coastal ocean circulation model for the Columbia River plume in summer 2004. Journal of Geophysical Research. 2009;**114**:C00B04. DOI: 10.1029/2008gl036447

[59] Bourrin F, Friend PL, Amos CL, Manca E, Ulses C, Palanques A, et al. Sediment dispersal from a typical Mediterranean flood: The Têt River, Gulf of Lions. Continental Shelf Research. 2008;**28**:1895-1910. DOI: 10.1016/j.csr.2008.06.005

[60] Zhao J, Gong W, Shen J. The effect of wind on the dispersal of a tropical small river plume. Frontiers of Earth Science. 2018;**12**:170-190. DOI: 10.1007/s11707-016-0628-6

[61] Zhurbas NV. The wind-induced drift velocity of the freshwater layer on the sea's surface. Oceanology. 2013;**53**:136-144. DOI: 10.1134/s0001437013020161

[62] Choi BJ, Wilkin JL. The effect of wind on the dispersal of the Hudson River plume. Journal of Physical Oceanography. 2007;**37**:1878-1897. DOI: 10.1175/JPO3081.1, 2007

[63] Xia M, Xie L, Pietrafesa LJ. Modeling of the Cape Fear River estuary plume. Estuaries and Coasts. 2007;**30**:698-709. DOI: 10.1007/BF02841966

[64] Xia M, Xie L, Pietrafesa LJ, Whitney MM. The ideal response of a Gulf of Mexico estuary plume to wind forcing: Its connection with salt flux and a Lagrangian view. Journal of Geophysical Research, Oceans. 2011;**116**:C08035. DOI: 10.1029/2010JC006689

[65] Jurisa JT, Chant R. The coupled Hudson River estuarine-plume response to variable wind and river forcings. Ocean Dynamics. 2012;**62**:771-784. DOI: 10.1007/s10236-012-0527-7

[66] Rennie SE, Largier JL, Lentz SJ. Observations of a pulsed buoyancy current downstream of Chesapeake Bay. Journal of Geophysical Research. 1999; **104**:18227-18240. DOI: 10.1029/1999JC900153

[67] Pullen JD, Allen JS. Modeling studies of the coastal circulation off northern California: Shelf response to a major Eel River flood event. Continental Shelf Research. 2000;**20**:2213-2238. DOI: 10.1016/S0278-4343(00)00068-6

[68] Johnson D, Weidemann A, Arnone R, Davis C. Chesapeake Bay outflow plume and coastal upwelling events: Physical and optical properties. Journal of Geophysical Research. 2001;**106**: 11613-11622. DOI: 10.1029/1999JC000185

[69] Alexeevsky NI, Magritsky DV, Koltermann KP, Krylenko IN, Toropov PA. Causes and systematics of inundations of the Krasnodar territory on the Russian Black Sea coast. Natural Hazards and Earth System Sciences. 2016;**16**:1289-1308. DOI: 10.5194/nhess-16-1289-2016

[70] Zalesny VB, Diansky NA, Fomin VV, Moshonkin SN, Demyshev SG. Numerical model of the circulation of the Black Sea and the Sea of Azov. Russian Journal of Numerical and Analytical Mathematical Modelling. 2012;**27**:95-112. DOI: 10.1515/rnam-2012-0006

[71] Zalesny VB, Gusev AV, Moshonkin SN. Numerical model of the hydrodynamics of the Black Sea and the Sea of Azov with variational initialization of temperature and salinity. Izvestiya Atmospheric and Oceanic Physics. 2013;**49**:642-658. DOI: 10.1134/S0001433813060133

[72] Osadchiev AA. Small mountainous rivers generate high-frequency internal waves in coastal ocean. Scientific Reports. 2018;**8**:16609. DOI: 10.1038/ s41598-018-35070-7

[73] Nezlin NP, DiGiacomo PM, Stein ED, Ackerman D. Stormwater runoff plumes observed by SeaWiFS radiometer in the Southern California Bight. Remote Sensing of Environment. 2005;**98**:494-510. DOI: 10.1016/j. rse.2005.08.008

Chapter 6

Circulations in the Pearl River Estuary: Observation and Modeling

Jiayi Pan, Wenfeng Lai and Adam Thomas Devlin

Abstract

This chapter reports a cruise survey on the Pearl River Estuary (PRE) and adjacent costal water in the period between May 3, 2014 and May 11, 2014. The circulation and salinity structure were sampled for different tidal phases. With the cruise data, a "sandwich" structure of the lateral salinity distribution and a two-layer structure of longitudinal circulation were identified, together with high variations influenced by wind and tide. Furthermore, longitudinally orientated convergence or divergence of the lateral velocity close to the channel location for certain tidal conditions was observed. The finite volume community ocean model (FVCOM) is configured and run with high spatial resolution of 100 m in the PRE. An atmospheric model, the Weather Research and Forecasting (WRF) Model, is also run to provide high spatial and temporal resolution of atmospheric forcing for the FVCOM. The FVCOM modeling skill assessment is conducted using the cruise salinity and velocity data, as well as water levels, showing that the model can well simulate the velocity and salinity structures. The numerical model reveals that there is a strong neap-spring cycle for the PRE de-tided circulation with 0.37 m s^{-1} during the neap tide about 42% stronger than that (0.26 m s^{-1}) during the spring tide in the surface layer.

Keywords: Pearl River Estuary, cruise observation, FVCOM, estuarine circulation

1. Introduction

The Pearl River Estuary (PRE) is located along the coast of Guangdong Province in China between 113°E and 115°E and 21°N and 23°N, in a trumpet-like shape with a width of ∼5 km at the northern (upper) end and ∼35 km at the southern (lower) end (**Figure 1**). The Pearl River freshwater flows into the northern South China Sea (NSCS) through eight inlets, named Modaomen, Humen, Hongqili, Jiaomen, Jitimen, Hengmen, Yamen, and Hutiaomen, with an annual average discharge of 10,000 m^3 s^{-1} [1]. The river discharge reaches a maximum of 20,000 m^3 s^{-1} in the wet summer and has a minimum of 3600 m^3 s^{-1} in the dry winter, combining the discharge of all eight inlets together. In particular, four major inlets (Humen, Jiaomen, Hongqimen, and Hengmen) located along the west shore of the PRE contribute more than half of the total discharge [2]. There are two longitudinal channels in the central region and on the eastern side, connecting the Pearl River Estuary with the NSCS. The east channel connects the coastal water through the
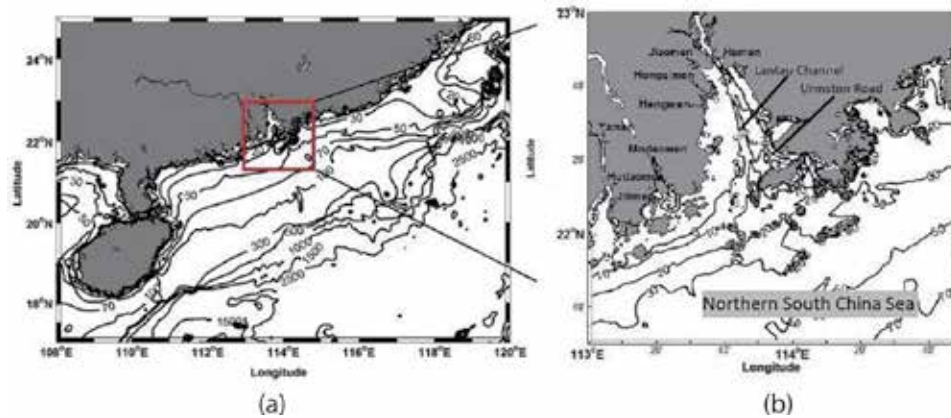
Figure 1.
The northern South China Sea region (a) and the Pearl River estuary (b) with bathymetry contours (meter).

Urmston Road near the east bank of the PRE and the west one through the Lantau Channel along the middle estuary. Except for these channels where the water depth varies between 5 and 15 m, most of the PRE is shallow with a water depth between 2 and 10 m; outside the estuary, the water depth increases to more than 20 m, and the isobaths are approximately parallel with the coastline with a strong cross-shelf gradient on the shelf. Furthermore, the coastline is complex around the PRE and its adjacent shelf, with many small islands scattered around the estuary mouth and coastal bays. These geometric and topographic features can greatly affect the circulation in both the estuary and the coastal region.

Generally, the circulations of the PRE consist of the buoyant gravitational circulation associated with the freshwater discharge and the complicated bathymetry, the tidal currents, and the wind-driven currents [1, 3]. The PRE is a micro-tidal estuary, and the M2 and K1 constituents dominate the tidal currents, which have a 1.0 m tidal range inside the PRE [4]. The mean tidal range just outside the PRE is 0.85–0.95 m [2]. The tidal currents also can change stratification structures in the PRE and play a vital role in the vertical mixing, especially in the shallow near-shore region [5, 6]. Using the Princeton Ocean Model (POM) with curvilinear orthogonal grid to study the Pearl River plume, Wong et al. [3] found that the water column near the head of the estuary becomes well mixing owing to tidal mixing and the moderate southwesterly wind has limited effects on the circulation inside the PRE [3, 7]. The circulation in the upper estuary and northern part of the lower PRE is characterized by the seaward gravitational current. However, the southern part of the lower estuary is governed by the competition between gravitational current and geostrophic intrusive currents from the shelf [5]. Based on cruise survey data and numerical modeling of the PRE for the summer time, Pan et al. [6] revealed the role that wind and tidal forcing play in determining plume dynamical properties and concluded that the density structure in the PRE can be modulated by the wind with strong stratification under the southwesterly wind and weak stratification under the southeasterly wind [8]. Under the southeasterly wind during spring tide, an anticyclonic circulation bulge appeared, with a Kelvin number of 0.93 and a supercritical Froude number of 1.45. Under southwesterly wind during a neap tide, the plume displayed a diffusive front, with a Kelvin number of 2.9 and a Froude number of only 0.07 [8]. The turbulent mixing in PRE is governed by the tidal strength, and the wind stirring tends to increase the internal shear instability mixing in the recirculating plume bulge [6]. Observation and modeling reveal that

strong mixing appeared in the bottom layer on the larger ebb, caused by the vigorous bottom stress.

The spreading of the plume in the surrounding coastal waters is controlled by the wind stress and ambient currents. The easterly or southeasterly wind drives the plume westward, and southerly or southwesterly wind forces the plume eastward [3, 8, 9]. The wind-driven coastal current closely interacts with the estuarine circulation in the lower part of the PRE [1]. Ou used the field measurement data to investigate the dynamics of the buoyant plume near the PRE, suggesting four major horizontal plume types in summer [9]. These types are offshore bulge spreading, westward alongshore spreading, eastward offshore spreading, and symmetrical alongshore spreading. In this chapter, we report detailed cruise observations on the PRE water current and the salinity structure. A numerical model of high spatial resolution is developed in the PRE, which can well simulate the circulations of the PRE.

2. Cruise observation

A hydrographic cruise survey for collecting in situ data of marine environmental parameters in the PRE was conducted during the period between May 3, 2014 and May 11, 2014. The instruments used to collect the in situ data in this cruise survey were a sea surface sampling Seabird CTD (conductivity, temperature, and depth) for sea surface sampling, an RDI 600 kHz acoustic Doppler current profiler (ADCP), and a Sea and Sun Technology CTD. The RDI ADCP was mounted on the right side of the cruise ship. With these instruments, the underway surface
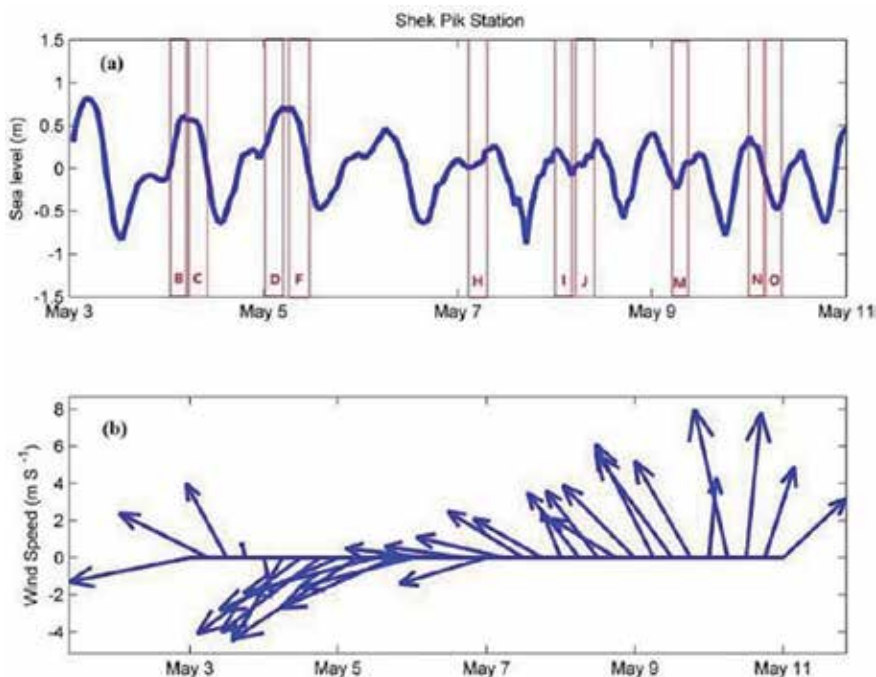
Figure 2.
Time periods of cruise transects together with the sea level at the Shek Pik Station (the location is shown in Figure 3c) (a). The 6-hourly wind condition from the NCEP/NCAR reanalysis data over the PRE (b).

salinity, temperature, density, and underway profiles of currents were collected, and additionally, the CTD profiles at a number of CTD cast stations along the cruise transects were also collected. **Figure 2a** displays the tidal conditions at the Shek Pik Station, located in the south of the Lantau Island near the mouth of the PRE (as shown in **Figure 3c**), and the observed periods of different transects. The 6-hourly wind conditions from the NCEP/NCAR reanalysis data over the PRE region during the cruise period are shown in **Figure 2b**. The cruise transects and CTD cast stations across the PRE are illustrated in **Figure 3**. During this cruise, a typical East Asian monsoon transition process happened with relatively weak wind strength. The northeasterly/easterly winds prevailed during a spring to neap tide transition from May 4, 2014 to May 6, 2014 (**Figure 3a**). From May 7, 2014 to May 9, 2014, the winds turned to be the easterly/southeasterly and the spring tide changed to neap tide (**Figure 3b**), and the southerly/southwesterly winds prevailed during a neap tide from May 10, 2014 to May 11, 2014 (**Figure 3c**).

Table 1 lists the tidal phases and wind conditions during different observed transects. Transects B and D were in flood phases during the spring tide under northeasterly winds, whereas transects C and F were in ebb phases. Transect H was during the flood under the easterly wind. In the neap tide period, transect I was during ebb under the southeasterly wind, whereas Transect J was during on the flood tide. Under the southerly wind, transect M was from flood to ebb, whereas transects N and O were during ebb. This data set has high sampling spatial resolution coverage over the PRE in a spring-neap cycle, which is particularly useful to identify the salinity and circulation characteristics and to validate model results.
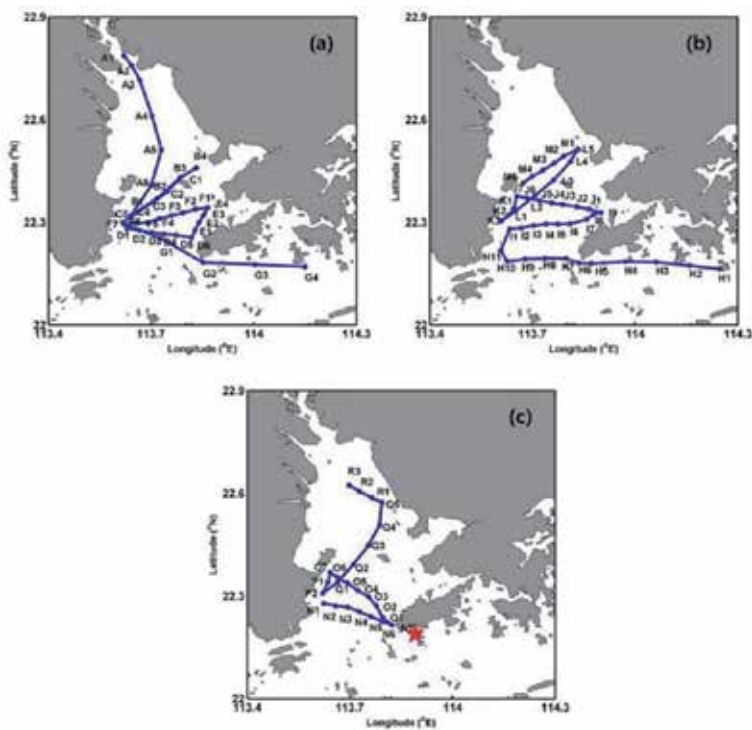
Figure 3.
The cruise transects and the CTD cast stations: Under northeasterly/easterly winds (a), under easterly/ southeasterly winds (b), under southerly/southwesterly winds (c). The red pentagram shows the location of the Shek Pik tide gauge station.

Date and time (local time)	Transect	Tidal phase	Wind
04 May 09:43–13:13	Transect B	Flood/spring	Northeasterly
04 May 13:53–16:16	Transect C	Ebb/spring	Northeasterly
05 May 09:01–11:51	Transect D	Flood/spring	Northeasterly
05 May 14:22–16:45	Transect F	Ebb/spring	Northeasterly
07 May 07:22–15:09	Transect H	Flood/neap	Easterly
08 May 08:58–12:38	Transect I	Ebb/neap	Southeasterly
08 May 13:00–15:23	Transect J	Flood/neap	Southeasterly
09 May 13:50–15:16	Transect M	Flood to ebb/neap	Southerly
10 May 9:00–11:33	Transect N	Ebb/neap	Southerly
10 May 12:00–15:01	Transect O	Ebb/neap	Southerly

Table 1.
Observed tidal phases and wind conditions for different transects.

3. Observation results

3.1 Surface salinity

Figure 4 displays the observed surface salinity along the cruise tracks under the wind mainly in the northeasterly during the spring tide from 4 to 7 May (a) and during the neap tide under the wind mainly in the southerly from May 8, 2014 to May 11, 2014 (b). Under the northeasterly wind during the spring tide, freshwater flowed into the coastal sea mainly on the west side of the estuary due to the Coriolis force and the wind forcing, and high salinity water appeared in mid-estuary of the Lantau Channel, implying a high salinity intrusion along the channel. There was a strong salinity gradient in the cross-estuary direction. When the southerly winds dominated during the neap tide, the surface salinity in the estuary is lower than that under the northeasterly wind during the spring tide in the mid-estuary and on the west side, and the surface low salinity water may further spread to the west side. The asymmetry in the surface spatial distribution of the salinity suggests the influence of the wind and tidal forcing on the estuary stratification. In the spring tide and the easterly wind, the low salinity water is confined on the west side and the stratification is weak, while in the neap tide and southerly wind, the stratification is enhanced. Wind forcing is an obvious factor influencing the spatial surface salinity distribution and the stratification [8]. Another important factor is the tidal mixing that is higher in the spring tide and weaker in the neap tide. The stronger turbulent mixing in the spring tide might further decrease the stratification, resulting in higher horizontal salinity gradient in the cross-estuary direction. In the neap tide, the weaker mixing may facilitate the formation of the stratified water in the PRE.
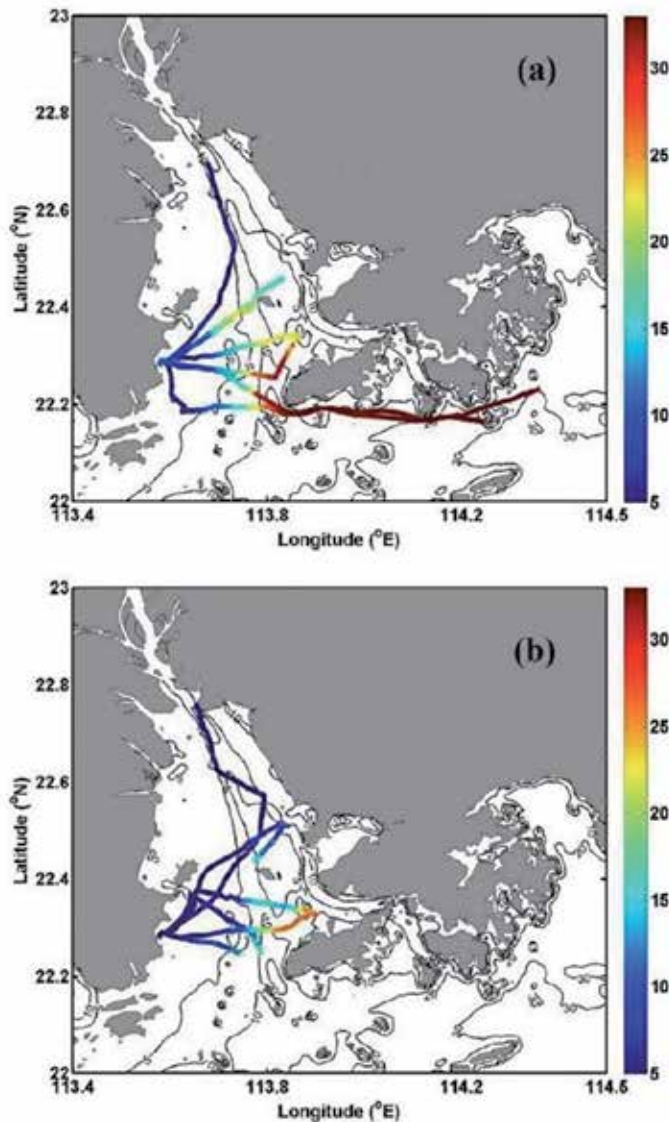
Figure 4.
Observed surface salinity along the cruise tracks under the wind mainly in the northeasterly during spring tide from 4 to 7 May (a) and during neap tide under the wind mainly in the southerly from May 8, 2014 to May 11, 2014 (b).

3.2 Cross-channel salinity distribution and velocity

Figure 5 shows the sectional salinity and current velocity along transects B and C. Transects B and C were under the northeasterly wind during the spring tide on the flood and ebb, respectively. In order to remove high-frequency noises, a 2D rotationally symmetric Gaussian low-pass filter with a (3 × 3) size is used to process the ADCP data. The positive directions of the coordinate system of the current field are in the northward (y) and the eastward (x). Both transects B and C are almost the cross-estuary survey tracks, crossing the Lantau Channel in the mid-estuary. On the flood tide during transect B, the higher salinity water occupied the Lantau Channel, and lower salinity water was located on the two sides (**Figure 5a**). The freshwater was confined on the west side of the estuary; therefore,
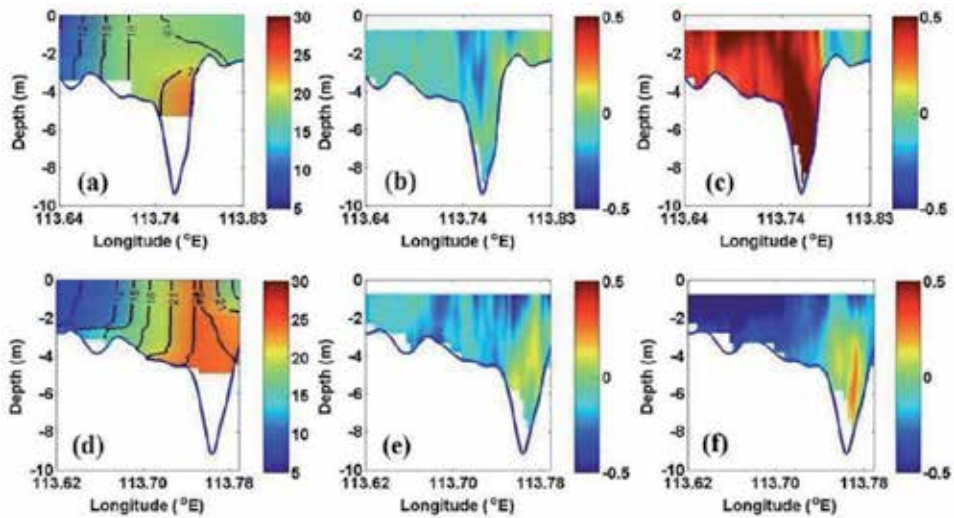
Figure 5.
The sectional salinity (practical salinity unit, psu) (a, d), cross-channel circulation (m s⁻¹) (b, e), and along-channel circulation (m s⁻¹) (c, f) along transects B (upper) and C (lower), respectively.

the salinity on the east side was higher than that on the west side. The isohalines were almost vertical on the west side with relatively strong stratification just in the Lantau Channel. The cross-estuary current was relatively weak with a westward flow at the surface, whereas a velocity divergence appeared in the Lantau Channel, with the eastward (positive) velocity on the east side and westward (negative) velocity on the west side of the Lantau Channel (**Figure 5b**). On the flood tide of transect B, the water flowed into the estuary (northward/landward) with the strongest current on the west side of the Lantau Channel; when the flood tide turned to the ebb tide, the northward current was weaker and reversed on the east side (**Figure 5c**).

When the tide was turning from flood to ebb during transect C, the salinity reached a maximum (more than 24 psu) in the Lantau Channel (**Figure 5d**) (vs. 21 psu for transect B). Furthermore, the turbulent mixing was enhanced in the Lantau Channel, resulting in weak stratification during transect C. On the ebb in transect C, the freshwater flowed out of the estuary with seaward current in the surface, especially on the west side; at the bottom layer in the Lantau Channel, a landward current appeared for the flood to ebb transition (**Figure 5f**). The cross-channel current was highly complex with alternating convergence and divergence (**Figure 5e**).

During both of the transect B and C periods, the high salinity water flowed into the estuary in the deep Lantau Channel, which could facilitate the appearance of the high-density water in the mid-estuary of the Lantau Channel even during the ebb tide. The survey data indicate that the salinity intrusion could exist on the early ebb for transect C at the bottom of the Lantau Channel during the spring tide and northeasterly wind.

Figure 6 displays the sectional salinity and current velocity along transects D and F. Both transects D and F crossed the Lantau Channel in the lower estuary under the northeasterly wind during the spring tide. In the flood period for transect D, the water flowed into the estuary (northward/landward) with the strongest current appearing in Lantau Channel, reflecting the salinity intrusion along the deep channel, except at the surface on the west side, where the water flowed out of estuary (southward/seaward) influenced by the river discharge (**Figure 6c**). Due to
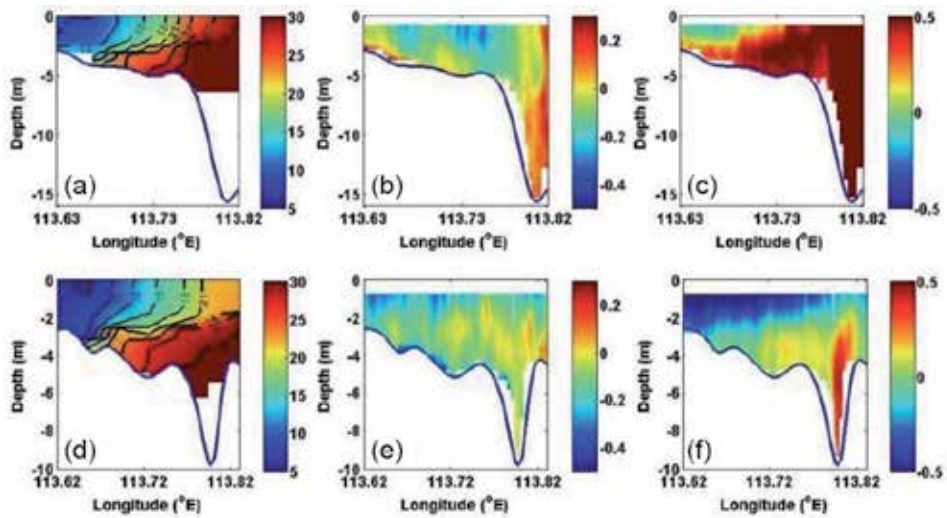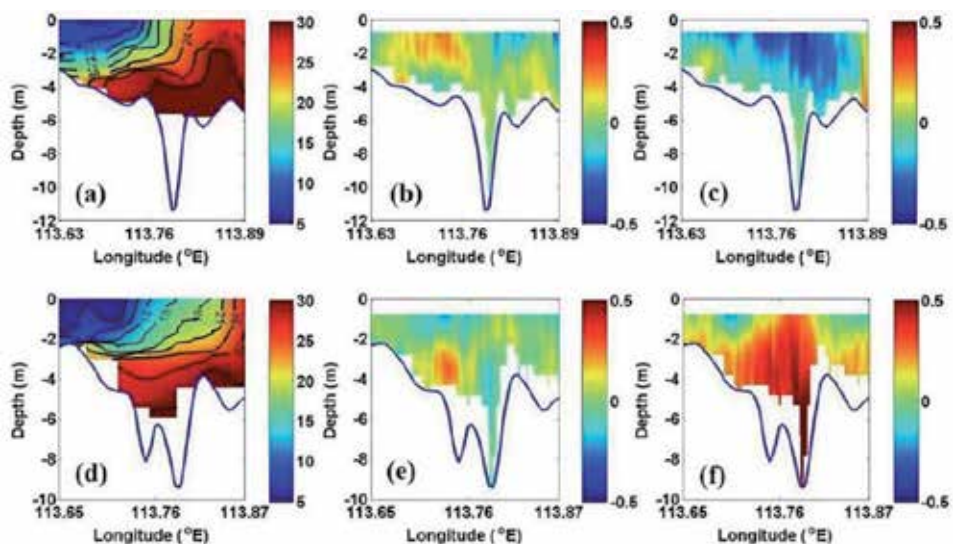
Figure 6.
The sectional salinity (psu) (a, d), cross-channel circulation (m s⁻¹) (b, e), and along-channel circulation (m s⁻¹) (c, f) along transects D (upper) and F (lower), respectively.

flood tide during transect D, the inflow might bring high salinity water into the estuary especially in the Lantau Channel. This flow pattern might cause the strong density gradient in the cross-estuary direction (**Figure 6a**). The low salinity water resided on the estuary west side, and the high salinity water was located on the east side. In the cross-estuary direction, the westward current appeared throughout the whole depth of the water column, implying that the cross-estuary surface current was induced by the northeasterly wind, while in the deep Lantau Channel, a velocity divergence appeared with eastward (positive) velocity on the east side and westward (negative) velocity on the west side of the deep channel (**Figure 6b**) [10].

On the ebb tide during transect F, the maximum seaward (southward) flow in the surface layer reached as large as 0.8 m s⁻¹ with a weak current on the east side of the estuary. However, the bottom water flowed landward (northward) into the estuary, especially in the channel (**Figure 6f**). This was typical of a two-layer structure of density-driven estuarine circulation. Compared with transect D on the flood, the salinity gradient was weak and showed the two-layer structure, although the general pattern of the west low and east high salinity still appeared (**Figure 6d**). The cross-estuary velocity exhibited weak westward flow at the surface and strong eastward flow beneath the surface, related to the wind-driven current in the estuary (**Figure 6e**).

The observation suggests the salinity intrusion existed both for the flood (transect D) and ebb tide (F) same as that for transects B and C. However, different from the observation from transects B and C, the low salinity water further expanded to the east side of the estuary. This may be due to the fact that the seaward flow appeared on the west side both for the flood (transect D) and ebb (transect F) periods.

Transect H surveyed near the estuary mouth and south of Hong Kong Island under the easterly wind. **Figure 7** shows the sectional salinity and current velocity along transect H. Near the mouth, low salinity water resided in the whole surface layer (west of 113.87°E) and high salinity water in the bottom layer, while east of 113.87°E, the vertical sectional salinity was well-mixed with the coastal water, indicating that the plume water was appearing most of the surface layer in the estuary mouth (**Figure 7a**). In the along-estuary direction, water flowed into the
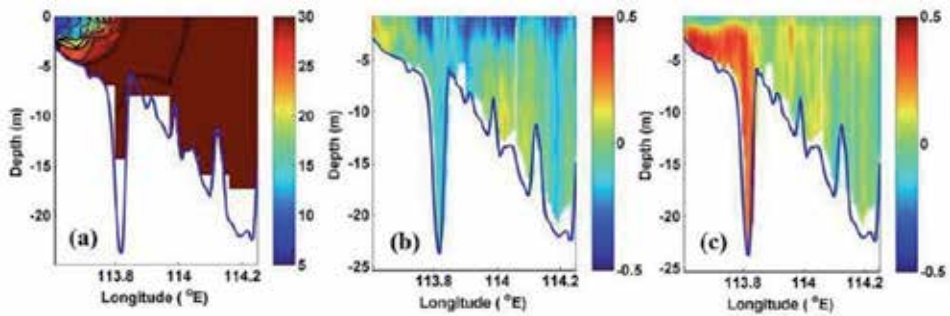
Figure 7.
The sectional salinity (psu) (a), cross-channel circulation (m s⁻¹) (b), and along-channel circulation (m s⁻¹) (c) along transect H.

estuary (northward/landward) during the flood tide (**Figure 7c**). At the surface in the estuary mouth, the water flowed out of estuary (southward/seaward), as it was influenced by the river discharge. In the cross-estuary direction, there appeared a strong westward current on the surface, indicating a wind-driven current induced by the easterly wind. However, a strong eastward current was found in the surface of the estuary mouth due to the plume water spreading, resulting in a velocity convergence at the plume water boundary, indicating a supercritical plume front at the plume boundary (**Figure 7b**).

During the neap tide period, the wind direction changed from the northeasterly to the southeasterly, and the easterly wind component was weaker than that in the spring tide (**Figure 3b**). The sectional salinity and current velocity along transects I and J are displayed in **Figure 8**. During the ebb tide of transect I, the upper layer water flowed out of the estuary (southward/seaward), with a strong current in Lantau Channel, while there was a bottom current flowing into the estuary (**Figure 8c**). In the cross-estuary direction, on the surface of the deep channel, there appeared a strong velocity convergence, an eastward current on the west side and a

Figure 8.
The sectional salinity (psu) (a, d), cross-channel circulation (m s⁻¹) (b, e), and along-channel circulation (m s⁻¹) (c, f) along transects I (upper) and J (lower), respectively.

westward current on the east side, with a weak velocity divergence on the left of the channel at the bottom (**Figure 8b**) [10]. The salinity had a sharp gradient at the velocity convergence location of 113.80°E. The salinity front was more apparent as compared with that during flood tide (**Figure 8a**).

In the early flood of transect J, the current was landward/northward (into the estuary) in Lantau Channel, while outside the channel on both sides, the water flowed seaward/southward (out of the estuary), especially in the surface layer (**Figure 8f**). In the cross-estuary direction, a velocity convergence appeared on the west side of the Lantau Channel in the bottom layer (**Figure 8e**). The density structure had still kept an ebb-like structure for a while until flood tide returned in this early flood.

4. Numerical model and settings

4.1 The finite volume community ocean model (FVCOM)

The FVCOM is a 3D unstructured-grid, free-surface, primitive equation, finite volume coastal ocean and estuarine circulation model with triangular grids in the horizontal and terrain-following coordinates in the vertical and wet/dry treatment, developed originally by the University of Massachusetts Dartmouth (UMASSD) and improved by the efforts of Woods Hole Oceanographic Institution (WHOI) [11–13]. The finite volume approach used in FVCOM, combined with a flexible unstructured grid, provides a better representation of mass, salt, momentum, and heat conservation in an estuarine area with irregular coastline and geography than that used in a rectangular grid system. Mode-split or semi-implicit schemes can choose to solve the governing equations in Cartesian or spherical coordinates. The governing equations, including momentum, continuity, temperature, salinity, and density equations, are closed by using the Mellor and Yamada level 2.5 (MY-2.5) turbulence closure for vertical eddy viscosity [14], or the Smagorinsky eddy parameterization for the computation of the horizontal diffusion [15], as well as an alternative selection of the General Ocean Turbulence Model (GOTM) [16]. For more computational speed, a "mode-splitting" time-stepping scheme is employed to solve the integration process, dividing into internal and external modes with two different time steps. FVCOM has been widely used in estuarine circulation and river plume dynamic studies worldwide, such as the Pearl River Estuary [17], Changjiang River [18, 19], Okatee River [20], Puget Sound estuarine system [21], and Tampa Bay [22].

4.2 FVCOM settings

In the FVCOM, the horizontal grid uses unstructured triangular cells, and the realistic topography is represented using terrain-following coordinates. The greatest advantage of this model is its geometric flexibility since it uses the unstructured and triangular grid meshes, which can provide a real fitting of the irregular coastal boundary. **Figure 9a** shows the unstructured triangular model grids of the FVCOM for the PRE and coastal water regions. The model domain (111.5–116.5°E, 20–23°N) covers the entire Pearl River Estuary with an open boundary in the northern South China Sea. The total node number in the model grid is 41,027 with 78,539 cells. The horizontal grids have spatial resolutions that vary from 0.1 km to 10 km over the entire domain, with 0.1–0.3 km inside the Pearl River Estuary, 0.3–0.5 km in the estuary mouth, 1.0–2.0 km in the Guangdong coastal water, and 10 km close to the open boundary. The vertical coordinate has 20 levels in uniform hybrid
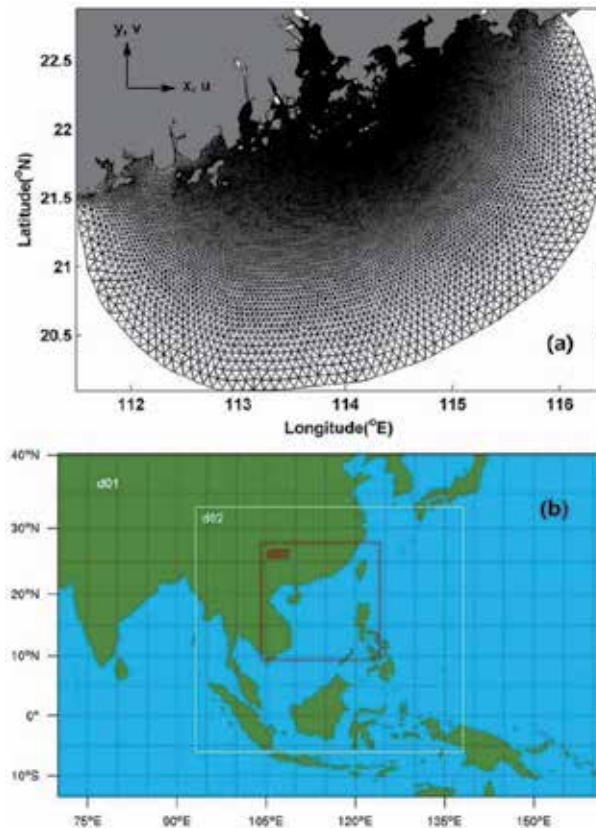
Figure 9.
Model domains for the FVCOM (a) and the WRF model (b).

terrain-following grids. The numerical simulations are run for the period from March 1, 2014 to May 30, 2014, during which the observations obtained from the cruise survey conducted between May 3, 2014 and May 11, 2014 were available for model comparisons.

Tidal forcing is applied to the open boundary including the eight major tidal constituents of M2, N2, S2, K2, K1, O1, P1, and Q1, which are obtained through interpolation from the 1/6° inverse tidal model results of [23], together with the salinity, temperature, and velocity on the open boundary from Hybrid Coordinate Ocean Model (HYCOM) (https://hycom.org/dataserver/glb-analysis) outputs. The meteorological forcing including the wind stress, net heat flux, and evaporation-precipitation (E-P) balance is generated by the Weather Research and Forecasting (WRF) Model. The monthly means of freshwater discharges from the eight river inlets constitute the lateral boundary conditions on the land side [2, 7]. The model is initialized with the March climatology of salinity and temperature fields derived from the World Ocean Atlas 2009 (WOA2009) (https://www.nodc.noaa.gov/OC5/WOA09/pr_woa09.html) and spun up from zero velocity and an undisturbed sea surface elevation. The topographic data for the FVCOM model are derived by interpolation of an electronic navigation chart data for the estuary and coastal water area, and for the offshore region, they are obtained from the global bathymetry data of the General Bathymetric Chart of the Oceans (GEBCO) (http://www.gebco.net/) with 30 seconds (1/120°) horizontal resolution.

The temporal integration of the model uses a split-mode time-stepping method with a 2-second external time step and a split number of 5. The wet/dry treatment is

used since some upstream coastal areas can be inundated in high tide. The MY-2.5 and Smagorinsky turbulent closure schemes are used for vertical and horizontal mixing, respectively [14, 15].

In addition to the ocean model, an atmospheric model, the WRF Model, is implemented to provide high spatial and temporal resolution atmospheric forcing for the FVCOM. The WRF Model is supported and developed by the National Center for Atmospheric Research (NCAR), the National Centers for Environmental Prediction (NCEP), the Air Force Weather Agency (AFWA), the Naval Research Laboratory, the University of Oklahoma, and the Federal Aviation Administration (FAA) in the USA. This model is a next-generation mesoscale numerical weather forecasting system that was designed to serve both weather forecasting and atmospheric research needs [24]. A dynamical downscaling technique is employed in the WRF for the regional atmospheric modeling to obtain a higher-resolution output. To realize this, a three-domain nested configuration is designed, as shown in **Figure 9b**. The outer domain, d01 for the atmospheric model, covers the western Pacific Ocean, the entire South China Sea, and the eastern Indian Ocean, with a horizontal resolution of 72 km; the middle domain, d02, covers the entire South China Sea and southern China, with a horizontal resolution of 24 km; the inner domain, d03, covers the northern South China Sea with a horizontal resolution of 8 km. All domains have 27 layers in the vertical. The NCEP FNL Operational Global Analysis data (http://rda.ucar.edu/datasets/ds083.2/) with a horizontal resolution of $1° \times 1°$ is used to provide initial conditions and lateral boundary conditions for the outer domain. The physics options of the WRF model include the Ferrier microphysics scheme [25], RRTM longwave radiation scheme [26], Dudhia shortwave scheme [27], YSU PBL scheme [28], and Kain-Fritsch cumulus scheme [29]. The model simulation period is from April 20, 2014 to May 30, 2014 covering the cruise survey period. The sea surface winds from the inner domain of WRF model are used to drive the ocean model.

5. Model validation

For the modeling, the coordinate is shown in **Figure 9a** with the eastward as the positive x-axis and u velocity, the northward as the positive y-axis and v velocity, and the upward as the positive z-axis and w velocity. Since the PRE is generally along the meridional direction, we choose the u to represent the cross-estuary velocity and the v the along-estuary velocity.

The comparison of the cruise observations and FVCOM modeling salinity profiles at a number of stations (B3, D4, D6, F2, G2, G3, H3, H8, I5, J3, M3, and N7 illustrated in **Figure 2**) is shown in **Figure 10**. It reveals good agreements between the observations and modeled salinity profiles except at B3, D6, H8, J3, and N7, where the model underestimates the salinity profiles. B3, D6, and N7 were close to coastal land (or island), which may affect the simulation results. Another possible reason is that the river discharge used for the modeling is the climatological data that may not represent the actual discharges, which can cause biases in the salinity profiles between the modeling results and the observations.

The comparison of sea levels between the model results and observations at eight tide gauge stations from 1 to 30 May is shown in **Figure 11**. The locations of the tide gauge stations are shown in **Figure 12**. The hourly tide gauge sea level data during the period between May 1, 2014 and May 3, 2014 are provided by the Hong Kong Observatory (HKO) and Marine Department for the model validation. The
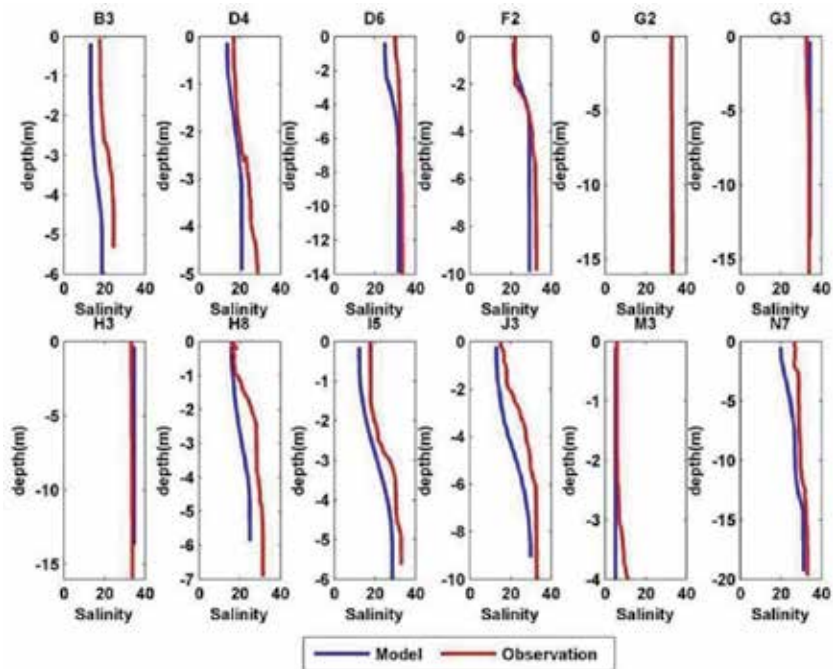
Figure 10.
Comparison of the modeling salinity profiles (blue lines) with the cruise observation (red lines).

modeled sea levels agree well with the observed records both at spring and neap tides for this period.

To further quantify the accuracy of model results, four statistical parameters are calculated, namely, root-mean-square (RMS) error, relative average error (RE), correlation coefficient, and the model skill parameter used by [30].

The RMS error is defined as:

$$\text{RMS} = \left\{ \frac{1}{N} \sum_{i=1}^{N} (\eta_{\text{mo}} - \eta_{\text{ob}})^2 \right\}^{1/2} \tag{1}$$

The relative average error (E) is defined as:

$$E = \frac{\sum_{i=1}^{N} (\eta_{\text{mo}} - \eta_{\text{ob}})^2}{\sum_{i=1}^{N} \left\{ (\eta_{\text{mo}} - \overline{\eta}_{\text{mo}})^2 + (\eta_{\text{ob}} - \overline{\eta}_{\text{ob}})^2 \right\}} \times 100\% \tag{2}$$

The correlation coefficient is defined as:

$$R = \frac{\sum_{i=1}^{N} \left\{ (\eta_{\text{mo}} - \overline{\eta}_{\text{mo}})(\eta_{\text{ob}} - \overline{\eta}_{\text{ob}}) \right\}}{\left[\sum_{i=1}^{N} (\eta_{\text{mo}} - \overline{\eta}_{\text{mo}})^2 \sum_{i=1}^{N} (\eta_{\text{ob}} - \overline{\eta}_{\text{ob}})^2 \right]^{1/2}} \tag{3}$$

The model skill parameter is:

$$\text{Skill} = 1 - \frac{\sum_{i=1}^{N} (\eta_{\text{mo}} - \eta_{\text{ob}})^2}{\sum_{i=1}^{N} (|\eta_{\text{mo}} - \overline{\eta}_{\text{ob}}| + |\eta_{\text{ob}} - \overline{\eta}_{\text{ob}}|)^2}, \tag{4}$$
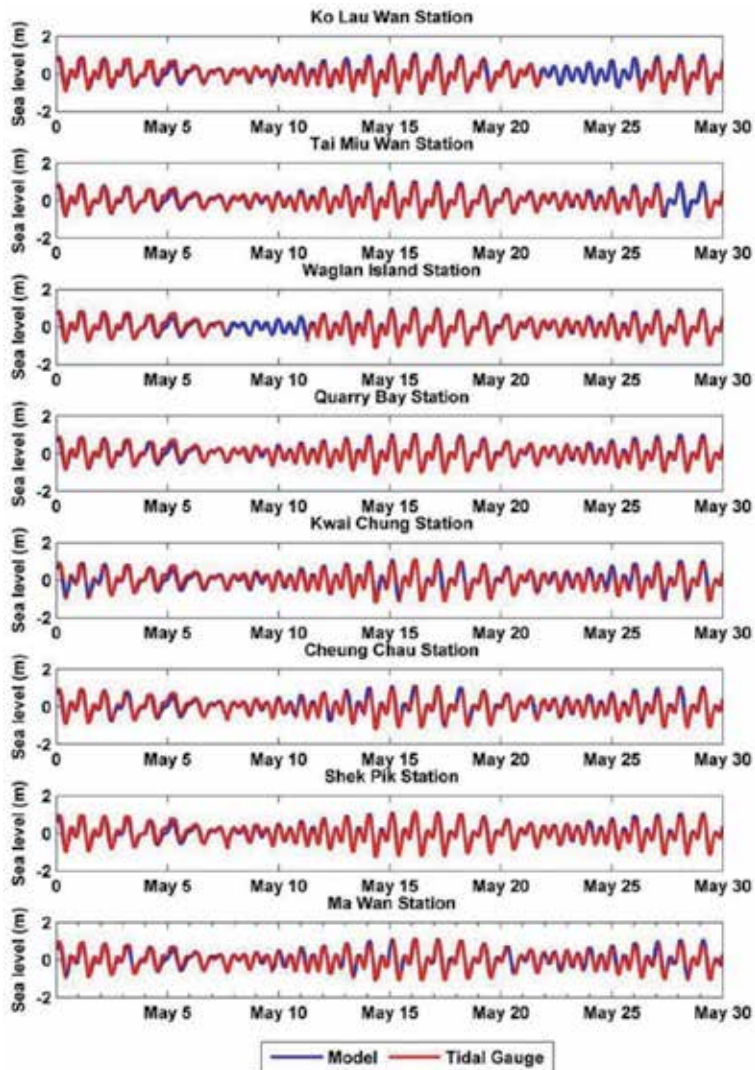
Figure 11.
Comparison of modeled (blue lines) and observed (red lines) sea surface elevations at eight tidal gauge stations.

where η_{mo} and η_{ob} represent the model sea level data and the observations, respectively, and the overbar denotes the temporal average. N is the number of records.

Table 2 provides the validation results at the eight tidal gauge stations. The RMS errors are less than 0.15 m, and the relative average errors are less than 3% except at the Ko Lau Wan Station. The correlation coefficients are higher than 0.97, and the skill parameters reach 0.98. Based on the skill assessment results, the model works well in simulating the sea level variations.

Figure 13 presents the comparison of cross-estuary and along-estuary velocities between the cruise observations and FVCOM modeling for transects D and I. The observation duration of transect D was in the flood tide with the northeasterly wind. In the cross-estuary direction, for transect D, the modeled velocity agrees well with the observation, which reveals that the lateral current flows westward (negative) on the left side of the Lantau Channel and eastward
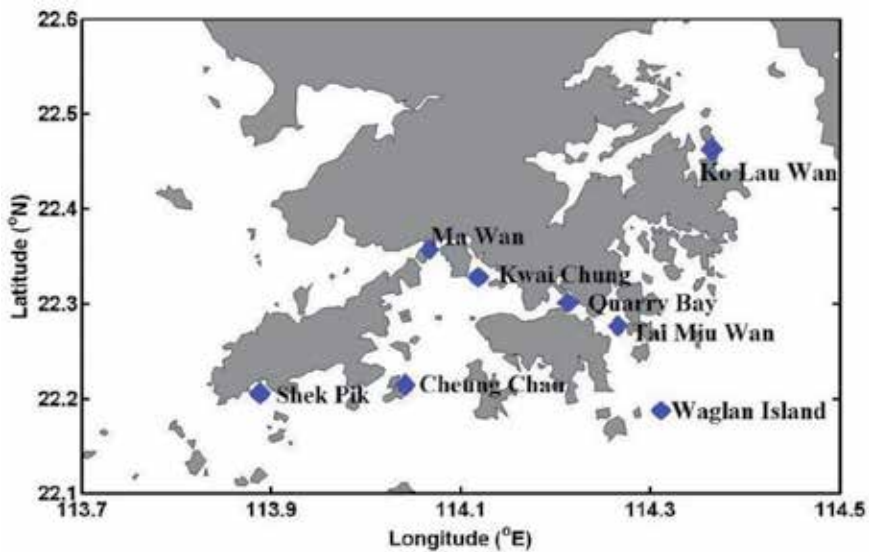
Figure 12.
The locations of the tide gauge stations.

	Kwai Chung	Cheung Chau	Shek Pik	Ma Wan	Ko Lau Wan	Tai Miu Wan	Waglan Island	Quarry Bay
RMS (m)	0.11	0.09	0.10	0.09	0.15	0.10	0.11	0.10
RE (%)	2.8	2.1	2.1	2.0	5.3	3.5	2.9	2.9
CC	0.97	0.98	0.99	0.98	0.95	0.97	0.97	0.97
Skill	0.99	0.99	0.99	0.99	0.97	0.98	0.99	0.99

Table 2.
The RMS error, RE, correlation coefficient (CC), and the skill assessment parameter (skill).

(positive) on the right, forming a divergence on the deep channel, although the modeled current speed has some biases from the observed speed, especially for the eastward flow in the Lantau Channel where the modeling underestimates the current (**Figure 13a** vs. **Figure 13b**). In the along-estuary direction for transect D, the modeled current flows northward with maximum velocity in the surface at the Lantau Channel location, in accordance with the observed current (**Figure 13c** vs. **Figure 13d**). For transect I with the southeasterly wind during the ebb tide, there was a velocity convergence occurred in the Lantau Channel in the cross-estuary direction as revealed in both observations and modeling (**Figure 13e** vs. **Figure 13f**). In the along-estuary direction, the modeled velocity agrees well with the observations, and both of the observations and modeling show that the exchange flows exist along the estuary with the strong seaward current in the surface and weak landward current in the bottom (**Figure 13g** vs. **Figure 13h**). Since the smoothed topography is applied to the modeling, the simulated velocity is spatially less varied than that from the observation; however, the general patterns of the modeling velocity and the observed velocity are similar and consistent, indicating that the FVCOM modeling can well simulate the estuarine water dynamics of the PRE.
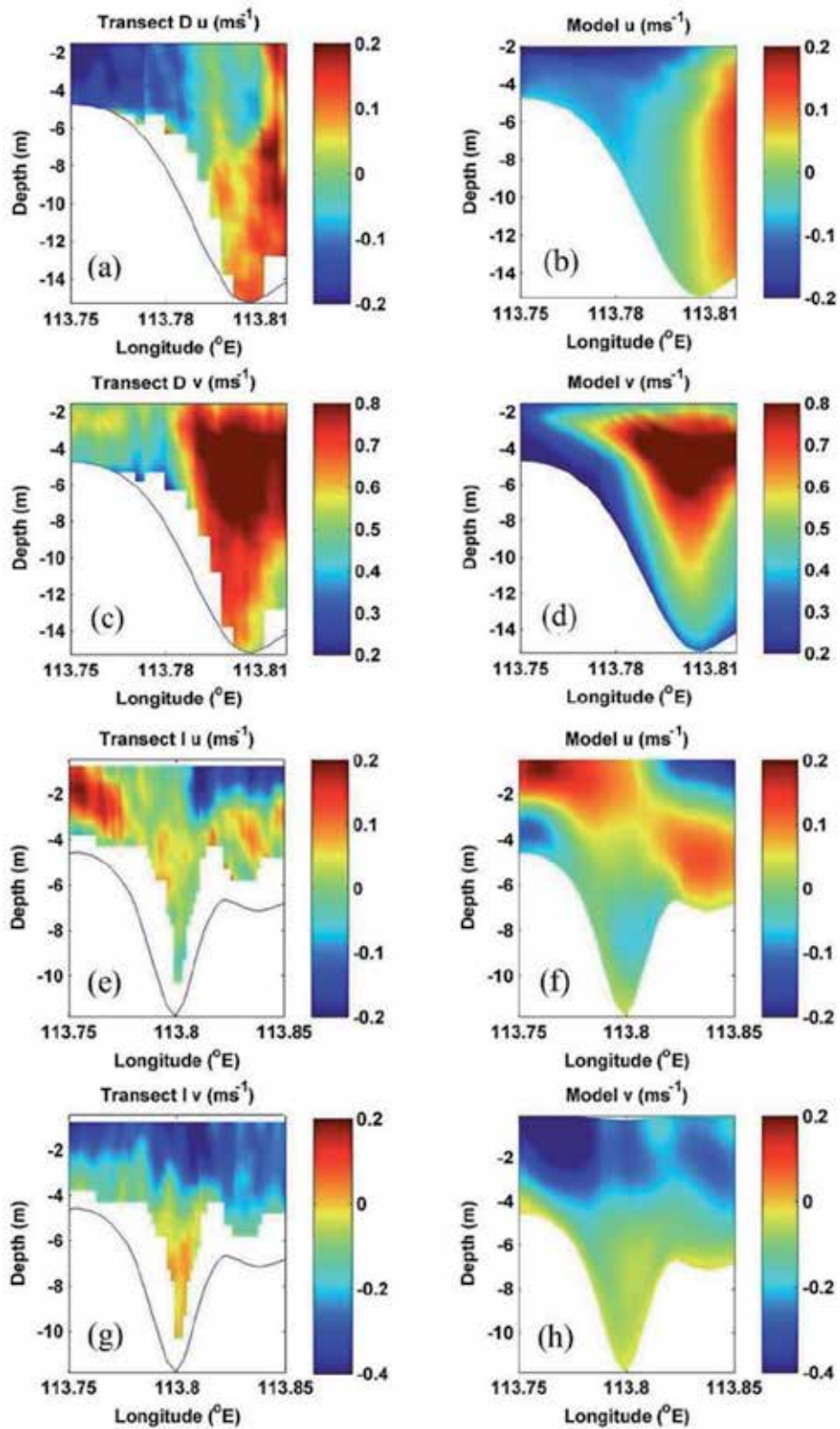
Figure 13.
The cruise-observed cross-estuary (a for Transect D, e for Transect I) and along-estuary (c for Transect D, g for Transect I) velocities vs. the model cross-estuary (b for Transect D, f for Transect I) and along-estuary (d for Transect D, h for Transect I) velocities.

6. Variation of estuarine circulation in the PRE

In order to identify the variation of the longitudinal circulation in the spring and neap tide cycle in the PRE, the wind forcing is withdrawn in a modeling run of the FVCOM in the PRE, and modeling results without wind forcing are generated. To remove tidal oscillations, a 25-hour low-pass filter is applied to the modeling outputs of the velocity, salinity, and eddy viscosity. An along-estuary and cross-estuary sections are selected to display modeling results, as shown in **Figure 14**.

6.1 Along-estuary circulations

Figure 15 illustrates the tidally averaged along-estuary velocity, salinity, and vertical viscosity for the spring and neap tides along the Lantau Channel section. A prominent two-layer exchange flow is shown, with seaward current in the surface and landward current in the bottom (**Figure 15a, b**). The maximum surface seaward current speed is 0.37 m s^{-1} during the neap tide about 42% stronger than that (0.26 m s^{-1}) during the spring tide in the lower estuary. The bottom landward current is weaker in the spring tide than that in the neap tide. This suggests that the exchange circulation is stronger in the neap tide than that in the spring tide. However, although the bottom landward current is weaker in the spring tide, it may extend farther landward toward the estuary head (**Figure 15a** vs. **Figure 15b**).

Vertical salinity difference of 2–4 psu appears in the estuary during the spring, whereas it is 4–10 psu during the neap tide, revealing that the stratification during the neap tide is stronger than that during the spring (**Figure 15c** vs. **Figure 15d**). The maximum stratification is located in the middle of the estuary, and the well-mixed freshwater appears in the upper estuary from 22.5°N during both the spring and the neap tide. It is obvious that the surface salinity is higher in the spring tide
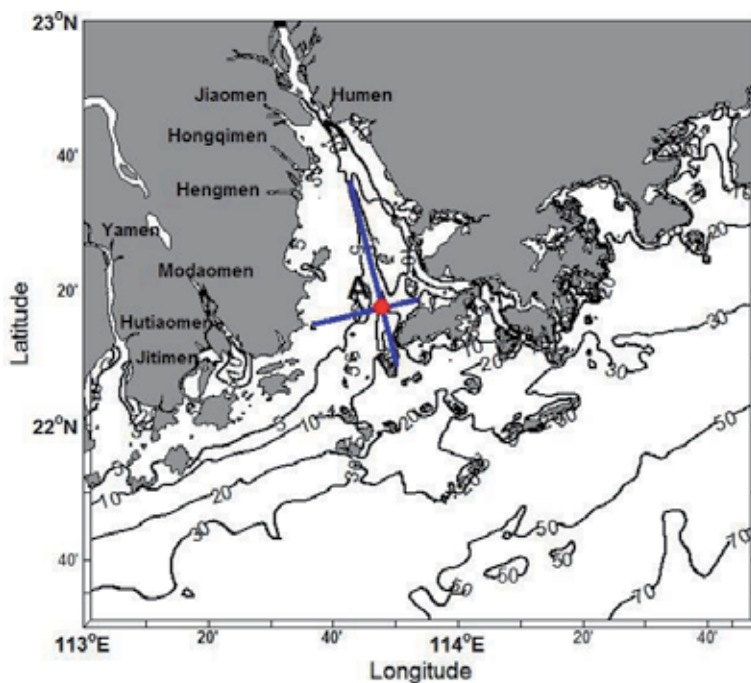
Figure 14.
The Pearl River estuary with bathymetry contours (m). The along-estuary and cross-estuary sections are shown in blue lines. The intersection is marked as A.
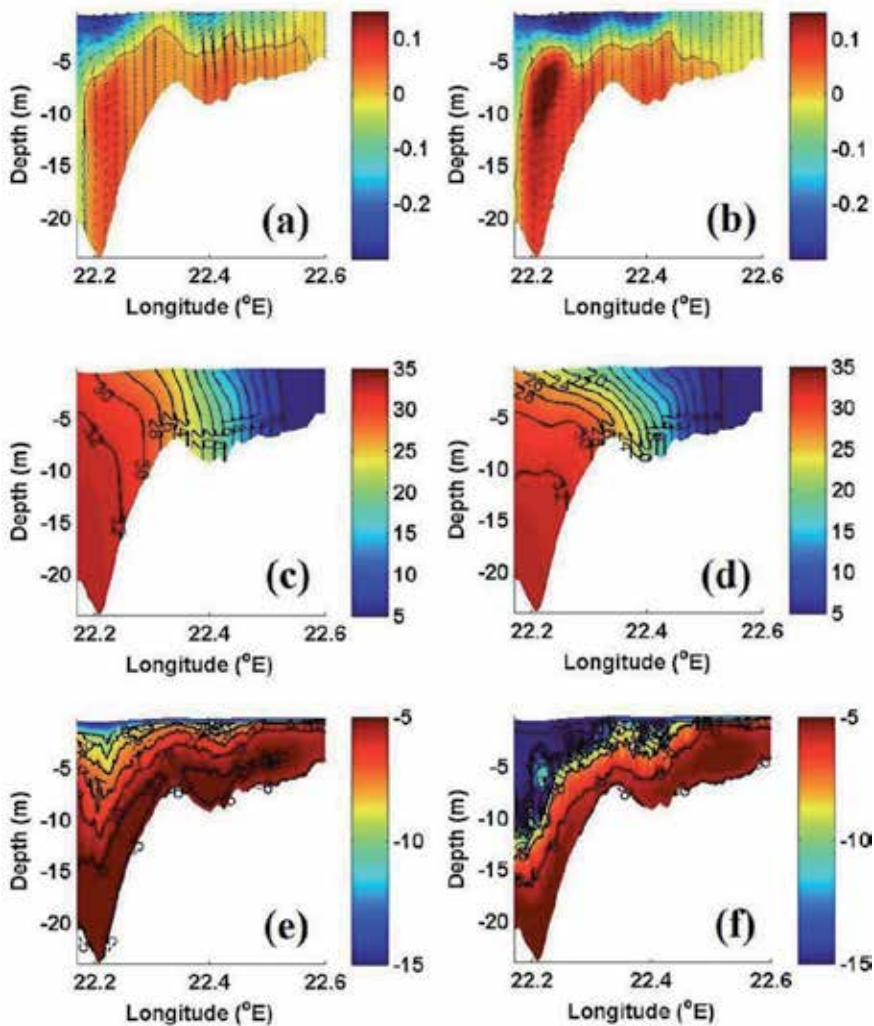
Figure 15.
Tidally averaged along-estuary circulation (m s⁻¹) (a, b), salinity (pus) (c, d), logarithm of vertical viscosity [log(m² s⁻¹)] (e, f) during spring tide (left) and neap tide (right) without wind forcing.

than that during the neap tide; however, in the bottom, the salinity intrusion during the neap tide is stronger than that during the spring tide. Without the wind forcing, the estuarine exchange flow pattern is more controlled by the mixing inside the estuary.

As shown in **Figure 15e** and **f**, the bottom vertical viscosity is higher than that on the surface both during the spring and neap tides, suggesting that the mixing is generated by the bottom friction that applies to the tidal current inside the PRE [6]. The vertical viscosity is higher during the spring tide than that during the neap tide, indicating that the turbulent mixing is more energetic during the spring tide. The averaged viscosity over the along-channel section is 0.0041 m² s⁻¹ during the spring and is 0.0026 m² s⁻¹ during the neap tide. The PRE shows a classical pattern of the spring-neap cycle of the along-estuary circulation which is mainly controlled by the mixing inside the estuary. The higher mixing dissipates more kinetic energy of the residual current, resulting in a reduced exchange flow in the PRE. Although the horizontal density gradient is stronger during the spring tide, the vertical diffusion

may overwhelm the forcing aroused by the density gradient, leading to the weaker longitudinal circulation on the spring tide than on the neap tide.

6.2 Cross-estuary circulations

Figure 16 shows the tidally averaged cross-estuary velocity, salinity, and vertical viscosity for the spring and neap tides across the Lantau Channel. The freshwater outlets are mainly located on the west side of the PRE, which helps to build up a density gradient in the cross-estuary direction, and therefore, a clockwise gravitational circulation (eastward current in the surface and westward current in the bottom) can be formed west of the Lantau Channel as shown in **Figure 16a,b** (looking into the estuary). The clockwise circulation is stronger in the neap tide than that in the spring tide. Due to the weaker westward current on the east side of the estuary, the eastward current in the surface may extend farther eastward in the spring tide (**Figure 16a** vs. **Figure 16b**). On the other hand, during the neap tide, there is a convergence in the surface layer located on the east side of Lantau Island, and the stratification is weak on the west side of estuary due to that the well-mixed freshwater reduces the vertical salinity difference (**Figure 16c, d**). However, in the Lantau Channel, the vertical salinity difference is greater in the neap tide, revealing that the stratification during the neap tide is stronger than that during the spring (**Figure 16c** vs. **Figure 16d**). The vertical viscosity is higher during the spring tide than that during the neap tide, especially on the west side of estuary with shallow
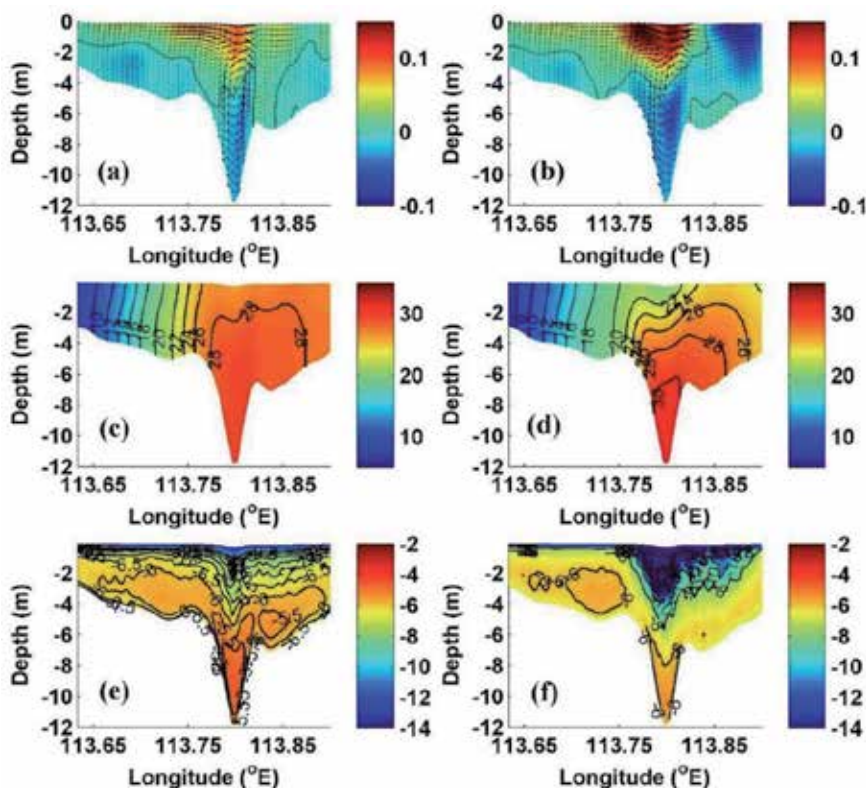
Figure 16.
Tidally averaged cross-estuary circulation (m s⁻¹) (a, b), salinity (pus) (c, d), logarithm of vertical viscosity [log(m² s⁻¹)] (e, f) during spring (left) and neap (right) tide without wind forcing.

water, indicating that the turbulent mixing is more energetic during the spring tide and the circulation is controlled by the tidal mixing over the shoal (**Figure 16e** vs. **Figure 16f**).

7. Discussions and conclusions

The investigation on the Pearl River estuarine circulation is pursued toward better understanding the Pearl River estuarine circulation dynamics. A hydrographic cruise survey for collecting in situ data of marine environmental parameters in the PRE was conducted in the period between May 3, 2014 and May 11, 2014.

The observation shows that the salinity intrusion along the Lantau Channel exists both for the flood and ebb. The intruded salinity should be responsible for the appearance of the high surface salinity water in the channel located inside the estuary, which facilitates the formation of the "sandwich" structure of the horizontal salinity distribution (high salinity in the channel location and low salinity on the east and west sides). However, instead of the "sandwich" type of the horizontal salinity distribution, the lower estuary shows a two-layer structure of the salinity in the horizontal cross-estuary direction, which may be associated with the stronger salinity intrusion in the lower estuary. The observation reveals that there is an exchange flow structure in the longitudinal direction in the PRE with the surface water flowing out of the estuary and bottom water flowing into the estuary, especially along the Lantau Channel. Another important observation is that there is longitudinal convergence or divergence of the cross-estuary velocity close to the channel location for certain tidal conditions. The observation also indicates that the circulation and density structures are highly varied due to the difference in the wind and tidal forcing for different periods.

The numerical simulations of the FVCOM in the PRE and the adjacent water area are conducted with a horizontal spatial resolution as high as 100 m inside the estuary and 20 vertical levels. An atmospheric model, the WRF Model is also implemented to provide with high spatial and temporal resolution atmospheric forcing for the FVCOM. The comparison of model outputs with in situ observations of salinity and velocity profiles and sea level suggests that the modeling in the PRE can well simulate the estuarine circulations. In a model experiment with tide excluding wind forcing, the PRE longitudinal exchange circulation exhibits a strong spring-neap cycle with the maximum circulation in the neap tide and the minimum in the spring tide, revealing that the mixing induced by the tidal current is a dominant factor influencing the circulation. The higher mixing dissipates more kinetic energy of the residual current, resulting in a reduced exchange flow in the PRE.

Acknowledgements

Author details

Jiayi Pan[1,2*], Wenfeng Lai[2] and Adam Thomas Devlin[1,2]

1 School of Geography and Environment, Jiangxi Normal University, Nanchang, China

2 Institute of Space and Earth Information Science, The Chinese University of Hong Kong, Shatin, Hong Kong, China

*Address all correspondence to: panj@cuhk.edu.hk

IntechOpen

References

[1] Dong L, Su J, Wong LA, Cao Z, Chen JC. Seasonal variation and dynamics of the Pearl River plume. Continental Shelf Research. 2004;**24**:1761-1777. DOI: 10.1016/j.csr.2004.06.006

[2] Zhao H. The Evolution of the Pearl River Estuary. Beijing: China Ocean Press; 1990. p. 357. (In Chinese)

[3] Wong LA, Chen JC, Xue H, Dong LX, Cuan WB, Su JL. A model study of the circulation in the Pearl River estuary (PRE) and its adjacent coastal waters: 2. Sensitivity experiments. Journal of Geophysical Research-Oceans. 2003; **108**:3157. DOI: 10.1029/2002JC001452

[4] Mao Q, Shi P, Yin K, Gan J, Qi Y. Tides and tidal currents in the Pearl River estuary. Continental Shelf Research. 2004;**24**:1797-1808. DOI: 10.1016/j.csr.2004.06.008

[5] Zu T, Gan J. A numerical study of coupled estuary–shelf circulation around the Pearl River estuary during summer: Responses to variable winds, tides and river discharge. Deep Sea Research Part II: Topical Studies in Oceanography. 2015;**117**:53-64. DOI: 10.1016/j.dsr2.2013.12.010

[6] Pan J, Gu Y. Cruise observation and numerical modeling of turbulent mixing in the Pearl River estuary in summer. Continental Shelf Research. 2016;**120**: 122-138. DOI: 10.1016/j.csr.2016.03.019

[7] Wong LA, Chen JC, Xue H, Dong LX, Su JL, Heinke G. A model study of the circulation in the Pearl River estuary (PRE) and its adjacent coastal waters: 1. Simulations and comparison with observations. Journal of Geophysical Research-Oceans. 2003;**108**:3156. DOI: 10.1029/2002jc001451

[8] Pan J, Gu Y, Wang D. Observations and numerical modeling of the Pearl River plume in summer season. Journal of

Geophysical Research, Oceans. 2014;**119**: 480-2500. DOI: 10.1002/2013JC009042

[9] Ou S, Zhang WD. Dynamics of the buoyant plume off the Pearl River estuary in summer. Environmental Fluid Mechanics. 2009;**9**:471-492. DOI: 10.1007/s10652-009-9146-3

[10] Pan J, Lai W, Devlin AT. Channel-trapped convergence and divergence of lateral velocity in the Pearl River estuary: Influence of along-estuary variations of channel depth and width. Journal of Geophysical Research-Oceans. 2020;**125**:e2019JC015369. DOI: 10.1029/2019JC015369

[11] Chen C, Liu H, Beardsley R. An unstructured grid, finite volume, three-dimensional, primitive equations ocean model: Application to coastal ocean and estuaries. Journal of Atmospheric and Oceanic Technology. 2003;**20**:159-186

[12] Chen C, Huang H, Beardsley RC, Liu H, Xu Q, Cowles G. A finite volume numerical approach for coastal ocean circulation studies: Comparisons with finite difference models. Journal of Geophysical Research-Oceans. 2007;**112**: C03018. DOI: 10.1029/2006JC003485

[13] Chen C, Gao G, Qi J, Proshutinsky A, Beardsley RC, Kowalik Z, et al. A new high-resolution unstructured-grid finite-volume Arctic Ocean model (AO-FVCOM): An application for tidal studies. Journal of Geophysical Research-Oceans. 2000;**114**:C08017. DOI: 10.1029/2008jc004941

[14] Mellor GL, Yamada T. Development of a turbulence closure model for geophysical fluid problem. Reviews of Geophysics. 1982;**20**:851-875. DOI: 10.1029/RG020i004p00851

[15] Smagorinsky J. General circulation experiments with the primitive equations, I. the basic experiment. Monthly Weather Review. 1963;**91**:99-164

[16] Burchard H, Bolding K. GETM – A General Estuarine Transport Model. Scientific Documentation. Technical Report EUR 20253 EN. Brussels: European Commission; 2002. p. 1559

[17] Lai Z, Ma R, Huang M, Chen C, Chen Y, Xie C, et al. Downwelling wind, tides, and estuarine plume dynamics. Journal of Geophysical Research, Oceans. 2016;**121**:4245-4263. DOI: 10.1002/2015jc011475

[18] Chen C et al. Physical mechanisms for the offshore detachment of the Changjiang diluted water in the East China Sea. Journal of Geophysical Research-Oceans. 2008;**113**:C02002. DOI: 10.1029/2006JC003994

[19] Ge J, Chen C, Qi J, Ding P, Beardsley RC. A dike-groyne algorithm in a terrain-following coordinate ocean model (FVCOM): Development, validation and application. Ocean Modelling. 2012;**47**:26-40. DOI: 10.1016/j.ocemod. 2012.01.006

[20] Huang H, Chen C, Blanton JO, Andrade FA. Numerical study of tidal asymmetry in the Okatee Creek, South Carolina. Estuarine, Coastal and Shelf Science. 2008;**78**:190-202

[21] Yang Z, Khangaonkar T. Multi-scale modeling of Puget Sound using an unstructured-grid coastal ocean model: From tide flats to estuaries and coastal waters. Ocean Dynamics. 2010;**60**: 1621-1637. DOI: 10.1007/s10236-010-0348-5

[22] Weisberg RH, Zheng LY. Circulation of Tampa Bay driven by buoyancy, tides, and winds, as simulated using a finite volume coastal ocean model. Journal of Geophysical Research, Oceans. 2006;**111**:C01005. DOI: 10.1029/2005JC003067

[23] Egbert GD, Erofeeva SY. Efficient inverse modeling of barotropic ocean tides. Journal of Atmospheric and Oceanic Technology. 2002;**19**:183-204

[24] Michalakes JG, Dudhia J, Gill D, Klemp J, Skamarock W. Design of a next generation regional weather research and forecast model. In: Towards Teracomputing. River Edge, New Jersey: World Scientific; 1998. pp. 117-124

[25] Ferrier BS, Lin Y, Black T, Rogers E, DiMego G. Implementation of a new grid-scale cloud and precipitation scheme in the NCEP Eta model. Preprints, 15th Conf. on Numerical Weather Prediction. San Antonio, TX: American Meteorological Society; 2002. pp. 280-283

[26] Mlawer EJ, Taubman SJ, Brown PD, Iacono MJ, Clough SA. Radiative transfer for inhomogeneous atmospheres: RRTM, a validated correlated-k model for the longwave. Journal of Geophysical Research-Atmospheres. 1997;**102**:16663-16682

[27] Dudhia J. Numerical study of convection observed during the winter monsoon experiment using a mesoscale two-dimensional model. Journal of the Atmospheric Sciences. 1989;**46**: 3077-3107

[28] Hong SY, Noh Y, Dudhia J. A new vertical diffusion package with an explicit treatment of entrainment processes. Monthly Weather Review. 2006;**134**:2318-2341

[29] Kain JS, Fritsch JM. Convective parameterization for mesoscale models: The Kain–Fritsch scheme. In: Emanuel KA, Raymond DJ, editors. The Representation of Cumulus Convection in Numerical Models. Boston: Meteorological Monographs, American Meteorological Society; 1993. p. 165-170

[30] Warner JC, Geyer WR, Lerczak JA. Numerical modeling of an estuary: A comprehensive skill assessment. Journal of Geophysical Research-Oceans. 2005; **110**:C05001. DOI: 10.1029/2004JC002691

Chapter 7

Phytoplankton Biomass and Environmental Descriptors of Water Quality of an Urban Lagoon

Marco V.J. Cutrim, Francinara S. Ferreira,
Lisana F. Cavalcanti, Ana K.D.S. Sá,
Andrea Christina Gomes de Azevedo-Cutrim
and Ricardo Luvizotto Santos

Abstract

The Jansen lagoon is a coastal system formed by damming the Ana Jansen Creek, which is located in the northwest of São Luís Island (northern Brazil) and is under high urban influence. The use of indexes to assess the water quality in aquatic systems is important because they show the degradation degree of an area and give support to measures for the sustainability and protection of aquatic life, consequently. For the seasonal and spatial analysis of environmental and biological variables, six bimonthly surveys between November 2011 and September 2012 were carried out at five sampling sites. In addition, indexes such as the index of minimum parameters for the protection of aquatic communities, Trophic State Index, and Aquatic Life Protection Index were applied to evaluate the water quality. High levels of dissolved oxygen (DO), pH, total phosphorus, and chlorophyll *a* were observed in the lagoon waters. In general, the water quality indexes showed that the Jansen lagoon has a poor water quality due to elevated DO and pH as well as high concentration of surfactants and phenols. These environmental conditions favored the intense process of eutrophication (hypereutrophy) and environmental degradation of the area, affecting the development of aquatic biota.

Keywords: coastal lagoon, water quality, aquatic life protection, eutrophication, pollutants

1. Introduction

Water quality is vital when it comes to determining how society uses and values aquatic environments associated with natural resources [1] and their monitoring provides empirical evidence to support decision-making on health and environmental issues [2]. Thus, water quality can be assessed through variables such as dissolved oxygen, temperature, pH, toxic substances (heavy metals, surfactants, and phenols) and others [3, 4].

Among the aquatic ecosystems, the coastal lagoons stand out for offering important environmental services (e.g., food production, nutrient cycling,

recreational activities, and aquaculture). However, they have been degraded worldwide by human activities associated with rapid urbanization [5–8]. Therefore, coastal ecosystems need constant evaluation to provide the protection of the populations and the improvement of the quality of life.

Indexes and indicators of water quality work as tools that represent simplified models of the environmental structure, which makes it easy to understand the impacts and to present the results to the general public [9, 10]. Indicators are quantified information of environmental variables that help in the explanation of processes that undergo changes of anthropic or natural origins in time and space, thus allowing the dynamic monitoring of the real situation and identification of trends [11, 12].

The most complex indicator models integrate information from different ecosystem compartments, such as physical and chemical parameters of water, phytoplankton, zooplankton, benthos, submerged aquatic vegetation, macroalgae, sediments, etc. [13]. In this context, the indexes related to water quality are considered the most widely known water indicators in the world. They are represented by a dimensionless number, being the result of the aggregation of physical, chemical, and microbiological indicators obtained by specific methodologies [14].

The use of indexes to assess the quality of water becomes fundamental in the measurement of how and how much aquatic management is moving from the perspective of sustainability, observing the reflexes of the actions implemented in the aquatic environments as units of management of the water resources. Thus, the use of the aquatic life protection index (ALPI) is essential and therefore considers the physical-chemical quality of the water and its degree of enrichment regarding nutrients (phosphorus and nitrogen), as well as the degree of toxicity, and it can be used as an indicator of trophic status and pollution in aquatic ecosystems [9, 15].

In Brazil, studies that aim the measurement of the water quality through the application of indexes have been carried out mainly in reservoirs and rivers [16–18]. Considering the Brazilian coast, mainly in lagoon ecosystems such as the Jansen lagoon, these studies are still scarce, making the understanding of the behavior of this environment regarding the impacts that take place there evident. Thus, we propose to carry out an assessment of the water quality in the Jansen lagoon through the use of indexes and environmental descriptors as a way of assisting the management of local resources, as well as to subsidize the sustainability of this ecosystem in the global scope.

2. Brazilian coastal lagoons

Coastal lagoons are considered as depressions, with depths less than 10 meters, parallel to the coast, being connected to the sea temporarily or permanently by one or more channels and separated from it by a physical barrier [19, 20]. These coastal environments, although highly productive, are very fragile and subject to strong anthropogenic pressures, such as disordered population growth [21, 22].

In the Brazilian coast, it is possible to see lagoon complexes, as well as coastal lagoons impacted by man and in the stage of advanced eutrophication. Among them are the Mundaú-Manguaba lagoon complex, Jacarepaguá, Patos lagoon, Jacuném lagoon, Açu lagoon, and Rodrigo de Freitas lagoon that have the disposal of untreated sewage *in natura* directly into the water bodies as the main aggravating factor of water pollution [23–25].

The Jansen lagoon is the result of successive anthropic changes in the landscape. In the 1970s, the area was an estuarine region intersected by the Jansen and Jaracati streams with extensive mangrove forest represented by species such as *Rhizophora*

mangle, *Avicennia germinans*, *Avicennia schaueriana*, and *Laguncularia racemosa*. However, the construction of roads altered the main drainage network of the Jansen stream with the sea leading to the salt water damming, forming consequently the lagoon [26].

The lagoon is located in the northwest of São Luís Island, between the coordinates 02°29′08″S and 44°18′02″W, northern Brazil (**Figure 1**). It covers 140 ha with an average depth of 1.5 m and is still surrounded in the east by a mangrove forest.

The lagoon is under a semidiurnal macrotidal system typical of the Amazon coastal zone [27], with amplitudes that can reach up to 7 m. It is connected with the sea and the water exchange occurs during the spring tides in the rainy season, when the freshwater supply ensures the flow toward the sea (115 m length and 3 m deep) [28]. According to the classification of Kjerfve [29] which is based on the geomorphological typology, the Jansen lagoon is classified as restricted (**Figure 2**), depending on fluctuations in sea level and rainfall.
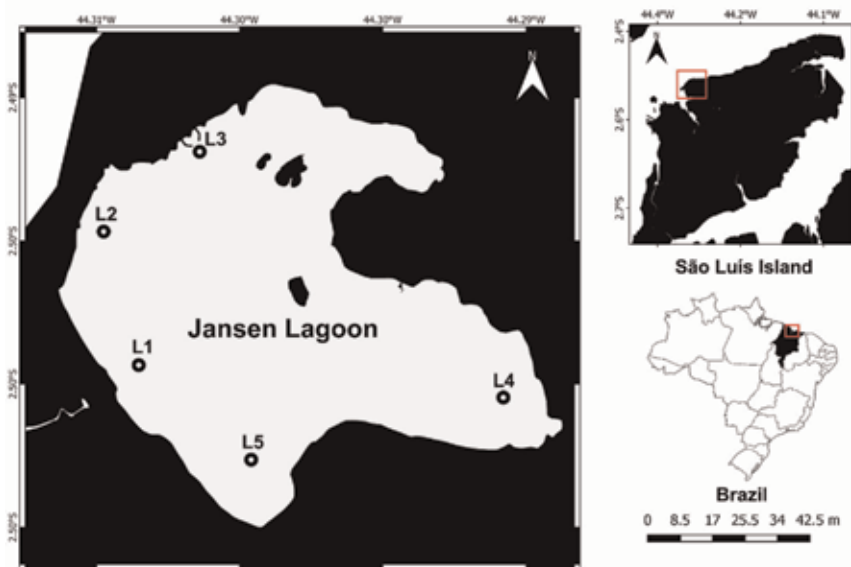
Figure 1.
Location of the study area with sampling points (L1–L5), Jansen lagoon, São Luís Island-Maranhão, Brazil.
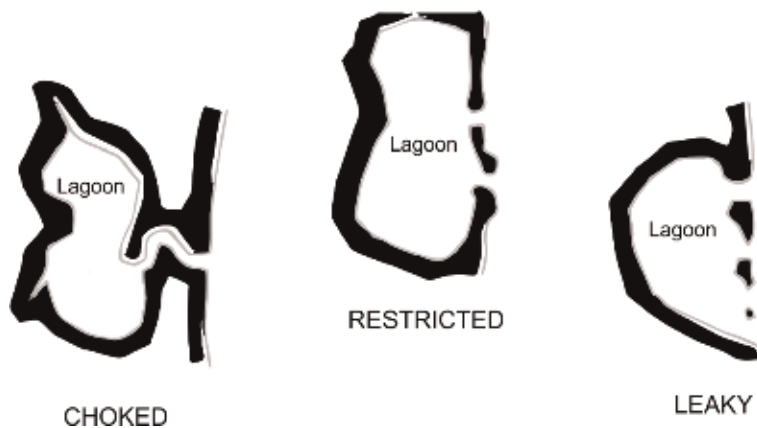
Figure 2.
Schematic representation of the types of coastal lagoons according to Kjerfve [29].

Regarding local climate, the region is hot and humid because it is situated in the equatorial belt with equatorial air mass influence originating in low-latitude regions where the southern boreal and trade winds converge. As a result, it has intrinsic characteristics such as high temperatures throughout the year as well as two well-defined seasonal periods strongly marked by precipitation: rainy season (January-June) and dry season (July-December).

The Jansen lagoon is a eutrophic environment, where most of the material found in it is of allochthonous origin, that is to say, originating from the release of fresh domestic sewage, which decisively influences the distribution of many nutrients, and consequently the biodiversity and water quality of the lagoon, with recurrent processes of eutrophication and algal blooms [26].

3. Material and methods

3.1 Sampling

From 2011 to 2012, samplings were carried out every 2 months, with a total of six surveys (November 2011–September 2012) performed at five sampling sites. In those samplings, tide (ebb tide and spring tide) and season (dry and rainy seasons) were considered. The rainfall data were obtained from the National Institute of Meteorology (INMET). Physical and chemical parameters are described in **Table 1**, considering the Federal Legislation of Classification of Water Bodies (CONAMA 357/05) [30] and the Aquatic Life Protection Index (ALPI).

Variable	Symbol	Units	Methods and equipment
Temperature	Water temp.	°C	Multiparametric Probe/Hanna 9828
Salinity	Sal.	—	
Dissolved oxygen	DO	$mg\,L^{-1}$	Sodium azide used in the Winkler method
pH	pH	—	Multiparametric Probe/Hanna 9828
Phenol	Phen.	$\mu g\,L^{-1}$	**USEPA SW 846-8270D e 3510C, *SMWW 6410B
Total phosphorus	TP	$mg\,L^{-1}$	Ascorbic acid method/SMEWW 4500
Surfactants	***LAS	$mg\,L^{-1}$	POP PA023/*SMWW 5540C
Cadmium	Cd	$\mu g\,L^{-1}$	POP PA038
Lead	Pb	$\mu g\,L^{-1}$	*SMWW 3125 B
Copper	Cu	$\mu g\,L^{-1}$	**USEPA 6020
Chrome	Cr	$\mu g\,L^{-1}$	
Manganese	Mn	$\mu g\,L^{-1}$	
Nickel	Ni	$\mu g\,L^{-1}$	
Zinc	Zn	$\mu g\,L^{-1}$	
Chlorophyll-a	Chla	$\mu g\,L^{-1}$	Spectrophotometry

*SMWW, standard methods for water and wastewater [31].
**USEPA, United States Environmental Protection Agency.
***LAS, linear alkylbenzene sulfonate.

Table 1.
Physiochemical parameters applied to the determination of the aquatic life protection index (ALPI) in Jansen lagoon, São Luís-Maranhão.

3.2 Aquatic life protection index (ALPI)

The Aquatic Life Protection Index (ALPI) is one of the most complete indexes for the assessment of the quality of aquatic ecosystems. It allows analyzing the water quality differently from other indexes, taking into account the presence and concentration of contaminants and their effects (toxicity), comprising two indexes: IMPAC (Index of Minimum Parameters for the Protection of Aquatic Communities) and TSI (Trophic State Index), which provide information on water quality and degree of trophy [32].

The IMPAC, proposed by Zagatto et al. [17] is composed of two groups of parameters: toxic substances (copper, zinc, lead, chromium, mercury, nickel, cadmium, surfactants, and phenols) and essential parameters (dissolved oxygen, pH and toxicity analyzes). For each parameter, three different levels were set, with numerical weightings of 1, 2, and 3. Weighting 1 corresponds to the water quality standards established by the Brazilian legislation [30] and weightings 2 and 3 consider the American and French legislations [33, 34], respectively, which establish maximum permissible limits of chemical substances in water to avoid chronic and acute effects on the aquatic biota.

Environmentally speaking, these weightings mean the following:

a. **Weighting 1**: waters with suitable characteristics of maintaining survival and reproduction of organisms;

b. **Weighting 2**: waters with suitable characteristics for the survival of aquatic organisms, but reproduction may be affected in the long term;

c. **Weighting 3**: waters that may compromise the survival of organisms.
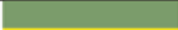
The IMPAC is calculated as follows (Eq. (1)):

$$\textbf{IMPAC} = \text{PE} \times \text{ST} \tag{1}$$

where PE = value of the highest weighting in the group of essential parameters; ST = average value of the three highest weightings in the group of toxic substances.

If the value of the toxic substances is an integer, the following rounding criterion is considered: values smaller than 0.5 will be rounded down and values greater than or equal to 0.5 will be rounded up. Using this methodology, the value of the index can vary from 1 to 9. For the water classification, the IMPAC was subdivided into four levels (**Table 2**).

Toxicity tests followed the regulation ABNT/NBR 15088 [35] adapted for the euryhaline species *Poecilia sphenops* [36], considering salinity variation between sampling sites in the Jansen lagoon.

Quality	Color Scale	Weighting
Good		1
Regular		2
Bad		3–4
Very Bad		> 6

Table 2.
Water quality according to the index of minimum parameters for the protection of aquatic communities (IMPAC) by Zagatto et al. [17].

The TSI, used to determine the trophic levels of the Jansen lagoon, followed the standards proposed by Carlson [37], modified by Toledo et al. [38], who updated the original formula using the water parameter transparency, phosphate, ortho-phosphate, and chlorophyll *a* for tropical environments.

In this study, the calculation of the ALPI considered the Trophic State Index for phosphorus-TSI (TP) and the Trophic State Index for chlorophyll *a*-TSI (Chl), modified by Lamparelli [18], established for lotic environments, according to the equations (Eqs. (2) and (3)):

$$TSI\,(TP) = 10 \times (6 - ((0.42 - 0.36 \times (\ln TP))/\ln 2)) - 20 \qquad (2)$$

$$TSI\,(Chl) = 10 \times (6 - ((-0.7 - 0.6 \times (\ln Chl))/\ln 2)) - 20 \qquad (3)$$

where TP: total phosphorus concentration measured at the water surface ($\mu g\,L^{-1}$); Chl: chlorophyll *a* concentration measured at the water surface ($\mu g\,L^{-1}$) ln: natural logarithm.

Regarding the TSI, the result shown in the tables is the simple arithmetic mean of the indexes related to the total phosphorus and chlorophyll *a*, expressed in the following equation (Eq. (4)):

$$TSI = [TSI_{TP} + TSI_{Chl}]/2 \qquad (4)$$

According to Lamparelli [18], the different values of TSI lead to the following water classification (**Table 3**):

Based on the data obtained and associated by IMPAC [17] and the Trophic State Index (TSI) as shown in **Table 4**, the ALPI (Aquatic Life Protection Index) was calculated according to the following equation (Eq. (5)):

$$ALPI = (IMPAC \times 1.2) + TSI \qquad (5)$$

Quality	Color Scale	TSI	Weighting
Ultraoligotrophic		TSI < 47	0.5
Oligotrophic		47 < TSI < 52	1
Mesotrophic		52 < TSI < 59	2
Eutrophic		59 < TSI ≤ 63	3
Supereutrophic		63 < TSI < 67	4
Hypereutrophic		TSI > 67	5

Table 3.
Water quality according to the state trophic index (TSI) by Carlson [37] modified by Toledo et al. [38].

		IMPAC				
	Weighting	1	2	3	4	5 a 9
TSI	0.5	1.7	2.9	4.1	5.3	7.7-11.3
	1	2.2	3.4	4.6	5.8	8.2-11.8
	2	3.2	4.4	5.6	6.8	9.2-12.8
	3	4.2	5.4	6.6	7.8	10.2-13.8
	4	5.2	6.4	7.6	8.8	11.2-14.8
	5	6.2	7.4	8.6	9.8	12.2-15.8

Table 4.
Calculation of the ALPI integrating the values of the TSI and IMPAC. Where: excellent (blue), good (green), regular (yellow), bad (red), and very bad (purple).

Table 5.
Water quality according to the aquatic life protection index (ALPI) by Zagatto et al. [17] modified by CETESB [32].

The classification of the waters can be represented according to the ALPI index values, being divided into five categories as described below (**Table 5**):

Phytoplankton was analyzed in terms of chlorophyll *a*. Water samples for chlorophyll *a* (μg L^{-1}) determinations were filtered through Whatman GF/F glass fiber filters, and a pigment extraction was performed with 90% acetone. To obtain the fractional values of chlorophyll, sub-samples were passed through a 20 μm mesh and then filtered. Pigment concentration was measured by spectrophotometry [39, 40] and the calculations were done according to Strickland and Parsons [41].

4. Results and discussion

4.1 Climatological scenario and environmental descriptors

During the sampling period, an atypical pattern was observed, with annual rainfall amounts ranging from 995 mm (2012) to 2530 mm (2011), which was the result of a combination of the effects of the El Niño–Southern Oscillation (ENSO) [42].

The characteristics of the estuarine waters of the Jansen lagoon are summarized in **Table 6** and **Figure 3**, with significant differences in environmental variables occurring between the rainy and dry seasons.

The water temperature is typical of environments near the equator, and regarding the salinity values, the waters of Jansen lagoon during the study period were

Variables	Units	CONAMA 357/05	Dry	Rainy	Anova	KW
			Mean $\pm$ SD	Mean $\pm$ SD		
Dissolved oxygen	(mg L^{-1})	>4	3.73 $\pm$ 1.43	7.05 $\pm$ 2.61	0.000[*]	—
pH	—	6.5–8.5	8.89 $\pm$ 0.56	8.54 $\pm$ 0.40	0.075	—
Salinity	—	0.5–30	28.34 $\pm$ 5.82	24.50 $\pm$ 8.91	—	0.120
Water temperature	(°C)	—	28.60 $\pm$ 1.07	28.53 $\pm$ 1.64	0.906	—
Total chlorophyll *a*	(μg L^{-1})	—	74.64 $\pm$ 55.69	71.61 $\pm$ 96.74	—	—
Total phosphorus	(μg L^{-1})	0.186	5.73 $\pm$ 3.67	6.05 $\pm$ 4.26	—	0.917
Phenols	(mg L^{-1})	0.003	0.24 $\pm$ 0.22	0.42 $\pm$ 0.39	—	—
Surfactants (LAS)	(mg L^{-1})	0.2	0.81 $\pm$ 0.59	1.15 $\pm$ 0.41	—	—

Variables with significant difference.
KW = Kruskal-Wallis.

Table 6.
Seasonal variation of environmental variables in Jansen lagoon, São Luís-Maranhão.
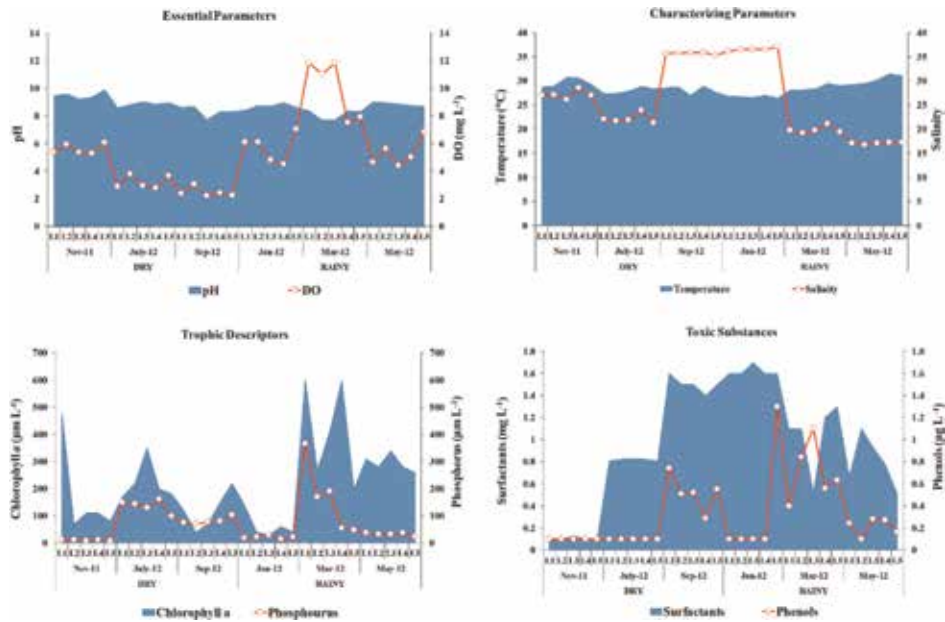
Figure 3.
Seasonal variation of environmental variables during the study period in Jansen lagoon, São Luís-Maranhão.

classified as brackish waters. Total chlorophyll *a* concentrations showed higher values in the dry season. The TP showed higher values in the rainy season. For toxic substances, phenol and surfactants also showed higher values in the rainy season.

The water samples from the Jansen lagoon did not show any acute effect for the *Poecilia sphenops* juveniles during 96 hours of exposure, without water renewal and in stable physicochemical conditions (temperature, salinity, oxygen, and pH), considering 100% of survival during acute toxicity tests.

4.2 Water quality indexes

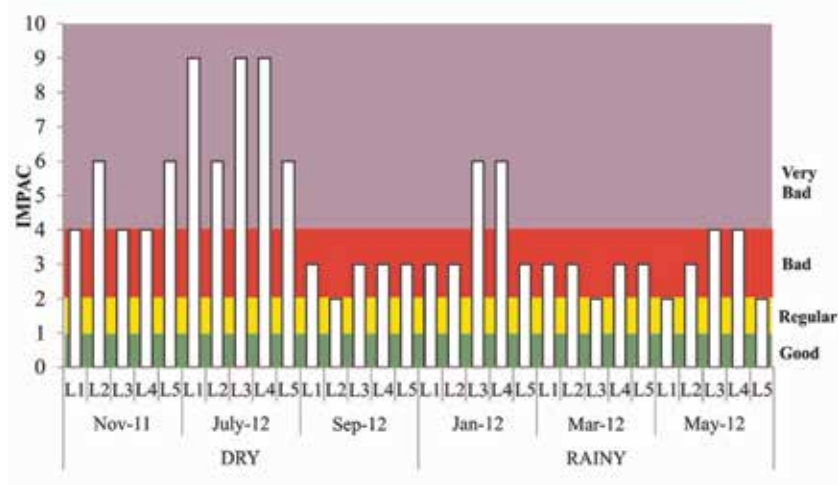### 4.2.1 Index of minimum parameters for the protection of aquatic communities (IMPAC)

According to the results obtained for the essential parameters and the toxic substances, the IMPAC was calculated for the Jansen lagoon waters with weightings ranging from 2 to 9, being 5.13 during the dry season and 3.3 in the rainy season. In general, the quality of the water in Jansen lagoon was considered bad in 56.66% (**Figure 4**).

Regarding the seasonal variation of IMPAC, the waters had the pattern shown in **Table** 7. During the study period, the presence of dead fish was not observed. However, some species that are possibly the ones that could adapt and remain in that environment were observed.

Due to the decomposition of the organic matter in the lagoon, the bad smell from the release of the hydrogen sulfide gas was constant. Besides that, blooms of indicator phytoplankton (*Microcystis aeruginosa*) and *Ruppia maritima* specimens were observed at the study area, resulting in a mass of greenish-dark coloration [26, 43].

The surfactants were the main toxic substances that determinate the classification of water quality in the Jansen lagoon. July 12 was the period in which the lagoon had the lowest water quality. In that period, all sampling sites were classified as very bad where dissolved oxygen and surfactants reached the highest weightings, indicating that the whole environment was very much compromised.

Figure 4.
Representation of the index of minimum parameters for the protection of aquatic communities (IMPAC) in Jansen lagoon, São Luís-Maranhão.

IMPAC							
Sampling point	Dry			Rainy			Spatial average
	Nov-11	July-12	Sep-12	Jan-12	Mar-12	May-12	
L1	4	9	3	3	3	2	**4**
L2	6	6	2	3	3	3	**4**
L3	4	9	3	6	2	4	**5**
L4	4	9	3	6	3	4	**5**
L5	6	6	3	3	3	2	**4**
Temporal average	**5**	**8**	**3**	**4**	**3**	**3**	

Table 7.
Spatiotemporal distribution of IMPAC mean values according to Zagatto et al. [17] in Jansen lagoon, São Luís-Maranhão.

This scenario was favored by the season. In the beginning of the dry season, the confined waters presented a typical oxygen profile of that environmental scenario and the increase of surfactants could be expected due to the fact that it is a holiday season, which means that people will stay longer in their residences and consequently there will be a greater use of cleaning products, which are sources of these substances, and that will be released to the sewage system.

The quality of the lagoon waters ranged from regular to very bad. For this index, the most important elements for classification of the Jansen lagoon were the dissolved oxygen in the group of essential parameters, and the surfactants in group of toxic substances. These parameters presented high values, being above the allowed by CONAMA Resolution 357/05 [30], evidencing a high degree of pollution caused by the disordered occupation that occurs in the area and by problems of sanitary sewage that still persist.

The heavy metals were detected in small quantities; however, even when quantified above the limit allowed by the federal legislation, their weightings did not have the same weighting as the other indicators in the calculation and final values of IMPAC.

4.2.2 State trophic index (TSI)

With the TSI based on two partial indexes (TSI-TP and TSI-Chl *a*), the trophic state of Jansen lagoon showed a variation of 190.69 μg L^{-1} in the dry season and 191.04 μg L^{-1} in the rainy season, and Jansen lagoon was classified as hypereutrophic (**Figure 5**). When the parameters are analyzed individually, the environment is classified as very eutrophic, and when they are aggregated for the final calculation of this index, the result obtained corroborates this pattern, with a weighting of 5.

Combining the two partial indexes, it was possible to observe that the TSI-TP showed higher weighting with regard to the increase of the degree of eutrophication in Jansen lagoon, considering that the total TSI showed an intermediate quantification in relation to the one observed in the TSI-TP and in the TSI-Chl *a*; however, all of them had the same weighting and classification. When that happens, it is inferred that the system is already under eutrophication, since the trophic state indicated by the TSI-TP coincided with TSI-Chl *a*.
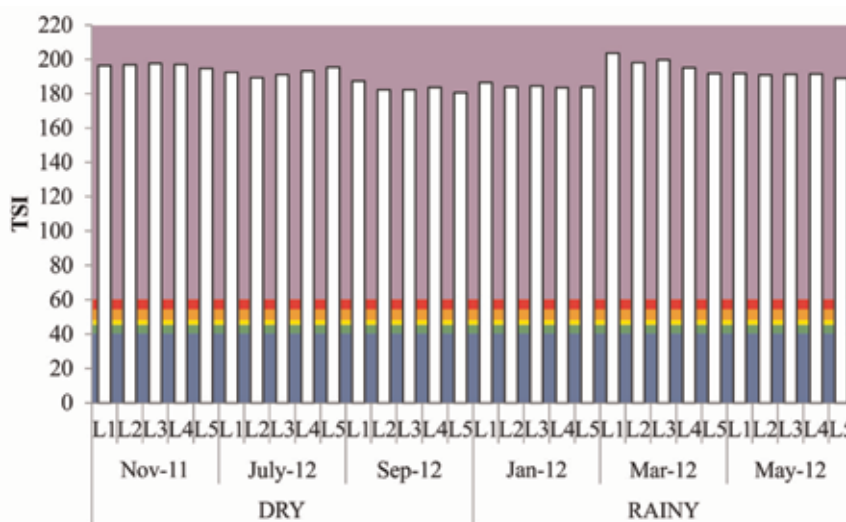

Figure 5.
Representation of the trophic state index (TSI) in Jansen lagoon, São Luís-Maranhão: ultraoligotrophic (blue), oligotrophic (green), mesotrophic (yellow), eutrophic (orange), supereutrophic (red), and hypereutrophic (purple).

	TSI						
	Dry			**Rainy**			
Sampling point	**Nov-11**	**July-12**	**Sep-12**	**Jan-12**	**Mar-12**	**May-12**	**Spatial average**
L1	196	192	187	187	204	192	193
L2	197	189	182	184	198	191	190
L3	198	191	182	185	200	191	191
L4	197	193	184	184	195	192	191
L5	195	195	181	184	192	189	189
Temporal average	197	192	183	185	198	191	

Table 8.
Spatial-temporal means of TSI values according to Lamparelli [18] in Jansen lagoon, São Luís-Maranhão.

Comparing the values obtained in the final TSI, it was possible to observe a small variation in the degree of eutrophication. In this perspective, in a general average for the sites, L1 was considered the most eutrophic and L5 as the less eutrophic (**Table 8**). Regarding the sampling campaigns, Mar-12 was the most eutrophic because it had maximum values of the TSI (TP) and the TSI (Chl *a*) and the least eutrophic was set/12 because it had high values for the TSI (TP) only.

This scenario is explained by the high concentration of total phosphorus available in the system and because it has not been considered as a limiting element for photosynthetic organisms, since even though it was being consumed, there was still a large amount of it.

Regardless of the sampling site or campaign, Jansen lagoon was classified as hypereutrophic, because according to the classification of Lamparelli [18], all sites obtained a weighting of 5, which equals TSI values above 67.

The trophic level observed in this study through the use of the TSI showed to be very high, being even higher than what is reported for other environments that also suffer from cultural eutrophication as verified by Knoppers et al. [44] in six coastal lagoons in Rio de Janeiro (Brazil), Herrera-Silveira et al. [45] in three coastal
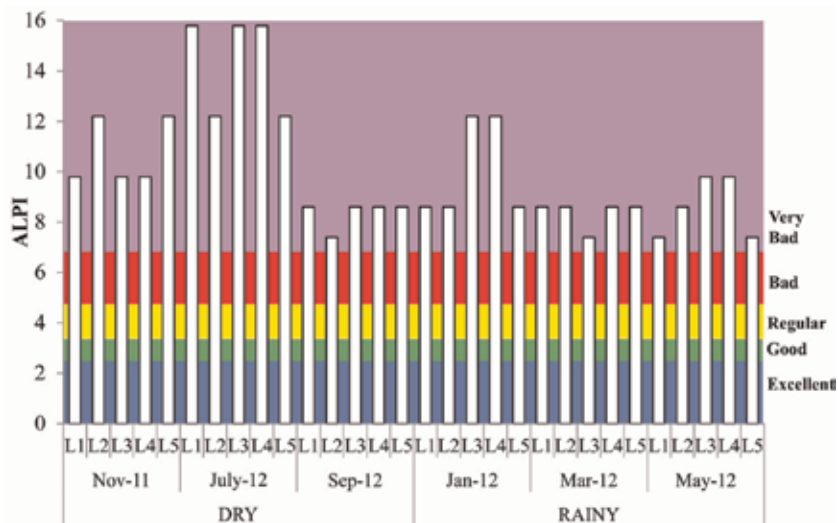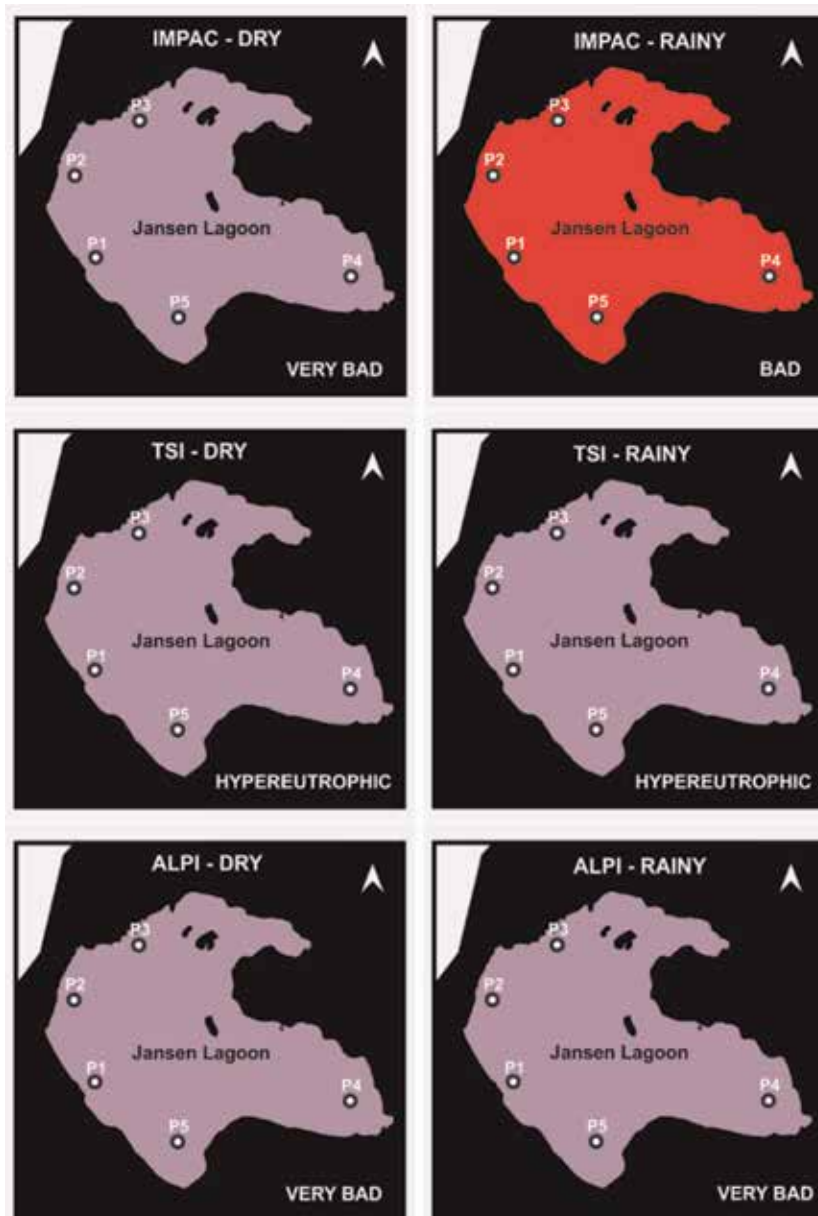

Figure 6.
Representation of the aquatic life protection index (ALPI) at Jansen lagoon, São Luís-Maranhão.

	ALPI						
Sampling point	**Dry**			**Rainy**			**Spatial average**
	Nov-11	**July-12**	**Sep-12**	**Jan-12**	**Mar-12**	**May-12**	
L1	9.8	15.8	8.6	8.6	8.6	7.4	9.8
L2	12.2	12.2	7.4	8.6	8.6	8.6	9.6
L3	9.8	15.8	8.6	12.2	7.4	9.8	10.6
L4	9.8	15.8	8.6	12.2	8.6	9.8	10.8
L5	12.2	12.2	8.6	8.6	8.6	7.4	9.6
Temporal average	10.8	14.4	8.4	10.0	8.4	8.6	

Table 9.
Mean values of the aquatic life protection index (ALPI) according to Zagatto et al. [17] modified by CETESB [32] in Jansen Lagoon, São Luís-Maranhão.

lagoons in Yucatán (México), and Fia et al. [46] in Mirim lagoon (Brazil). These authors also observed that cultural eutrophication plays an important role in the determination of water quality, besides influencing the self-purification capacity of the environment, leading to loss of water quality and intensification of the eutrophication process.

Therefore, the use of these waters for any secondary contact activity (recreation and amateur fishing-subsistence) is not appropriate, as for these purposes, the acceptable trophic state in environments such as lakes is mesotrophic or even slightly eutrophic [15].

Figure 7.
Representation of IMPAC (index of minimum parameters for the protection of aquatic communities), TSI (state trophic index), and ALPI (aquatic life protection index) classification categories at Jansen Lagoon, São Luís-Maranhão.

4.2.3 Aquatic life protection index (ALPI)

The general characterization of water quality in the Jansen lagoon from the ALPI interpretation was classified as bad, with values of 11.16 in the dry season and 9.0 in the rainy season (**Figure 6**).

Knowing that the first two indexes have already shown that water quality in Jansen lagoon is not suitable for the activities indicated for class 2 brackish waters, according to CONAMA 357/05 [30], it is confirmed by the ALPI which classifies this environment as inappropriate. The weightings obtained from the ALPI calculation were above 6.8 resulting in a very bad classification. It can be observed that the poor water quality was more critical at the site L4 and in the July-12 campaign, with average weightings of 10.8 and 14.4 (**Table 9**), respectively.

Comparing the weightings obtained from the first two indexes with the weightings obtained from the ALPI calculation, it was observed that the higher IMPAC weightings were responsible for raising the weightings of the ALPI in 30% of the sites monitored, mainly in July-12, being again the campaign with a higher degree of impairment of water quality. Thus, it was verified that the worst weightings defined the final value of the index [9]. The result obtained through the ALPI index for the Jansen lagoon was much higher when compared to the environments studied by Coelho [47] and Barbosa [9]. Besides, they do not have a constant classification pattern in relation to the TSI as verified in this study.

Based on CONAMA Resolution [30], which was used to classify the waters of the Jansen lagoon, the preponderant conditions verified through the application of the indexes and the limits established for each environmental parameter analyzed showed that this lagoon environment is very much affected by a loss of water quality and decreased protection of aquatic life.

In this scenario, the application of IMPAC and TSI showed that the renewal of the water of Jansen lagoon by the spring tides is not enough to improve its quality. According to Schettini [48], this deterioration in coastal lagoons is favored by their morphometry that makes them more susceptible mainly due to the exchange with the ocean and the increase in the time of renovation; for this environment, the ideal would be around 90% every 28 days if all polluting sources were eliminated. In view of this situation, the Jansen lagoon does not have a spatial and temporal difference, with poor water quality, subject to the conditions of the environmental descriptors, trophic degree, and toxic substances (**Figure 7**).

5. Conclusion

The ALPI showed that the Jansen lagoon has a very high degree of deterioration reflecting poor water quality that could endanger the local aquatic biota, with inappropriate conditions for reproduction, stages of development, and the permanence of aquatic organisms, reflecting a framework of environmental degradation of the area.

The use of IMPAC and TSI to obtain the ALPI was an effective tool for the quantification and representation of the degree of deterioration of water quality and, consequently, in the evaluation of the extreme conditions that the aquatic biota that inhabit in the lagoon is subjected to, besides showing the importance of the tides for the underestimation of the detected values for each parameter analyzed, being an important auxiliary element in the self-purification of this environment.

Acknowledgements

Author details

Marco V.J. Cutrim[1]*, Francinara S. Ferreira[1], Lisana F. Cavalcanti[2], Ana K.D.S. Sá[2], Andrea Christina Gomes de Azevedo-Cutrim[3] and Ricardo Luvizotto Santos[1]

1 Marine Science Institute-ICMar, Federal University of Maranhão, São Luís, Maranhão, Brazil

2 Department of Oceanography, Federal University of Pernambuco, Recife, Pernambuco, Brazil

3 Department of Chemistry and Biology, State University of Maranhão, São Luís, Maranhão, Brazil

*Address all correspondence to: marco.cutrim@ufma.br

IntechOpen

References

[1] Kennicutt MC. Water quality of the Gulf of Mexico. In: Ward CH, editor. Habitats and Biota of the Gulf of Mexico: Before the Deepwater Horizon Oil Spill. Vol. 1. Cham: Springer; 2017. 868 p

[2] Simedo MBL, Martins ALM, Pissarra TCT, Lopes MC, Costa RCA, Valle-Junior RF, et al. Effect of watershed land use on water quality: A case study in Córrego da Olaria Basin, São Paulo state, Brazil. Brazilian Journal of Biology. 2018;**78**(4):625-635. DOI: 10.1590/1519-6984.168423

[3] Cotovicz-Junior LC, Brandini N, Knoppers BA, Souza WFL, Medeiros PRP. Comparação de Modelos e Índices para Avaliação do Estado Trófico do Complexo Estuarino-Lagunar Mundaú-Manguaba, (AL). Geoquímica Brasiliensis. 2012;**26**(1):7-18. DOI: 10.21715/gb.v26i1.353

[4] Duarte-dos-Santos AK, Cutrim MVJ, Ferreira FS, Luvizotto-Santos R, Azevedo-Cutrim ACG, Araújo BO, et al. Aquatic life protection index of an urban river Bacanga basin in northern Brazil São Luís–MA. Brazilian Journal of Biology. 2017;**77**(3):602-615. DOI: 10.1590/1519-6984.01016

[5] Coelho S, Gamito S, Pérez-Ruzafa A. Trophic state of Foz de Almargem coastal lagoon (Algarve, South Portugal) based on the water quality and the phytoplankton community. Estuarine, Coastal and Shelf Science. 2007;**71**(1–2):218-231. DOI: 10.1016/j.ecss.2006.07.017

[6] Christia C, Giordani G, Papastergiadou E. Assessment of ecological quality of coastal lagoons with a combination of phytobenthic and water quality indices. Marine Pollution Bulletin. 2014;**86**:411-423. DOI: 10.1016/j.marpolbul.2014.06.038

[7] González FUT, Herrera-Silveira JA, Aguirre-Macedo ML. Water quality variability and eutrophic trends in karstic tropical coastal lagoons of the Yucatan peninsula. Estuarine, Coastal and Shelf Science. 2008;**76**(2):418-430. DOI: 10.1016/j.ecss.2007.07.025

[8] Silva VEC, Franco D, Fonseca ALF, Fontes ML, Donnangelo AR. Space time evolution of the trophic state of a subtropical lagoon: Lagoa da Conceição, Florianópolis Island of Santa Catarina, Brazil. Revista Brasileira de Recursos Hídricos. 2017;**22**:1-17. DOI: 10.1590/2318-0331.011716027

[9] Barbosa RP. Aplicação do Índice De Proteção Da Vida Aquática (IVA) ao sistema estuarino da Baía de Vitória [thesis]. Vitória: Universidade Federal do Espírito Santo; 2010

[10] Poonam T, Tanushree B, Sukalyan C. Water quality indices—Important tools for water quality assessment: A review. International Journal of Advances in Chemistry. 2013;**1**(1):15-28

[11] Toledo LG, Nicolella G. Índice de qualidade de água em microbacia sob uso agrícola e urbano. Scientia Agricola. 2002;**59**(1):181-186

[12] Magalhães-Júnior AP. Indicadores ambientais e recursos hídricos: realidade e perspectivas para o Brasil a partir da experiência francesa. 2nd ed. Rio de Janeiro: Bertrand Brasil; 2007. p. 688

[13] Newton A, Icely JD, Nobre M, Nobre A, Nunes JP, Ferreira JG, et al. Evaluation of eutrophication in the Ria Formosa coastal lagoon, Portugal. Continental Shelf Research. 2003;**23**:1945-1961. DOI: 10.1016/j.csr.2003.06.008

[14] Coradi PC, Pereira-Ramirez O, Fia O, de Matos AT. Qualidade da água

superficial da bacia hidrográfica da Lagoa Mirim. Revista de Ciências Ambientais. 2009;**3**(1):53-64

[15] Tundisi JG. Água no Século XXI: Enfrentando a Escassez. 2nd ed. São Carlos: RiMa; 2005. p. 251

[16] CETESB. Companhia de Tecnologia de Saneamento Ambiental. Relatório de Qualidade das Águas Interiores do Estado de São Paulo. São Paulo: CETESB; 1999

[17] Zagatto PA, Lorenzetti ML, Lamparelli MC, Salvador MEP, Menegon JR. Aperfeiçoamento de um índice de qualidade de águas. Acta Limnologica Brasiliensia. 1999;**11**: 11-129

[18] Lamparelli MC. Grau de trofia em corpos d'água do estado de São Paulo: Avaliação dos métodos de monitoramento [thesis]. São Paulo: Instituto de Biociências da Universidade de São Paulo; 2004

[19] Kjerfve B. Coastal Lagoons Processes. New York: Elsevier; 1994. 577 p

[20] Miranda LB, Castro BM, Kjerfve B. Princípios de oceanografia física de estuários. 2nd ed. São Paulo: Editora da Universidade de; 2002. p. 432

[21] Barros HM, Eskinazi-Leça E, Paranaguá MU. The disappearing fish: An understanding of sustainability among estuarine fishermen communities of Bragança, PA. Aquatic Ecosystem Health & Management. 2000;**3**(4):553-560. DOI: 10.1016/S1463-4988(00)00040-3

[22] Albaret JJ, Lae R. Impact of fishing on fish assemblages in tropical lagoons: The example of the Ebrie lagoons, West Africa. Aquatic Living Resources. 2003;**16**:1-9. DOI: 10.1016/S0990-7440(03)00002-0

[23] Chagas GG, Suzuki MS. Seasonal hydrochemical variation in a tropical coastal lagoon (Açu lagoon, Brazil). Brazilian Journal of Biology. 2005;**65**(4): 597-607. DOI: 10.1590/S1519-69842005000400006

[24] Sampaio GF. Cianobactérias como parâmetro de qualidade ambiental: um estudo do ceomplexo lagunar de Jacarepaguá [thesis]. Rio de Janeiro: Universidade do Estado do Rio de Janeiro, Faculdade de Engenharia; 2008

[25] Gomes AM, Sampaio PL, Ferrão-Filho AS, Magalhães VF, Marinho MM, Oliveira ACP, et al. Florações de cianobactérias tóxicas em uma lagoa costeira Hipereutrófica do Rio de Janeiro/Rj (Brasil) e suas consequências para saúde humana. Oecologia Australis. 2009;**13**(2):329-345. DOI: 10.4257/oeco.2009.1302.08

[26] Cutrim MVJ, Ferreira FS, Duarte dos Santos AK, Cavalcanti LF, Araújo BO, Azevedo-Cutrim ACG, et al. Trophic state of an urban coastal lagoon (northern Brazil), seasonal variation of the phytoplankton community and environmental variables. Estuarine, Coastal and Shelf Science. 2019;**216**: 98-109

[27] Souza-Filho PWM. Costa de manguezais de macromare da Amazonia: cenários morfológicos, mapeamento e quantificação de áreas usando dados de sensores remotos. Revista Brasileira de Geofísica. 2005; **23**(4):427-435

[28] Masullo YAG, Santos BAMO, Silva EG, Ferreira AJA. Caracterização e risco ambiental na área da laguna da Jansen, São Luís–Maranhão. In: Simpósio Brasileiro de Geografia Física e Aplicada. Minas Gerais, Viçosa: Universidade Federal de Viçosa; 2009

[29] Kjerfve B. Comparative oceanography of coastal lagoons. In:

Wolfe DA, editor. Estuarine Variability. Orlando: Academic Press; 1986. pp. 63-81. DOI: 10.1016/B978-0-12-761890-6.50009-5

[30] Conama (Conselho Nacional do Meio Ambiente). Resolução CONAMA n° 357 de março de 2005. Dispõe sobre a classificação dos corpos de água e diretrizes ambientais para o seu enquadramento, bem como estabelece as condições e padrões de lançamento de efluentes e dá outras providências. Brasília: Diário Oficial [da] República Federativa do Brasil; 2005. pp. 58-63

[31] APHA. American Public Health Association. Standard Methods for Water and Wastewater. 21st ed. Washington, DC: APHA; 2005

[32] CETESB. Companhia de Tecnologia de Saneamento Ambiental. Variáveis de qualidade da água [Internet]. 2010. Available from: http://www.cetesb.sp.gov.br/Agua/rios/variaveis.asp [Accessed: 10 January 2010]

[33] EPA-U.S. Environmental Protection Agency. Methods for Measuring the Acute Toxicity of Effluents and Receiving Waters to Freshwater and Marine Organisms. 4th ed. Washington, DC: EPA; 1991. 293 p

[34] Code Permanent. Environnement Et Nuisances (1986). Éditions législatives et administratives. Paris, França. Vol. 1 e 2 ;1974 p. apud Zagatto PA, Lorenzetti ML, Pers LSN, Monegon JN. Proposta de um Novo índice de Qualidade de Água. In: XXVI Sil Congress. July 23–29, São Paulo, BR. 1995

[35] ABNT. Associação Brasileira de Normas Técnicas. Ecotoxicologia Aquática–Toxicidade crônica de curta duração–Método de ensaio com peixes. São Paulo, Brazil: ABNT NBR; 2007

[36] Feltkamp CA, Kristensen I. Ecology and morphological characters of different populations of *Poecilia sphenops vandepolli* (Cyprinidontidae). Studies on the Fauna of Curaçao and other Caribbean Islands. 1970;**32**(1): 102-130

[37] Carlson RE. A trophic state index for lakes. Limnology and Oceanography. 1977;**22**(2):261-269. DOI: 10.4319/lo.1977.22.2.0361

[38] Toledo AP Jr, Talarico M, Chinez SJ, Agudo EG. A aplicação de modelos simplificados para a avaliação do processo da eutrofização em lagos e reservatórios tropicais. In: Congresso Brasileiro de Engenharia Sanitária e Ambiental. Balneário Camboriú, Santa Catarina: ABES – Associação Brasileira de Engenharia Sanitária e Ambiental; 1983. pp. 1-34

[39] Parsons TR, Maita Y, Lalli CM. A Manual of Chemical and Biological Methods for Seawater Analysis. 1st ed. Great Britain Oxford: Pergamon Press; 1984. 173p. DOI: 10.1017/S0016756800035494

[40] Greenberg AE, Clesceri LS, Eaton AD. Standard Methods for the Examination of Water and Wastewater. 18th ed. Washington, DC: American Public Health Association; 1992. 550 p

[41] Strickland JDH, Parsons TS. A practical handbook of seawater analysis. Bulletin of the Fisheries Research Board of Canada. 1972;**167**(2):1-205

[42] Rodrigues RR, McPhaden MJ. Why did the 2011–2012 La Niña cause a severe drought in the Brazilian Northeast? Geophysical Research Letters. 2014;**41**(3):1012-1018. DOI: 10.1002/2013GL058703

[43] Castro AJV, Colares IG, Franco TCRS, Cutrim MVJ, Luvizotto-Santos R. Using a toxicity test with *Ruppia maritima* (Linnaeus) to assess the effects of roundup. Marine

Pollution Bulletin. 2015;**91**(2):506-510.
DOI: 10.1016/j.marpolbul.2014.10.006

[44] Knoppers BA, Kjerfve B, Carmouze
JP. Trophic state and water turn-over
time in six choked coastal lagoons in
Brazil. Biogeochemistry. 1991;**14**:
149-166. DOI: 10.1007/BF00002903

[45] Herrera-Silveira JA, Medina-Gomez
I, Colli R. Tropic state based on nutrient
concentration scales and primary
producers community of tropical coastal
lagoons influenced by groundwater
discharges. Hydrobiologia. 2002;**475**:
91-98. DOI: 10.1023/A:1020344721021

[46] Fia R, Matos AT, Coradi PC,
Pereira-Ramirez O. Estado trófico da
água na bacia hidrográfica da Lagoa
Mirim, RS, Brasil. Revista Ambiente &
Água-An Interdisciplinary Journal of
Applied Science. 2009;**4**(1):132-141.
DOI: 10.4136/ambi-agua.78

[47] Coelho RS. Avaliação da qualidade
da água do córrego Franquinho, sub-
bacia Tiquatira/Franquinho, unidade
hidrográfica do alto Tietê, São Paulo–SP
[thesis]. São Paulo: Instituto de
Pesquisas Energéticas e Nucleares; 2001

[48] Schettini CAF. Hidrologia do Saco
da Fazenda, Itajaí, SC. Brazilian Journal
of Aquatic Sciences and Technology.
2008;**12**(1):49-58

Variations of the Absorption of Chromophoric Dissolved Organic Matter in the Pearl River Estuary

Xia Lei, Jiayi Pan and Adam Thomas Devlin

Abstract

Analysis of in-situ measurements during a spring cruise survey in the Pearl River Estuary (PRE) reveals that, controlled by the two-layer gravitational circulation, chromophoric dissolved organic matter (CDOM) absorption shows a clear horizontal distribution pattern at both water surface and bottom, with higher CDOM absorption and lower spectral slope in the northwestern estuary, and a reversed pattern in the southeastern estuary and near the Hong Kong waters. The surface CDOM has higher absorption and lower spectral slope than the bottom. Horizontal transport is suggested to be the dominant hydrodynamic mechanism affecting CDOM distribution pattern in the PRE. With a regional algorithm tailored for the PRE CDOM absorption retrieval, a time series of CDOM absorption and spectral slope in the PRE and the Hong Kong waters in spring from 2012 to 2018 is produced based on satellite images obtained by four sensors with different spatial and spectral resolutions: the Visible Infrared Imaging Radiometer Suite (VIIRS), the Ocean and Land Colour Instrument (OLCI), the Hyperspectral Imager for the Coastal Ocean (HICO), and the Operational Land Imager (OLI). A correlation is revealed between the multi-temporal CDOM absorption and the monthly averaged river discharge, indicating the capability of CDOM ocean color products in identifying hydrodynamic processes in estuaries and coastal waters.

Keywords: chromophoric dissolved organic matter, absorption, ocean color, time series, Pearl River Estuary

1. Introduction

The chromophoric (or colored) dissolved organic matter (CDOM) is the light-absorbing part of the dissolved organic matter (DOM) in natural waters, which may cause a yellow or brown water color at high concentrations [1]. Chemically, CDOM refers to an ensemble of structures including carboxylic acids and carboxyl-rich alicyclic molecules, substituted phenols, ketones, aldehydes, quinones, carbohydrates, saturated and unsaturated hydrocarbons, and nitrogenous material [2].

The major sources of CDOM in the marine environment are terrestrial-derived, oceanic-produced, or sediment-introduced [1]. The terrestrial CDOM is originally synthesized by land and water plants, subsequently processed and modified in limnic systems and eventually exported to coastal waters. The oceanic CDOM is originally fixed by marine plants or phytoplankton, produced by heterotrophic and

autotrophic organisms, or formed by photooxidation of colorless DOM [3–5]. The sediment CDOM is often observed in coastal waters and shelf seas where sediment resuspension, hypoxia events or hydrothermal events occur [6–8].

The processes involved in the removal of CDOM in nature waters include photodegradation and microbial activities. The photochemical reaction triggered by CDOM absorption of high-energy (low wavelength) light can have great impacts on biogeochemical processes and water ecology [9–11]. Heterotrophic microbes either incorporate or respire organic matter and modify CDOM into labile DOM, which are rapidly degraded in the process [12].

Estuaries and coastal waters are very productive systems, where high loading of terrestrial CDOM and high local production are mixed, processed and exported to shelf seas [1]. Therefore, a better understanding of CDOM variation in estuaries and coastal waters can help estimating the oceanic carbon budget and evaluating the anthropogenic impacts on marine environments and global climate change. Furthermore, in estuarine and coastal waters, CDOM absorption usually co-varies with salinity. Variation of CDOM absorption can be used as a tracer of water mass mixing in near shore waters [13]. Investigating and explaining CDOM variations are therefore crucial for understanding various processes in the aquatic environment.

The Pearl River Estuary (PRE) is located on the southern coast of Guangdong, China (22–22.75°N, 113.5–114°N) (**Figure 1**), adjacent to the Northern South China Sea (NSCS). Its major part, the Lingdingyang Estuary, has a trumpet-like shape, with four gates (Humen, Jiaomen, Hongqili, and Hengmen) on the west side of the upper estuary, discharging freshwater of 6.83×10^{10} m^3 into the NSCS every year [14]. The eastern side, however, has two deep channels, along which the coastal sea water can flood into [15]. The various water masses with complex properties make it difficult to interpret the CDOM variations in the estuary.

Furthermore, as China's second largest river in terms of water discharge, the Pearl River has an annual mean discharge of 10,000 m^3 s^{-1} [15–17]. A significant seasonal variation exists in the Pearl River discharge. Therefore, the optical properties of the estuarine water can be strongly influenced by river discharge, especially during the wet season [15], which leads to distinctive characteristics when interpreting and quantifying CDOM variations in the PRE in different seasons.

Studies on CDOM absorption in the PRE last for decades. Previous studies of CDOM optical properties have covered the entire estuary in different seasons of the year, but detailed picture of CDOM variation in the estuary remains poorly understood, the dynamics of CDOM optical properties under control of multiple
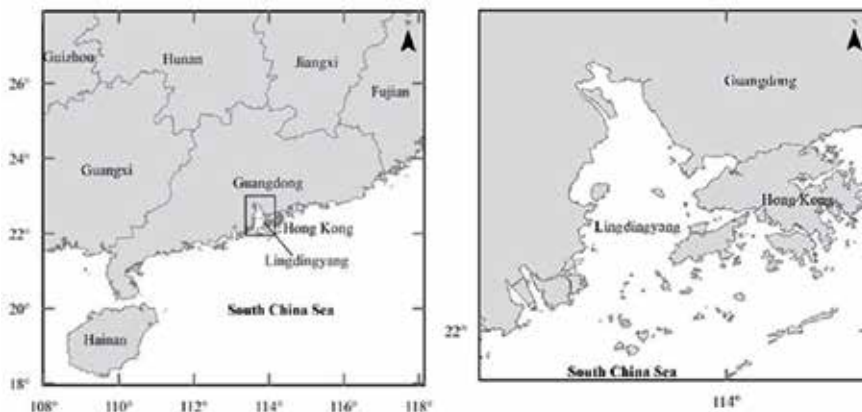
Figure 1.
Location of Lingdingyang Estuary, the major part of the Pearl River Estuary.

hydrodynamic and biogeochemical processes are not yet to be revealed satisfactorily, and the ocean color algorithms for CDOM optical property retrieval with high reliability are still needed to be developed, as well as the CDOM ocean color products with high spatial and temporal resolutions. Therefore, a comprehensive investigation of CDOM optical properties synthesizing advantages of in-situ observations and ocean color interpretations is still in necessity.

The aim of this research is to enhance the understanding of the spatial and temporal variations of CDOM optical properties in the PRE through analyzing in-situ measurements and interpreting satellite ocean color observations. The horizontal and vertical variations of CDOM absorption in the PRE are depicted based on dense and detailed in-situ observations and the dominant driven forces affecting the variations are discriminated. Spatial and temporal variations of CDOM optical properties in the PRE are analyzed based on the CDOM products derived from multi-source ocean color data with complemented spatial and temporal resolutions.

2. Materials and methods

2.1 In-situ observations

Generally, the absorption coefficient ($a_g(\lambda)$, m^{-1}) is a direct measure of CDOM absorptivity. The spectrum of a_g usually spans from ultraviolet band to red band. The spectral shape is unstructured and typically decreases with increasing wavelength in an exponential fashion (Eq. (1)) [18–23].

$$a_g(\lambda) = a_g(\lambda_0) \exp\left[-S_g(\lambda - \lambda_0)\right], \quad (1)$$

where λ_0 is the reference wavelength, and S_g is the spectral slope, describing the decreasing rate of the spectrum.

The absorptivity of CDOM is first measured on a spectrophotometer as absorbance ($A(\lambda)$), a unit-less ratio of spectral radiant power transmitted through the sample across a path length (L) [24]. $A(\lambda)$ is then converted to the (Napierian) absorption coefficient ($a_g(\lambda)$) according to Eq. (2):

$$a_g(\lambda) = 2.303A(\lambda)/L. \quad (2)$$

Typically, measurements are performed using a long-path length quartz cuvette (e.g., 0.1 m) or a liquid core waveguide (0.5–5 m) with submicron-filtered (0.2 or ~0.7 μm) seawater. In low-CDOM waters, measurement of the absorption spectrum of CDOM using a conventional spectrophotometer is challenging. Due to the exponential decline of absorption with increasing wavelength, absorbance values can fall below the detection threshold of the detectors used, typically 0.03–0.06 m^{-1} [25]. Devices with longer effective path lengths, such as reflective tube absorption meters (up to 25 cm [26]), liquid waveguide cells (up to 200 cm [27, 28]), and integrating cavity meters (up to 25 m [29]) attempt to resolve this problem.

A cruise was implemented in the PRE previously from 2 to 12 May 2014. A total of 148 water samples were collected (**Figure 2**) from the water surface (with sampling depth of 0 and 1 m) and the bottom (with sampling depth 1 m above the bottom). CDOM absorbance ($A(\lambda)$) was measured in a 10-cm quartz cell using a Shimadzu UV-2550 spectrophotometer. The absorption coefficient ($a_g(\lambda)$) is calculated at 1 nm interval from 250 to 700 nm according to Eq. (2). Spectral slope, S_g, over wavelength range of UV (250–400 nm), noted as $S_g(250–400)$, is used as a
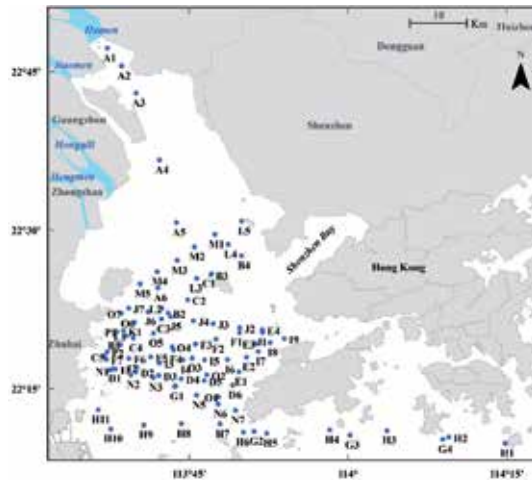
Figure 2.
Location of the sampling stations in the May 2014 cruise in the Pearl River Estuary.

representative of CDOM spectral slope when analyzing the spatial heterogeneity of CDOM [30].

In addition to the spectroscopic analysis of CDOM absorption, in-situ measurements of remote sensing reflectance in visible range (400–900 nm) are also conducted.

2.2 Satellite imagery

The in-situ measurements provide detailed observations on CDOM optical properties. However, the spatial and temporal resolutions of in-situ observations are always limited by high costs in the survey implementation. The satellite imagery can offer better temporal and spatial coverage with high efficiency and low cost. Therefore, space-born and airborne sensors have been used to monitor spectral properties of natural waters for over four decades, and ocean color remote sensing has become an important technology to study water environment.

Nevertheless, the applicability of satellite observation depends on the reliability of CDOM ocean color algorithms. The spectral properties of water bodies may change substantially with geographical locations and time. The color (spectrum) of water can be used to estimate concentrations of optically active constituents in water, such as the phytoplankton, suspended solids, and CDOM based on effective ocean color algorithms.

A regional algorithm for CDOM absorption estimation from satellite ocean color imagery is developed for the spring PRE (Eqs. (3)–(5)), which derives CDOM UV absorption and spectral slope from the visible remote sensing reflectance $[R_{rs}(\lambda)]$, which is established based on the in-situ measured above water remote sensing reflectance (**Figure 3**). The algorithm is with an overall mean absolute percentage difference (MAPD) of ~30 and ~5% for the estimation of CDOM absorption and the spectral slope over 250–450 nm, respectively.

$$a_g(290) = 108.2\,R_{rs}(596) - 0.5324 \tag{3}$$

$$R_{rs}\_Gradient = [R_{rs}(max) - R_{rs}(min)]/[\lambda(max) - \lambda(min)] \tag{4}$$

$$S_g(250\text{--}400) = 0.01187\,R_{rs}\_Gradient^{-0.1741} \qquad (5)$$

Using all available satellite image data obtained by four ocean color sensors with different spatial and spectral resolutions: the Visible Infrared Imaging Radiometer Suite (VIIRS) on board Suomi National Polar-orbiting Partnership (Suomi NPP), the Ocean and Land Colour Instrument (OLCI) on board Sentinel-3A (S3A), the Hyperspectral Imager for the Coastal Ocean (HICO) integrated in the International Space Station (ISS) Window Observational Research Facility (WORF), and the Operational Land Imager (OLI) on board Landsat 8 (LS8) (**Table 1**), a time series of CDOM absorption and spectral slope in the PRE and the Hong Kong waters in spring from 2012 to 2018 is produced. Relevant factors related to the temporal variation of CDOM absorption and spectral slope are analyzed.

To match the season of the in-situ observations in this study, a set of satellite images acquired in spring (April and May) from 2012 to 2018 is selected for the application of the developed algorithm. For the OLI data with a 16-day revisit cycle, the time constraint is relaxed to March and June. The study area covers 22° and 23°N, 113.5° and 114.5°E. The images with cloud coverage below 20% are downloaded (see **Tables 2** and **3** for detailed information of the available images).
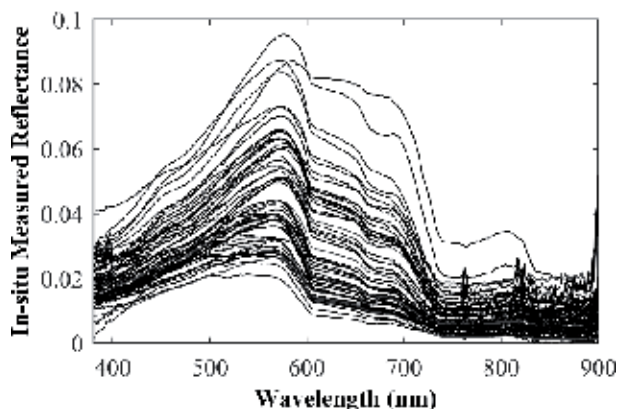
Figure 3.
Normalized in-situ water surface reflectance in 380–900 nm measured by an Ocean Optics 4000 spectrometer using above-water method.

Sensor	VIIRS	OLCI	HICO	OLI
Location	SNPP	Sentinel-3	ISS	Landsat 8
Data period	Jan 2010 to Now	Oct 2016 to Now	Sep 2009 to Sep 2014	Feb 2013 to Now
Number of bands	22	21	128	9
Spectral ranges (nm)	402–12,490	400–1020	353–1080	435–2294
Spatial resolution (m)	375/750/1000	300	100	15/30
Revisit days	1	~2	~10	16

Table 1.
The properties of ocean color remote sensors utilized in this paper.

Sensor	VIIRS	OLCI	HICO	OLI
Data period	Jan 2010 to Now	Oct 2016 to Now	Sep 2009 to Sep 2014	Feb 2013 to Now
Years searched	2012–2018	2017–2018	2012–2014	2013–2018
Months searched	Apr to May	Apr to May	Apr to May	Mar to Jun
Available images	19	5	1	8

Table 2.
Satellite images used for ocean color application.

Sensor	Acquisition time						
	2012	2013	2014	2015	2016	2017	2018
VIIRS	Apr10 May07 May23	Apr20 Apr09 May30 May31	Apr05 Apr15	Apr13 Apr14 Apr24 Apr30	Mar26	Apr02 Apr29 May31	Apr01 Apr10
OLCI						Apr01 Apr02 Apr29	Apr04 Apr08
HICO		Apr20					
OLI			Jun09	Jun12 Jun28	Mar26 May29	Apr30	Apr01 May03

Table 3.
Acquisition time of the available images.

| Sensor	Spectral bands in visible range (nm)	$R_{rs}(596)$
VIIRS	412/445/488/555/672	$[0.66B(555) + 0.34B(672)]/2$
OLCI	400/412.5/442.5/490/510/560/620/665/673.75/681.25	$[B(560) + B(620)]/2$
HICO	404–696 (52 bands with interval of ~5.7 nm)	$[B(593) + B(599)]/2$
OLI	433–453/450–515/525–600/630–680	B3 (525–600)

Table 4.
The criterion used to match $R_{rs}(596)$ with the bands of four sensors.

Eq. (3) is applied to derive $a_g(290)$ from the selected satellite images. The $R_{rs}(596)$ is matched to the bands of the four sensors by the criteria listed in **Table 4**. When retrieving $S_g(250–400)$, considering the available spectral range of the satellite imagery and the performance of atmospheric correction, the lower ends for R_{rs} gradient calculation (the λ_{min} in Eq. (4)) are set as 445, 415.5, 400, and 443 nm for the VIIRS, HICO, OLCI and OLI data, respectively. The range for the R_{rs} maximum is limited below 700 nm for all sensors. $S_g(250–400)$ is afterward derived from R_{rs} gradient by Eq. (5).

3. Results

Figures 4 and **5** present time-series products of ocean color-retrieved CDOM absorption ($a_g(290)$) and spectral slopes ($S_g(250–400)$) from 2012 to 2018, which are derived from the satellite images listed in **Table 3** using Eqs. (3)–(5). All the products can capture the general distribution pattern of CDOM in the PRE,
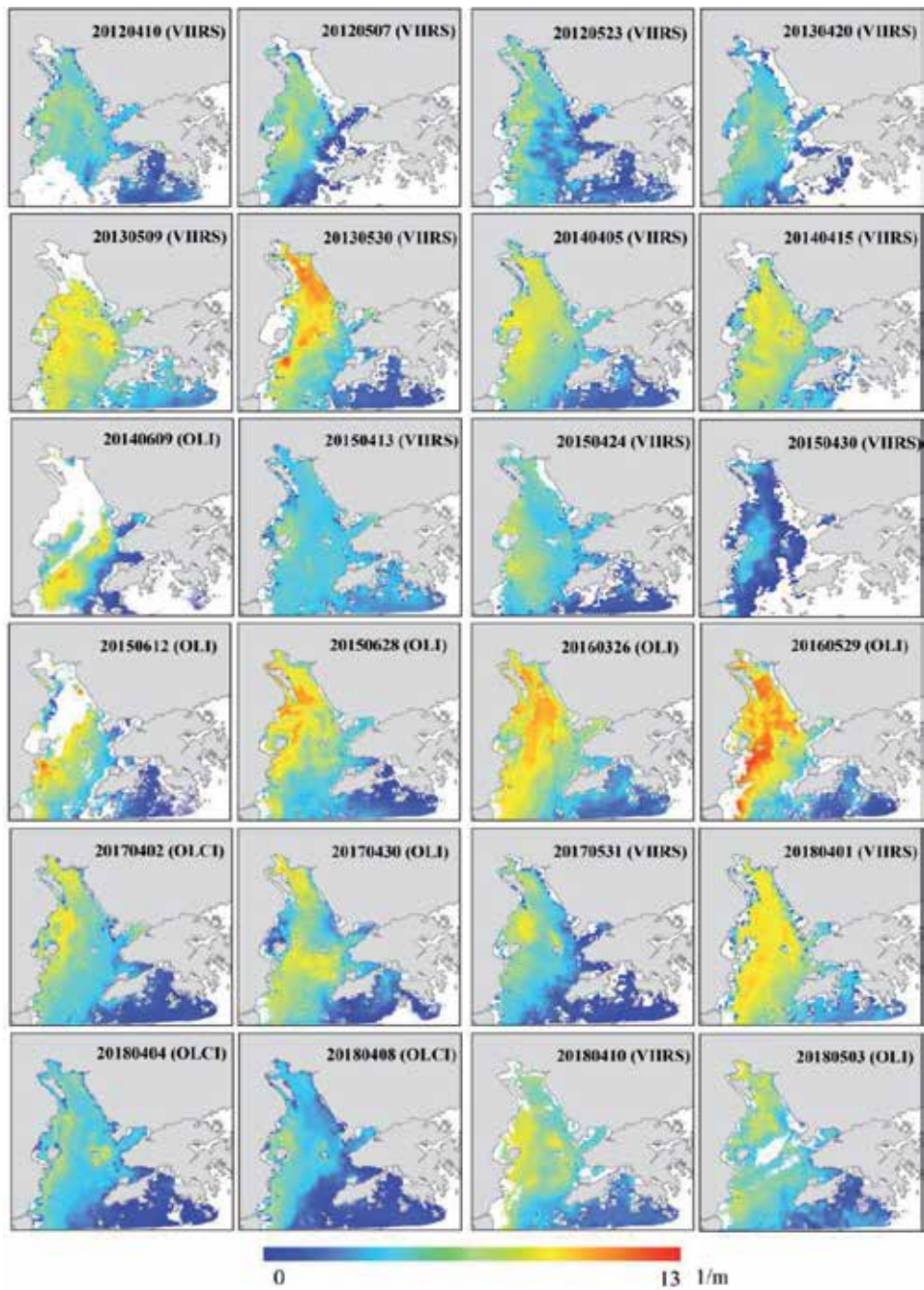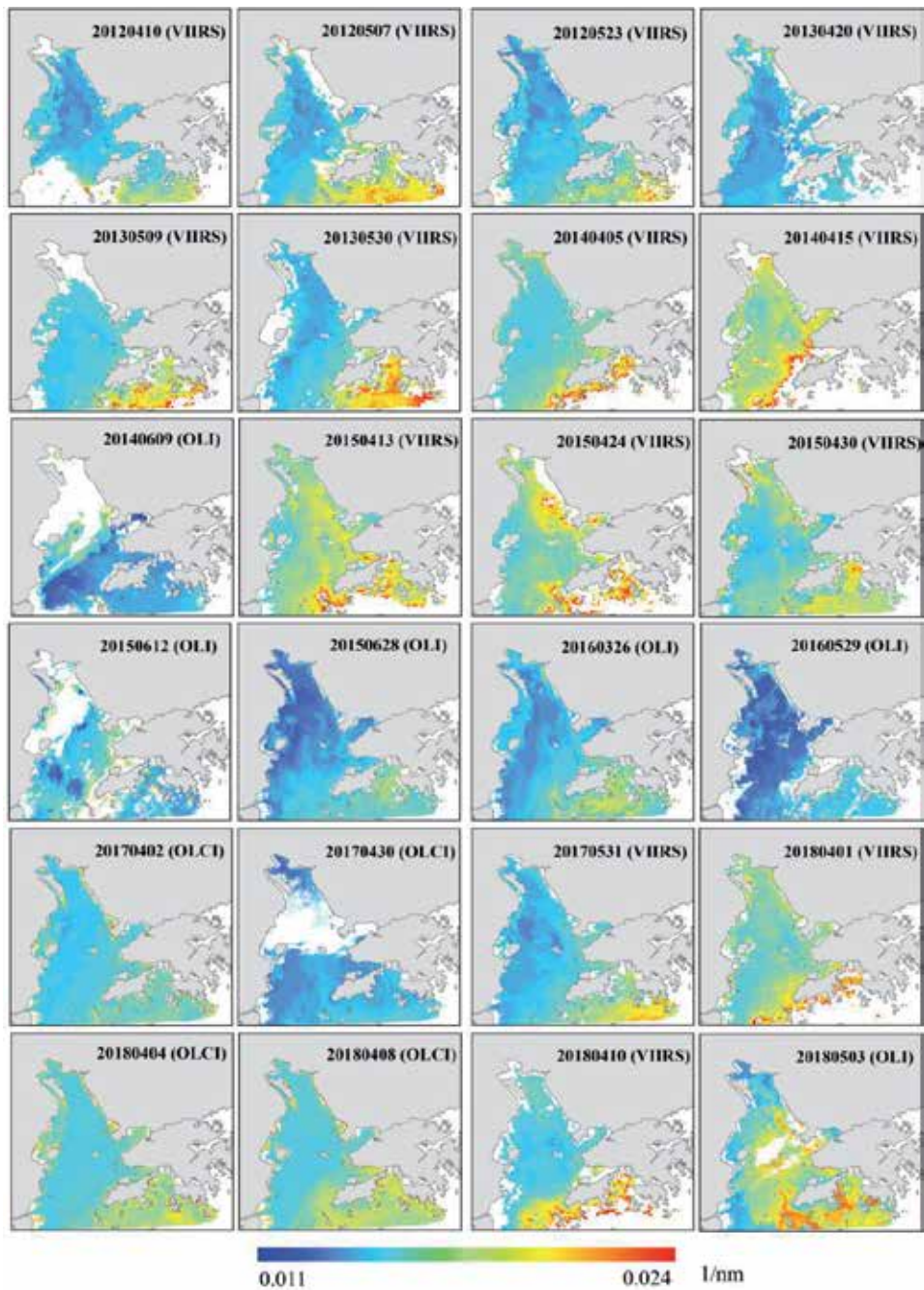
Figure 4.
Time-series of CDOM absorption (a$_g$(290)) in the PRE in spring in 2012–2018 derived from VIIRS, OLCI, HICO, and OLI.

showing the gradual decrease of absorption and the increase of spectral slope along the northwest to southeast direction.

In addition to the clear and consistent trend illustrated in **Figures 4** and **5**, the quantitative variations of CDOM absorption and spectral slope with time are also remarkable. The temporal fluctuation is especially evident in the upper and western PRE, where the water properties are greatly influenced by freshwater discharge, especially during the flooding season.

Figure 5.
Time-series of spectral slope of CDOM absorption ($S_g(250–400)$) in the PRE in spring in 2012–2018 derived from VIIRS, OLCI, HICO and OLI.

Source and removal are the two major aspects that control and balance the CDOM absorption budget in nature waters. In open oceans, phytoplankton production and upwelling of deep water can bring new CDOM into upper layer to elevate CDOM absorption in surface water, while the photobleaching and high stratification can strongly decrease the absorptivity of surface CDOM and increase the spectral slope. In estuaries and coastal waters, the most distinctive condition different from the open oceans is the terrestrial input, which is a significant source of organic
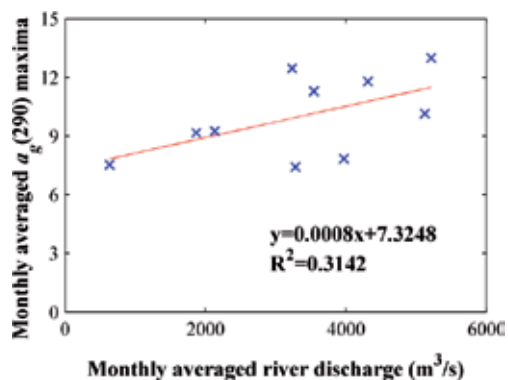
Figure 6.
Correlation between the monthly averaged river discharge of the sum of values measured by two gauging stations (Boluo and Shijiao) and the monthly averaged $a_g(290)$ maxima from the CDOM Ocean color products.

matter in surface water, and leads to the highest variation of CDOM concentration in the region [1]. Therefore, in estuaries and coastal waters, river flow is always an important factor influencing the temporal variation of CDOM absorption during the wet season.

A positive correlation between the monthly averaged river discharge and the monthly averaged $a_g(290)$ maxima from the CDOM ocean color products is shown in the PRE (**Figure 6**), suggesting the high CDOM absorption in the PRE is always associated with high river flow. This pattern is especially typical in spring, when the Pearl River enters the flood season, and the river discharge can dramatically increase after a heavy rainfall. As a contrast to the high river flow, the existing CDOM in surface water of the PRE can be rapidly photodegraded or microbial consumed under the low river discharge with limited inputs of new CDOM, resulting in low level of CDOM absorption and large value of spectral slopes. In this point of view, the time-series of CDOM absorption can be well correlated with river discharge, and therefore is a good indicator of estuarine hydrodynamic conditions.

4. Discussion

For dissolved matter in water, the variation of CDOM is greatly influenced by hydrodynamic conditions, such as horizontal transport and vertical mixing. The PRE circulation is dominated by the gravitational exchange current with the surface freshwater flowing seaward in the surface, mainly on the west side, and the compensated seawater in the lower layer flowing landward along the east coast [31, 32].

As illustrated by in-situ observations and satellite interpretation, CDOM shows the strongest absorption and lowest spectral slope at the head of the estuary (Station A1, A2 and A3) (**Figures 4** and **5**). Water in this region comes from the discharge of the Humen and Jiaomen Gates (**Figure 2**), carrying abundant dissolved organic materials. These CDOM components with complex composition are then transported seaward along the west coast, causing the western estuary to have stronger CDOM absorption and lower spectral slope than the eastern estuary, where the intrusive seawater brings large amount of marine CDOM with lower absorption and higher spectral slope.

It has been reported that terrestrial CDOM is much more sensitive to photo-chemical reactions than marine CDOM [33]. DOM originating from upper streams during high-flow events is abundant in aromatic compounds, and therefore is highly susceptible to solar irradiation, which is in agreement with laboratory

experiments which reveal a high degree of riverine DOM photoreaction [34]. Thus, photodegradation can be a possible reason for the removal of terrigenous CDOM in the surface water of the PRE, therefore the decrease of CDOM absorption. Furthermore, photobleaching can convert high molecular weight CDOM species to lower molecular weight species, result in a great decrease in $a_g(295)$ than in $a_g(275)$, and consequently cause the spectral slope increase [30, 35, 36].

With respect to the ocean color applications, the spatial distribution pattern of CDOM absorption in upper layer is successfully captured by the algorithm, and the time-series CDOM variation which collaboratively changes with river discharge, is also reflected from satellite multi-senor imagery. Furthermore, the variation of CDOM spectral slope (S_g) within the PRE is depicted with very high spatial resolution, by retrieving S_g from satellite imagery pixel by pixel using Eq. (5). This can lead to much more delicate CDOM absorption products (**Figures 4** and **5**), because previous algorithms to derive CDOM absorption spectra generally use a uniform S_g for the entire water area of interest to calculate a_g [37], which is evidently unreasonable for estuarine and coastal waters, where the CDOM of different sources may have different levels of S_g.

5. Conclusion

This research analyzes the variation of the CDOM optical properties (absorption) in the PRE based on the in-situ measurements during a spring cruise survey and the ocean color interpretations. Based on a UV to visible scheme to retrieve CDOM absorption from remote sensing reflectance, the time-series product of CDOM absorption in the PRE waters is produced from satellite images with multiple spatial and spectral resolutions, and an evident correlation with the temporal variation of river discharge is captured in the time-series variation of CDOM absorption in the PRE in spring.

Acknowledgements

Appendices and nomenclature

A	absorbance
a_g	absorption coefficient of CDOM
CDOM	chromophoric dissolved organic matter
DOC	dissolved organic carbon
DOM	dissolved organic matter
HICO	hyperspectral imager for the coastal ocean
ISS	International Space Station
MAPD	mean absolute percent difference
OLCI	Ocean and Land Colour Instrument
OLI	Operational Land Imager
UV	ultraviolet
VIIRS	Visible Infrared Imaging Radiometer Suite

Author details

Xia Lei[1], Jiayi Pan[2]* and Adam Thomas Devlin[2]

1 Institute of Space and Earth Information Science, The Chinese University of Hong Kong, Shatin, Hong Kong, China

2 School of Geography and the Environment, Jiangxi Normal University, Nanchang, Jiangxi, China

*Address all correspondence to: panj@cuhk.edu.hk

IntechOpen

References

[1] Stedmon CA, Nelson NB. The optical properties of DOM in the ocean. In: Hansell D, Carlson C, editors. Biogeochemistry of Marine Dissolved Organic Matter. 2nd ed. San Diego, CA: Academic Press; 2015. 481-508 p

[2] Sharpless CM, Blough NV. The importance of charge-transfer interactions in determining chromophoric dissolved organic matter (CDOM) optical and photochemical properties. Environmental Science: Processes & Impacts. 2014;**16**:654-671

[3] Steinberg DK, Nelson NB, Carlson CA, Prusak AC. Production of chromophoric dissolved organic matter (CDOM) in the open ocean by zooplankton and the colonial cyanobacterium *Trichodesmium* spp. Marine Ecology Progress Series. 2004;**267**:45-56

[4] Kieber RJ, Hydra LH, Seaton PJ. Photooxidation of triglycerides and fatty acids in seawater: Implication toward the formation of marine humic substances. Limnology and Oceanography. 1997;**42**:1454-1462

[5] Swan CM, Nelson NB, Siegel DA, Kostadinov TS. The effect of surface irradiance on the absorption spectrum of chromophoric dissolved organic matter in the global ocean. Deep Sea Research Part I: Oceanographic Research Papers. 2012;**63**:52-64

[6] Osburn CL, Handsel LT, Mikan MP, Paerl HW, Montgomery MT. Fluorescence tracking of dissolved and particulate organic matter quality in a river-dominated estuary. Environmental Science & Technology. 2012;**46**:8628-8636

[7] Skoog A, Hall POJ, Hulth S, Paxéus N, Rutgers van der Loeff M, Westerlund S. Early diagenetic production and sediment-water

exchange of fluorescent dissolved organic matter in the coastal environment. Geochimica et Cosmochimica Acta. 1996;**60**:3619-3629

[8] Yang L, Hong H, Guo W, Chen CA, Pan P, Feng C. Absorption and fluorescence of dissolved organic matter in submarine hydrothermal vents off NE Taiwan. Marine Chemistry. 2012;**128-129**:64-71

[9] Blough NV, Zepp RG. Reactive oxygen species in natural waters. In: Foote CS et al., editors. Active Oxygen in Chemistry. Glasgow, UK: Chapman & Hall; 1995. pp. 280-333

[10] Johannessen SC, Miller WL. Quantum yield for the photochemical production of dissolved inorganic carbon in seawater. Marine Chemistry. 2001;**76**:271-283

[11] Nieto-Cid M, Álvarez-Salgado XA, PÉrez FF. Microbial and photochemical reactivity of fluorescent dissolved organic matter in a coastal upwelling system. Limnology and Oceanography. 2006;**51**:1391-1400

[12] Nelson NB, Carlson CA, Steinberg DK. Production of chromophoric dissolved organic matter by Sargasso Sea microbes. Marine Chemistry. 2004;**89**:273-287

[13] Laane RWPM, Kramer KJM. Natural fluorescence in the North Sea and its major estuaries. Netherlands Journal of Sea Research. 1990;**26**:1-9

[14] Deng Z, He Q, Yang Q, Lin J. Observations of in situ flocs characteristics in the Modaomen Estuary of the Pearl River. Haiyang Xuebao. 2015;**37**(9):152-161. (In Chinese with English abstract)

[15] Chen ZQ, Li Y, Pan JM. Distributions of colored dissolved

organic matter and dissolved organic carbon in the Pearl River Estuary, China. Continental Shelf Research. 2004;**24**:1845-1856

[16] Callahan J, Dai MH, Chen RF, Li XL, Lu ZM, Huang W. Dissolved organic matter in the Pearl River Estuary, China. Marine Chemistry. 2004;**89**:211-224

[17] Hong HS, Wu JY, Shang SL, Hu CM. Absorption and fluorescence of chromophoric dissolved organic matter in the Pearl River Estuary, South China. Marine Chemistry. 2005;**97**:78-89

[18] Blough NV, Del Vecchio R. Chromophoric dissolved organic matter (CDOM) in the coastal environment. In: Hansell D, Carlson C, editors. Biogeochemistry of Marine Dissolved Organic Matter. San Diego, CA: Academic Press; 2002. pp. 509-546

[19] Jerlov NG. Optical Oceanography. New York: Elsevier; 1968

[20] Bricaud A, Morel A, Prieur L. Absorption by dissolved organic matter of the sea (yellow substance) in the UV and visible domains. Limnology and Oceanography. 1981;**26**(l):43-53

[21] Carder KL, Steward RG, Harvey GR, Ortner PB. Marine humic and fulvic acids: Their effects on remote sensing of ocean chlorophyll. Limnology and Oceanography. 1989;**34**(1):68-81

[22] Green SA, Blough NV. Optical absorption and fluorescence properties of chromophoric dissolved organic matter in natural waters. Limnology and Oceanography. 1994;**39**(8):1903-1916

[23] Stedmon CA, Markager S, Kaas H. Optical properties and signatures of chromophoric dissolved organic matter (CDOM) in Danish coastal waters. Estuarine, Coastal and Shelf Science. 2000;**51**(2):267-278

[24] Braslavsky SE. Glossary of terms used in photochemistry, 3rd edition

(IUPAC Recommendations 2006). Applied Chemistry. 2007;**79**:293-465

[25] Nelson NB, Siegel DA, Michaels AF. Seasonal dynamics of colored dissolved material in the Sargasso Sea. Deep Sea Research, Part I. 1998;**45**:931-957

[26] Zaneveld JRV, Kitchen JC, Bricaud A, Moore CC. Analysis of in-situ spectral absorption meter data. In: Gilbert GD, editor. Ocean Optics XI. San Diego: International Society for Optics and Photonics; 1992. pp. 187-200

[27] Miller RL, Belz M, Del Castillo C, Trzaska R. Determining CDOM absorption spectra in diverse coastal environments using a multiple pathlength liquid core waveguide system. Continental Shelf Research. 2002;**22**:1301-1310

[28] Nelson NB, Siegel DA, Carlson CA, Swan C, Smethie WM, Khatiwala S. Hydrography of chromophoric dissolved organic matter in the North Atlantic. Deep-Sea Research Part I: Oceanographic Research Papers. 2007;**54**:710-731

[29] Röttgers R, Doerffer R. Measurements of optical absorption by chromophoric dissolved organic matter using a point-source integrating-cavity absorption meter. Limnology and Oceanography: Methods. 2007;**5**:126-135

[30] Helms JR, Stubbins A, Ritchie JD, Minor EC, Kieber DJ, Mopper K. Absorption spectral slopes and slope ratios as indicators of molecular weight, source, and photobleaching of chromophoric dissolved organic matter. Limnology and Oceanography. 2008;**53**(3):955-969

[31] Wong LA. A model study of the circulation in the Pearl River Estuary (PRE) and its adjacent coastal waters: 2. Sensitivity experiments. Journal of Geophysical Research. 2003;**108**:3157

[32] Dong L, Su J, Ah Wong L, Cao Z, Chen JC. Seasonal variation and dynamics of the Pearl River plume. Continental Shelf Research. 2004;**24**:1761-1777

[33] Miller WL, Moran MA. Interaction of photochemical and microbial processes in the degradation of refractory dissolved organic matter from a coastal marine environment. Limnology and Oceanography. 1997;**42**(6):1317-1324

[34] Ramond PA, Spencer RGM. Riverine DOM. In: Hansell D, Carlson C, editors. Biogeochemistry of Marine Dissolved Organic Matter. 2nd ed. San Diego, CA: Academic Press; 2015. pp. 509-533

[35] Dalzell BJ, Minor EC, Mopper KM. Photodegradation of estuarine dissolved organic matter: a multi-method assessment of DOM transformation. Organic Geochemistry. 2009;**40**:243-257

[36] Fichot CG, Benner R. The spectral slope coefficient of chromophoric dissolved organic matter (S275-295) as a tracer of terrigenous dissolved organic carbon in river-influenced ocean margins. Limnology and Oceanography. 2012;**57**(5):1453-1466

[37] Cao F, Miller WL. A new algorithm to retrieve chromophoric dissolved organic matter (CDOM) absorption spectra in the UV from ocean color. Journal of Geophysical Research, Oceans. 2015;**120**:496-516

Chapter 9

Response of Coastal Upwelling East of Hainan Island in the South China Sea to Sudden Impact and Long-Term Variability of Atmospheric Forcing

Lingling Xie and Mingming Li

Abstract

The wind-driven coastal upwelling east of Hainan Island (UEH) in the northwestern South China Sea (SCS) is sensitive to the multi-scale variability of atmospheric forcing. This chapter focuses on two ends of time scales of atmospheric forcing: very short-time or sudden impact, i.e., typhoon passages; and long-term variability associated with El Niño events. The response of the sea surface temperature (SST) associated with the UEH to typhoon passages was investigated based on concurrent satellite SST and wind products. The long-term variability and response of the UEH to super El Niño events were analyzed based on recent 30 years of satellite data. The results show that the UEH has significant responses to atmospheric forcing. Meanwhile, the ocean circulation also plays an important role in modulation of the coastal upwelling.

Keywords: coastal upwelling, typhoon, ENSO, long-term variability, South China Sea

1. Introduction

As one of the important dynamic processes in continental shelf seas, coastal upwelling is capable of bringing the cold and nutrient-rich subsurface water to the surface [1–3]. Thus, it plays a crucial role in the local fishery [4, 5], sedimentation process [6, 7], and weather system [8, 9]. Meanwhile, the coastal upwelling is of significance for the air-sea CO_2 flux and the global carbon cycle [10, 11]. Hence, oceanographers have paid much attention to the coastal upwelling in various ocean areas [12–18].

The wind-forced offshore Ekman transport is the general mechanism for the coastal upwelling [16, 19–21]. In recent decades, with global climate change, the long-term and interannual variability of upwelling, particularly its response to extreme events, such as the El Niño-Southern Oscillation (ENSO) events, has been paid more and more attentions [22–27]. On the other hand, the coastal upwelling in low latitudes is susceptible to frequently passing tropical cyclones. The sudden impacts by typhoon passages on the upwelling process are worth pursuing [28–31].

As shown in **Figure 1**, upwelling east of Hainan Island (UEH) is seasonal coastal upwelling in the northwestern South China Sea (SCS). It occurs mostly within a
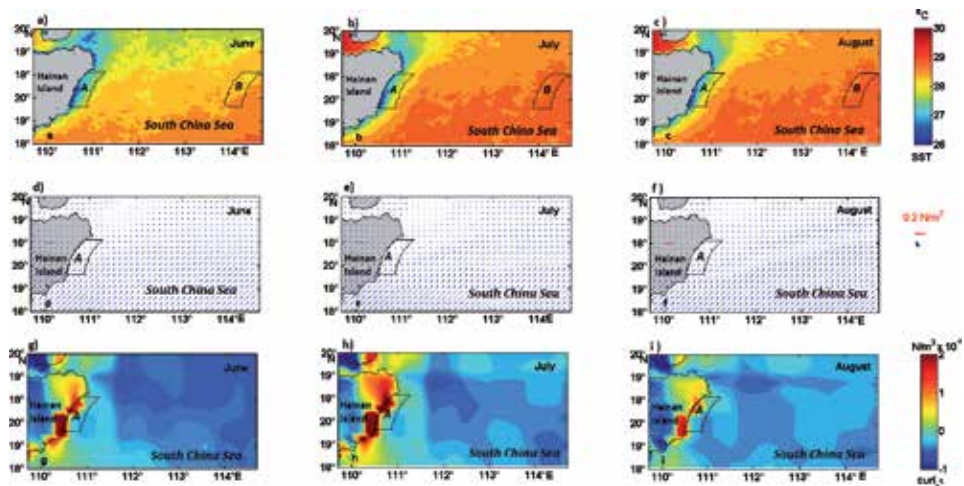
Figure 1.
Climatological monthly mean SST (a–c), wind stress vector (d–f), and wind stress curl (g–i) in summer months of June, July, and August in northern SCS. Black boxes A and B represent the coastal upwelling zone of the UEH and the background zone without upwelling in deep water, respectively.

range of 40 km off the coastline in summer months as the southwesterly monsoon prevails [16, 21, 32]. The wind-driven offshore Ekman transport and Ekman pumping, as well as the topography effect, are main mechanisms of the UEH [33–35]. Since pioneer studies in the 1960s, researchers have investigated the hydrographic features and the variability of the UEH [16, 31, 33, 36–39]. In recent years, the 3D vertical circulation and diapycnal turbulent mixing in the UEH zone have been investigated from cruise observations [21, 40].

2. Long-term variability of UEH

2.1 Climatology

As shown in **Figure 1a–c**, the SST reaches above 28°C in the most northern SCS. One can see that the low-temperature area along the eastern coast of Hainan Island formed by upwelling is quite evident with SST decreasing from 27.5°C at 40 km offshore to 26°C along the coast. In July and August, the SST reaches above 29°C in the deep water but is still lower than 27.5°C in the coastal upwelling zone. Influenced by East Asia monsoon, the southwesterly winds prevail in the northern SCS in summer as shown in **Figure 1d–f**. One can see that the wind stress in the offshore water east of Hainan Island is lower than that in the deep water. The winds blow northeastward over the offshore water. The non-zero wind stress curl is produced by nonuniform spatial distributions of wind speed and wind direction. From the wind stress curl shown in **Figure 1g–i**, one can see that in summer, the wind stress curl east of 112°E in the northern SCS is generally negative, while that over the coast upwelling zone between 110° and 111°E is positive in June–August, and the value and extent are larger in July. Driven by the positive wind stress curl, the Ekman pumping can cause upwelling of lower layer cold water, leading to the UEH with low SST.

2.2 Variability of upwelling intensity

We use the SST difference between the upwelling zone (Zone A in **Figure 1**) and that in the deep water without upwelling (Zone B in **Figure 1**) as the upwelling
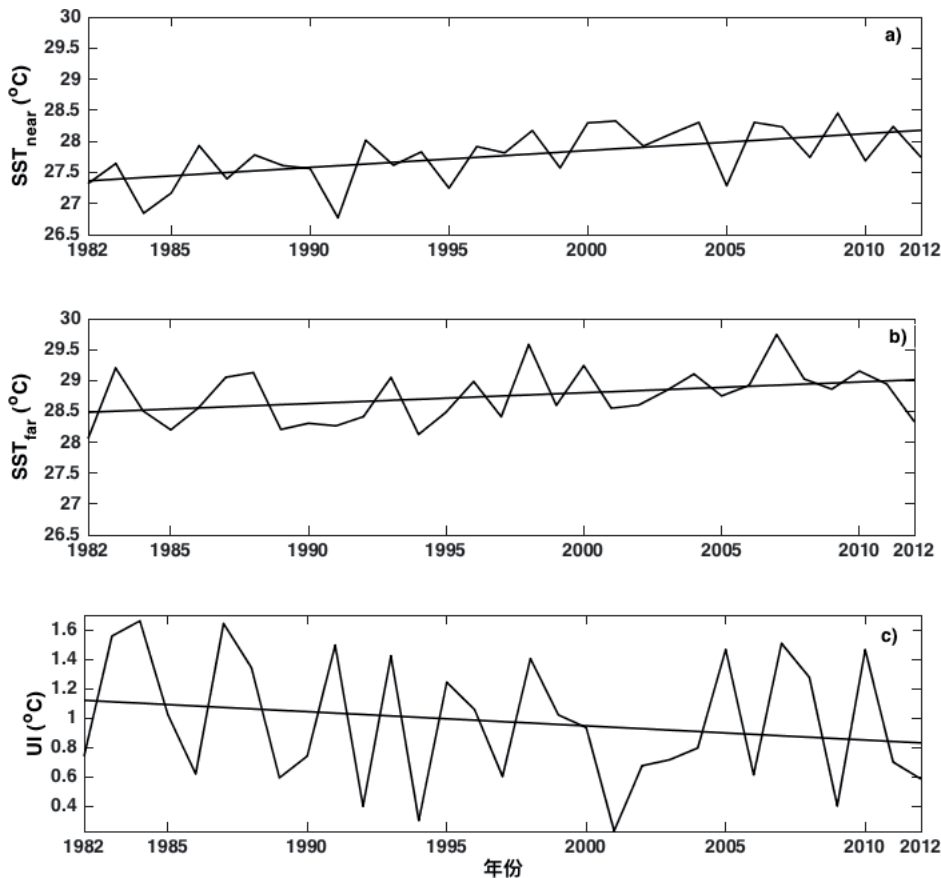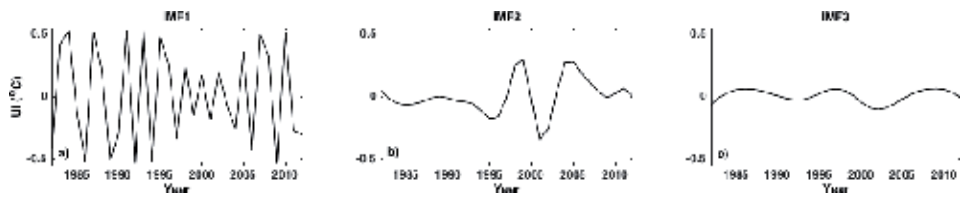
Figure 2.
*Variation of the averaged SST in summer in the upwelling zone (zone A in **Figure 1**) (a) and the background zone in the deep water (zone B in **Figure 1**) (b) and the upwelling index (UI) of UEH (c) from 1982 to 2012. The straight lines represent the linear trends of the variations (cited from [26]).*

index (UI) to denote the upwelling intensity (refer to [26] for details). **Figure 2** shows the variation of SST in zones A and B and the UI of the UEH from 1982 to 2012. One can see that both the SST in the upwelling zone A, i.e., SST_{near}, and that in the deep water without upwelling, i.e., SST_{far}, have increasing trends in recent 30 years. The increase rate is 0.03°C/a for zone A and 0.02°C/a for zone B, respectively. The warming in the upwelling zone is faster than that in the open-sea waters. Thus, the UI of the UEH has a decreasing trend with a rate of −0.01°C/a. The UEH weakens as the global climate changes. This is opposite to the intensification in the coastal upwelling zones on the east coast of the ocean basin [22, 24–25, 41].

In order to investigate the interannual variability of the UEH, we decompose the UI time series using the empirical mode decomposition (EMD) method [42]. The first three intrinsic mode functions (IMFs 1–3) are shown in **Figure 3**. One can see that the periods of the IMFs 1–3 are about 3 a, 5 a, and 10 a, respectively. The corresponding variance contributions are 82, 10, and 1%. The IMF1 has the largest amplitude and dominates the interannual variability of the UEH. On the other hand, the 3-year variation is highly related to the ENSO events [33].

2.3 Variability of upwelling center

Taking the latitude of the maximum UI as the upwelling center, one can investigate the variation of the position of the UEH. As shown in **Figure 4a**, one can see

Figure 3.
First three intrinsic mode functions (IMFs 1–3) of the UI series of the UEH (a) IMF1, the first and largest mode, (b) IMF2, the second mode and (c) IMF3, the third mode (cited from [26]).
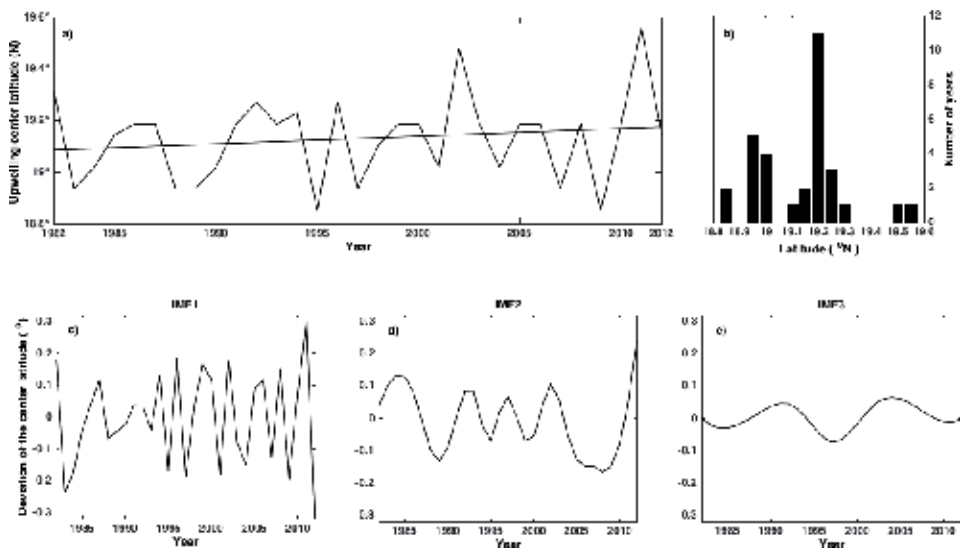
Figure 4.
*The interannual variation (a) and the statistics (b) of the upwelling center of the UEH in 1982–2012 and three IMFs of the variation (c–e) (cited from [26]).*

that the center of UEH oscillated north-southward along the Hainan coast between 18.9° and 19.3°N in the past 30 years. The center positions of the largest probability are in 19.2°–19.3°N and 18.9°–19°N. For the long-term variation trend, one can see that the center position shifted northward from 1980 to 2012. The IMFs of the center position series also show interannual variability with three intrinsic periods of 3 a, 5 a, and 10 a, of which IMF 1 has the largest amplitude and dominates the variance.

2.4 Effects of wind stress and wind stress curl

The UEH is generally driven by the alongshore wind stress. However, for the long-term variation, the alongshore wind stress has an increasing trend with a rate of 1.1×10^{-5} N/m^2/a as shown in **Figure 5a**. This is opposite to the decreasing trend of the UEH shown in **Figure 2c**. The correlation coefficient of the interannual variability of the UI with that of the alongshore wind stress is only 0.43 (P < 0.02). The alongshore wind stress seems not to be the dominant factor for the long-term variation of the UEH. **Figure 5b** shows the variation of the wind stress curl over the upwelling zone. One can see that the wind stress curl has a decreasing trend with a rate of -2.7×10^{-11} N/m^3/a. The correlation coefficient of the wind stress curl and the UI reaches 0.66 (P < 0.001). For the first two IFMs, the correlation coefficients reach 0.75 for IMF1 and 0.54 for IMF2 for the wind stress curl but are 0.52 for IMF1 and 0.46 for IMF2 for the alongshore wind stress. This result suggests that the wind
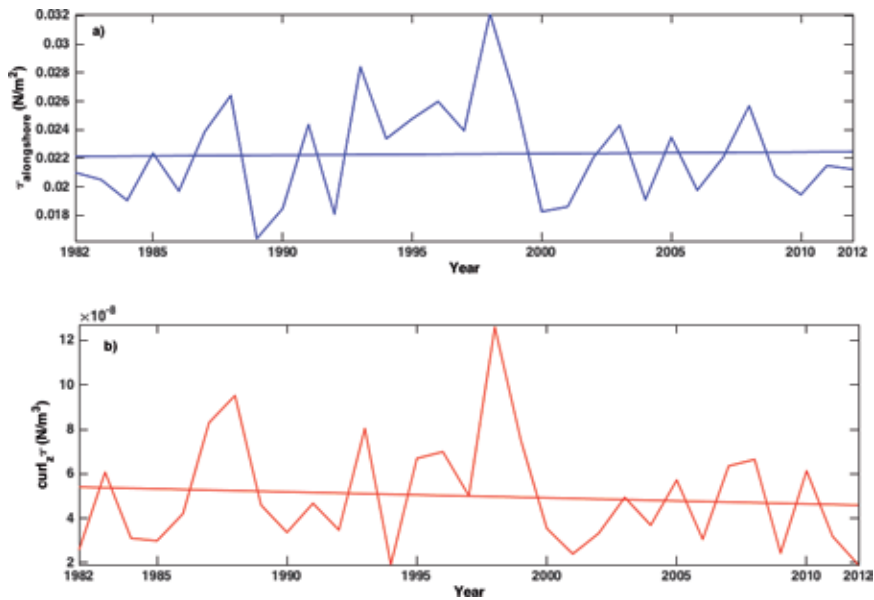
Figure 5.
Variations of the alongshore wind stress $\tau_{alongshore}$ (a) and the curl of wind stress $curl_z\tau$ (b) over the UEH zone in 1982–2012. The straight lines represent the linear trends (cited from [26]).

stress curl-induced Ekman pumping plays a more important role in the long-term variability of the UEH intensity.

By comparing the latitudes of maximum alongshore wind stress (around 19.1°N) and wind stress curl (around 19.25°N), one can see that the latitude of the maximum wind stress curl is more consistent with latitudes of the maximum UI at 19.2°–19.3°N. This shows the importance of the wind stress curl on the long-term variation of the UEH.

3. Response of UEH to super El Niño events

3.1 Background

As mentioned above and in previous studies, the UEH has interannual variability associated with the ENSO events [37]. Comparing with the UEH, the upwelling east of Vietnam coast (UEV) in the western SCS has different response to the ENSO events [8, 43]. Jing et al. [33] analyzed the response of UEH and UEV to a super El Niño event of 1997–1998 and found that in summer 1998, southerly winds were intensified in the northern SCS, so that UEH was strengthened, while easterly winds were abnormally intensified along the Vietnam coast over the southern SCS, so that UEV is weakened. Most of these previous investigations explained the mechanisms of response of coastal upwelling to El Niño events based on wind forcing, and less attentions are paid to the background ocean dynamic processes.

Recently, another super El Niño event occurred in 2015–2016, which lasted for longer than 12 months with sea surface temperature anomaly (SSTA) peaks higher than 2°C for longer than a half year as shown in **Figure 6**. Shen et al. [39] use SST, sea surface height (SSH), wind fields, and heat flux data from 1995 to 2016 to compare different responses of UEH and UEV to the two super El Niño events of 1997–1998 and 2015–2016 and found that ocean mesoscale eddies significantly affected the response of coastal upwelling to El Niño events.
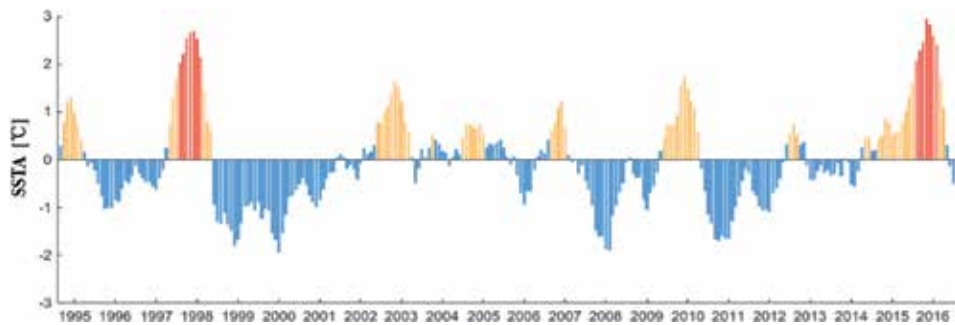
Figure 6.
Niño 3.4 index from 1995 to 2016. Blue, orange, and red color bars represent SSTA lower than 0.4°C, but higher than 0.4 and 2°C, respectively (cited from [39]).

3.2 SSTA

The SSTA with respect to climatologic SST is generally used as an indicator to represent response of upwelling to the El Niño events [8, 33, 43, 44].

Figure 7a–b shows the averaged SSTA fields of UEH and UEV in local summer (June–July–August) of 1998. One can see that the extent of cold water in UEH expanded with totally averaged SST 0.04°C lower than that of climatology, implying that UEH was slightly intensified. On the other hand, the extent of cold water in UEV was remarkably shrunk with greatly increased SSTA. The totally averaged SSTA was 1.15°C. In particular, at the cold center of climatology near 11° 30'N, SSTA was warmed up as high as 1.8°C. This implies that the UEV greatly weakened after the super El Niño event of 1997–1998 ended in spring 1998.

Super El Niño event of 2015–2016 ended in spring 2016 has the longest lifetime and the highest SST anomaly in the equatorial Pacific since 1900. In summer 2016, SSTAs in UEH and UEV are entirely different. As shown in **Figure 7c–d**, all SSTs in UEH show warm anomaly with the SSTA amplitudes of 0.4–1.0°C, and the warmest anomaly appeared at about 100 km offshore. Comparing SST distribution (not shown), the cold water area of UEH greatly decreased, with totally averaged SSTA of 0.67°C, implying that UEH weakened. Meanwhile, SST in the UEV decreased about 0.2°C in the area 50 km offshore from 11° 30'N to 12° 30'N, while SST slowly increased from the cold center to the deep water. The totally averaged SSTA was 0.17°C with a maximum warm anomaly of 0.4°C, implying that UEV was also slightly weakened.

3.3 Wind field anomaly

The variability of local wind field is an important factor that must be considered in response of coastal upwelling to super El Niño events. **Figure 8** shows the wind vector anomaly (arrows) and the wind stress curl anomaly (color) of the UEH and the UEV in summer 1998 and 2016. Forced by abnormal southerly winds and positive wind stress curl anomaly, both favorable conditions for upwelling, UEH was intensified with expanded sea surface cold water area and lower temperature in summer 1998 (**Figure 8a**). This is consistent with SSTA patterns shown in **Figure 7a**. Meanwhile, for the UEV, southerly wind anomaly was remarkable, and wind stress curl decreased with the negative anomaly of -2×10^{-7} N m^{-3}. The two factors restrained the upwelling development, so that SST in UEV increased in summer 1998 (**Figure 8b**). This is consistent with SSTA patterns shown in **Figure 7b**.

In summer 2016, southerly wind anomaly was still dominant over the UEH; the wind stress curl anomaly was positive and negative over the northern and southern
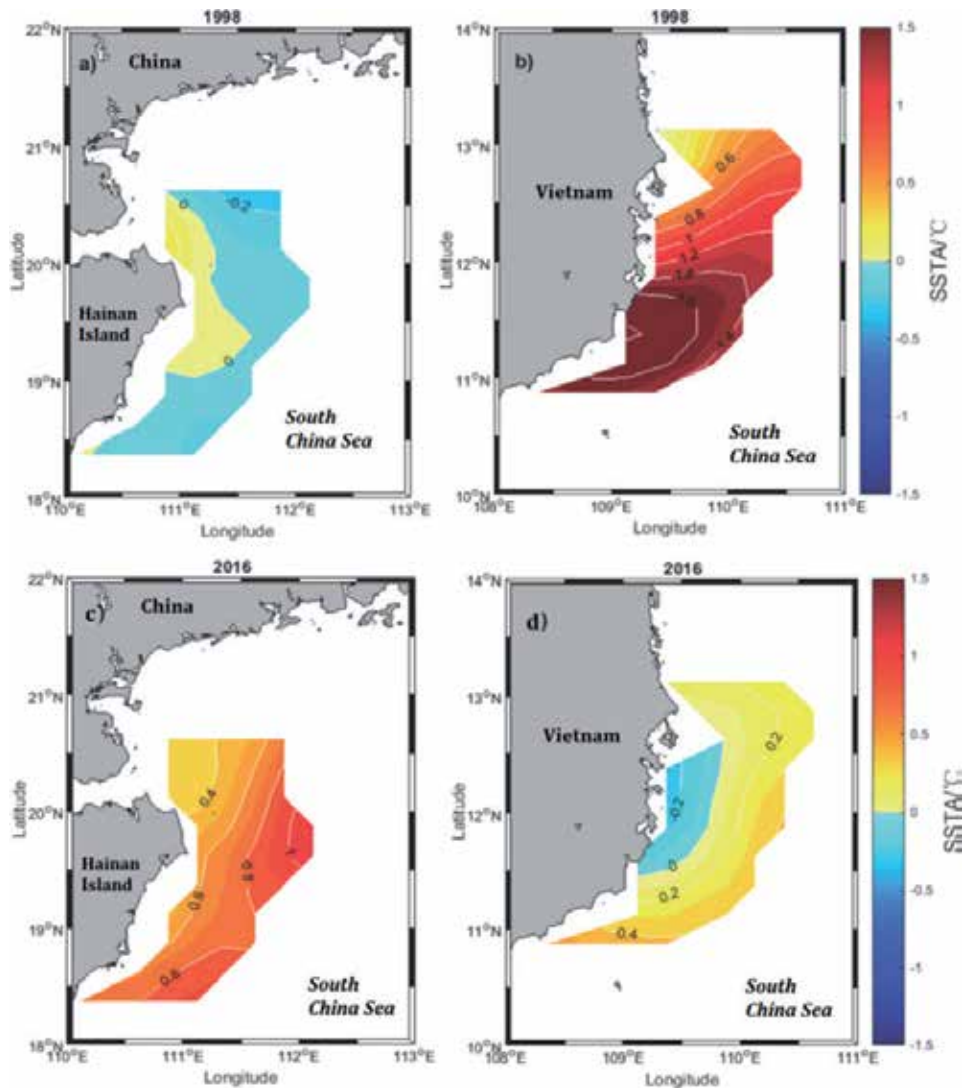
Figure 7.
SSTA in UEH (a, c) and UEV (b, d) in summers 1998 and 2016. Color codes are in °C (cited from [39]).

UEH, respectively (**Figure 8c**). The wind speeds were higher than the climatologic means. Theoretically, the wind fields were favorable to the upwelling development. However, the comparison with the SSTA patterns shown in **Figure 7c** indicates that the temperature in the UEH cold water area greatly increased and the region of cold water became narrower. Based on this fact, Shen et al. [39] speculate that there are other factors to weaken the UEH. In the UEV, the southerly wind anomaly was dominant, and the wind stress curl anomaly was positive in most cases with the mean positive anomaly as high as 1.5×10^{-7} N m^{-3} (**Figure 8d**). The wind speeds were greater than the climatologic values. Such wind field anomaly was greatly favorable to the upwelling development. However, results in the above section indicate that in summer 2016, the mean SST in the UEV was close to the climatologic mean, cold water area was not obviously expanded, and lower SST appeared in partial area only. This implies that there are some factors to counteract forcing of wind field, resulting in unchanged upwelling intensity in the UEV.
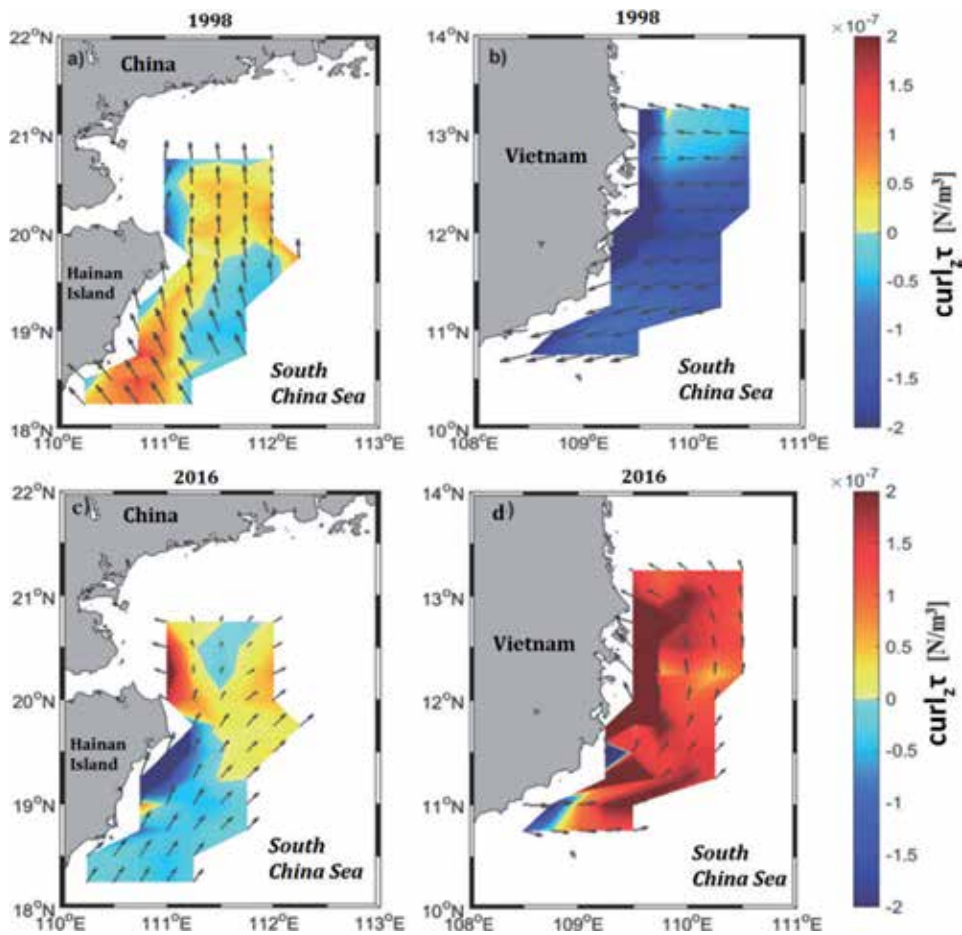
Figure 8.
Composite maps of wind vector anomaly (arrows) and wind stress curl anomaly (color codes in N m⁻³) of
UEH (a, c) and UEV (b, d) in summer 1998 and 2016 (cited from [39]).

3.4 Surface heat flux

The sea surface heat flux is an important factor to affect the SSTA. **Figure 9a**
shows summer mean net heat flux of the western SCS in 1998 and 2016. One can see
that the horizontal distributions are characterized by dipole patterns, i.e., a low-value
center, located at the deep basin coexisting with a high-value center at the northwest-
ern shelf. The extent of high net heat flux (NHF) ($>7.5 \times 10^6$ J m⁻²) in summer 2016
(**Figure 9b**) was much larger than that in summer 1998 (**Figure 9a**), suggesting that
the heat absorbed by UEH and UEV was higher than that in 1998 summer.

Figure 9c shows the difference of spatial mean NHF in summer 2016 from that
in summer 1998. For both of the UEH and the UEV, all the heat flux differences
are positive, i.e., the heat gain due to shortwave solar radiation in summer 2016
was greater than that in summer 1998, and the heat losses due to the long-wave
radiation, latent heat flux, and sensible heat flux were smaller than that in sum-
mer 1998. This result reveals that NHF absorbed by the sea water of two upwelling
zones in summer 2016 was near twice of that in summer 1998. The increase ampli-
tude of the NHF in UEV was twice of that in UEH. However, comparing that in
summer 1998, the mean SST in UEH in summer 2016 increased near 0.71°C, while
that in UEV decreased by 0.98°C as shown in **Figure 7**, namely, in the UEV, the
NHF increased, but SST decreased. Therefore, the NHF is not a dominant factor to
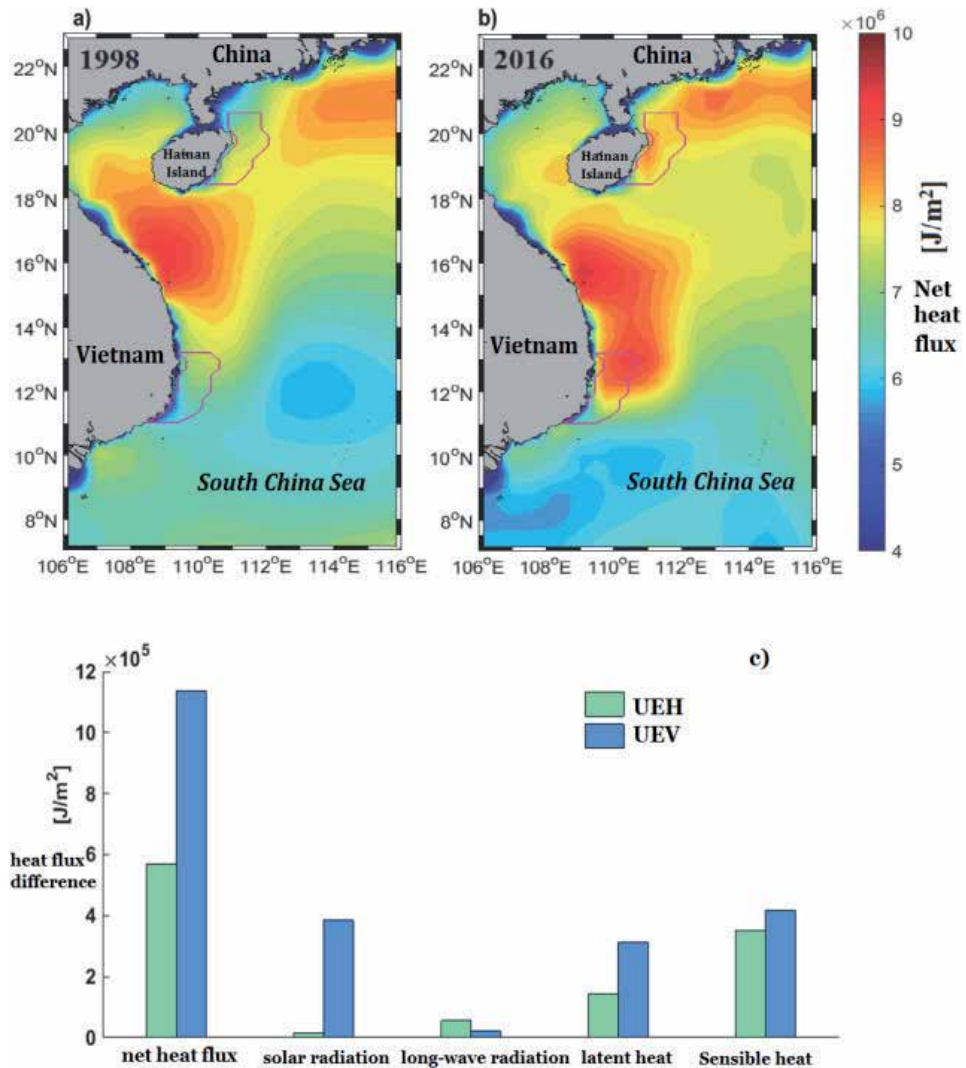
Figure 9.
Downward mean net heat flux (NHF) in the western SCS in summer 1998 (a) and 2016 (b) and difference of mean heat fluxes of summer 2016 from 1998 in UEH and UEV (c). Color codes in a–b represent NHF in J m^{-2} (cited from [39]).

affect SSTA in the upwelling cold water area during the El Niño events, but there must be other dynamic factors to counteract the SST increase in the upwelling cold water areas.

3.5 Effects of ocean dynamic processes on upwelling cold water

As a component of the ocean circulation, coastal upwelling is affected by the background current. The surface cold water in the upwelling zone is formed by transport of cold water in lower layers to upper layers carried by the vertical motion of sea water. Meanwhile, if horizontal currents transport water masses with different properties from other areas to the upwelling zone, or alter the current fields to affect divergence of upper layer sea water, it is possible to change the intensity and location of upwelling.

Mesoscale eddies are active in the SCS [45, 46]. The horizontal and vertical motions of eddies would modulate background current and mass transport, so
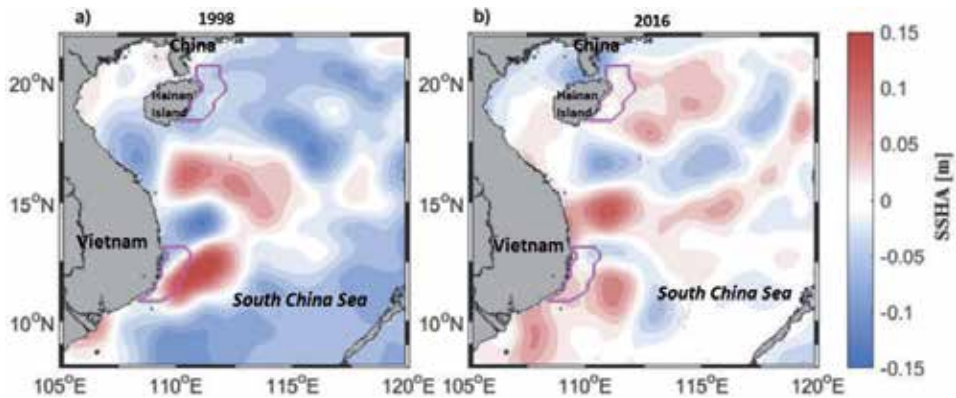
Figure 10.
SSHA distribution in the western SCS in summer 1998 (a) and 2016 (b). Color codes are in m (cited from [39]).

that they may be the important processes to affect UEH and UEV. Here, the SSH anomaly (SSHA) is used as an index to analyze effects of mesoscale eddies on SSTA in the upwelling zones. **Figure 10** shows SSHA distribution in the western SCS in summer 1998 and 2016. In summer 1998, SSHA in the northern SCS was negative (**Figure 10a**), favorable for UEH development. Meanwhile, there was an ellipse-shaped warm eddy in SW-NE direction off the South Vietnam coast. The UEV was located within the extent of warm eddy, so that the UEV was restrained. On the other hand, in summer 2016, the UEH was located in the positive SSHA area, and there were multiple weak warm eddies east of Hainan Island (**Figure 10b**). The SSHA was also positive in the offshore water of Vietnam. Near the Indo-China Peninsula, there were a train of stronger warm eddies centered at 10°, 12°, and 15°N, respectively. This might explain that although the wind field anomaly along the Vietnam coast was quite favorable for upwelling development, the extent of cold water did not expand, and SST also did not decrease with respect to the climatology. It is the warm eddies that may counteract the wind forcing effect.

4. Response of UEH to typhoon passage

4.1 Statistics of typhoon

Previous investigators have addressed that the hydrological characteristics and dynamic structure of the upwelling may have dramatic changes after typhoon passage [28, 38, 47]. The UEH is located in the pathway of typhoons formed both in the western Pacific Ocean and the SCS [47, 48]. In order to investigate the sudden impact of typhoon forcing on the UEH, Xie et al. [31] analyzed the statistics of typhoons passing the UEH zone during the past 34 years from 1982 to 2015.

As shown in **Figure 11**, there were a total of 42 tropical cyclones passing the UEH between April and September from 1982 to 2015, of which 24 cyclones originated from the western Pacific and 18 from the SCS. The cyclones originating from the Pacific passed over the UEH mostly in July, while the locally generated cyclones in the SCS appeared mostly in August. Most cyclones moved northwestward into the research area, while several cases passed this region north-/northwestward or even parallel to the coastline. **Figure 11g** shows the incidence angles of the cyclones, which is defined as the angle between the pathway of cyclone when entering the upwelling region and the trend of coastline, i.e., 0° for the passage parallel to the coastline and 90° for perpendicular. Twenty-five cyclones entered this area with
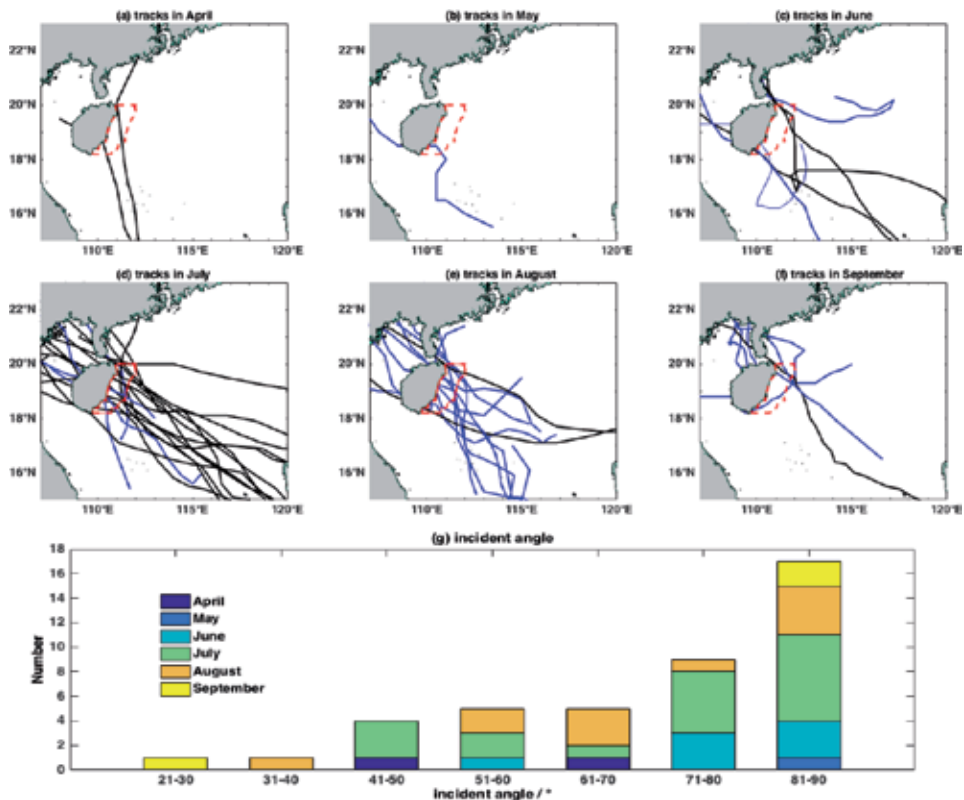
Figure 11.
Tracks and incidence angles of cyclones passing over the UEH zone (red box) during the period from April to September of 1982 to 2015. Black lines in (a)–(f) are tracks of tropical cyclones originated from the Pacific and blue lines from the SCS. Red boxes represent the UEH zone for statistics (cited from [31]).

incidence angle between 70° and 90°, among which seventeen passages were nearly perpendicular to the coastline (80°–90° of the incidence angle). Only in two cases the incidence angles were smaller than 40°.

As for the monthly distribution, the passages of tropical cyclones were prevailing in summer from June to August, when upwelling had been well developed. There are 36 cases in summer, accounting for 86% of all passing cyclones, in which 18 cases occurred in July. As of the cyclone intensity, the most frequent category was severe tropical storm (STS) with 12 cases during 34 years, followed by the tropical depression (TD) and typhoon (TY) of 10 and 9 cases, respectively. The three most prevailing types account for 74% of all passing tropical cyclones. The severest super typhoon (super TY) occurred in July 2014.

4.2 Statistics of SST variation

The SST variations in the UEH induced by cyclone passages during 1982 and 2015 are shown in **Figure 12**. The SST difference (ΔSST) between the post-cyclone and pre-cyclone values is used to specify the response of UEH to typhoon passages. Here the pre- and post-SST are averaged values of the whole region within 7 days before cyclones enter or after passing the upwelling zone (outlined by red dashed lines in **Figure 11**), respectively. In most cases, the SST in the upwelling zone decreased ($\Delta SST < 0$) after the typhoon passage, with the greatest decrease of −2.4°C induced by the severe typhoon (STY) Zeke in 1991. The SST increase occurred in 1985, 1989, and 2001, with the greatest increase of 3.4°C after the passage of a nameless weak
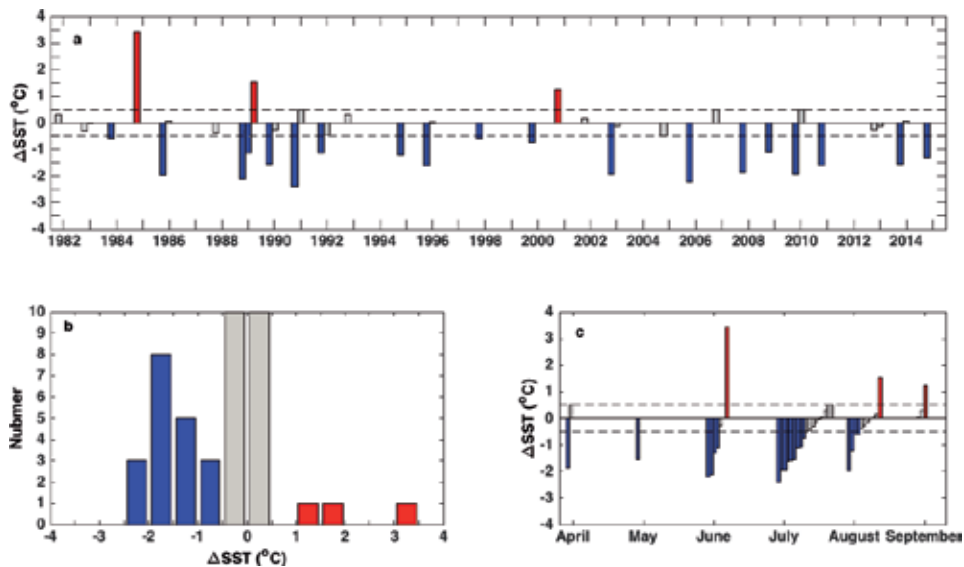
Figure 12.
SST changes induced by the 42 tropical cyclones passing over the UEH from 1982 to 2015. (a) Yearly distribution. (b) Number of typhoons in different cases. (c) Monthly distribution. Warming cases are in red, cooling cases in blue, and no-significant-change cases in gray (cited from [31]).

tropical depression (WTD). The warming of sea surface after typhoon passages is distinguished from the prevailing cooling in the open ocean.

All 42 cases are categorized into three types according to the SST variation ΔSST: cooling with $\Delta SST < -0.5°C$, no-significant-change with $-0.5 \leq \Delta SST \leq 0.5°C$, and warming with $\Delta SST > 0.5°C$. The statistical result is listed in **Figure 12b**. Nineteen cases of forty-two cyclones triggered surface cooling, with ΔSST concentrated mainly between -2 and $-1.5°C$ and averaged to $-1.5°C$; twenty cases were in the category of no-significant-change with a mean value of $0°C$, accounting for 48% of all cases and the number of slightly warming is larger than that of slightly cooling; three warming cases were found with a mean value of $2.1°C$. The magnitude of averaged warming is greater than that of cooling.

In monthly distribution (**Figure 12c**), most warming cases occurred from June to September, with a maximum in June. The largest magnitude and most frequent cooling were in July, preceding that in June and August.

4.3 SST changes vs. typhoon parameters

It is usually assumed that the intensity and moving speed of tropical cyclone are two predominant factors influencing SST decrease in the open ocean. The stronger or slower-moving cyclones are supposed to induce more SST decrease [49]. Other studies suggested that the incidence angle and path of tropical cyclone may also play an important role in SST variation in coastal regions [29, 50]. In the UEH, all the four mentioned parameters are analyzed in 42 cases from 1981 to 2015.

The distributions of ΔSST on two joint parameters are illustrated in **Figure 13**. One can see that all three warming cases occurred after passage of low-wind-speed tropical cyclones, with duration period of 5–9 h, and the magnitude of SST variation increases with the incidence angle. For cooling cases, the relation between SST variation and maximal wind speed is not significant, with correlation coefficient $R^2 = 0.29$. The magnitude of SST decrease is not dependent on the duration period of tropical cyclone. Most cooling cases occurred after tropical cyclones with the
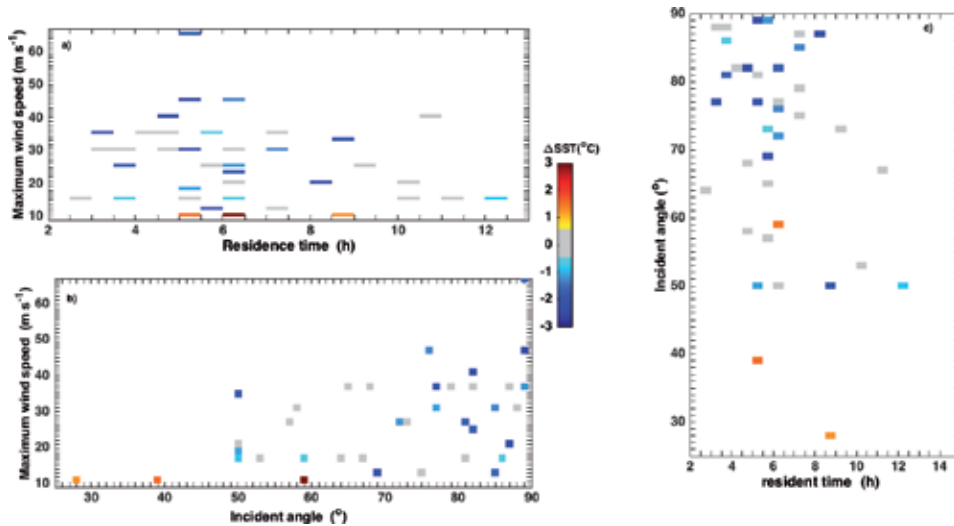
Figure 13.
2-D distribution of SST variation with tropical cyclone parameters (a) SST variation vs. maximum wind speed and residence time. (b) SST variation vs. maximum wind speed and incident angle. (c) SST variation vs. incident angle and residence time (cited from [31]).

duration time smaller than 8 h. All cooling cases occurred with the incidence angles greater than 50°, and there is an increasing trend of ΔSST magnitude with the incidence angle. The SST variation in no-significant-change is independent of the wind speed or the duration time of tropical cyclone. The incidence angles were all larger than 50°. It seems that the maximal wind speed and the incidence angle contribute more to the SST response, and the duration time might have slight influence.

4.4 Mechanisms of SST change

The change in SST induced by passage of tropical cyclone depends on the net heat flux in the research area. As a severe local disturbance, strong vertical convection and turbulent mixing during the momentum transfer from the cyclone to the sea water are generally regarded as the primary mechanism for sea surface cooling [47]. The magnitude of cooling increases as the strength of the cyclone increases or the movement speed decreases, due to the enhancement of vertical pumping and mixing. Generally, the heat variations of the upper ocean due to vertical convection and mixing induced by tropical cyclone, denoted as Q_v and Q_m, respectively, are negative. However, 20 no-significant-changes and even 3 warming cases appear in the above statistical analysis, indicating that there are other mechanisms inducing the positive heat flux via tropical cyclones.

As illustrated in **Figure 14**, the typhoon approaching the upwelling zone might decrease or increase the SST in the offshore water due to onshore or offshore Ekman transport induced by the typhoon winds. The heat flux due to the typhoon Ekman flow is denoted by Q_E, and its sign depends on the relative locations of the typhoon track and the upwelling zone [29]. For three SST warming cases mentioned above, the locations of tropical cyclone tracks relative to the upwelling zone are variant: one was south to the upwelling core, one passed the central upwelling zone, and one veered from the north to the south. The local typhoon-induced heat advection Q_{Ea} by Ekman transport is merely one factor influencing the SST variation.

Zheng et al. [50] suggested that typhoon could force a single sea-level soliton in the deep offshore water with the positive amplitude. Warm water was thus transported onshore with the shoreward propagation of the soliton due to nonlinearity and resulted in net positive heat flux shoreward. The onshore amplitude of
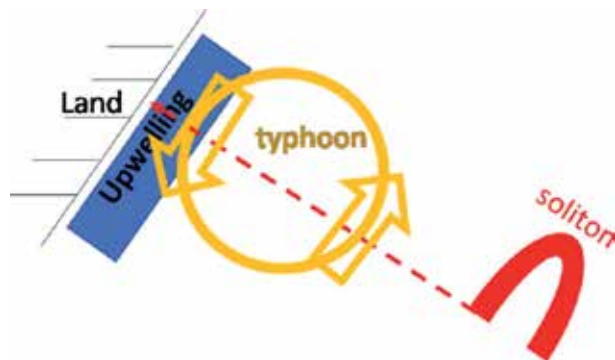
Figure 14.
Sketch of typhoon-induced upwelling-favorable/upwelling-unfavorable wind and shoreward propagating soliton.
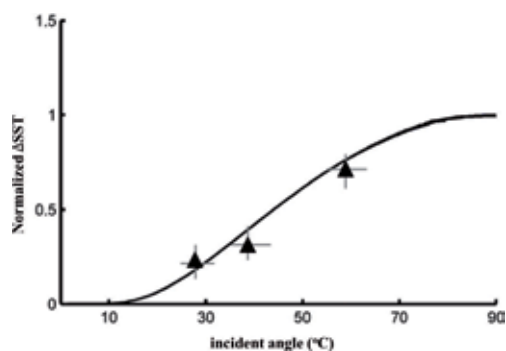
Figure 15.
SST variation vs. incidence angle of tropical cyclone for three SST warming cases in UEH (cited from [31]).

soliton induced by typhoon (thus the heat advection marked as Q_{ra}) depends on the typhoon incidence angle, i.e.,

$$\beta_d \cong \alpha_1 sin^{1/2}\theta\, exp\left(-\frac{\alpha_2}{sin\theta}\right) \tag{1}$$

in which β_d is the amplitude of soliton, θ the typhoon incidence angle, and α_1 and α_2 are parameters related to the continental shelf width, the turbulent viscosity and the propagation velocity of the soliton (refer to [50] for detail).

The normalized SST variation vs. the incidence angle of tropical cyclone in three warming cases is shown in **Figure 15**. One can see that the normalized ΔSST increases with the incidence angle and conforms to the idealized curve suggested by Zheng et al. [50]. It shows that the heat transport by the offshore soliton is a significant mechanism of SST increase in UEH after typhoon passages.

To sum up, the heat flux induced by tropical cyclone in UEH consists of two main categories: nonlocal heat transport Q_r through shoreward transport of the offshore warm water by the tropical cyclone induced soliton, here $Q_r = Q_{ra}$ and is positive; local heat flux by the momentum input of tropical cyclone Q_1, including the heat change due to vertical convection/mixing Q_{vm} (negative) and Ekman flow Q_{Ea} (positive/negative), here $Q_1 = Q_{vm} + Q_{Ea}$. Thus, the net heat flux by tropical cyclone is summarized as

$$Q_{net} = Q_r + Q_1 \begin{cases} > 0 & if\ Q_1 > 0\ or\ Q_r > \\ = 0 & if\ Q_1 < 0\ and\ Q_r = -Q_1 \\ < 0 & if\ Q_1 < \ and\ Q_r < -Q_1 \end{cases} \tag{2}$$

The above statistics of 42 tropical cyclone passages indicate that the SST response in the UEH could be warming, no-significant-change, or cooling, accounting for 7, 48, and 45%, respectively. The heat flux is affected by the intensity, the moving speed, the incidence angle, and the relative location of tropical cyclone. The combination of these factors modifies the relative magnitudes of Q_r and Q_1, thus influences the SST response signatures.

5. Summaries

The wind-driven UEH is a typical seasonal coastal upwelling in the northwestern SCS. Satellite SST data and wind products help to investigate the variability of UEH to multi-scale atmospheric processes. This chapter overviews the recent progress, including the long-term and interannual variability of UEH with the global climate change in recent decades, the response of UEH and UEV to super El Niño events in 1998 and 2016, the variation of UEH after sudden impacts of typhoon passages, and the variability mechanisms. The main results are summarized as follows:

1. Different from intensification trend of most east-coast upwelling, the UEH has a weakened trend in the recent 30 years from 1982 to 2012. The decreasing rate of UI is 0.01°C/a. The UEH has higher correlation coefficient with the variation of the local wind curl, which also has decreasing trend than the alongshore wind stress. Meanwhile, the latitude of UEH core tends to move northward, so does the latitude of the maximum wind curl location. Three intrinsic modes with periods of 3, 5, and 10 years are found both for the upwelling intensity and the core location variation, of which the mode with a 3-year period dominates the variation. The local wind curl plays an important role in the interannual variation of the UEH.

2. The response of the UEH to the super El Niño event in 2016 was different from that in 1998. The responses of the UEH to two super El Niño events were also different from that of the UEV. Specifically, the upwelling-favorable wind anomaly enhanced the UEH, while the upwelling-unfavorable wind anomaly weakened the UEV in summer 1998. In summer 2016, there were upwelling-favorable wind anomalies in both the UEH and the UEV. However, the cool water zone shrunk with warmer SSTA in the UEH region, and the UEV became warmer, indicating other mechanisms beside the ENSO-induced wind anomaly. It is found that mesoscale eddies may significantly affect the response of upwelling to super El Nino events.

3. There are three categories of SST response for 42 cases of typhoons passing through the UEH from 1982 to 2015, i.e., increasing SST (19 cases), no-significant-changing SST (20 cases), and decreasing SST (3 cases). The averaged SST increase is 2.1°C, higher than the averaged decrease of −1.5°C. The intensity and the incidence angle are found to be main factors affecting the variation of SST. The typhoon-induced elevation nonlinear soliton transports heat from the open ocean to the coastal upwelling zone, so that SST increases. The observed SST variation vs. the incidence angle of typhoon track conforms to the theoretical predictions, namely, the SST variation may be caused by both local and remote heat transports induced by typhoon.

Acknowledgements

Author details

Lingling Xie* and Mingming Li
College of Ocean and Meteorology, Guangdong Ocean University, Zhanjiang, China

*Address all correspondence to: llingxie@163.com

IntechOpen

References

[1] Huyer A. Coastal upwelling in the California current system. Progress in Oceanography. 1983;**12**(3):259-284. DOI: 10.1016/0079-6611(83)90010-1

[2] Smith RL. Coastal upwelling in the modern ocean. Geological Society London Special Publications. 1992;**64**(1):9-28

[3] Cropper TE, Hanna E, Bigg GR. Spatial and temporal seasonal trends in coastal upwelling off Northwest Africa, 1981-2012. Deep Sea Research Part I. 2014;**86**:94-111. DOI: 10.1016/j. dsr.2014.01.007

[4] Silva A, Palma S, Oliveira PB, Motia MT. Composition and interannual variability of phytoplankton in a coastal upwelling region (Lisbon Bay, Portugal). Journal of Sea Research. 2009;**62**(4):238-249. DOI: 10.1016/j. seares.2009.05.001

[5] Kuvaldina N, Lips I, Lips U, Liblik T. The influence of a coastal upwelling event on chlorophyll A and nutrient dynamics in the surface layer of the Gulf of Finland, Baltic Sea. Hydrobiologia. 2010;**639**(1):221-230. DOI: 10.1007/ s10750-009-0022-4

[6] Suess E, Thiede J. Coastal Upwelling its Sediment Record: Part A: Responses of the Sedimentary Regime to Present Coastal Upwelling. Berlin: Springer Science & Business Media; 2013. DOI: 10.1007/978-1-4615-6651-9

[7] Hu DX. Upwelling and sedimentation dynamics. I. The role of upwelling in sedimentation in the Huanghai Sea and East China Sea—A description of general features. Chinese Journal of Oceanology & Limnology. 1984;**2**(1): 13-19. DOI: 10.1007/BF02888388

[8] Xie SP, Xie Q, Wang DX, Liu WT. Summer upwelling in the South China Sea and its role in regional climate variations. Journal of Geophysical Research. 2003;**108**(C8):3261. DOI: 10.1029/2003JC001867

[9] Zheng Z-W, Zheng QA, Kuo Y-C, Gopalakrishnan G, Lee C-Y, Ho C-R, et al. Impacts of coastal upwelling off East Vietnam on the regional winds system: An air-sea-land interaction. Dynamics of Atmospheres & Oceans. 2016;**76**(1):105-115. DOI: 10.1016/j. dynatmoce.2016.10.002

[10] Ianson D, Feely RA, Sabine CL, Juranek LW. Features of coastal upwelling regions that determine net air-sea CO_2 flux. Journal of Oceanography. 2009;**65**(5):677-687. DOI: 10.1016/j.dsr.2014.01.007

[11] Lachkar Z, Gruber N. Response of biological production and air-sea CO_2 fluxes to upwelling intensification in the California and canary current systems. Journal of Marine Systems. 2013;**109-110**:149-160. DOI: 10.1016/j. jmarsys.2012.04.003

[12] Li L. Summer upwelling system over the northern continental shelf of the South China Sea a physical descriptor. In: Su J, Chuang WS, Hsurh RY, editors. Proceedings of the Symposium on the Physical and Chemical Oceanography of the China Seas. Beijing: China Ocean Press; 1993. pp. 58-68

[13] Gan JP, Allen JS. Modeling upwelling circulation off the Oregon coast. Journal of Geophysical Research. 2005;**110**:C10S07. DOI: 10.1029/2004JC002692

[14] Schafstall J, Dengler M, Brandt P, Bange H. Tidal-induced mixing and diapycnal nutrient fluxes in the Mauritanian upwelling region. Journal of Geophysical Research Oceans. 2015;**115**(C10). DOI: 10.1029/2009JC005940

[15] Hu JY, Wang XH. Progress on upwelling studies in the China seas. Reviews of Geophysics. 2016;**54**(3): 657-673. DOI: 10.1002/2015RG000505

[16] Xie LL, Zhang SW, Zhao H. Overview of studies on Qiongdong upwelling. Journal of Tropical Oceanography. 2012;**31**(4):35-41. DOI: 10.3969/j.issn.1009-5470.2012.04.005 (in Chinese)

[17] Chegini F, Lu Y, Katavouta A, Ritchie H. Coastal upwelling off southwest nova scotia simulated with a high resolution baroclinic ocean model. Journal of Geophysical Research. 2018;**123**(4):2318-2331. DOI: 10.1002/2017JC013431

[18] Joseph KA, Jayaram C, Nair A, George MS, Balchand AN, Pettersson LH. Remote sensing of upwelling in the Arabian Sea and adjacent near-coastal regions. In: Barale V, Gade M, editors. Remote Sensing of the Asian Seas. Cham: Springer; 2019. DOI: 10.1007/978-3-319-94067-0_26

[19] Shetye SR, Shenoi SSC, Gouveia AD, Michael GS, Sundar D, Nampoothiri G. Wind-driven coastal upwelling along the western boundary of the bay of Bengal during the southwest monsoon. Continental Shelf Research. 1991;**11**(91):1397-1408. DOI: 10.1016/0278-4343(91)90042-5

[20] Belmadani A, Echevin V, Codron F, Takahashi K, Junquas C. What dynamics drive future wind scenarios for coastal upwelling off Peru and Chile? Climate Dynamics. 2017;**43**(7-8):1-22. DOI: 10.1007/s00382-013-2015-2

[21] Xie LL, Enric P-S, Zheng QA, Zhang SW, Zong XL, Yi XF, et al. Diagnosis of 3D vertical circulation in the upwelling and frontal zones east of Hainan Island. China. Journal of Physical Oceanography. 2017a;**47**(4):755-774. DOI: 10.1175/JPO-D-16-0192

[22] Bakun A. Global climate change and intensification of coastal ocean upwelling. Science. 1990;**247**(4939):198-201. DOI: 10.1126/science.247.4939.198

[23] Vargas G, Pantoja S, Rutllant José A, Lange CB, Ortlieb L. Enhancement of coastal upwelling and interdecadal ENSO-like variability in the Peru-Chile current since late 19th century. Geophysical Research Letters. 2007;**34**(13):L13607. DOI: 10.1029/2006gl028812

[24] Wang DW, Gouhier TC, Menge BA, Ganguly AR. Intensification and spatial homogenization of coastal upwelling under climate change. Nature. 2015;**518**(7539):390-394. DOI: 10.1038/nature14235

[25] Sydeman WJ, Garcíareyes M, Schoeman DS, Rykaczewski RR, Thompson SA, Black BA, et al. Climate change. Climate change and wind intensification in coastal upwelling ecosystems. Science. 2014;**345**(6192): 77-80. DOI: 10.1126/science.1251635

[26] Xie LL, Zong XL, Yi XF, Li M. Interannual variation and long-term trend of Qiongdong upwelling. Oceanologica et Limnologia Sinica. 2016;**47**(1):1-9 (in Chinese)

[27] Xiu P, Chai F, Curchitser EN, Castruccio FS. Future changes in coastal upwelling ecosystems with global warming: The case of the California current system. Scientific Reports. 2866;**8**:2018. DOI: 10.1038/s41598-018-21247-7

[28] Rao AD, Babu SV, Dube SK. Impact of a tropical cyclone on coastal upwelling process. Natural Hazards. 2004;**31**:415-443. DOI: 10.1023/B:NHAZ.0000023360.37260.5b

[29] Pan AJ, Guo XG, Xu JD, Jiang H, Wan XF. Responses of Guangdong coastal upwelling to the summertime typhoons of 2006. Science China Earth

Sciences. 2012;**55**(3):495-506. DOI: 10.1007/s11430-011-4321-z

[30] Xu JD, Cai SZ, Xuan LL, Qui Y, Zhu DY. Study on coastal upwelling in eastern Hainan I land and western Guangdong in summer 2006. Hiayang Xuebao. 2013;**35**(4):11-18. DOI: 10.3969/j.issn.0253-4193.2013.04.002 (in Chinese)

[31] Xie LL, He CF, Li MM, Tian JJ, Jing ZY. Interannual variation and long-term trend of Qiongdong upwelling. Advances in Marine Science. 2017;**35**(1):1-13. DOI: 10.3969/j.issn.1671-6647.2017.01.002 (in Chinese)

[32] Guo F, Shi MC. Two-dimensional diagnosis model to calculate upwelling on offshore of the east coast of Hainan Island (in Chinese). Acta Oceanologica Sinica. 1998;**20**:109-116

[33] Jing ZY, Qi YQ, Du Y. Upwelling in the continental shelf of northern South China Sea associated with 1997-1998 El Niño. Journal of Geophysical Research. 2011;**116**(C2). DOI: 10.1029/2010JC006598

[34] Wang DK, Wang H, Li M, Liu GM, Wu XY. Role of Ekman transport versus Ekman pumping in driving summer upwelling in the South China Sea. Journal of Ocean University of China. 2013;**12**(3):355-365. DOI: 10.1007/s11802-013-1904-7

[35] Su J, Pohlmann T. Wind and topography influence on an upwelling system at the eastern Hainan coast. Journal of Geophysical Research. 2009;**114**(C6). DOI: 10.1029/2008JC005018

[36] Jing ZY, Qi YQ, Du Y, Zhang SW, Xie LL. Summer upwelling and thermal fronts in the northwestern South China Sea: Observational analysis of two mesoscale mapping surveys. Journal of Geophysical Research. 2015;**120**:1993-2006. DOI: 10.1002/2014JC010601

[37] Liu Y, Pend ZC, Wei GJ, Chen T, Sun W, He J, et al. Variations of summer coastal upwelling at northern South China Sea during the last 100 years. Geochimica. 2009;**38**(4):314-319 (in Chinese)

[38] Su J, Xu MQ, Pohlmann T, Xu DF, Wang DR. A western boundary upwelling system response to recent climate variation (1960-2006). Continental Shelf Research. 2013;**57**:3-9. DOI: 10.1016/j.csr.2012.05.010

[39] Shen YF, Jing ZY, Tan KY, Xie LL. Comparison of responses of the Qiongdong upwelling and the Vietnam coastal upwelling to super El Nino events. Advance in Marine Science. 2019;**37**(3):374-386

[40] Li MM, Xie LL, Zong XL, Zhang SW, Zhou L, Li JY. The cruise observation of turbulent mixing in the upwelling region east of Hainan Island in the summer of 2012. Acta Oceanologica Sinica. 2018;**37**(9):1-12. DOI: 10.1007/s13131-018-1260-y

[41] Santos F, Gomez-Gesteira M, Decastro M, Alvarez I. Differences in coastal and oceanic SST trends due to the strengthening of coastal upwelling along the Benguela current system. Continental Shelf Research. 2012;**34**:79-86. DOI: 10.1016/j.csr.2011.12.004

[42] Huang NE, Shen Z, Long SR. The empirical mode decomposition and the Hilbert spectrum for nonlinear and non-stationary time series analysis. Proceedings of the Royal Society of London A: Mathematical, Physical and Engineering Sciences. 1998;**454**(1971):903-995. DOI: 10.1098/rspa.1998.0193

[43] Kuo NJ, Zheng QA, Ho CR. Response of Vietnam coastal upwelling to the 1997-1998 ENSO event observed by multisensor data. Remote Sensing of Environment. 2004;**89**(1):106-115. DOI: 10.1016/j.rse.2003.10.009

[44] Yu J, Wang X, Li Y, Chen B. Analysis of the upwelling in the fishing ground in Midwestern South China Sea. Marine Sciences. 2015;**39**(6):104-113 (in Chinese)

[45] Zheng QA, Xie LL, Zheng Z-W, Hu JY. Progress in research of mesoscale eddies in the South China Sea. Advances in Marine Science. 2017;**35**(2):131-158 (in Chinese)

[46] Xie LL, Zheng QA. New insights to the South China Sea: The Rossby normal modes. Acta Oceanologic Sinica. 2017;**36**(7):1-3. DOI: 10.1007/s13131-017-1077-0

[47] Chen DK, Lei X, Wang W, Wang G, Han G, Zhou L.Upper Ocean response and feedback mechanisms to typhoon. Advances in Earth Science. 2013;**28**(10):1077-1086

[48] Zhang SW, Xie LL, Hou YJ, Zhao H, Qi YQ, Yi XF. Tropical storm-induced turbulent mixing and chlorophyll-enhancement in the continental shelf southeast of Hainan Island. Journal of Marine Systems. 2014;**129**:405-414. DOI: 10.1016/j.jmarsys.2013.09.002

[49] Dare RA, Mcbride JL. Sea surface temperature response to tropical cyclones. Monthly Weather Review. 2011;**139**:3798-3808

[50] Zheng QA, Zhu BL, Li JY, Sun ZY, Xu Y, Hu JY. Growth and dissipation of typhoon-forced solitary continental shelf waves in the northern South China Sea. Climate Dynamics. 2015;**45**(3-4):853-865. DOI: 10.1007/s00382-014-2318-y

Section 3

Coastal Environment Management

Strengthening Democracy in Indonesian Marine Spatial Planning through Open Spatial Data

Adipandang Yudono and Permana Yudiarso

Abstract

Sea and coastal areas are locations that have enormous potential that can contribute greatly to the national economic growth. The potential of marine and coastal areas includes the potential of fisheries. Fish life in shallow water or estuary is relevant to the existence of seagrass beds as their habitat. Seagrass in coastal waters is one of the attractions of fish for reproduction (spawning ground), fish growth place (nursery ground) and feeding ground. Good management requires a well-structured plan that takes into account geographical conditions and the sustainability of the plan in the future for the role of marine spatial planning. Marine spatial planning is a spatial guidance to manage well coastal and ocean areas with more integration and sustainability through identifying and mapping all marine issues. One method of mapping issues in marine spatial planning is open spatial data. The coherence and synergy of spatial planning can be achieved through dialogue between the elites and the public. A solution to bridge political communication between the elite and the public is open spatial data. In this context, the technicalities of open spatial data are important factors for achieving consensus. Relevant non-technical issues, such as data management, human resources and leadership factors are critical points for this potential open spatial data.

Keywords: seagrass, fishing areas, coastal conflicts, marine spatial planning, open spatial data

1. Introduction

The aim of this study is to explore the model of open spatial data between communities and official government to meet bottom-up and top-down approaches in achieving consensus of marine spatial planning for strengthening democracy and sustainability, particularly in social pillar. The social problem between local coastal communities and coastal developers gives attention for the sustainability of coastal and marine resources. Discussions were held in the neighborhood until it was agreed to do an open spatial data by all coastal communities who still maintain the local traditional culture with technical assistance from the Indonesian Ministry of Maritime Affairs and Fisheries. An agreement was reached from the preparation of spatial data as to how the community then utilized the spatial information for the purpose of protecting and managing coastal and marine resources in Indonesia.

Managing sustainability of marine and coastal resources, it is recognized that the crucial process in open spatial data is a change in the way people think about the use of natural resources, so that they are not damaged and depleted. The people who initially thought that marine resources were not their property finally realized that in fact they had allowed the destruction process because they have not exercised control when there were parties who used it excessively, such as investors who develop coastal areas for massive business activities. The development of local knowledge led the community to try to organize themselves by forming groups which were then used as a part of essential actor for negotiating and mapping the use of coastal areas through a legal context in the form of Indonesian marine spatial planning.

2. Marine spatial planning applied to seagrass management

Seagrasses thrive in aquatic ecosystem, especially in open tidal areas and coastal waters or lagoon that are basically mud, sand, gravel, and dead coral faults, with a depth of 4 meters. Seagrass beds are formed on the seabed which is still penetrated by enough sunlight for growth [1]. In the world, there are estimated 55 species of seagrass, 12 of which are found in Indonesia. Almost all substrates can be overgrown with seagrass, ranging from muddy to rocky substrates. But extensive seagrass beds are more often found in thick sandy-mud substrates between mangrove swamp forests and coral reefs [2]. Some species such as *Thalassia testudinum* can grow rapidly, with a leaf growth rate of 2 cm per day.

Coastal water seagrass habitats are of critical importance to many factors in the life cycle of fish such as spawning ground, nursery grounds, and feeding grounds. The costal living organisms that live in association with physical coastal and marine environment include baronang fish (*Siganus sp.*), groupers, green turtles, dugong, crustaceans, mollusks (*Pinna sp., Lambis sp., Strombus sp.*), Echinodermata (*Holothuria sp., Synapta sp., Diadema sp., Archanster sp., Linckia sp.*), and sea worms (*Polychaeta*). Therefore, waters that have seagrass beds are productive fishery regions, where many methods can be employed, such as net sets, lift nets, clam collectors, and seaweed collectors.

The existence of seagrass beds makes the location of fish life relevant to the fishing area at the marine spatial planning areas. The utilization of Indonesian marine fish resources in various regions is uneven. In some territorial waters, there are still big opportunities for underexploited development, while in some other areas, it has reached overfishing conditions. The division of fishing areas between small- and medium-scale fisheries has not been well implemented. Fishing pressure is common in coastal areas where small- and medium-sized fishermen carry out fishing activities at the same time.

The main problem faced in an effort to optimize fishing is the very limited data and information regarding oceanographic conditions that are closely related to potential fishing areas. The Indonesian fishing fleet is dominated by small-scale community fishing fleets, while the number of fishermen from year to year shows significantly increasing numbers. The fleet of fishers departs from the base not to catch but to find fishing locations so that it is always in an uncertainty about the potential location for fishing, so the catch is also uncertain. Besides that, as a result of the uncertainty of fishing locations, fishing vessels spend a lot of time and fuel searching for fishing ground locations, and this means there is a waste of fuel.

3. Seagrass distribution in Indonesia

Seagrass ecosystems are dynamic, where conditions are not always the same at all times. Changes in environmental conditions can affect the growth of seagrass, having increased or decreased numbers, so that the area of seagrass in a location can change at any time. Information on the area of seagrass can provide an indication of overall seagrass status. If there is a highly damaged physical ocean condition, this shows the pressure or threat to the ecosystem. Conversely, if the area is stable or rising, this shows the high chance of seagrass to be sustainable. Calculation of seagrass area is done in two ways. First, step by conducted remote sensing analysis using Landsat ETM + satellite images, Landsat 8 OLI, SPOT-5 that have
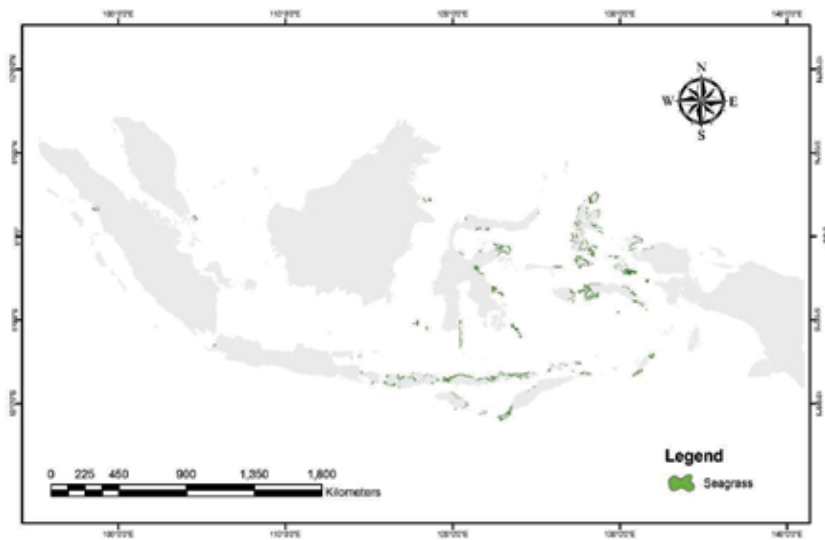
Figure 1.
Seagrass distribution in Indonesia.

Species	Number of locations to be found (out of 423)
Enhalus acoroides	357
Thalassia hemprichii	371
Cymodocea rotundata	311
Cymodocea serrulata	141
Halodule pinifolia	85
Halodule uninervis	201
Halophila ovalis	247
Halophila minor	21
Halophila spinulosa	3
Halophila decipiens	2
Thalassodendron ciliatum	37
Syringodium isoetifolium	200

Table 1.
Seagrass species in Indonesia.

been verified on the ground (ground truth) of 22 seagrass monitoring locations in Indonesia. Secondly, collecting seagrass area data generated from mapping activities is carried out by various agencies such as the Indonesian Geospatial Information Agency (BIG), Ministry of Maritime Affairs and Fisheries (KKP), and also The Nature Conservancy [3]. The analysis shows that the area of Indonesian seagrass is 150,693.16 ha. In Western Indonesia, the area of seagrass calculated is 4409.48 ha, while in the eastern part of Indonesia, it is 146,283.68 ha (See **Figure 1**) [3].

In general, *Enhalus acoroides* and *Thalassia hemprichii* are types of seagrass that are often found in Indonesian waters. From the information gathered from 423 locations, it was found that *Thalassia hemprichii* had a wider distribution, *T. hemprichii* was found in 371 locations, while *Enhalus acoroides* was found in 357 locations (See **Table 1**) [3].

4. Threats to seagrass habitats in Indonesia and the world

The main problems affecting seagrass ecosystems throughout the world are due to continuous dredging and stockpiling activities and water pollution including salt waste disposal from desalinization activities and oil production facilities, the inclusion of pollution around industrial facilities, and waste hot water from a power plant. Until now the world's seagrass damage has reached 58%, and since 1980 every 30 minutes, the world lost seagrass the size of a soccer field [4, 5]. Furthermore, the distribution of global seagrasses has been lost by about 29% since the nineteenth century [6]. The main cause of the loss of seagrass globally is a decrease in water brightness, both due to increased turbidity of the water and increased input of nutrients to the waters. In temperate regions, the loss of seagrass is caused by the conversion of coastal areas into industrial estates, settlements, and flooding from the mainland. Meanwhile, the main cause of the loss of seagrass beds in the tropics is an increase in sediment input into coastal waters due to logging on land and logging of coastal mangroves that coincide with the direct influence of fishery cultivation activities.

The widespread decline of seagrass beds in Indonesia can be caused by natural factors and the results of human activities, especially in coastal environments. Natural factors include strong waves and currents, storms, earthquakes, and tsunamis. Meanwhile, human activities that contribute to the decline of seagrass areas are coastal reclamation, sand dredging and mining, and pollution. For example, seagrass cover on Pari Island (Thousand Islands) has been reduced by 25% from 1999 to 2004 allegedly due to rampant development on the island [3].

5. Achieving consensus to diminish natural coastal conflict management through marine spatial planning

Sea and coastal areas are locations that have enormous potential that can contribute greatly to the national economy. The potential of marine and coastal areas include the potential of fisheries, the potential of environmental services, the potential of marine energy, and the potential of mining. This potential must be managed well in an integrated and sustainable manner. Good management requires a well-structured plan that takes into account geographical conditions and the sustainability of the plan in the future.

Preparation of marine spatial plans and small islands is a crucial point to achieve optimal management of marine and coastal areas. An integrated spatial plan between land and sea, which does not only consider ecological and environmental

aspects, should also be implemented in the planned area, in accordance with Law No. 26 of 2007 concerning Spatial Planning and Law No. 1 of 2014 concerning Management of Coastal Areas and Small Islands.

Environmental balance aspects that will be influenced by the physical construction activities in the sea and coastal areas need a study in the activities of the preparation of the intended spatial plan, so that activities can run in a harmonious and sustainable manner. Thus the spatial planning for the sea and coastal areas to be compiled should implement an integrated spatial plan between the sea area and its land area as well as accommodate the aspirations of the community from the planning and utilization to control processes.

Marine spatial planning has a crucial policy for solving spatial use conflicts, namely, by identifying and mapping all uses, regulations, and conflicts that occur [7]. Initially, conflicts occurred in the ecological aspects, then toward social conflict, and finally toward economic conflict [8, 9]. The conflict mapping is a technique used to describe graphically, connecting parties to problems and with other parties. One method of mapping this conflict under open spatial data context is a participatory mapping from local coastal communities.

6. Aquatic ecosystem management through participatory mapping in marine spatial planning context

Updating marine data and information can be done by involving communities who live in coastal and marine habitats through participatory mapping. To examine in detail the role of participatory mapping as a tool of negotiation between the community and the government, the author will explore the journey of participatory mapping in general and its application in Indonesia.

Participatory mapping was initiated from participatory research that was created in the 1960s with the rise of social oppression due to the Second World War triggered in Europe. Furthermore, the emergence of Marxist influences in overcoming the entry of the problem of social justice in the social sciences in the 1970s triggered the development of marginal community-based research methods. One of the innovations in the social research method was participatory mapping initiated by Freire to bridge dialog between elites and citizens in alleviating the problems of marginal communities [10].

Society as an actor who directly receives the results of spatial planning determined by the government has a role to participate in the spatial planning process in various forms, one of which is the provision of spatial information. In Indonesia, the provision of spatial information has been regulated under Law No. 4 of 2011 of The Indonesian Geospatial Information, article 23, paragraphs 1 and 4, and Law No. 26 of 2007 of The Indonesian Spatial Planning, article 65, that spatial planning provides opportunities to the community with a participatory-based approach in the procurement of spatial data and information to achieve spatial planning consensus.

There have been many manuscripts published by geospatial and spatial planning scholars regarding community management based on spatial data and information for planning and management purposes [11–14]. In general, based on the political elite point of view, the government is greatly assisted in making decisions related to spatial planning as a valuable input in creating harmonization of the development agenda of the government with the needs of affected communities from planning.

Participatory mapping in Indonesia was initiated by nongovernmental organizations (NGOs) with indigenous peoples to advocate spatial planning to protect their land ownership from land development by investors for commercial activities that often receive support from the government, such as establishing oil palm

plantations. In this spatial planning advocacy, the role of participatory mapping has a crucial point to provide input to the government and investors on the land ownership belonging to indigenous peoples.

Participatory mapping activities relevant to spatial planning activities in Indonesia can be identified in two parts:

1. Mapping management activities for inter-ethnic advocacy zones.

2. Mapping the activities of advocacy zones management among indigenous or rural communities on the development agenda of the government.

Participatory mapping activities related to advocacy zoning mapping can be taken as an example in the case of Pahawang Island (see **Figure 2**). Here, the local community is mapping the area to create a consensus between traditional fishermen and modern fishermen in fishing arrangements. The result of this participatory mapping is that an agreement is reached between the two groups of fishermen who are only allowed to catch fish using conventional methods (e.g., using fish hooks) and do not use equipment that can disrupt massive fish ecosystems, such as the use of trawls, bombs, and potassium cyanide [15].

The impact of participatory method that carried out by traditional fishermen groups, who always using traditional equipments for fishing advocacy, with modern fishermen groups, who usually the equipments that can disrupt massive fish ecosystems, achieved the consensus to use only traditional fishing equipment was the number of fish around Pahawang Island increases and traditional fishermen can continue fishing. Furthermore, participatory mapping by traditional fishing communities on Pahawang Island has encouraged the government to establish a legal basis through the establishment of a basic map of fishing zones in the form of village regulations.

Another example of seagrass mapping project in Indonesia is Dugong and Seagrass Conservation Project (DSCP) granted by GEF, UNEP, and Mohamed bin Zayed Species Conservation Fund, 2016–2018. Dugong (*Dugong dugon*) and

Figure 2.
Pahawang Island in Indonesia.

seagrass are the main issue where the threat to seagrass ecosystem can affect dugong. The project is set up in four locations, namely, Bintan-Riau Archipelago, Kotawaringin Barat-Central Kalimantan, Alor-East Nusa Tenggara, and Toli-Toli, Central Sulawesi, where the population and habitat mapping are developed. One of the goals is a community-based conservation and management.

Participatory mapping activities in inventorying natural resources in the areas where indigenous peoples live have created local spatial knowledge in identifying the types of natural resources. According to Sabu [16], the implementation of participatory mapping in Indonesia has opened the insights of indigenous people in the management of natural resources that exist in their regions into four aspects, including political, social, economic, and cultural aspects.

- Political aspects

Participatory mapping provides basic territorial information as a tool for communicating and negotiating between parties (communities, governments, and entrepreneurs) who have an interest in particular areas in achieving territory management consensus [16].

- Social aspects

Participatory mapping activities open up the insights of indigenous people in managing natural resources in their homes through:

  - Local spatial knowledge about the identification of natural resources and threats faced in the area of residence

  - Identifying communities involved in managing resources in the homes of indigenous peoples

  - Contributing to create solidarity between indigenous peoples [16].

- Economic aspects.

Participatory mapping helps to identify valuable local natural resources, so as to create a sustainable fulfillment of the daily needs of indigenous peoples' living environments [16].

- Cultural aspects

Participatory mapping can create local wisdom to identify, preserve, and develop traditional customs and habits in area management inherited from indigenous ancestors. Examples of areas that have religious purposes can be planted with plants that have a symbolic value, such as banyan trees [16].

7. The strategies of open spatial data alliances in the context of marine spatial planning

Studies conducted by scholars in the management of geospatial information show that open spatial data alliances are closely related to transparent and open institutional governance and organizational behavior [17–20]. Specifically, Budhathoki and Nedovic-Budic argue that the main factor in creating an atmosphere of spatial data

and information sharing within and between institutions is the existence of collaboration-cooperation-coordination (3C) [21]. To examine in more detail about this 3C, in this section a broader concept of 3C will explore relevant open spatial data.
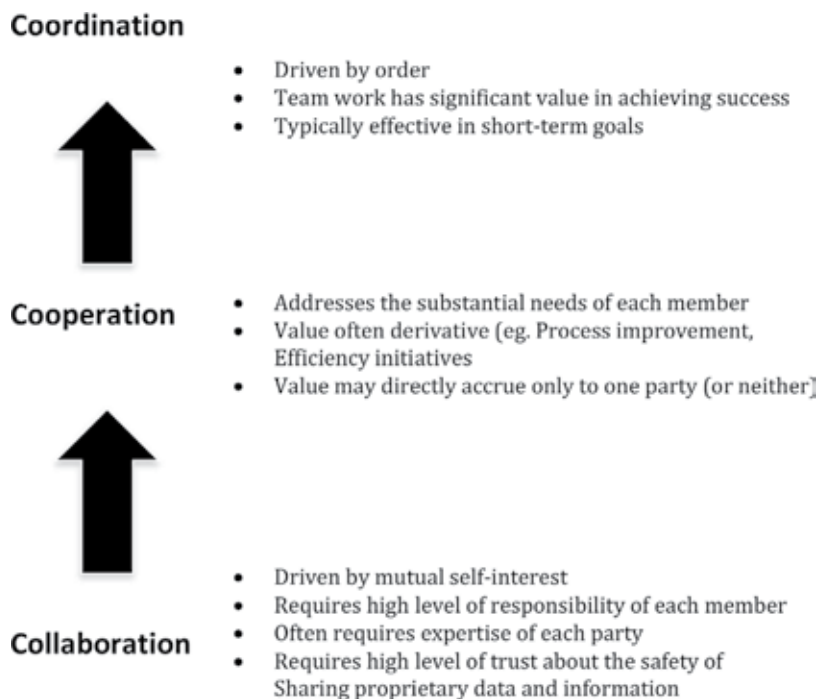
• Collaboration

In the 3C concept, collaboration is the first step toward creating transparency and openness between institutions to share in realizing shared goals, which in general is an improvement in the quality of institutions. Colleagues involved in collaboration must trust and respect each other in correspondence and open readiness to acknowledge the information provided [22, 23]. (Characteristics of collaboration and relations with cooperation and coordination can be seen in **Figure 3**).

As the first step toward creating openness conditions, collaboration has not guaranteed any commitment or responsibility for an individual, association, or foundation. In general, this collaboration does not yet have full legal force if disputes/problems occur in the future. Relevant to the context of this research, collaboration between organizations that produce and manage spatial data and information initiates the creation of willingness for each institution to share their knowledge and assets in order to achieve the common goal of achieving national welfare.

• Cooperation

Cooperation is the second stage in the 3C concept in order to create mutually beneficial relationships between the institutions involved. At this stage, the formed partnership already has a legal basis, in the form of a memorandum of understanding (MoU), to share capabilities, skills, knowledge, and assets to achieve common goals [24].

Coordination
- Driven by order
- Team work has significant value in achieving success
- Typically effective in short-term goals

Cooperation
- Addresses the substantial needs of each member
- Value often derivative (eg. Process improvement, Efficiency initiatives
- Value may directly accrue only to one party (or neither)

Collaboration
- Driven by mutual self-interest
- Requires high level of responsibility of each member
- Often requires expertise of each party
- Requires high level of trust about the safety of Sharing proprietary data and information

Figure 3.
Characteristics of collaboration-cooperation-coordination (3C) and the relationship of 3C elements.

The relevance of the concept of cooperation in this research is the collaboration between institutions in producing and managing spatial data and information on the coastal areas in order to create a commitment to safeguard the unity and sovereignty of the state through coherent marine governance in various levels. (Characteristics of collaboration and relations with cooperation and coordination can be seen in **Figure 3**).

• Coordination

In the 3C concept, coordination has the highest level of partnership between institutions. At this stage, between institutions, they have understood the interdependence between responsibilities and coordinated their respective tasks [25]. Coordination ensures that all units, divisions, and parts of an institution recognize their targets to be achieved. At this stage, all individuals must be well organized in ensuring that the institution's great goals can be achieved by implementing agreed commitments. (Characteristics of collaboration and relationships with collaboration and coordination can be seen in **Figure 3**).

In the context of this research, coordination between institutions in producing and managing spatial data and information is able to integrate, synchronize, and carry out tasks in a sustainable manner to realize the strengthening of safeguarding state unity and sovereignty through effective and efficient marine governance.

8. The proposed model of open spatial data in the context of marine spatial planning

Strengthening democracy in marine spatial planning, including general spatial planning context, can be done through open spatial data between actors, both between communities and between elites, as well as from the community/public to elites and vice versa. Based on the arguments given in the previous subsection, the researchers propose a model of open spatial data between public and elites.

The form of democracy in the context of marine spatial planning is carried out through active communication between the government and public, especially the coastal communities. In determining the level of communication activities by both parties, this model refers to the model of Arnstein's participation [26] and the model of the level of participation and public involvement in government science projects from Haklay [14]. The purpose of this model proposal is to identify the level of public participation in the government in creating collaboration, cooperation, and coordination to share spatial data and information on marine spatial planning, including general spatial planning context. (See **Figure 4**).

• Level 1: taken for granted

At this stage, political communication between public and elites regarding the planning agenda and development agenda has not been achieved. In terms of the people who live in affected areas, planning is passive, that is, just accepting the agenda set by the government, whereas from the government perspective, it is assumed that the community does not need to be involved in the planning process, so that the government has full authority for the direction of planning in the targeted area.

• Level 2: information sharing

At this stage, collaboration between public and elites has taken place. People who live in areas affected by planning from the government take the initiative to provide
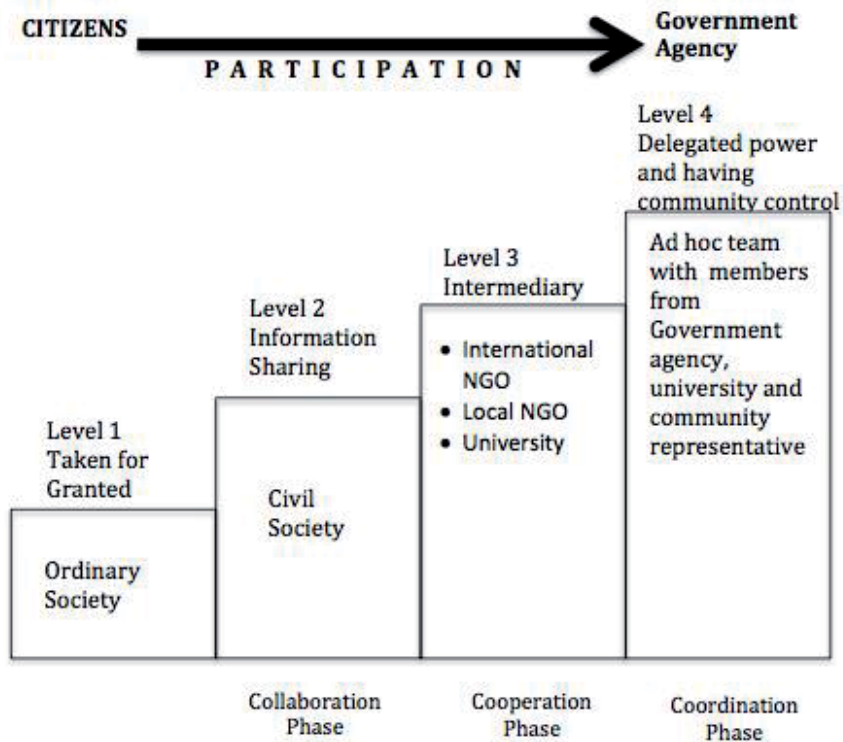
Figure 4.
A stepped model for community participation in government agency agendas.

up-to-date information on issues and problems in their neighborhoods to be submitted to the government. Providing information is delivered through public hearings or delivered online on applications that have been built in several areas. One of the public hearings is participatory mapping as a form of open spatial data from the public to the government. While from the government's point of view, they began to accept public input to harmonize the planning and development agenda that had been made.

- Level 3: intermediary

At this stage, the partnership that exists between public and elites has shifted from a form of collaboration to cooperation through the role of a neutral intermediary in bridging input from the community and ideas from the government. The planning process from the government to the community sometimes gets a deadlock. Thus, this situation requires a facilitator who can bridge political communication in planning, in which an intermediary actor is generally chosen based on a credible reputation that is trusted by both parties, for example, academics.

In the context of open spatial data, the provision of spatial data in the form of participatory mapping from public to elites sometimes does not meet the standards set by the government. This complicates and confuses the government, so that intermediaries from professionals or academics are able to transform spatial ideas from the public into standard formats from the government so that it can be conveyed.

- Level 4: delegated power and having community control

At this highest stage, the form of public-elite partnership has achieved coordination. At this level, there is a representation of the community affected by the

planning target to be part of an ad hoc team together with intermediaries, namely, academics in formulating a joint planning agenda for the realization of a harmonious life in accordance with community input and government programs. For the context of open spatial data both from the coastal community and the government, it has been realized very well without anything being covered up. In other words, transparency and openness of spatial data are guaranteed and reliable.

Overall, the proposed open spatial data in a nontechnical organization is strongly influenced by a willingness to change and transform to be more open. It requires the active participation of public and elites to collaborate, cooperate, and coordinate.

9. Conclusion

The study of open spatial data in government institutions cannot be separated from open data application in which the system of government agencies, which are concerned about public service interests, are willing to publicly share their data and information. This provides explanation and transparency of government performance in terms of the implementation of development and planning agendas.

This study has assessed potential spatial data integration between official spatial data and crowdsourced geographic information, which predominantly look from nontechnical perspectives. The nontechnical appraisal demonstrates that the integration of participatory mapping into official spatial data and information requires extensive rebuilding of data management, particularly human resources, policy, and organizational factors, which have a significant impact on geographical information utilization in government agencies and integration with participatory mapping products.

The coherence and synergy of spatial planning can be achieved through dialog between the elites and the public. A solution to bridge political communication between the elite and the public is open spatial data. By this, the technicalities of open spatial data are important factors to achieve consensus. Relevant nontechnical issues, such as data management, human resources, and leadership factors are critical points for this potential open spatial data.

The findings of this research attempt to make a significant contribution to knowledge in bringing together the management of official spatial and crowdsourced geographic information in planning practice. Official spatial data and crowdsourcing geographic information integration will require extensive rebuilding of spatial data streams and institutional plans. The official spatial data and crowdsourcing geographic information integration approach present spatial data streams, which are genuinely two-way and include plans of action. It enhances transparency and ease of working in a transparent environment, and it is an important step toward developing a more democratic from spatial planning.

The researcher concluded with an analysis of the management of open spatial data in government agencies at all administration levels and interactive mapping communities among citizens to indicate that the success of open spatial data can be achieved when government agencies can implement collaboration, cooperation, and coordination (3C) and citizens can actively participate in creating and sharing spatial data and information.

Acknowledgements

Conflict of interest

I confirm there are no conflicts of interest.

Copyright

Any copyright information that the author created in this paper is protected by moral rights. Anyone who intends on using material from this work must acknowledge the author as the creator.

Author details

Adipandang Yudono[1]* and Permana Yudiarso[2]

1 Department of Urban and Regional Planning, Brawijaya University, Malang, Indonesia

2 The Indonesian Ministry of Marine Affairs and Fisheries, Jakarta, Indonesia

*Address all correspondence to: adipandang@ub.ac.id

IntechOpen

References

[1] Dahuri R. Keanekaragaman Hayati Laut Aset Pembangunan Berkelanjutan Indonesia (Marine Biodiversity Indonesia's Sustainable Development Assets). Jakarta: Gramedia Pustaka Utama Publisher; 2003

[2] Bengen DG. Ekosistem Dan Sumberdaya Alam Pesisir Dan Laut Serta Prinsip Pengelolaannya (Coastal and Marine Natural Ecosystems and Resources and their Management Principles). Bogor: PK-SPL. IPB; 2002

[3] Hernawan UE, Sjafrie NDM, Supriyadi IH, Suyarso Iswari MY, Anggraini K, Rahmat. Status Padang Lamun Indonesia 2017 (Status of Indonesian Seagrasses 2017). Puslit Oseanografi – LIPI: Jakarta; 2017

[4] Sachra N. Spatial distribution and carbon sequestration capacity of indonesian blue carbon ecosystems: Result of preliminary analysis. In: International Indonesian Student Conference Edition 2017. 2017. ISSN: 2338-1043

[5] Dennison WC. Global trajectories of seagrass, the biological sentinels of coastal ecosystem. In: Duarte CM, editor. Global Loss of Coastal Habitat Rates, Causes and Consequences. Bilbao, Spain: Fundacion BBVA; 2009. pp. 91-107

[6] Waycott M, Duarte CM, Carruthers TJB, Olyamik S, Calladine A, Fourqurean JW, et al. Accelerating loss of seagrass across the globe threaten coastal ecosystems. PNAS. 2009;**106**(30):12377-12381

[7] Prestelo L, Vianna EM. Identifying multiple-use conflicts prior to marine spatial planning: A case study of a multi-legislative estuary in Brazil. Marine Policy. 2016;**67**:83-93

[8] Brown G, Raymond CM. Methods for identifying land use conflict potential using participatory mapping. Landscape dan Urban Planning. 2014;**122**:196-208

[9] Fisher S, Abdi DK, Ludin J, Smith R, Williams S, Williams S. Mengelola konflik: keterampilan dan strategi untuk bertindak (Managing Conflict: Skills and Strategies for Acting). Jakarta, Indonesia: The British Council; 2001

[10] Freire P. Pedagogy of the Oppressed. New York: Continuum; 1971

[11] Roche S. Geographic information science I: Why does a smart city need to be spatially enabled? Progress in Human Geography. 2014;**38**(5):703-711

[12] Roche S, Zimmermann EP, Merickskay B. GeoWeb and crisis management: Issues and perspectives of volunteered geographic information. GeoJournal. 2013;**78**:21-40

[13] Heipke C. Crowdsourcing geospatial data. ISPRS Journal of Photogrammetry and Remote Sensing. 2010;**65**:550-557

[14] Haklay M, Weber P. OpenStreetMap: User-generated street maps. IEEE Pervasive Computing. 2008;**7**(4):12-18

[15] Rizani, Karim MS. Pemetaan Partisipatif: Sebagai upaya masyarakat melindungi dan mengelola sumberdaya alam pesisir laut di Pulau Pahawang (Participatory Mapping: As the community's efforts to protect and manage the natural resources of marine coasts on the Pahawang island). In: Pramono AH, Samperante F, Safitri H, Achmaliadi R, editors. Menuju Demokratisasi Pemetaan: Refleksi Gerakan Pemetaan Partisipatif di Indonesia (Toward Mapping Democratisation: Reflectinos on the Participatory Mapping Act in Indonesia, Jaringan Kerja Pemetaan Partisipatif (JKPP)). Indonesia: Bogor; 2009

[16] Sabu ASSS. Mengambil alih hutan lindung: Kasus Komunitas Adat Nian Uwe Wari Tana Kera PU Hikong-Boru Kedang, Nusa Tenggara Timur (Taking over the protected forest: The case of indigenous communities Nian Uwe Wari Tana Kera Hikong PU- Boru Kedang, East Nusa Tenggara). In: Pramono AH, Samperante F, Safitri H, Achmaliadi R, editors. Menuju Demokratisasi Pemetaan: Refleksi Gerakan Pemetaan Partisipatif di Indonesia (Toward Mapping Democratisation: Reflections on Participatory Mapping Act in Indonesia, Jaringan Kerja Pemetaan Partisipatif (JKPP)). Indonesia: Bogor; 2009

[17] Doherty N, King M. An investigation of the factors affecting the successful treatment of organizational issues in systems development projects. European Journal of Information Systems. 2001;**10**(3):147-160

[18] Lambert R, Peppard J. Information technology and new organizational forms: Destinations but No road map? Journal of Strategic Information Systems. 1993;**2**(3):180-205

[19] Williams T. Interorganisational information systems: Issues affecting interorganisational cooperation. Journal of Strategic Information Systems. 1997;**6**(3):231-250

[20] Suomi R. What to take into account when building an inter-organizational information system. Information Processing and Management. 1994;**30**(1):151-159

[21] Budhathoki NR, Nedovic-Budic Z. Expanding the spatial data infrastructure knowledge Base. In: Onsrud H, editor. Research and Theory in Advancing Spatial Data Infrastructure Concepts. Redlands, USA: ESRI Press; 2007

[22] Denise L. Collaboration vs. C-three (cooperation, coordination, and communication). Innovating. 1999;**7**(3)

[23] Gulati R, Wohlgezogen F, Zhelyazkov P. The two facets of collaboration: Cooperation and coordination in strategic alliances. Academy of Management Annals. 2012;**6**:531-583

[24] Ramjit DM. Strategic Planning: Collaboration, Cooperation, and Coordination. Available from: https://publicpuzzle.wordpress.com/2011/02/18/strategic-planning-collaboration-cooperation-and-coordination/ [Accessed: 07-12-2015]

[25] Crowston K, Rubleske J, Howison J. Coordination theory: A ten-year retrospective. In: Zhang P, Galletta D, editors. Human-Computer Interaction in Management Information Systems: Foundation (Advances in Management Series). London, UK: Routledge; 2006

[26] Arnstein SR. A ladder of citizen participation. Journal of the American Planning Association. 1969;**35**(4):216-224

Chapter 11

Environmental Problems and Coastal Mitigation in South America: Examples from Northeast Brazil and Northern Colombia

Vanda Claudino-Sales, Ping Wang, Fábio Perdigão Vasconcelos and Adely Pereira Silveira

Abstract

In the state of Ceará, northeast Brazil, in the 1950s, an industrial harbor was built. The harbor structures and other factors, such as the destruction of the bypass of dunes, produced a large erosive process downstream, responsible for the loss of 400 m of beach in six decades. In Canoa Quebrada beach—an internationally famous tourist area—recently, the partial collapse of sea cliffs occurred because of inappropriate uses and occupations, causing landscape and economic damage. In Colombia, beaches are under an intense process of erosion, due to construction for housing and tourism. With the abrasive action of waves associated with rising sea level, coastal areas in both countries are under risk of major degradation. These environmental situations are the object of technical and scientific analysis and discussion in this chapter, and mitigation propositions are considered.

Keywords: Northeast Brazilian coast, northern Colombian coast, coastal erosion, coastal mitigation

1. Introduction

Coastal erosion is a worldwide concern, affecting virtually all coastal countries. In some cases, erosion reaches stages where it results in a high rate of environmental degradation. The economic repercussions are diverse, such as damage to the natural environment and loss of public infrastructure and/or private property. These facts can have extremely serious consequences in economy, ecosystems, tourism, and public health.

The main causes of coastal erosion are the rising of sea level that is underway globally and inadequate management of coastal areas. Frequently, it is associated with the installation of urban and industrial equipment or with structures dedicated to leisure, housing, and tourism.

In the state of Ceará, Northeast Brazil, in the 1950s, an industrial harbor was built. The harbor structures, with other factors such as the destruction of dune bypass, produced a large erosive process downdrift. It was responsible for the loss

of more than 400 m of beach in six decades. At Canoa Quebrada beach (a nationally and internationally famous touristic area), a recent partial process of collapse of the cliffs occurred as an answer to inappropriate uses and occupation. This fact produced landscape and economic damage. In the northern coast of Colombia, anthropogenic interruption of the longshore transport caused by the construction of groins, as well as some harbors, produced severe beach erosion along the downdrift shoreline.

With the abrasive action of waves associated with rising sea level, these coastal areas in both countries are at risk of more substantial degradation. These environmental situations will be the object of synthetic technical and scientific analysis and discussion in this chapter. Mitigation propositions for both countries coastal areas are also considered.

2. Methodology

The data displayed are the result of bibliographic research, analysis of maps and satellite images, and fieldwork on the studied areas. In relation to Fortaleza, Brazil, data of direction and velocity of currents were also collected from the Brazilian Ministry of Navy. Data of bathymetry and sea level rise were digitized from the Brazilian navigation charts. Finally, measurements were made on satellite images on Google Earth, in order to define volumes of sediments available and accumulated on the shoreline. In relation to Canoa Quebrada beach, Brazil, topographic profiles covering a 300 m stretch were made in six distinct points, using a total station. High-resolution satellite images were analyzed in a 2004, 2008, and 2017 time series, in order to define the behavior of the cliff break line and determine its retreat speed. For the analysis and georeferencing of the images, the software QGIS, version 2.12, developed by the Open Source Geospatial Foundation—OSGeo, was used with DATUM SIRGAS 2000, projection UTM zone 24 S.

For northern Colombia, beach profiles along 600 km and bathymetry survey were conducted. The beach profiles were made using a total station. The bathymetry survey (10 m water depth) was conducted using a precision echo sounder and a GPS (Global Positioning System) mounted on a vessel. The bathymetry beyond 10 m water depth was digitized from the south Caribbean navigation charts. A total of 270 sediment samples were also collected. The up-to-date nearshore bathymetry data were used in the modeling of nearshore wave field. Finally, time-series aerial photos available from Google Earth were analyzed to depict beach/dune changes at various locations.

3. Environmental problems in the coast of Ceará State, Northeast of Brazil

3.1 Natural settings of the study area

Ceará is one of the states of the Brazilian equatorial northeastern region. Its coastal area spans between the latitudes of 2°47′S and 4°50′S for 573 km and is characterized by long and gently sloping sandy beaches, irregularly interrupted by headlands, small estuaries with mangroves, sea cliffs, and beach rocks, with large dunes and small barrier islands [1–2] (**Figure 1**).

The headlands are characterized, with few exceptions, by the occurrence of sea cliffs with heights varying from 2.7 to 20 m. Tertiary rocks are present, named Barreiras Formation, and create a low-lying tabular surface with less than 40 m in elevation, which extends from the shoreline up to 60 km inland. It outcrops as sea cliffs 3 to 15 m high [e.g., 3] (**Figure 1**).
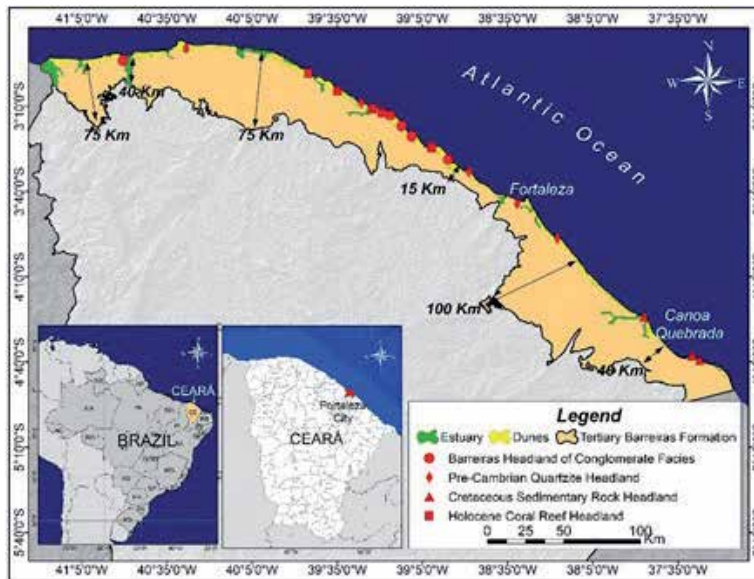
Figure 1.
Location and geological/geomorphological settings of Ceará state coastal area, northeast Brazil.

The mobile dunes orient E to W and are mostly barchans and transverse dune ridges [4–7]. The rate of dune migration ranges from 9 m/y to 22 m/y, with an average of approximately 11 m/y [4–7]. Frequently, the dunes bypass across the headlands, nourishing the beaches downdrift. This process is an important element of the sedimentological budget of this coastal area, considering that it counterbalances the downdrift erosion resulting from the impoundment of the longshore sand by the headlands.

Climatic conditions are controlled by the ITCZ [8]. During fall, the ITCZ is at its southernmost position, resulting in the rainy season. After April, the ITCZ shifts northward, leading to the dry season [9]. The climate is tropical subhumid, with average precipitation between 1000 mm and 1420 mm/y [3]. Temperatures remain largely constant throughout the year, with monthly averages ranging between 25.5° and 27.5°C [10].

The trade winds dominate the area and present a similar pattern to that of precipitation but with an opposite trend: As the precipitation rate decreases, the wind speed increases; during the wet season, the average wind speed is approximately half of that in the dry season. On average, maximum wind speed is around 8 m/s in the dry season. A particular characteristic of the wind condition is its constant easterly direction, coming from southeast or northeast [10].

The predominant wave direction is 90°, with heights ranging from 1.0 to 1.5 m [4, 11]. The waves are mainly of the sea type, with occasional occurrence of NE swell [12]. The area is characteristic of a semidiurnal mesotidal regime with a spring tidal range of approximately 3.1 m [13]. The most referenced Holocene sea level curve [14] indicates +5 m at 5.1 Ky BP, followed by two rises and falls until the present level.

A unique aspect of this stretch of coastal area is that it is not influenced by storm-induced surge and extreme wave conditions. Instead, extremely persistent unidirectional wind and wave forcing dominate, creating a strong and persistent longshore forcing that induces a large net rate of longshore sediment transport [15].

The mean sea level rose 14 cm in the last 73 years, as seen in Fortaleza (for location, see **Figure 1**). The data was obtained by the analysis of the nautical maps of 1945 and 2018 of Fortaleza coast, taking into account the level of the sea in both years in each map [16]. It indicates that a rising of sea level is an important element of the present dynamics in the area.

The rising of sea level, with inadequate and inappropriate uses, occupation, and development of the coast and of the shoreline, is producing large degradation of this coastal area, destroying ecosystems, construction, and equipment, thus causing economic, social, and environmental problems. The situation will be analyzed in two segments of the state coastal area, which are Mucuripe harbor headland, in Fortaleza city, and Canoa Quebrada beach, on the east coast (for location, see **Figure 1**).

3.2 Coastal environmental problems in Fortaleza area

The Mucuripe headland, in Fortaleza city, is characteristic of a low-lying (~1.5 in mean tide) outcrop of Precambrian quartzite (**Figure 2A**). It trends ESE-WNW and has been heavily engineered since the 1950s, following the installation of a harbor (**Figure 2B**).

The longshore current and transport of sand in the area take place from east to west. The sands, before the installation of the harbor, bypassed the headland and were transported to the west, nourishing the beaches downdrift, for dozens of kilometers. The two extensive jetties built to protect the harbor from waves and silting interrupted the longshore current, eliminating the transport of sediments downdrift [4, 12, 16–18]. Quantification of the sand intercepted by the headland and harbor structures yielded a reasonably accurate estimate of longshore sand transport rate of approximately 860,000 m^3/y [12].

This interruption of littoral drift induced a large accumulation of sand updrift, of the order of 825,000 m^3/y [16, 19]. Since the installation of the harbor, the total amount of sand accumulated updrift is approximately 26.4 million m^3, creating a new beach of 65.5 ha of area (Serviluz beach, for location, see **Figure 2B**) [16].

However, part of the sand accumulated in Serviluz beach, despite the jetties, bypasses them and the headland, being transported around these features and deposited by wave diffraction along the northern side of the harbor, creating the Mansa Beach and silting the harbor's basin (**Figure 3**). For this reason, dredging is frequently needed in the harbor basin, in order to let large boats dock without stranding. Surveys carried out by [16] indicated that the amount of sand dredged from the harbor's basin since the 1950s is of the order of 21 million m^3.
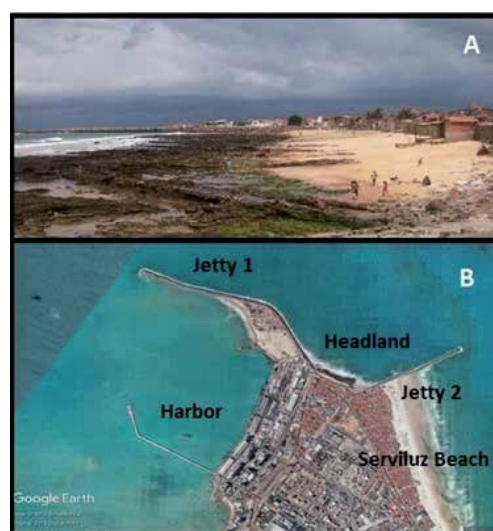
Figure 2.
(A) Mucuripe low-lying headland, in Fortaleza city, a natural feature that changes the orientation of the shoreline, from SE-NW to NE-SW. (B) The Mucuripe/Fortaleza harbor, installed in the 1950s, and the jetties built to protect the harbor's basin from waves and silting. The jetties interrupted the longshore transport, which came from the east.

Figure 3.
The residual bypass of sand across the jetties and the headland created the Mansa Beach and keep nourishing it regularly. The bypass also produces the silting of the harbor's basin, which has to be frequently dredged.

Figure 4.
Jetties installed in Fortaleza coastal area, in order to protect the shoreline against the erosion resulted from the interruption of the longshore transport produced by the harbor and associated jetties constructed updrift (east of the shown area) (source: Google Earth, 2019).

Figure 5.
(A). East coast of Fortaleza city and Mucuripe harbor vicinity, with large dunefields. The red arrow shows the area where the bypass of dunes still took place after the construction of the harbor. (B). Complete urbanization of the dunefields, with cessation of dunes bypass.

The aggressive interruption of the tremendous amount of net longshore sand transport has induced up to 100 m of beach erosion downdrift of the headland/harbor between 1960 and 1970 [17]. Numerous shoreline structures, such as groin fields, were constructed to protect the shoreline from this beach recession (**Figure 4**), further disrupting the longshore sand transport system and extending the artificial influence further downdrift [12, 17].

In addition to the blockage of longshore bypassing, the dune bypass is also completely obstructed by buildings densely constructed over the entire area during the last decades [4] (**Figure 5**). Practically no sand reaches the downdrift beach through headland dune migration anymore [4] or through the flux of the Ceará river mouth,

to where the dunes of the western segment of Fortaleza city migrated before [16] (for location of Ceará river estuary, see **Figure 4**).

The consequences of these processes in the coastal dynamics are dramatic. The shoreline retracted some 400 m in 60 years at places 15 km from the headland [4, 13]. The erosion is still happening: In Icarai Beach, 25 km downdrift, beach recession of magnitude of 100 m took place between the years 2004 and 2016 [4].

The retraction of the beaches indicates that the coastal dynamics in the area are completely disturbed. The sand introduced in the littoral drift by means of this erosion is the probable source of the sediment that is now accumulating in the area around the pier of another harbor, the Pecém harbor, located in the next headland downdrift, 60 km west of Fortaleza harbor [4]. The degradation illustrates the changes related to extreme human interventions on a unidirectional system, associated with rising sea level.

3.2.1 Coastal mitigation in the metropolitan region of Fortaleza

As erosion travels west, real estate owners along the shoreline try to protect their property by building coastal protection with their own resources or by pushing public power to build structures with public resources. In this way, several interventions were made in the last decades, of the rock-fill and bag-wall types.

The rock-fills protect the coast from erosion; however, it results in the loss of the beach area and in increased erosion downdrift (**Figure 6A**). The bag-wall, built in the 2010s, on the other hand, has already been destroyed by the action of the waves (**Figure 6B**), showing it completely inefficient for solving the kind of problems created by the construction of the Mucuripe harbor and by the unsustainable type of urbanization of Fortaleza city.

Figure 6.
(A) Erosion in Icarai Beach, 25 km downdrift of Mucuripe harbor, resulting from the interventions in Fortaleza city and in the area around the harbor. The rising of the sea must also be a factor producing the erosion. (B) Bag-wall installed in Icarai Beach in the 2010s, already destroyed by the waves.

It seems clear that the erosion in the area will not cease with the kind of intervention that has been taking place in the last six decades. Effectively, it is necessary to consider that the waves are very active and that sand is missing in the shoreline. In addition, the sea level is rising. In [19], it is pointed out that the sands which are dredged from the harbor's basin could be used to mitigate the erosion, by means of artificial nourishment of the beaches, as it takes place in other countries (e.g., [20]). Vasconcelos [16] advanced in this point of view, considering that the sand of the dredging could be dispersed along the littoral of Fortaleza, at the bathymetry of 5 m. Effectively, at 5 m deep, the longshore current would naturally transport the sands to the beaches downdrift, rebuilding coastal dynamics. This measure would waive nourishment of beaches, as well as the installation of rock-fills, bag-walls or other engineering structures and actions, implicating in less cost and less disturbance of the shoreline and of the social life related to it.

Nevertheless, these suggestions have not yet been considered by public authorities. In fact, a new dredging took place in August/September 2018, and as before, the sands were transported offshore, to be deposed and lost in areas far away from the shoreline. Meanwhile, the aggressive, dramatic, disastrous, and degrading erosion and destruction of the north part of Ceará State coastal area keep taking place.

3.3 Environmental problems in Canoa Quebrada beach

The town of Canoa Quebrada is located 140 km east of the city of Fortaleza and represents one of the most visited tourist destination in the coastal zone of the Northeast Brazil. It is characterized by the presence of active sea cliffs modeled in the Barreiras Formation, with the occurrence of a narrow beach in its foothills, plus beach rocks nearshore, which partially protects the sea cliffs (**Figure 7**). Clays and friable sands make up the sediments of the sea cliffs, which are bare or only partly protected by vegetation [21].

The morphodynamics in the area is very active: the strong rains that characterize the rainy season cause ravines and acute ridges, resulting in transport and deposition of sediments in the foothills, in the form of cones of dejection (**Figure 8**). The rain also contributes to the softening of the material of the cliff and to the increase of the water table, which produces dissolution in the slope and increases the internal pressure in the sediments, thus increasing the fragilization of the feature (e.g., [22]).

An important anthropogenic factor of the dynamics of the sea cliffs is the installation of numerous tourist facilities on their top and slope. These structures cause trampling and compacting of the sands, increasing ravines and generating gullies, which contributes to the acceleration of the erosive processes caused by rainwater (e.g., [23]) (**Figure 9**).

The cliffs of Canoa Quebrada have an average height of 15 m and can be considered as small- to medium-sized cliffs. However, the volume of material that is
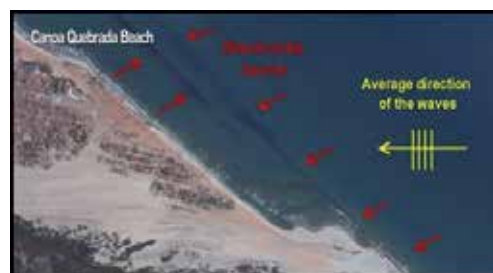
Figure 7.
Reef line at Canoa Quebrada beach (adapted from Google Earth image, 2018).

Figure 8.
Grooves at the top and cone of dejection at the base of the sea cliffs of Canoa Quebrada.

Figure 9.
Occupation of the top and bottom of the sea cliffs of Canoa Quebrada.

removed from these features is not negligible due to the high frequency of landslides. The occurrence of successive episodes of landslides is due to the combination of three factors: the friable nature of the clay-sandstone material, high anthropogenic presence, and strong tropical rainfall.

The sea cliffs present slope angle usually under 45° and are characterized mostly by the occurrence of retreat controlled by milder gravitational sliding more than by abrupt collapses (**Figures 10** and **11**). Together with the type of wave breaking, sea level rising, tidal amplitude, and sediment granulometry, the inclination directly influences the erosive process that characterizes the sea cliffs today [24–25].

The analysis of the set of points where topographic profiles were made indicates that from east to west (profiles 1,2,3, **Figure 11**), the slope presents relatively smooth landslides, while in the westernmost portion of the beach, where the profile assumes an angulation of more than 45° (profiles 5 and 6, **Figure 11**), landslides occur. The analysis of satellite images containing a time series of the years 2004, 2008, and 2017 indicates that the velocity of retreat of the Canoa Quebrada sea cliffs is very high when compared to hard rock cliffs.

Retreat velocity was calculated in three distinct sections, with the following results: in the east, the retreat was the smallest, of the order of 90 cm between 2004 and 2017, representing an average retreat of 8.2 m per century. In the central areas, which have many tourist developments, the retreat was slightly faster, of the order of 1.2 meters in 13 years, representing approximately 10.9 m per century. To the west,

Figure 10.
(A) The cliff on January 16, 2016, and to the right on February 20, 2016. (B) The retreat of the sea cliff by gravitational slip is visible in the 2016 picture.
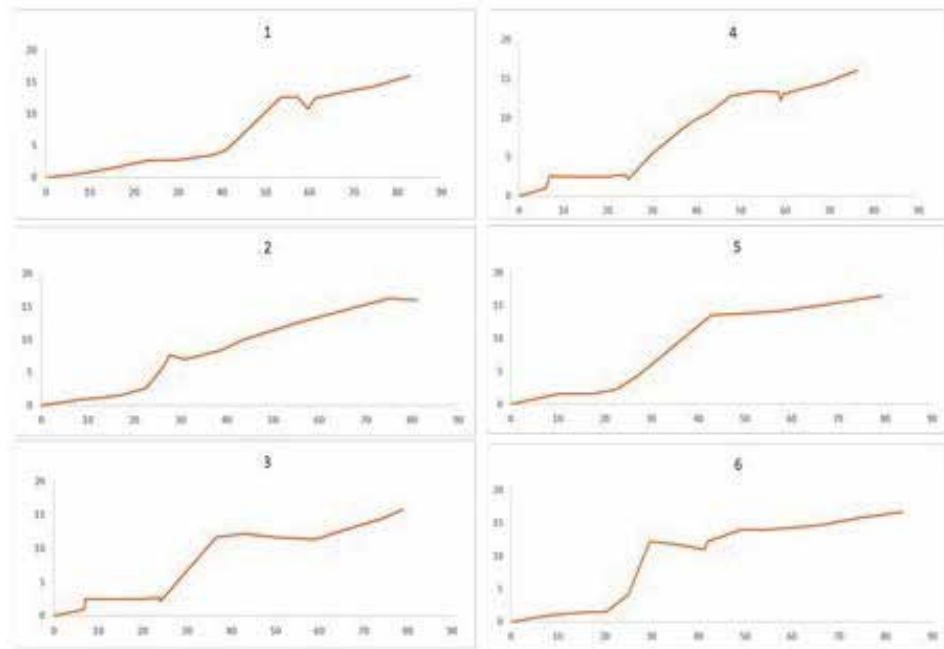
Figure 11.
Topographic profiles of Canoa Quebrada sea cliffs.

less sheltered area in relation to the attack of the waves due to smaller presence of beach rocks, the cliff receded 1.7 m in 13 years, equivalent to 15.5 m per century. The average speed of retreat of the cliff for the studied area is of 11.5 m per century.

It is also observed that the line of rupture of the sea cliff in the image of 2017 presents recesses, with gaps and gullies that did not exist in 2004, indicating morphogenetic processes acting differently over the years. In 2004, the performance of the marine processes at the base of the cliff was dominant, with more intense and uniform retreat of the slope. The presence of retreat in the image of 2017 indicates that there was a change in the relation of forces between the active processes, being now the subaerial processes more intense than the marine ones. In synthesis, it is concluded that the cliffs rapidly recede by the combined action of wave attack, rising sea levels, rainfall, and human action.

Figure 12.
Tourist equipment installed very close to the unstable sea cliffs, running the risk of being buried by landslides.

The average retreat velocity of the Canoa Quebrada sea cliff is compatible with the soft nature of the sediments that compose it. However, it is a very high speed if we consider the presence of an important urban nucleus and many tourist facilities located near or on the edge of the cliffs.

Environmental risk prevention was never present in the urban planning of Canoa Quebrada. Natural and anthropic factors were not taken into account in the expansion of the village on the cliffs. However, the cliffs of Canoa Quebrada are fragile and present strong risks of landslides, as indicated by the survey realized and exposed above. These factors must be taken into account in planning the future use and occupation of the area, under penalty of material damages, environmental degradation, and unsafety to the public. It is also noted that in the central portion of the beach, there are ventures located very close to the foot of the cliff, running at great risk of burial by materials from the top, through the frequent landslides (**Figure 12**).

In this central area, it is strongly advisable to remove part of the existing tourist structures, thus ensuring the use of this equipment safely by tourists and inhabitants of the town.

4. Coastal environmental problems in northern Colombia

### 4.1 Natural settings of the study area

The northern Colombia coast is located along the south side of the Caribbean Sea (latitude and longitude of the west and east boundaries are 11.1 north 74.9° west and 12.2 north 72.0 west, respectively) (**Figure 13**). The meteorological and oceanographic conditions are dominated by northeast trade wind, which results in the dominating northeasterly approaching wave occurring over 95% of the time. Effectively, northeasterly approaching waves occur by far the most frequently (**Figure 14**), driving a persistent westward longshore sediment transport.

The general shoreline orientation of the study area is roughly 60 degrees, or striking WSW-ENE. The relatively straight shoreline is interrupted by two protruding headlands, Santa Marta and Cabo De La Vela. A broad shoreline orientation change occurs near Riohacha. To the west, the shoreline orientation is roughly 68°, while to the east, the orientation is roughly 52° or a change of 16° around the broad Riohacha headland. These shoreline orientation changes play a significant role in beach processes.

Rocky coast dominates at both the Cabo de la Vela and Santa Marta headlands, with pocket sandy beaches distributing in the numerous embayment areas (**Figure 15**). Sandy beaches distribute along most of the coastline except at the

Figure 13.
The northern Colombia coast, located on the south side of the Caribbean Sea.
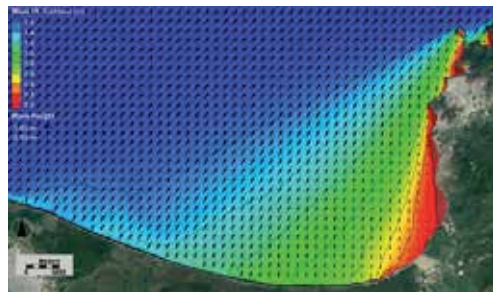
Figure 14.
Regional wave modeling results for NE (45°) approaching wave. Example of the area Santa Marta—Barranquilla Cienaga.

Figure 15.
Example of rocky coast at Santa Marta headland.

headlands. Numerous rivers discharge into the Caribbean Sea. Most of the sandy beaches distribute directly along the mainland. The westward longshore sand transport is illustrated in this example from Riohacha by the sand impoundment along the east updrift side of the long groin (**Figure 16**).

Several spit type barrier islands extend along this stretch of coastline, originated from westward spit growth, and are of the wave-dominated type [26]. All the tidal inlets are quite narrow with small flood and ebb deltas. This is controlled by the fact that the tidal range is mostly less than 0.3 m even during spring tides, while wave forcing is relatively strong. Therefore, beach-inlet interaction only has

Figure 16.
Example of sandy beach at Riohacha, accreted updrift by the help of jetties.

localized influences on beach erosion and accretion. Wave plays a dominant role in shaping the coastline, since it is the dominating forcing, causing beach erosion or accretion. Extreme energetic conditions associated with direct hit or nearby passage of tropical storms can have significant and long-lasting impacts on coastal morphology.

The beach processes along northern Colombia coast are relatively simple, driven predominantly by westward longshore sand transport. The trend of beach erosion or accretion and the state of the beach are largely controlled by the gradients of longshore sand transport, which can be caused by both natural and artificial factors.

4.2 Environmental problems at Santa Marta: Barranquilla area

About 19 km west of Barranquilla (km-19 site) (for location, see **Figure 13**), severe beach erosion has threatened a section of a major coastal highway (**Figure 17**). Presently, the highway is protected by recently installed riprap revetment. However, continued beach erosion is undermining the foundation of the riprap and likely the road in the near future. Furthermore, the erosion may continue to expand westward and propagate the problem over a larger area.

Figure 17.
Severe beach erosion at 19 km site threatening a major highway. The recently installed riprap is experiencing toe scour due to continued erosion.

Analysis of time-series aerial photos from Google Earth has shown that the beach along the km-19 coast is experiencing persistent rapid erosion from 2009 to 2015, at over 15 m per year. The sediment transport gradient along this stretch of coastline is caused by the shadowing effect of the Santa Marta headland, which creates a westward increasing wave height along the km-19 site. This results in more sediment being transported westward from the km-19 site than being transported into the site. A major coastal road to the city of Barranquilla is now practically at the shoreline (see **Figure 17**). Originally, the road was several hundred meters from the shoreline. In 2009, the distance was only 115 m. The waves along this section of the coast is quite energetic nearly all year round, and the longshore sediment transport gradient resulting is induced by natural morphological conditions.

4.3 Environmental problems at Riohacha coastline

The Riohacha coastline (for location, see **Figure 13**) provides an example of beach accretion and erosion associated with artificial interruption of the persistent westward longshore sand transport. **Figure 18** shows the aerial view of the Riohacha coastal line with a groin field. The groins were installed with the perspective to allow accretion of beaches.

Effectively, it is apparent that the groins at the updrift end have impounded a large amount of sand and resulted in a quite wide beach there (**Figure 19**). Several small rivers to the east and updrift of the beach contribute to the sand supply.

However, the field of these 150-m long groins nearly completely interrupted the westward longshore sand transport and resulted in severe beach erosion along a long and extending stretch of downdrift coast. **Figure 20** illustrates the erosion along the beach downdrift of the groin field. In addition, due to the depleted sand supply, the groins downdrift of the large beach failed to impound any sand. Similar sand bypassing patterns around and through a groin were found by [27] in a large-scale laboratory study on interaction of a groin with longshore sand transport.

4.4 Environmental problems at Costa Verde Cienega

Costa Verde Cienega (for location, see **Figure 13**) is located within the greater shadow zone of the Santa Marta headland and at the edge of the secondary shadow zone. The waves along this stretch of the coast are low due to the shadowing effect of the Santa Marta headland. A wave-height gradient exists along this stretch of the coast due to the secondary shadowing by the headland, although the rate of

Figure 18.
Aerial view of the Riohacha shoreline. Note the large amount of sand accumulation at the east-most three groins and little to no sand accumulation at the rest of the groins and erosion further downdrift.

Figure 19.
Large amount of sand accumulation updrift of the first groin. The groin is considerably higher than the beach.

Figure 20.
Severe beach erosion downdrift of the Riohacha groin field, exposing a crucial infrastructure to direct wave attack.

Figure 21.
Severe beach erosion along the Costa Verde Cienega coast, exposing a crucial pipeline (yellow marker). Note the low-profile sandbag groin and the earth-moving machine at the top of the picture. The earth-moving machine was moving sand from the upland to nourish the beach and attempting to control the erosion.

longshore sand transport should be much smaller due to the low wave. Beach erosion here has exposed a crucial pipeline along the coast (**Figure 21**). Various low-profile groins made of sand bags were installed in an effort to control the erosion. Based on field observations, the sandbag groins have very limited and localized effect.

In addition to the longshore sand transport gradient induced by natural processes, anthropogenic activities also play a significant role in the beach erosion in the area. The westward longshore sand transport and a transport gradient were induced by a 140-m long groin installed between January 2011 and May 2012. Rapid sand accumulation east and updrift of the long groin occurred. By May 2012, the updrift beach had grown to about 35 m landward of the tip of the long groin. Only 5 months later in October 2012, the updrift of the long groin was filled to the tip of the groin.

The impoundment at the groin created a transport gradient at the downdrift, which further contributed to the beach erosion problems caused by the natural wave-height gradient associated with the secondary shadowing of the Santa Marta headland. Therefore, similar to the long groins at Riohacha, the downdrift beach did not benefit from sand bypassing even when the updrift beach reached the tip of the groin.

4.5 Coastal mitigation in northern Colombia

The above examples, along with numerous other cases in the northern Colombia coast, strongly suggest that caution should be carefully exercised in artificially interrupting the persistent westward longshore sand transport. Impounding the longshore moving sand by engineering structures, many times by groin field, is quite easy to do. The often very rapid beach accretion at the updrift side of the structure may lead to construction of longer and more groins. This can quickly turn into a very destructive practice along the tropical trade wind-dominated coast, where longshore sand transport is westward almost 100% of the time.

Well-planned regional scale study should be developed in order to avoid these types of problems in the future. The study should investigate (1) the source and availability of the sand to the beach, (2) rate of longshore sand transport, and (3) most importantly, existing natural and anthropogenic causes of longshore sediment transport gradient. The study should have adequate temporal and spatial scales. Spatially, the study should include a long stretch of beach, particularly along the downdrift coast, to ensure that the downdrift effect induced by the shore protection structures is fully considered over a long period.

5. Conclusions

Coasts along Northeast Brazil and northern Colombia are beautiful environments. Being popular tourist destinations as well as desirable living areas, these coasts can be very valuable economically. Tourism along the coast, particularly at sandy beaches, constitutes a large income for the two countries. The increasing of urban activities in these areas also induces to the installation of many key structures to the functioning of the urban and economic life, such as harbors. For instance, the areas are very vulnerable to numerous natural and anthropogenic stressors.

The present study showed examples of the coastal environmental degradation caused by these stressors in two areas of northeast Brazil and three areas of northern Colombia. The erosion of the beaches in Brazil and Colombia and the collapse of sea cliffs of Canoa Quebrada, Brazil, cause damage to the population, either through the alteration of marine ecosystems or through the reduction of artisanal fishing, leisure, and recreation spaces or the reduction of fishing activities, vacation, and tourism. It leads to heavy losses to economic activity, such as job losses, decrease in the income and tax generation, and real estate depreciation.

In such a context, it is necessary to better plan the occupation and uses of these coastal areas, in order to promote a sustainable development. Specifically,

it is necessary to consider the fact that easterly trade wind has significant influence along the coastal area of both countries. It results in a dominating easterly approaching wave occurring over 95% of the time and then, in a unidirectional longshore transport, which has to be carefully considered in the moment to introduce equipment, structures, and housing in the shoreline. Considering that trade winds are in action in tropical areas, these findings should be applicable to many other tropical coasts.

Acknowledgements

Author details

Vanda Claudino-Sales[1*], Ping Wang[2], Fábio Perdigão Vasconcelos[3]
and Adely Pereira Silveira[3]

1 Federal University of Ceara State, and Master on Geography, Acarau Valley State University, Fortaleza, Brazil

2 University of South Florida (USF), Tampa, USA

3 State University of Ceará (UECE), Fortaleza, Brazil

*Address all correspondence to: vcs@ufc.br

IntechOpen

References

[1] Claudino-Sales V. Les littoraux du Ceará Evolution géomorphologique de la zone côtière de l'Etat du Ceará, Nord-est du Brésil [Thesis]. Paris: Université Paris-Sorbonne; 2002

[2] Claudino-Sales V. Os litorais cearenses. In: Borzacchiello J, Cavalcante T, Dantas E. (Org.). Ceará: Um novo olhar geográfico. Fortaleza: Edições Demócrito Rocha. 2005:189-210

[3] Claudino-Sales V. Cenários Litorâneos: Natureza e Ambiente na Cidade de Fortaleza, Ceará [Master's Dissertation]. São Paulo: University of São Paulo; 1993

[4] Claudino-Sales V, Wang P, Carvalho AM. Interactions between various headlands, beaches and dunes in the coast of Ceará state, Northeast Brazil. Journal of Coastal Research. 2018;**34**:413-428. DOI: 10.2112/JCOASTRES-D-16-00173

[5] Pedrosa AA. A geodinâmica e morfogênese das dunas eólicas na Praia de Canoa Quebrada, Aracati, Ceará, Brasil [Thesis]. Fortaleza: Universidade Federal de Ceará; 2016

[6] Castro JWA. Burying processes carried out by a mobile transversal dunefield, Paracuru County, state of Ceará, Brazil. Environmental Geology. 2005;**49**:214-218. DOI: 10.1007/s00254-005-0055-6

[7] Jiminez JA, Maia LP, Serra J, Morais JO. Aeolian dune migration along the Ceara Coast, northeastern Brazil. Sedimentology. 1999;**46**:689-701. DOI: 10.1046/j.1365-3091.1999.00240.x

[8] Wang W, Saha S, Pan HL, Nadiga S, White G. Simulation of ENSO in the new NCEP coupled forecast system model (CFS03). Weather Review. 2005;**133**:1574-1593. DOI: 10.1175/mwr2936.1

[9] Zanela ME. As características climáticas e os recursos hídricos do Estado do Ceará. In: Silva JB, Dantas EWC, Meireles AJA, editors. Ceará: um novo olhar geográfico. Fortaleza: Edições Demócrito Rocha, 2a edição; 2007. pp. 169-188

[10] FUNCEME (Fundação Cearense de Metereologia e Recursos Hídricos). Dados dos postos pluviométricos do Estado do Ceará. Retrieved from www.funceme.br/calendario/produto/municipio/; 2018

[11] INPH (Instituto Nacional de Pesquisas Hidroviárias). Simulação do regime de ondas no Pecém, Ceará (Report). Rio de Janeiro; 1996

[12] Maia LP. Procesos costeiros y balancio sedimentario ao largo de Fortaleza (NE Brasil): Implicaciones para un gestión adecuada de la zona litoral [Thesis]. Barcelona: University of Barcelona; 1998

[13] DHN (Diretoria de Hidrografia e Navegação). Tábua de Marés do Porto do Mucuripe (Report). Fortaleza; 2018

[14] Martin L, Suguio K. Variation of coastal dynamics during the last 7000 years recorded in beach-ridge plains associated with river mouths: Example from the central Brazilian coast. Palaeogeography, Palaeoclimatology, Palaeoecology. 1999;**99**:119-140

[15] Vasconcelos FP, Morais JSD, Diniz MT, Rego-Filho FF, Rocha GC Determination of shoreline variations of the metropolitan region of Fortaleza (Ceará State - Brazil) using methodology of GIS. In: Proceeding of CoastGIS 2007; Vol. 2. Santander, Spain: Copicentro-Bonifaz; 2007. pp. 233-343

[16] Vasconcelos FP. Dinâmica Costeira do Litoral de Fortaleza e os impactos da construção dos aterros das praias do

Meireles (Beira-Mar) e Iracema sobre o litoral de Caucaia (Report). Universidade Estadual do Ceará - UECE. Laboratório de Gestão Integrada da Zona Costeira – LAGIZC. Fortaleza; 2018

[17] Morais JO. Aspectos de Geologia Ambiental Costeira do Município de Fortaleza, Ceará [Thesis]. Fortaleza: Universidade Federal do Ceará; 1980

[18] Pitombeira ES. Litoral de Fortaleza – Ceará – Brasil, um exemplo de degradação. In: Anais do 1º Simpósio sobre Processos Sedimentares e Problemas Ambientais na Zona Costeira do Nordeste do Brasil. Recife: ABEQUA; 1995. pp. 59-62

[19] Morais JO. Geological assessment of environmental impact on the Littoral of Fortaleza, Ceará, Brazil. Urban Risk. 1993;**4**:23-39

[20] Paskoff R. Les Littoraux: L'impact des aménagements sur leur évolution. Paris: Editora Armand Colin; 2010

[21] Meireles AJA. Falésias do litoral leste do estado do Ceará – Análise dos Processos Morfogenéticos e Impactos Ambientais. Revista Geonotas. 1999;**3**(2):1-29

[22] Veyret Y. Les Risques. Paris: SEDES; 2003

[23] Miossec A. De l'érosion cotiére em general et le cas français en particulier. La Géographie Terre de Hommes. Numéro Especial: L'érosion. Octobre - Décembre 2018;**1571**:28-34

[24] Bird E. Coastal Geomorphologie, An Introduction. Chichester: Wiley; 2000

[25] Merlotto A, Bértola GR, Isla FI, Cortizo LC, Piccolo MC. Short and medium-term coastal evolution of Necochea municipality, Buenos Aires province, Argentina. Environment and Earth Science. 2014;**71**:1213-1225. DOI: 10.1007/s12665-013-2525-6

[26] Davis RA, Hayes MO. What is a wave-dominated coast? Marine Geology. 1984:313-329

[27] Wang P, Kraus N. Movable-bed model investigation of groin notching. Journal of Coastal Research. 2004, special issue;**33**:342-368

Edited by Jiayi Pan and Adam Devlin

Estuaries and their surrounding wetland regions are among the most productive ecosystems in the world, with more than half of humanity inhabiting their shores. Anthropogenic factors make estuaries highly susceptible to ecosystem degradation. Coastal waters are closely connected with human activity, and their dynamic processes may greatly affect coastal environments. This book provides a compendium of studies on estuarine dynamics, river plumes, and coastal water dynamics, studies that have investigated the changes in estuarine and coastal zones in response to sea-level rise and other environmental factors, and policy and management strategies to ensure the health and economy of coastal zones. This book aims to display novel frontiers in these fields and may help to inspire in-depth studies in the future.

IntechOpen